

# **Silicon-Based Optical Sensors for Fungal Pathogen Diagnostics**

**Von der Naturwissenschaftlichen Fakultät der  
Gottfried Wilhelm Leibniz Universität Hannover**

**und**

**dem Senat des Technion – Israel Institute of Technology**

zur Erlangung des Grades

Doktor der Naturwissenschaften (Dr. rer. nat.)

und

Doctor of Philosophy (PhD)

genehmigte Dissertation

von

**Christopher Heuer, M. Sc.**

[2024]

Referent: Prof. Dr. rer. nat. Thomas Scheper

Korreferentin: Prof. Ester Segal, PhD

Korreferent: Prof. Dr. rer. nat. Roland Ulber

Tag der Promotion: 10. November 2023

## Abstract

The last years have witnessed a link between the COVID-19 pandemic with increasing numbers of vulnerable patients and globally emerging incidences of severe drug-resistant fungal infections, thus, calling for rapid, reliable, and sensitive diagnostic tools for fungal infections. However, despite strong warnings from health authorities, such as the World Health Organization, concerning the fatal consequences of the global spread of drug-resistant pathogenic fungi, progress in fungal infection diagnosis and therapy is still limited. Today, gold standard methods for revealing resistance and susceptibility in pathogenic fungi, namely antifungal susceptibility testing (AFST), require several days for completion, and thus this lengthy process can adversely affect antifungal therapy and further promote the spread of resistance.

In this work, the use of photonic silicon chips consisting of micropatterned diffraction gratings as sensitive sensors for rapid AFST of clinically relevant fungal pathogens is investigated. These photonic chips provide a surface for the colonization of microbial pathogens at a liquid-solid interface and serve as the optical transducer element for label-free monitoring of fungal growth by detecting real-time changes in the white light reflectance. These sensor elements are used to track morphological changes of fungi in the presence of clinically relevant antifungals at varying concentrations to rapidly determine the minimum inhibitory concentration (MIC) values that help to classify pathogens as resistant or susceptible. We show that by careful design of the chip dimensions, this optical method can extend from bacteria, through yeasts, to filamentous fungi for accelerated AFST, which is at least three times faster than current gold standard methods and can provide same-day results.

Moreover, a 3D-printed microfluidic gradient generator was designed to complement the assay and provide an integrated system, which can potentially be employed in point-of-care settings. This gradient generator produces the two-fold dilution series of clinically relevant antimicrobials in an automated manner and is interfaced with the photonic silicon chips to include a complete, on-chip, label-free, and phenotypic assay. Using the bacterial species *Escherichia coli* and ciprofloxacin as a model pathogen-drug combination, MIC values can be expeditiously determined within 90 minutes compared to current clinical practices, which typically require up to 24 h for bacterial species.

**Keywords:** fungal pathogens; drug resistance; antifungal susceptibility testing; optical sensor; photonic silicon; microfluidics; 3D-printing

## Kurzfassung

In den letzten Jahren wurde eine Verbindung zwischen der COVID-19-Pandemie mit gesteigerter Anzahl an geschwächten Patienten und der Zunahme resistenter Pilzinfektionen, die nach schnellen, verlässlichen und sensitiven Diagnostikmethoden verlangen, deutlich. Obwohl Organisationen wie die Weltgesundheitsorganisation vor den verheerenden Folgen der globalen Verbreitung resistenter pathogener Pilze warnen, wurden in den letzten Jahren kaum Fortschritte in der Entwicklung neuer diagnostischer und therapeutischer Methoden zur Behandlung von Pilzinfektionen erzielt. Goldstandard-Methoden zur Unterscheidung von resistenten und empfindlichen Erregern (antimikrobielle Empfindlichkeitstestung) benötigen mehrere Tage, sodass der Behandlungserfolg beeinträchtigt und die Verbreitung resistenter Erreger begünstigt wird.

In dieser Arbeit werden photonische Siliziumchips, welche aus mikrostrukturierten optischen Gittern bestehen, als Sensoren für eine schnelle antimikrobielle Empfindlichkeitstestung von krankheitserregenden Pilzen und der Bestimmung der minimalen Hemmkonzentration (MHK) verwendet. Diese Siliziumchips bieten eine Oberfläche für das Wachstum mikrobieller Krankheitserreger, welche für die Größe und Morphologie verschiedener Mikroorganismen angepasst wird. Außerdem fungieren die Chips als optisch aktive Elemente, welche dazu dienen, das Pilzwachstum markierungsfrei und in Echtzeit anhand von Änderungen der Weißlicht-Reflexionsspektren dieser Chips zu beobachten, sodass ein schnelle Empfindlichkeitstestung mit Ergebnissen am selben Tag möglich wird.

Darüber hinaus wurde ein 3D-gedruckter mikrofluidischer Gradientengenerator entworfen, welcher die gewünschten Verdünnungen klinisch relevanter Antibiotika und Antimykotika automatisch erzeugt, sodass erste Schritte hin zur Patienten-nahen Empfindlichkeitstestung aufgezeigt werden können. Die Integration der photonischen Siliziumchips in den Gradientengenerator erlaubt es ein umfassendes, markierungsfreies sowie automatisiertes und phänotypisches Verfahren für die Empfindlichkeitstestung zu erhalten. Mithilfe des bakteriellen Modellorganismus *Escherichia coli* und des Antibiotikums Ciprofloxacin wird gezeigt, dass die MHK innerhalb von 90 Minuten bestimmt werden kann; eine deutliche Reduzierung im Vergleich zu derzeitigen klinischen Verfahren, die bis zu 24 Stunden für bakterielle Krankheitserreger benötigen.

**Schlagwörter:** Pilzinfektionen; Arzneimittelresistenz; Empfindlichkeitstestung von Pilzen; Optischer Sensor; Photonisches Silizium; Mikrofluidik; 3D-Druck

## Table of Contents

<b>Abstract .....</b>	<b>I</b>
<b>Kurzfassung .....</b>	<b>II</b>
<b>Table of Contents.....</b>	<b>III</b>
<b>List of Figures .....</b>	<b>V</b>
<b>List of Abbreviations .....</b>	<b>VI</b>
<b>1 Preamble.....</b>	<b>1</b>
<b>2 Motivation and Research Aims.....</b>	<b>3</b>
<b>3 Literature Survey.....</b>	<b>4</b>
3.1 Antifungal Susceptibility Testing.....	4
3.2 3D-Printing in Biotechnology .....	25
3.3 Silicon Diffraction Gratings as Optical Sensors .....	42
<b>4 Experimental.....</b>	<b>45</b>
<b>5 Results.....</b>	<b>52</b>
5.1 Antifungal Susceptibility Testing of <i>Aspergillus niger</i> .....	54
5.2 Photonic Si Microwell Architectures for Rapid Antifungal Susceptibility Determination of <i>Candida auris</i> .....	72
5.3 A 3D-Printed Microfluidic Gradient Generator with Integrated Photonic Silicon Sensors for Rapid Antimicrobial Susceptibility Testing .....	92
<b>6 Discussion .....</b>	<b>118</b>
<b>7 Conclusion and Outlook.....</b>	<b>121</b>
<b>8 References.....</b>	<b>122</b>

Table of Contents

<b>Acknowledgements .....</b>	<b>127</b>
<b>List of Publications and Academic Activities.....</b>	<b>128</b>
<b>Curriculum Vitae.....</b>	<b>131</b>

## List of Figures

- Figure 1** Graphical abstract of the review article “Paving the Way to Overcome Antifungal Drug Resistance: Current Practices and Novel Developments for Rapid and Reliable Antifungal Susceptibility Testing”. ..... 4
- Figure 2** Graphical abstract of the review article “3D Printing in Biotechnology - An Insight into Miniaturized and Microfluidic Systems for Applications from Cell Culture to Bioanalytics”. This figure was created with Biorender.com. .... 25
- Figure 3** Optical properties of Si diffraction gratings. (A-i) The diffraction gratings reflect light into a set of diffraction orders, and (A-ii) create a 2D diffraction pattern when illuminated with a laser (here exemplarily for a HeNe laser at 632 nm). Images adapted with permission from Mirsky *et al.*<sup>35</sup> (B) Schematic of a silicon diffraction grating. The light is reflected from the top and bottom of the microstructure. Image created according to Leonard *et al.*<sup>34</sup> ..... 43
- Figure 4** Principle of photonic silicon chips consisting of microwell diffraction gratings. (A) The photonic silicon chips are illuminated by a white light source, and a spectrometer records the zero-order reflected light. The insert shows a scanning electron micrograph of the microwell structure (scale bar corresponds to 4  $\mu\text{m}$ ). (B-i) The resulting reflectance spectra exhibit interference fringes as the top and bottom of the microstructure partially reflect the light. (B-ii) The reflectance spectra are analyzed by fast Fourier transform (FFT), and in the resulting single peaks, the peak height corresponds to the intensity of the reflected light and the peak position to the  $2nL$  value. The lens in figure part A was obtained with permission from biorender.com. .... 44
- Figure 5** Graphical abstract of the research article “Antifungal Susceptibility Testing of *Aspergillus niger* on Silicon Microwells by Intensity-Based Reflectometric Interference Spectroscopy”. ..... 54
- Figure 6** Graphical abstract of the research article “Photonic Si Microwell Architectures for Rapid Antifungal Susceptibility Determination in *Candida auris*”. ..... 72
- Figure 7** Graphical abstract of the research article “A 3D-Printed Microfluidic Gradient Generator with Integrated Photonic Silicon Sensors for Rapid Antimicrobial Susceptibility Testing”. ..... 92

## List of Abbreviations

<b>2D</b>	two-dimensional
<b>3D</b>	three-dimensional
<i>A. niger</i>	<i>Aspergillus niger</i>
<b>AFST</b>	Antifungal susceptibility testing
<b>AST</b>	Antimicrobial susceptibility testing
<b>BMD</b>	Broth microdilution
<i>C. auris</i>	<i>Candida auris</i>
<b>CAD</b>	Computer-aided design
<b>CAMHB</b>	Cation-adjusted Muller Hinton Broth
<b>CDC</b>	Centers for Disease Control and Prevention
<b>CFD</b>	Computational fluid dynamics
<b>CLSM</b>	Confocal laser scanning microscopy
<b>COVID-19</b>	Coronavirus disease 2019
<b>DSMZ</b>	Deutsche Sammlung von Mikroorganismen und Zellkulturen (English: German Collection of Microorganisms and Cell Culture)
<i>E. coli</i>	<i>Escherichia coli</i>
<b>EDTA</b>	Ethylenediaminetetraacetic acid



## List of Abbreviations

<i>e.g.</i>	<i>exempli gratia</i>
<b>EOT</b>	Effective optical thickness
<i>et al.</i>	<i>et alii</i>
<b>EUCAST</b>	European Committee for Antimicrobial Susceptibility Testing
<b>FFT</b>	Fast Fourier transform
<b>FIB</b>	Focused ion beam
<b>HR-SEM</b>	High-resolution scanning electron microscopy
<b>iPRISM</b>	Intensity-based phase-shift reflectometric interference spectroscopic measurements
<b>ITS</b>	Internal transcribed spacer
<b>LB broth</b>	Luria-Bertani broth
<b>MIC</b>	Minimum inhibitory concentration
<b>MOPS</b>	3-( <i>N</i> -morpholino)propanesulfonic acid
<b>OPD</b>	Optical path difference
<b>PBS</b>	Phosphate-buffered saline
<b>PCR</b>	Polymerase chain reaction
<b>PDA</b>	Potato dextrose agar
<b>PDB</b>	Potato dextrose broth

## List of Abbreviations

<b>PDYC medium</b>	Potato dextrose yeast extract casein hydrolysate medium
<b>pH</b>	<i>potentia hydrogenii</i>
<b>PRISM</b>	Phase-shift reflectometric interference spectroscopic measurements
<b>RPMI 1640 medium</b>	Roswell Park Memorial Institute medium
<i>S. cerevisiae</i>	<i>Saccharomyces cerevisiae</i>
<i>S. marcescens</i>	<i>Serratia marcescens</i>
<b>SDA</b>	Sabouraud dextrose agar
<b>SDS</b>	Sodium dodecyl sulfate
<b>SEM</b>	Scanning electron microscopy
<b>Tris HCl</b>	Tris(hydroxymethyl)aminomethane hydrochloride
<b>UV</b>	Ultraviolet

# 1 Preamble

Drug-resistant pathogenic fungi, such as *Aspergillus* and *Candida* species, represent an underestimated source of harm and disease among humans. They account for more than 1.6 million deaths annually worldwide, and drug-resistant fungal pathogens are prevalent all over the globe.<sup>1-4</sup> The spread of fungal infections in recent years is linked to climate change,<sup>4-6</sup> and the emergence of resistant fungal pathogens is ascribed to the excessive use and misuse of antifungals in agriculture and clinical settings.<sup>7,8</sup> Notably, the COVID-19 pandemic was also correlated with the spread of resistant fungal infections owing to increasing numbers of vulnerable and hospitalized patients.<sup>1,9-11</sup> For instance, the multidrug-resistant pathogenic yeast *Candida auris* (*C. auris*), where some isolates are recognized as pan-resistant (resistant to all classes of antifungals),<sup>12</sup> is now classified by the United States Centers for Disease Control and Prevention (CDC) as an urgent threat.<sup>13</sup>

As part of the global mission of tackling antimicrobial-resistant fungi, proper antimicrobial stewardship requires rapid, reliable, and sensitive tools for fungal disease diagnostics.<sup>14,15</sup> Antimicrobial susceptibility testing (AST), specifically antifungal susceptibility testing (AFST), is used to classify fungal pathogens into “resistant” and “susceptible” categories and helps to guide treatment decisions.<sup>15</sup> In such diagnostic tests, pathogenic fungi are exposed to clinically-relevant antifungal agents at varying concentrations, and the minimum inhibitory concentration (MIC) is determined, allowing physicians to predict the outcome of antifungal therapy.<sup>16,17</sup> Thus, AFST, including MIC determination, is essential for the correct antifungal prescription, improving treatment and reducing the spread of resistance.<sup>15</sup> However, conventional methods for AFST suffer from several shortcomings which hamper their widespread usage. For example, traditionally employed methods for AFST, like broth microdilution (BMD) or agar-based tests, are laborious and lengthy (up to 3 days),<sup>18,19</sup> while commercially-available automated methods (*e.g.*, Vitek2, bioMérieux) are only available for yeast species and still require 12 – 18 h.<sup>20,21</sup> Also, novel phenotypic approaches (*e.g.*, mass spectrometry,<sup>22</sup> flow cytometry,<sup>23</sup> calorimetry,<sup>24,25</sup> fluorescence microscopy<sup>26</sup>) have been only demonstrated for a limited organisms spectrum, rely on sophisticated and expensive instrumentation, or do not effectively expedite the assay time compared to existing methods. Nucleic acid-based (genotypic) approaches indeed expedite resistance detection;<sup>18</sup> yet, they lack the ability to reveal the phenotypic behaviour of a pathogen and fail when resistance-conferring genes or mutations are unknown.<sup>27</sup> Previously, the Segal group has developed a label-free silicon-based optical sensor system for monitoring the behaviour of bacteria and performing rapid AST.<sup>28</sup> In this diagnostic platform, photonic silicon chips consisting of micropatterned diffraction gratings provide the optical transducer element as well as the surface for *Escherichia coli* (*E. coli*) colonization. Bacterial growth is optically tracked by phase-shift reflectometric interference spectroscopic measurements (termed PRISM), which analyze time-dependent phase shifts in the white light reflectivity from the photonic chips. MIC values were determined within

## Preamble

2 – 3 h (compared to 8 h with state-of-the-art methods, Vitek2) by monitoring bacterial growth at varying concentrations of different clinically-relevant antibiotics.<sup>28</sup> This work extends the concepts of PRISM for susceptibility testing of additional microorganisms and establishes for the first time a modified assay for rapid AFST of the yeast *C. auris* and the mould *Aspergillus niger* (*A. niger*) within only 6 h and 12 h, respectively.

The potential to perform such accelerated susceptibility testing at a point-of-care setting (testing at the patient site)<sup>29</sup> necessitates its successful miniaturization into a holistic device, where the integration of the various required steps (*e.g.*, generation of the antimicrobial dilution series, sensing, and MIC determination) is accomplished.<sup>14,30,31</sup> Thus, in this work, the use of 3D printing for the fabrication of a microfluidic gradient generator that automatically creates the desired antimicrobial concentrations (two-fold dilution series) for convenient on-chip susceptibility testing is demonstrated. The 3D-printed gradient generator is interfaced with the photonic silicon chips to include a complete and convenient on-chip assay for label-free and phenotypic AST. The MIC can be successfully and expeditiously determined within 90 min (compared to 8 – 24 h in current clinical practices) for the bacterial species *Escherichia coli* and ciprofloxacin as a model pathogen-drug combination.

## 2 Motivation and Research Aims

The primary motivation of this work is to harness the optical properties of photonic silicon chips consisting of periodic arrays of microwell diffraction gratings and develop a platform for rapid, label-free, and convenient AFST. The development of resistance in fungal pathogens is recognized as an emerging global health risk, and there is an urgent need for rapid and reliable diagnostic tools to assist in the treatment of invasive fungal infections.<sup>18</sup> Thus, this research aims to address this challenge by developing a new phenotypic, easy-to-use, cost-effective, and reliable assay for expeditious and label-free AFST that can potentially be performed in point-of-care settings. Such an assay can provide an alternative to existing techniques and enable advanced treatment decisions in antifungal therapy.

The Segal group has demonstrated the application of photonic silicon chips consisting of diffraction gratings for rapid AST of bacteria. The optical PRISM assay allowed real-time monitoring of bacterial growth patterns in the presence of different antimicrobials at varying concentrations and MIC values determination within 2 – 3 h for *E. coli*.<sup>28</sup> This research aims to extend this assay to fungal pathogens and develop a rapid AFST method for filamentous fungi and yeast species. Moreover, a second aim is to use high-resolution 3D printing to develop the PRISM AST assay into a convenient and automated method for point-of-care testing.

The specific aims of this research are:

**(a) Photonic Silicon Chips for Rapid AFST of Filamentous Fungi.** The research will focus on developing a protocol for rapid AFST of pathogenic filamentous fungi on photonic silicon chips using *A. niger* as a mould model species.

**(b) Rapid AFST of the Emerging Pathogenic Yeast *C. auris*.** *C. auris* is an emerging and often multidrug-resistant pathogenic yeast species.<sup>8</sup> Thus, this part of the research will focus on the application of photonic silicon chips for rapid AFST of this fungal species. Moreover, the potential to differentiate yeast cells and bacteria by their growth patterns will be studied.

**(c) 3D Printing for Convenient and On-Chip AST.** To evolve the PRISM assay into a method suitable for point-of-care testing, the potential of high-resolution 3D printing for the integration of various steps required for AST (*e.g.*, the combination of antimicrobial dilutions preparation and growth monitoring) is investigated.

### 3 Literature Survey

The following literature survey consists of three sections and gives an overview of AFST, the application of 3D printing in biotechnology, and the use of microstructured silicon diffraction gratings as sensitive sensors for microbial growth monitoring and AST. First, the review article “*Paving the Way to Overcome Antifungal Drug Resistance: Current Practices and Novel Developments for Rapid and Reliable Antifungal Susceptibility Testing*” emphasizes the need for rapid fungal pathogen diagnostics and describes traditional AFST methods, as well as the latest developments in this field. Second, the review article “*3D Printing in Biotechnology - An Insight into Miniaturized and Microfluidic Systems for Applications from Cell Culture to Bioanalytics*” explains the different 3D printing techniques for the fabrication of microfluidic devices and how this technology can be used in the various fields of biotechnology. The final section then describes the function and application of silicon-based optical sensors for rapid and label-free microbial growth monitoring and AST in real-time.

#### 3.1 Antifungal Susceptibility Testing

This section is reproduced from the following review article:

### “Paving the Way to Overcome Antifungal Drug Resistance: Current Practices and Novel Developments for Rapid and Reliable Antifungal Susceptibility Testing”

Christopher Heuer, Janina Bahnemann, Thomas Scheper and Ester Segal

*Small Methods*, 5, e2100713 (2021)

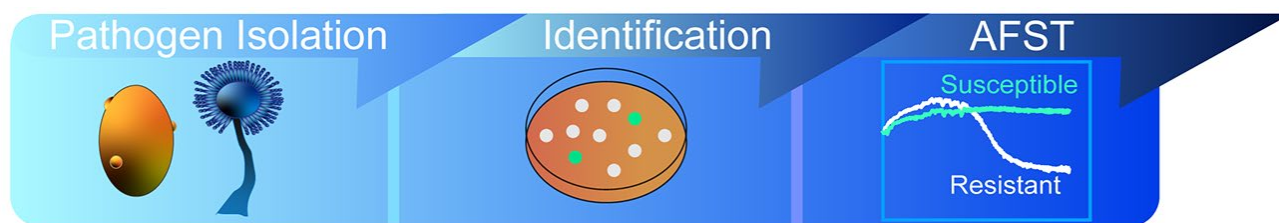


**Figure 1** Graphical abstract of the review article “Paving the Way to Overcome Antifungal Drug Resistance: Current Practices and Novel Developments for Rapid and Reliable Antifungal Susceptibility Testing”.

# Paving the Way to Overcome Antifungal Drug Resistance: Current Practices and Novel Developments for Rapid and Reliable Antifungal Susceptibility Testing

Christopher Heuer, Janina Bahnemann, Thomas Scheper, and Ester Segal\*

The past year has established the link between the COVID-19 pandemic and the global spread of severe fungal infections; thus, underscoring the critical need for rapid and realizable fungal disease diagnostics. While in recent years, health authorities, such as the Centers for Disease Control and Prevention, have reported the alarming emergence and spread of drug-resistant pathogenic fungi and warned against the devastating consequences, progress in the diagnosis and treatment of fungal infections is limited. Early diagnosis and patient-tailored therapy are established to be key in reducing morbidity and mortality associated with fungal (and cofungal) infections. As such, antifungal susceptibility testing (AFST) is crucial in revealing susceptibility or resistance of these pathogens and initiating correct antifungal therapy. Today, gold standard AFST methods require several days for completion, and thus this much delayed time for answer limits their clinical application. This review focuses on the advancements made in developing novel AFST techniques and discusses their implications in the context of the practiced clinical workflow. The aim of this work is to highlight the advantages and drawbacks of currently available methods and identify the main gaps hindering their progress toward clinical application.

treating IFI, rising resistance to these drugs is a cause of major concern.<sup>[1,3]</sup> For example, the globally emerging multi-drug-resistant species *Candida auris* is now recognized by the Centers for Disease Control and Prevention (CDC) as an urgent threat.<sup>[4]</sup> Thus, its proper treatment is therefore crucial for both individual therapeutic outcomes and preventing its spread.<sup>[5]</sup> The increasing and undirected use of antifungals in medicine and agriculture is associated with the rising numbers of acquired resistance in fungi.<sup>[3]</sup> The readers are referred to the following excellent reviews on fungal pathogens<sup>[6,7]</sup> and antifungal resistance<sup>[3]</sup> for further reading. The latter, in combination with the challenges associated with developing novel antifungals, emphasizes the need for rapid disease detection and adequate antifungal therapy protocols.<sup>[3,8]</sup> Implementing such measures is part of a proper antimicrobial stewardship aimed at reducing the excessive usage of antimicrobial therapies in

## 1. Introduction

Invasive fungal infections (IFI) are a rising cause of morbidity and mortality among humans with underlying medical conditions, causing more than 1.4 million deaths annually worldwide.<sup>[1,2]</sup> As only four antifungal classes (azoles, echinocandins, polyenes, and pyrimidine analogs) are currently available for

clinical settings by encouraging physicians to prescribe appropriate antimicrobials only when truly required.<sup>[9]</sup>

Antimicrobial susceptibility testing (AST), specifically antifungal susceptibility testing (AFST), is employed to reveal the susceptibility or resistance of fungal pathogens to clinically relevant antifungals.<sup>[10,11]</sup> In these tests, pathogenic fungi are exposed to various concentrations of a panel of antifungals to determine the minimum inhibitory concentration (MIC) values, which are typically defined as the lowest drug concentration inhibiting the pathogen's growth.<sup>[12]</sup> MIC values allow physicians to predict the success of antifungal treatments.<sup>[13]</sup> As such, rapid AFST is an essential tool to improve antifungal therapy by choosing the correct and most effective antifungal drug in a timely manner. Early therapy initiation is also crucial for enhancing the therapeutic outcome of patients with invasive fungal infections, such as life-threatening bloodstream infections.<sup>[14]</sup> Clinical AFST is conducted according to standardized methods and protocols, published by the European Committee on Antimicrobial Susceptibility Testing (EUCAST) or the Clinical and Laboratory Standards Institute (CLSI).<sup>[12,15]</sup> Yet, as these gold-standard methods are laborious and typically require at least 24 h (and in many cases, several days) for completion,<sup>[12,16]</sup> significant research efforts are now being directed toward the development of more expedited phenotypic and molecular AFST techniques.<sup>[17,18]</sup>

C. Heuer, J. Bahnemann, T. Scheper

Institute of Technical Chemistry

Leibniz University Hannover

30167 Hannover, Germany


C. Heuer, E. Segal

Department of Biotechnology and Food Engineering

Technion–Israel Institute of Technology

Haifa 320003, Israel

E-mail: esegal@technion.ac.il

 The ORCID identification number(s) for the author(s) of this article can be found under <https://doi.org/10.1002/smt.202100713>.

© 2021 The Authors. Small Methods published by Wiley-VCH GmbH. This is an open access article under the terms of the Creative Commons Attribution-NonCommercial License, which permits use, distribution and reproduction in any medium, provided the original work is properly cited and is not used for commercial purposes.

DOI: 10.1002/smt.202100713

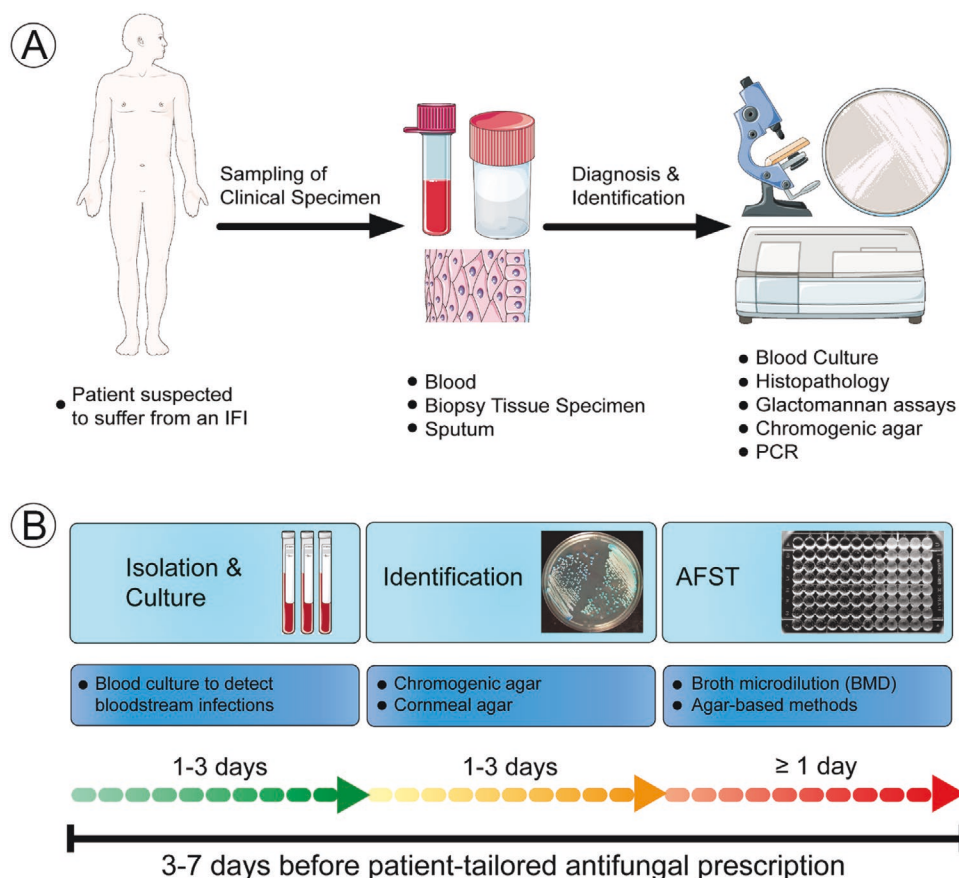


**Figure 1.** A) General workflow for IFI diagnosis. First, clinical specimens, such as blood or tissue, are sampled from a patient suspected to suffer from an IFI. Methods such as blood culture and histopathology, among others, are used for fungal diagnosis. Subsequently, procedures such as selective chromogenic agar or PCR are employed to discriminate fungal species. B) Workflow for suspected candidemia includes fungal pathogen isolation, identification, and AFST. First, blood cultures reveal the presence of bloodstream pathogens in a patient within 1–3 days. Subsequently, the employment of agar-based methods such as chromogenic agar or cornmeal agar enables fungal species identification within 1–3 days. Eventually, AFST and MIC determination requires at least another day but allows a patient-tailored antifungal prescription to improve antifungal treatment and reduce the spread of antifungal resistance. Images are adapted with permission under the terms of the Creative Commons CC BY license from Servier Medical Art (smart.servier.com). Chromogenic agar plate and BMD plate are adapted with permission.<sup>[34,35]</sup> Copyright 2006, Oxford University Press (chromogenic agar plate) and 2003, American Society for Microbiology (BMD plate) respectively.

## 2. Fungal Disease Diagnosis Precedes AFST

The diagnosis of IFIs predates AFST, and **Figure 1A** presents a generalized workflow. First, the fungal pathogen is isolated from a patient sample (i.e., blood, tissue biopsy specimens, etc.), and subsequently, various techniques are applied for disease diagnosis and species identification to confirm the type of infection (e.g., fungal, bacterial, or viral).<sup>[14]</sup> For instance, blood culture detects fungal bloodstream infections,<sup>[19]</sup> while histopathology reveals fungi in tissue samples.<sup>[20]</sup> Furthermore,  $\beta$ -glucan and galactomannan assays detect fungal cell wall antigens in body fluids such as serum.<sup>[14]</sup> Species identification can be performed on chromogenic agar,<sup>[21]</sup> and recently, molecular approaches like polymerase chain reaction (PCR) detecting species-specific DNA sequences have become of increasing importance.<sup>[22]</sup> For a comprehensive overview of IFI diagnosis techniques, the readers are referred to the recent review articles of Sanguinetti et al.<sup>[22]</sup> and Ruhnke et al.<sup>[19]</sup> Unfortunately,

due to the emergence of antifungal resistance in fungi, proper therapy cannot rely on IFI diagnosis alone, and subsequent AFST is inevitable.<sup>[3,23]</sup>

Conventional AFST methods, as practiced in clinical laboratories, include the gold standard broth microdilution (BMD) and the commercial agar-based Etest (bioMérieux, France). While these techniques are simple and well established, they are slow and require multiple preparation steps. The latter stems from the prerequisite for high cell densities; for example, for yeasts,  $0.5\text{--}2.5 \times 10^5$  CFU mL<sup>-1</sup> and  $1\text{--}5 \times 10^6$  CFU mL<sup>-1</sup> are required for BMD and Etest assays, respectively.<sup>[12,24]</sup> Thus, culturing remains an essential prerequisite before standard AFST.

Figure 1B schematically illustrates a typical workflow of a sample derived from a patient suspected of suffering from candidemia (a bloodstream infection with *Candida*), one of the most common types of life-threatening invasive fungal diseases.<sup>[2]</sup> First, blood samples are taken from the patient



and then added to designated bottles containing blood culture medium to improve fungal pathogen recovery.<sup>[25,26]</sup> These bottles are thereafter placed in blood culture systems, such as the automated BD BACTEC (Becton Dickinson, USA) or the BacT/ALERT (bioMérieux, France).<sup>[25]</sup> In the case of candidemia, these systems typically achieve detectable fungal growth within 1–3 days<sup>[14]</sup> (termed a “positive blood culture result”). Subsequently, the second step of species identification, using conventional agar-based techniques, requires another 1–3 days.<sup>[14,27]</sup> For instance, chromogenic agar enables differentiation of *Candida* species, relying on species-specific enzyme-based cleavage of chromogenic compounds, by naked eye observation of differently colored colonies.<sup>[21]</sup> Another approach employs cornmeal agar, a chlamyospore-inducing medium. It allows for morphological identification of *Candida albicans* (*C. albicans*), the most frequently found pathogenic yeast in humans,<sup>[6]</sup> by microscopically investigating its chlamyospore-formation.<sup>[28]</sup>

The subsequent and final diagnostic step of AFST takes at least another day when traditional broth and agar-based techniques are employed.<sup>[12,24]</sup> In these methods, the determination of MIC values for a specific pathogen drug is achieved by visual detection of fungal growth on agar plates or in a liquid medium in the presence of various antifungal concentrations.<sup>[12,29,30]</sup> Thus, the whole process (Figure 1B) of pathogen isolation, identification, and AFST, which precedes appropriate antifungal prescription, ideally takes between 3 and 7 days, assuming it is not even further delayed (e.g., by slow-growing strains or logistic influences such as transportation or laboratory opening hours).<sup>[31,32]</sup>

Accelerating AFST will, of course, shorten the time for a patient-tailored antifungal therapy, and more importantly, the introduction of new AFST methods may profoundly impact the lengthy preceding preparation steps. For example, genotypic techniques detecting antimicrobial resistance genes can be directly performed from sputum, swabs, and blood culture specimens alongside pathogen identification.<sup>[33]</sup> Analyzing single microbial cells by time-lapse microscopy reduces the required number of cells,<sup>[11]</sup> potentially avoiding the time-consuming prerequisite of obtaining high cell densities as required in conventional approaches. Thus, we believe that AFST techniques that are readily integrable with pathogen isolation, detection/identification could be a game-changer and potentially practiced in point-of-care settings.

### 3. The Ideal AFST Method

If we could design the perfect AFST method, this approach would be sensitive, accurate, and reliable in terms of the MIC value determination while also being easy to use and cost-effective. Furthermore, this method would allow parallelization and multiplexing to analyze multiple antimicrobials or pathogens simultaneously with a broad microorganism spectrum, minimal sample pre-processing steps, and integrability. Other factors, such as the preferential phenotypic or genotypic resistance determination and the test setting (e.g., centralized laboratories vs. point of care), should also be considered. Most importantly, this approach should yield MIC values and allow “resistant” and “susceptible” determinations as quickly as pos-

sible to improve therapy outcomes and reduce the spread of antifungal resistance.

#### 3.1. Phenotypic versus Genotypic AFST

In general, susceptibility testing methods can be divided into phenotypic and genotypic approaches. Phenotypic methods monitor the growth and other physiological changes (e.g., size and shape) of cells in the presence of different antimicrobials at varying concentrations.<sup>[11]</sup> As such, they reveal specific phenotypic susceptibility profiles and provide a comprehensive assessment of what antimicrobials agents can be used to treat infections caused by pathogenic microorganisms.<sup>[36]</sup> However, these phenotypic methods are time-consuming as, in most cases, they are culture-based. By contrast, genotypic techniques, representing a nonculture methodology, rely on detecting established resistance-conferring genes and mutations on the DNA level.<sup>[11]</sup> While offering rapidity, genotypic approaches only reveal the presence of resistance factors;<sup>[37]</sup> they do not allow susceptibility determination, and as such, they are correctly referred to as genotypic antimicrobial resistance (AMR) detection methods.<sup>[38]</sup> Nevertheless, genotypic AMR detection is fast and preferred if seeking specific resistance-conferring genes.<sup>[11,33]</sup>

In this review, we mainly focus on phenotypic methods that enable MIC determination and a more definitive prediction of how fungal pathogens will behave in the presence of clinically relevant antifungal drug concentrations. Although recent research efforts have increasingly focused on novel methods for phenotypic AFST, in an attempt to improve the current situation, traditional methods that have not changed since the first days of AST remain the gold standard in the context of clinical laboratory practice.

## 4. Standard Methods and Their Commercial Adaptations

AFST was first described in the 1970s and included broth and agar-based methods, such as BMD, disk diffusion, and agar screening.<sup>[39,40]</sup> Today, nearly half a century later, these techniques, validated by the EUCAST and the CLSI, are still widely used in clinical laboratories, and several commercial adaptations are available. **Table 1** summarizes these AFST techniques and briefly describes both their concept and typical assay time. That table also provides a short comparison of the main advantages and disadvantages of these methods, as discussed in the following few paragraphs.

#### 4.1. Standard Methods—Frequently Used But Not Changed for Decades

BMD is the current gold standard for AFST of yeasts and molds. Twofold serial dilutions of antifungals are made in a liquid medium (broth) and inoculated with a predefined and standardized cell number, as shown in **Figure 2A**. Growth is determined visually or spectrophotometrically in a 96-well plate,

**Table 1.** Summary of standard AFST methods and their commercial adaptations.

Name	Measuring principle	Assay time	Advantages	Disadvantages	Ref.
Standard methods					
Broth microdilution (BMD)	Visual or spectrophotometric measurement of turbidity in a liquid medium	24 h for <i>Candida</i> species, 46–50 h for <i>Aspergillus</i> species and up to 72 h for <i>Cryptococci</i>	Standardized by EUCAST and CLSI Available for yeasts and molds Cheap when prepared in the laboratory	Laborious and lengthy Subjective when read visually	[12,15,16,18,41]
Disk diffusion	Zone of inhibition around antifungal disks on agar plates	24 h for <i>Candida</i> and <i>Aspergillus</i> species	Standardized by CLSI Available for yeasts and molds Easy to perform and cheap	Lengthy No MIC values	[18,30,42]
Agar screening	Visual detection of growth in a liquid medium	48 h	Standardized by EUCAST Cheap, easy to perform, and read	Lengthy No MIC values Only screening of <i>Aspergillus</i> species	[43–45]
Commercial adaptations					
Vitek2 (bioMérieux, France)	Turbidity in a liquid medium	Usually 12–18 h	Automated Objective results Accelerates AFST compared to BMD	High investment costs Only available for yeast	[18,46,47]
Sensititre YeastOne (Thermo Fisher Scientific, USA)	Colorimetric detection in a liquid medium	24 h	Easy to perform Less subjective than BMD	Lengthy Not validated for molds	[18,48–50]
Etest (bioMérieux, France)	Zone of inhibition around a strip with an antifungal gradient	24–48 h for yeast (up to 72 h for <i>Cryptococcus</i> species) and 16–72 h for molds	Easy to use Available for yeast and molds An agar-based method that provides MICs	Lengthy Sometimes subjective	[18,24,51–53]

and the MIC is defined as the lowest growth-inhibiting drug concentration.<sup>[12,15,16,41]</sup> Both EUCAST and CLSI standardized this reference method for routine AFST of yeasts and molds. While BMD is a relatively cheap method, it is laborious and lengthy. For example, for *Candida* and *Aspergillus* species, the MIC is determined only after 24 or 48 h, according to EUCAST protocols.<sup>[12,16]</sup> Furthermore, these methods require high cell numbers for both yeasts and molds, typically  $\geq 10^5$  CFU mL<sup>-1</sup> according to EUCAST.<sup>[12,16]</sup>

Disk diffusion is a widely used agar-based AFST method standardized by CLSI for yeast and filamentous fungi.<sup>[30,42]</sup> Paper disks with a specific antifungal concentration are placed on an agar plate with a standardized inoculum. Antimicrobial activity is determined by measuring the inhibition zone diameter of the growth-free area around the disk (see Figure 2B), which correlates to the antifungal's diffusion rate through the agar and the fungus susceptibility to that drug.<sup>[18]</sup> While disk diffusion is simple and cheap, its main disadvantage is its inability to produce MIC values, impairing the interpretation of results for emerging fungal pathogens and novel antifungal agents.<sup>[18]</sup> Furthermore, this agar-based approach takes a long time of 24 h for *Candida* and *Aspergillus* species and requires a large inoculum size of  $\geq 10^6$  CFU mL<sup>-1</sup>.<sup>[30,42]</sup>

Azole agar screening, relevant only for *Aspergillus* species, was recently established by EUCAST and is based on the

commercially available VIP check assay (Mediaproducs BV, Netherlands).<sup>[43–45]</sup> A 4-well agar plate contains 4  $\mu\text{g mL}^{-1}$  itraconazole, 2  $\mu\text{g mL}^{-1}$  voriconazole, 0.5  $\mu\text{g mL}^{-1}$  posaconazole, and a drug-free well. *Aspergillus* growth is determined visually after 48 h (see Figure 2C) and used to screen for azole-resistant isolates.<sup>[43,45]</sup> While this method is easy to perform and cheap, it is time-consuming, requires a high number of cells (0.5 McFarland,  $\geq 10^6$  CFU mL<sup>-1</sup>)<sup>[16,43]</sup>, and importantly does not allow for MIC values determination.

#### 4.2. Commercial AFST Approaches—Adaptations of Standard Methods

The BMD method has several commercially available adaptations that simplify the assay procedure and MIC readout. For example, the Sensititre YeastOne (ThermoFisher) assay is performed in 96-well plates containing a growth medium with serial dilutions of the antifungal agent and the Alamar Blue redox indicator.<sup>[18]</sup> When entering the cells, the latter undergoes a color change from blue to red when reduced by enzymes of metabolically active fungi (reducing resazurin to resorufin; see Figure 2D).<sup>[50,57]</sup> Accordingly, the MIC is defined as the lowest antifungal concentration where no color change to red occurs, and the medium remains blue.<sup>[50]</sup> The endpoints are read after

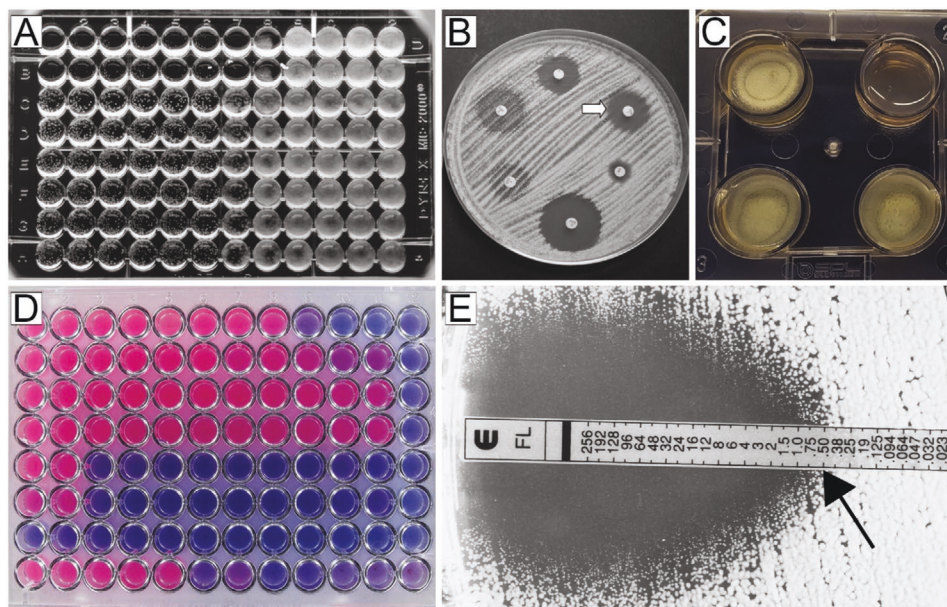


**Figure 2.** Standard methods and commercial adaptations for routine AFST. A) Visual detection of fungal growth in a liquid medium with twofold antifungal dilutions in the BMD method. Adapted with permission.<sup>[35]</sup> Copyright 2003, American Society for Microbiology. B) Characteristic disk diffusion assay with zones of inhibition (as indicated by the arrow) around paper disks on an agar plate. Adapted with permission.<sup>[54]</sup> Copyright 2007, American Society for Microbiology. C) Growth of *Aspergillus sp.* in a 4-well agar plate during the azole agar screening method. Reproduced with permission.<sup>[43]</sup> Copyright 2018, European Society of Clinical Microbiology and Infectious Diseases. D) The Sensititre YeastOne assay uses a colorimetric redox indicator to indicate fungal growth. Adapted with permission under the terms of the Creative Commons CC BY license.<sup>[55]</sup> Copyright 2011, the Authors. Published by PLoS ONE. E) Etest strip inhibiting the growth of *Candida sp.* on an agar plate. The MIC is read where the ellipse-shaped zone of inhibition and the strip intersect, as indicated by the arrow, and determined to be  $0.5 \mu\text{g mL}^{-1}$ . Adapted with permission.<sup>[56]</sup> Copyright 1998, American Society for Microbiology.

24 h and are found to be in good agreement with the reference MICs.<sup>[50]</sup> Although the Sensititre YeastOne assay is only validated for yeast species, some studies demonstrated its potential for AFST of molds.<sup>[49]</sup>

An automated commercially available BMD adaptation for susceptibility testing of yeast is the Vitek2 (bioMérieux). This system uses AFST cards with 64 wells containing dried medium with antifungal agents at varying concentrations. The machine introduces the cells into the wells, and their growth is monitored by turbidity measurements. MIC values are typically determined after 12–18 h for *Candida* species and comply well with MIC values determined by BMD.<sup>[46,47]</sup> The Vitek2 system is mostly used in centralized clinical laboratories where high throughput measurements are crucial. It should be noted that this system is not established for molds and suitable Vitek2 AFST cards are not available.

Another commercially available AFST assay is the agar-based Etest assay (bioMérieux, France), which is an adaptation of the disk diffusion test, where plastic strips containing an antifungal gradient and concentration scale are placed on an agar plate with a standardized inoculum size and incubated.<sup>[51,53]</sup> The MIC value is determined based on the intersection of the formed ellipse-shaped zone of inhibition and the drug concentration on the strip, as shown by the arrow in Figure 2E.<sup>[51,53,56]</sup> The Etest is inexpensive, easy to perform, and the MIC values comply well with the BMD gold standard<sup>[52]</sup>; yet, the time to readout is lengthy (24–48 h for yeasts and 16–72 h for molds).<sup>[24]</sup>

While these methods have simplified the AFST assay and, in some cases, allowed its automation, the required size of the initial inoculum size remains high and comparable to that of

standard methods. For AFST of yeast, the Etest and the Sensititre YeastOne use an inoculum size of  $\geq 10^6 \text{ CFU mL}^{-1}$ , whereas the Vitek2 employs a 2.0 McFarland equivalent ( $\approx 10^7 \text{ CFU mL}^{-1}$ ).<sup>[24,48,58,59]</sup>

## 5. New Tools for Phenotypic AFST

The time to readout remains the main bottleneck of current state-of-the-art phenotypic AFST methods. Therefore, a significant research effort is directed toward expediting phenotypic AFST, and new techniques, relying on mass spectrometry, flow cytometry, calorimetry, fluorescence microscopy, and optical on-chip assays, are emerging.<sup>[60–64]</sup> Table 2 summarizes these new AFST approaches and briefly describes their concept and typical assay time. The table also provides a short comparison of these methods' main advantages and disadvantages, as discussed in the next paragraphs.

### 5.1. Molecular Analysis by Mass Spectrometry

Mass spectrometry (MS) is already used in many clinical laboratories for the identification of bacteria and fungi, and, as such, it accelerates treatment decisions by classifying pathogens into high or low resistance prevalence categories, as shown in Figure 3A. In recent years, MS-based methods are emerging for AFST of microorganisms.<sup>[66,67,73]</sup> For example, MS was used to detect the presence of resistance-conferring enzymes, such as  $\beta$ -lactamases, revealing their activity by monitoring antibiotic

**Table 2.** Overview of new AFST methods.

Name	Measuring principle	Assay time	Advantages	Disadvantages	Ref.
Mass spectrometry	Shifts within mass spectral profiles	15 h incubation for minimal profile changing concentrations (MPPC) 3 h for differentiation between susceptible and resistant isolates	Rapid differentiation of susceptible and resistant isolates Different approaches possible (e.g., whole-cell profiles, antibiotic degradation analysis)	High investment costs for instrumentation Arduous workflow	[11,38,65–67]
Flow cytometry	Fluorescence signal to differentiate dead and viable cells	1–9 h exposure of fungal cells to antifungals	Rapid AFST Demonstrated for yeast and molds	Labor-intensive workflow and required technical expertise	[18,63,68–70]
Calorimetry	Heat flow related to fungal metabolism	24 h for <i>Candida</i> species and 48 for <i>Aspergillus</i> species	Available for yeast and molds	Does not accelerate AFST compared to reference methods	[64,71,72]
Fluorescence microscopy	Fluorescence microscopy analyzes microcolony area on porous aluminum oxide	3.5–7 h for various <i>Candida</i> species and 14 h for <i>Aspergillus</i> species	Rapid AFST	Arduous workflow including culturing, staining, and microscopy	[61]
On-chip optical assays	Intensity changes of light reflected from a silicon diffraction grating	10–12 h for <i>Aspergillus niger</i>	Rapid compared to reference BMD Label-free and real-time monitoring	Only demonstrated for <i>Aspergillus niger</i>	[60]

degradation, as depicted in Figure 3B.<sup>[66]</sup> In this case, cells suspected of encoding for antimicrobial degrading enzymes are incubated with antimicrobials, and subsequent MS reveals their degradation and allowed researchers to determine if resistance-conferring enzymes were present or not.<sup>[66]</sup> Although this concept requires only a few hours of incubation time (up to 3 h), it only provides information about specific resistance mechanisms.<sup>[11,65]</sup> A more holistic approach involves analyzing the entire MS profiles or the proteomic profiles of microorganisms after their exposure to varying concentrations of antimicrobial agents, as shown in Figure 3C, and is mainly applied for AFST of fungi. For example, in a study from 2009, *C. albicans* cells were exposed to different fluconazole concentrations, and the shifts in the proteome were examined after 15 h of incubation by MS.<sup>[62]</sup> Minimal profile changing concentrations (MPCC) were defined as the lowest antifungal concentration, leading to a shift in the mass spectrum compared to a no-drug control.<sup>[62]</sup> de Carolis et al. have extended this methodology to other *Candida* and *Aspergillus* species and demonstrated a complete agreement of MPCCs with CLSI MICs after 15 h of incubation.<sup>[74]</sup> Differentiation of resistant and susceptible isolates without determining MPCC values was even achieved within 3 h of incubation.<sup>[75]</sup> The main drawbacks of MS for AFST include the high costs of the instrument and, so far, insufficient validation.<sup>[11,65]</sup> Also, it should be noted that fungal cell incubation in the presence of various antifungal agents before MS-based AFST requires high cell densities (typically  $10^6$  cells mL<sup>-1</sup> and above).<sup>[62,74,75]</sup>

## 5.2. Flow Cytometry

In flow cytometry assays, the fungal cells are cultured in the presence of different antifungal concentrations following staining with fluorescence dyes such as propidium iodide, ethidium bromide, or acridine orange.<sup>[63,69,70,76]</sup> These

nucleic-acid selective dyes penetrate damaged membranes (propidium iodide, ethidium bromide)<sup>[63]</sup> or indicate alterations in the DNA's secondary structure during cell death by switching fluorescence from green to red (acridine orange).<sup>[77]</sup> Therefore, changes in the fluorescence are used to distinguish between dead and viable cells by flow cytometry, as depicted in Figure 4A-i. Characteristic flow cytometry results, where acridine orange is used to stain *Candida glabrata* (*C. glabrata*) after exposure of 4 h to various concentrations of the antifungal caspofungin, are presented in Figure 4A-ii. In this work, the MIC is referred to as the minimum fluorescence-enhancing concentration (MFEC), defined as the minimum drug concentration yielding an increased fluorescence signal in a pre-defined number of cells.<sup>[69]</sup> The determined MFEC values were found to agree well with BMD and Etest reference methods for most fungi–drug combinations.<sup>[69]</sup>

Flow cytometry allows for rapid AFST of various *Candida* and *Aspergillus* species; the exposure time of fungal cells to the antifungal agents varies between species and protocols but typically lies in the range of 1–9 h.<sup>[63,68–70,78]</sup> Yet, it should be noted that also flow cytometry requires high cell numbers (commonly around  $10^6$  CFU mL<sup>-1</sup>).<sup>[63]</sup> Furthermore, the labor-intensive workflow, the necessary technical expertise, and its limitations for resource-limited settings are perceived as disadvantages of this technique.<sup>[18]</sup>

## 5.3. Calorimetry

In calorimetric AFST techniques, such as isothermal microcalorimetry (IMC), vials contain growth medium at varying antifungal concentrations and cells at defined inoculum size (typically around  $10^4$ – $10^5$  CFU mL<sup>-1</sup>).<sup>[64,71,72]</sup> Changes in the differential heat flow between the sample vial and a reference vial, ascribed to the fungus metabolism, are measured over time at a constant temperature; see Figure 4B-i for a schematic layout

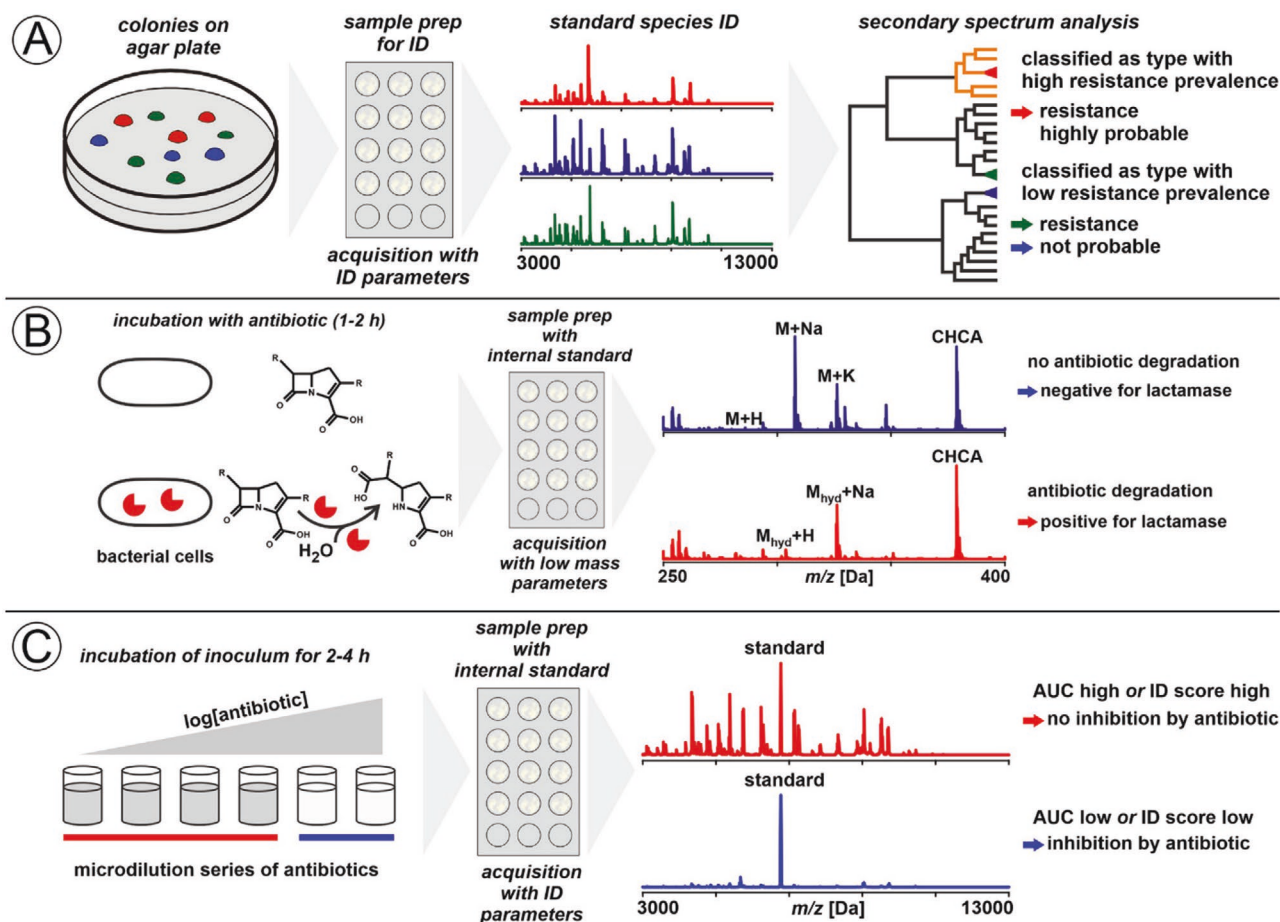


**Figure 3.** Mass spectrometry-based concepts to advance AST of bacteria and fungi. A) Species identification by MS gives a hint about drug resistance in the microbial pathogen. B) MS-based analysis of enzymatic antimicrobial degradation reveals the presence of resistance-conferring enzymes. C) Incubation of microbial pathogens in the presence of varying antimicrobial concentrations and analysis of entire mass spectral profiles or proteomic profiles. Reproduced with permission under the terms of the Creative Commons CC BY license.<sup>[66]</sup> Copyright 2019, the Authors. Published by Frontiers Media S.A.

of a typical microcalorimeter. The produced heat is correlated to microbial growth and enables MIC or minimum heat inhibitory concentration (MHIC) value determination as depicted in Figure 4B-ii.<sup>[64,71]</sup> Here, the MHIC was defined as the lowest drug concentration that reduces by 50% the total heat produced (after a designated time) compared to a drug-free fungus control.<sup>[71]</sup> IMC has been successfully applied for molds, planktonic yeast, and yeast biofilms; yet, it does not expedite AFST compared to reference methods. For example, MHIC values were determined after 24 h for *Candida* species and after 48 h for *Aspergilli* and biofilms.<sup>[64,71]</sup> However, IMC is recognized as a potential method for high-throughput AFST and testing novel antifungal drugs.<sup>[18]</sup>

#### 5.4. Fluorescence Microscopy to Analyzes Microcolonies on Porous Aluminum Oxide

Fluorescence microscopy has been applied for AFST of yeast and mold species by monitoring microcolonies on porous aluminum oxide (PAO).<sup>[61,80]</sup> This ceramic material retains cells on its surface, whereas nutrients and antimicrobials contained in agar can diffuse through the porous structure (pore sizes

20–200 nm; 60 μm thick) when a PAO strip is placed on an agar plate, see Figure 5A. Therefore, environmental conditions can be rapidly altered by transferring PAO strips between agar plates of different compositions. Importantly, the PAO substrate enables effective imaging of microcolonies by using microscopy techniques such as fluorescence and scanning electron microscopy (SEM).<sup>[81]</sup>

The employment of PAO substrates for AFST was first demonstrated for *Candida* species: In this assay, sterile PAO strips are placed on agar plates with a specific antifungal concentration (see Figure 5A representing a PAO strip on a sheep's blood agar plate), and subsequently, *Candida* cells are seeded onto the PAO strip (at a density of  $2 \times 10^3$  to  $2 \times 10^4$  CFU mm<sup>-2</sup>), as presented in Figure 5B and incubated. The microcolony area at varying antifungal concentrations is monitored by fluorescence microscopy following staining with Fun-1/Calcofluor White, as depicted in Figure 5C. These dyes stain nucleic acids (Fun-1) and the fungal cell wall (Calcofluor White), respectively.<sup>[82]</sup> Analyzing changes in the microcolony area allows for MIC determination after 3.5–7 h for *Candida* species, and the results agree well with standard BMD testing and Etest.<sup>[61]</sup> In another work, Ingham et al. extended this approach to AFST of *Aspergillus* species enabling

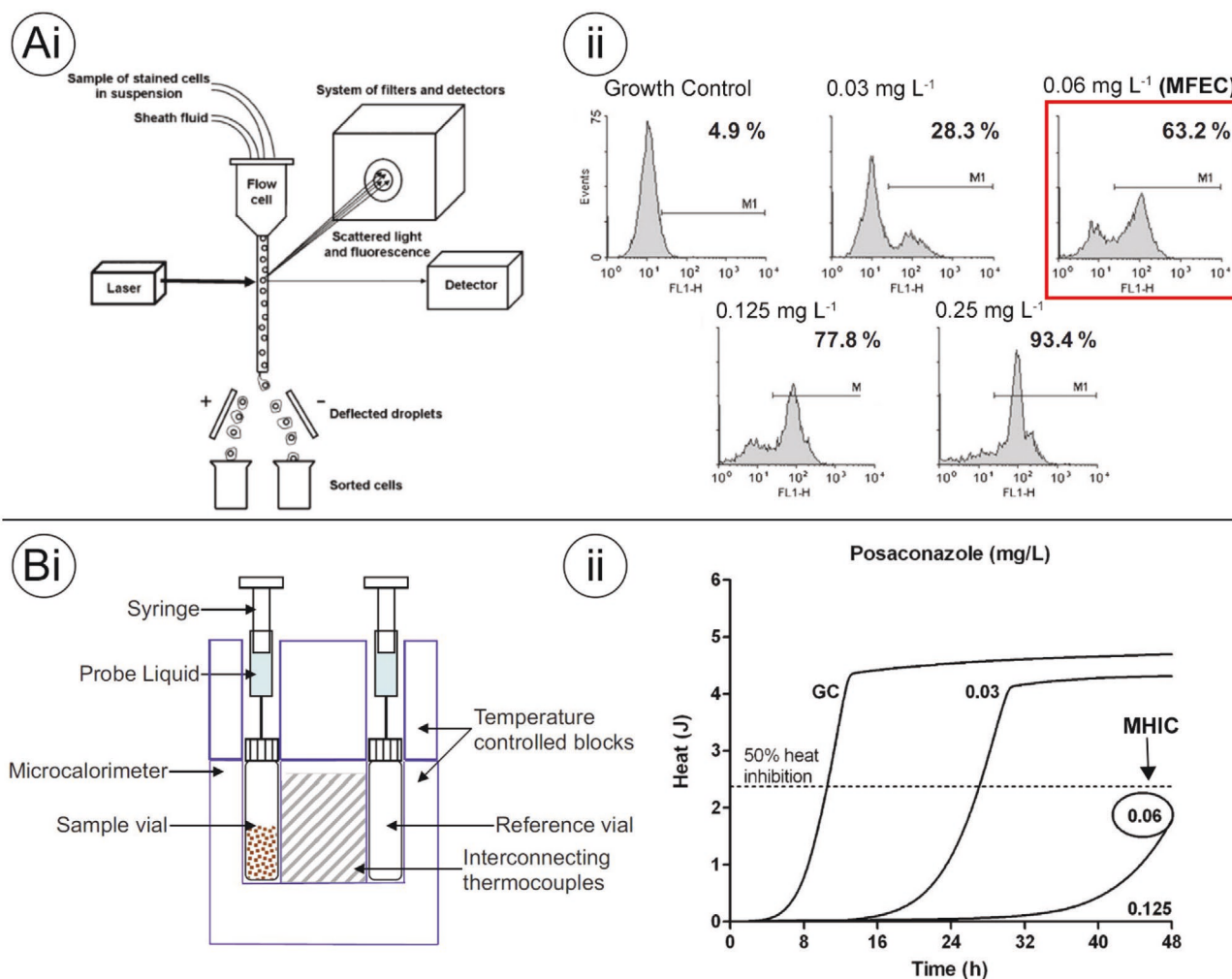


**Figure 4.** Flow cytometry and calorimetry for phenotypic AFST. A-i) Fungal cells are introduced into a flow cytometer which acquires light scattering and fluorescence emission of individual fungal cells using a system of laser beams, filters, and detectors after exposure to varying antifungal concentrations and staining with a fluorescence dye. A-ii) Flow cytometry histograms depict the number of *C. glabrata* cells versus fluorescence intensity caused by acridine orange upon entering the cells after exposure to different caspofungin concentrations. The MFEC is determined to be  $0.06 \text{ mg L}^{-1}$ , as indicated by the red frame. At this concentration, the number of cells exhibiting elevated fluorescence correlated to cell damage is 63.2%; this value is above the specific cutoff value of 50%. Adapted with permission.<sup>[63,69]</sup> Copyright 2006, Blackwell Verlag GmbH (A-i) and Copyright 2011, Springer Nature (A-ii), respectively. B-i) A schematic of an IMC device consisting of a sample vial and a reference vial within a temperature-controlled block. Thermocouples interconnecting both ampoules measure the differential heat flow between sample and reference. B-ii) Characteristic IMC heat flow curves of *Aspergillus fumigatus* (*A. fumigatus*) at varying posaconazole concentrations. The MHIC is determined to be  $0.06 \text{ mg L}^{-1}$  (indicated by the arrow) as at this concentration, a 50% inhibition of heat flow compared to a growth control without antifungal is visible after 48 h. Adapted with permission.<sup>[71,79]</sup> Copyright 2009, American Society of Civil Engineers (B-i) and Copyright 2012, European Society of Clinical Infectious Diseases (B-ii), respectively.

MIC determination for echinocandin antifungal agents within 14 h.<sup>[80]</sup> Although these PAO assays are a rapid AFST approach, and MICs mostly agree with standard AFST methods,<sup>[61,80]</sup> the workflow is complex as it requires fluorescence labeling, microscopy, and image analysis. Moreover, this method does not directly track changes in the cells' physiology but only relies on obtaining a fluorescence signal of stained cells.

### 5.5. On-Chip AST on Photonic Silicon Arrays

A recent approach for rapid AST employs optical sensors based on photonic silicon arrays for label-free monitoring of bacte-

rial and fungal behavior during exposure to antimicrobials in real time.<sup>[60,83–85]</sup> These sensors are based on diffraction gratings, consisting of periodic micropatterned silicon architectures of micrometer-dimensions, which are used as the optical transducer element and preferential surface for microbial colonization as presented in **Figure 6A**. These sensors were first demonstrated to optically track the growth of *Escherichia coli* (*E. coli*) and determine MIC values within 2–3 h (compared to 8 h with state-of-the-art automated methods) by monitoring bacterial growth patterns in the presence of varying concentrations of clinically relevant antibiotics.<sup>[83]</sup>

These on-chip optical assays were further extended for AFST of *Aspergillus niger* (*A. niger*) by tuning the chip architecture

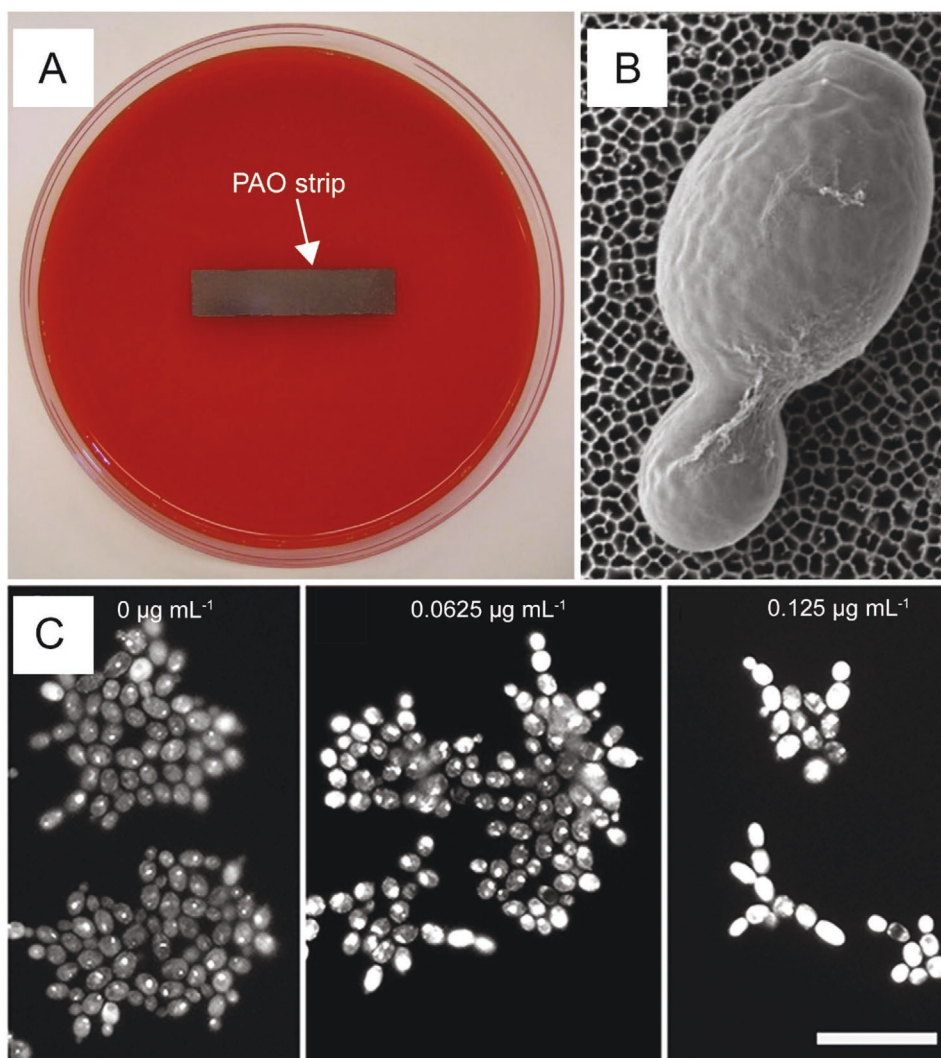


**Figure 5.** Fluorescence microscopy-based PAO assays for AFST. A) PAO strips of  $36 \times 8$  mm are placed on an agar plate allowing nutrients and antimicrobials to pass through the highly porous structure while B) *Candida* cells seeded on the porous material are retained on its surface. C) Microcolonies of *Candida tropicalis* on PAO are analyzed by fluorescence microscopy after exposure to increasing concentrations of voriconazole and fluorescence staining. The white scale bar indicates 20  $\mu\text{m}$ . Adapted with permission.<sup>[18]</sup> Copyright 2007, National Academy of Sciences, USA. (A) and adapted with permission under the terms of the Creative Commons CC BY license.<sup>[6]</sup> Copyright 2012, the Authors. Published by PLoS ONE (B,C).

to arrays of microwells with a width of  $\approx 3$   $\mu\text{m}$  and a depth of  $\approx 4$   $\mu\text{m}$ , allowing entrapment of individual *A. niger* conidia within the wells (see inset of Figure 6A-iv). The experimental setup is simple and includes a flow cell with temperature-controlled microfluidic channels in which the photonic chips are fixed individually and illuminated by a conventional white light source, as depicted in Figure 6B. The chip reflectance spectrum shows characteristic interference fringes as light is partially reflected from the silicon microstructure's top and bottom interfaces, as illustrated in Figure 6C. Applying frequency analysis to the collected spectrum results in a single peak (Figure 6E), where the peak amplitude corresponds to the intensity of the reflected light, and the peak position corresponds to the value  $2nL$  ( $n$  is the refractive index of the medium which fills the microstructure and  $L$  represent the depth of the microstructure/wells). The AFST assay is performed in two steps: first, fungal conidia are introduced onto the photonic

chip and given 15 min to settle within the microstructure. Subsequently, clinically relevant antifungals (e.g., amphotericin B and voriconazole) at varying concentrations are introduced into the channels (see Figure 6D), and fungal growth is monitored by analyzing changes in intensity as a function of time.<sup>[60]</sup> At drug levels at the MIC and above, growth is inhibited, as illustrated in Figure 6D-i, and no intensity reduction occurs, as depicted in Figure 6E-i. In contrast, at subinhibitory concentrations, the fungal hyphae formation on top of the photonic silicon chip, as shown in Figure 6D-ii, causes an intensity decrease in the reflected light, as illustrated in Figure 6E-ii. Accordingly, the MIC is defined as the lowest antifungal concentration at which the intensity does not change over time; see Figure 6F for characteristic intensity curves over time for fungal growth at varying voriconazole concentrations and corresponding optical micrographs. While this AFST approach is rapid (MIC determination within 12 h) compared to reference methods, it was only demonstrated

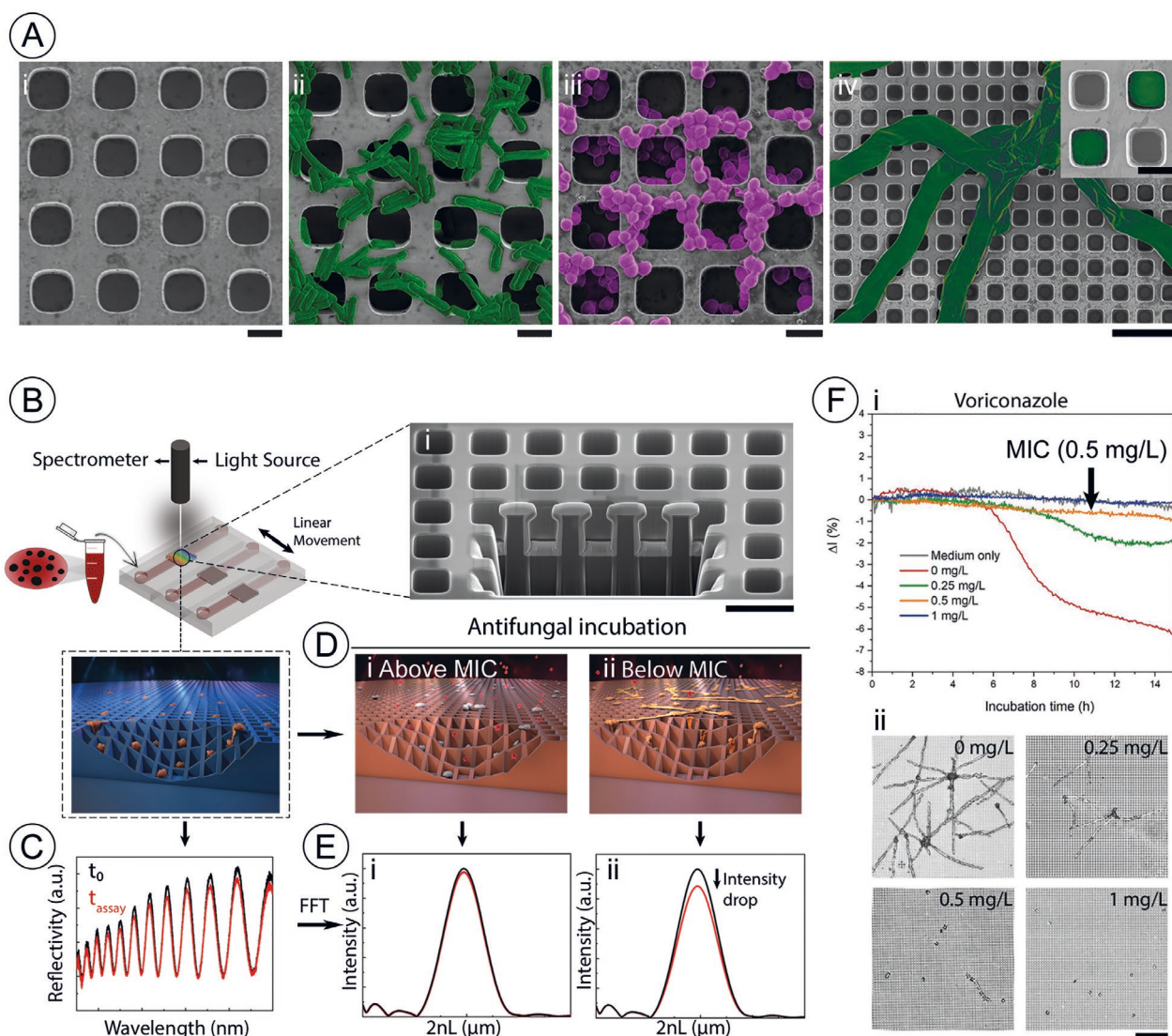


**Figure 6.** On-chip AFST on photonic silicon arrays. A-i) High-resolution SEM images of a silicon array consisting of microwells. These chips provide a unique surface for microbial colonization, for example of A-ii) *E. coli*, A-iii) *Staphylococcus aureus*, and A-iv) *A. niger*. The scale bars represent 2  $\mu\text{m}$  A-i to A-iii), 10  $\mu\text{m}$  A-iv), and 3  $\mu\text{m}$  (inset), respectively. B) The photonic silicon arrays entrap *A. niger* conidia while being illuminated by a white light source. B-i) A cross-sectional HR-SEM obtained by focused ion beam procedure depicts the periodic microwell structure with a width of  $\approx 3 \mu\text{m}$  and a depth of  $\approx 4 \mu\text{m}$ , creating C) interference fringes in the reflectance spectrum. D) Clinically relevant antifungals are introduced at varying concentrations after allowing the conidia to settle within the microwells resulting in D-i) growth inhibition and E-i) stable intensity values at concentrations above the MIC or D-ii) hyphal growth on top of the silicon array and E-ii) a resulting intensity decrease at subinhibitory antifungal concentrations. F-i) Characteristic intensity curves over time for *A. niger* growth at varying voriconazole concentrations and F-ii) corresponding optical micrographs. The scale bar represents 50  $\mu\text{m}$ . Adapted with permission.<sup>[60]</sup> Copyright 2020, American Chemical Society.

for *A. niger* as a model species. Furthermore, the inoculum suspension adhered to the high cell number ( $10^5$  conidia  $\text{mL}^{-1}$ ) used in EUCAST reference protocols.<sup>[60]</sup>

## 6. Molecular Resistance Detection—Nonculture Methods

As previously discussed in this review, the main advantage of nonculture methods is their rapidity in comparison to most phenotypic techniques, which rely on monitoring growth. The major nonculture approaches are molecular analysis by MS,

various genotypic techniques, and transcriptome analysis. In the following sections, we describe the concepts of these methods, focusing only on genotypic and transcriptome analysis. For MS, we refer the reader to Section 5.1. and note that while these MS-enabled AFST assays are nonculture by definition, extended time (up to 15 h) for microbial growth is required.<sup>[62,74]</sup>

### 6.1. Genotypic Antimicrobial Resistance Detection

Current phenotypic AFST methods and their preceding workflow (conventional and new) are still quite lengthy (2–6 days



for diagnosis and identification<sup>[14,27]</sup> and mostly >10 h for AFST<sup>[12,15,46,62,64]</sup>); genotypic approaches can expedite resistance analysis to only a couple of hours.<sup>[17,33]</sup> These methods can identify pathogens and reveal their antimicrobial resistance by detecting the pathogens' DNA, including resistance-conferring genes or mutations by PCR, or employing whole genome sequencing for a comprehensive overview of resistance genes and mutations in a pathogen's genome.<sup>[11,38,86]</sup>

### 6.2. PCR-Based Assays for the Detection of Resistance-Confering Mutations

For antifungal resistance in *Candida* species, most studies focused on detecting single nucleotide polymorphisms (SNP) in the glucan synthase encoding *FKS* genes.<sup>[17]</sup> Mutations in these genes alter the enzymes' amino acid structure and make it less affected by echinocandin-class antifungals.<sup>[1,3,17]</sup> Azole resistance is more challenging to detect in *Candida* species owing to the complexity of underlying resistance mechanisms. Yet, for *Aspergilli*, several mutations in the *CYP51A* gene associated with azole resistance have been identified.<sup>[18]</sup> Thus, classical genotypic approaches are limited to only predetermined genes, which reveal resistivity and cannot unveil susceptibility and determine MIC values.<sup>[11,33]</sup>

Most genotypic methods rely on PCR-based assays and allow resistance analysis within only a couple of hours.<sup>[87–89]</sup> For example, Dudiuk et al. have adapted classical PCR assays to detect mutations in the *FKS1* and *FKS2* genes, responsible for echinocandins resistance, in *C. glabrata*. Zhao et al. have combined asymmetrical PCR with molecular beacon probe-based melting curve analysis to detect mutated *FKS1* and *FKS2* genes in clinically collected *C. glabrata* samples within only 3 h. Furthermore, commercially available real-time PCR assays, such as the AsperGenius (PathoNostics, Netherlands) and MycoGENIE (Ademtech, France), were recently developed to detect *Aspergillus* DNA as well as few mutations that confer resistance to azole antifungals within 2.5 h.<sup>[90–92]</sup> A significant advantage of these genotypic approaches is their high sensitivity which enables species identification and resistance detection directly from body fluids such as sputum, bronchoalveolar lavage (BAL) fluids, or positive blood cultures,<sup>[33,93]</sup> thereby avoiding the prerequisite of obtaining high cell densities ( $10^3$ – $10^6$  cells mL<sup>-1</sup>) in most phenotypic AFST methods.<sup>[12,15,46,63,64]</sup> For example, the AsperGenius assay is validated for testing directly from BAL fluids and has a limit of detection for *Aspergillus fumigatus* species identification and resistance detection of 10 and 75 genomes per sample, respectively.<sup>[93]</sup> Additionally, commercially available PCR-based assays for *Candida* species identification, such as the T2Candida panel (T2 biosystems, USA) and the SeptiFast assay (Roche Diagnostics, Germany), have recently entered the market.<sup>[94,95]</sup> Exemplarily, the T2Candida panel permits the identification of five clinically relevant *Candida* pathogens with high specificity (~99%) and low detection limit (1–3 CFU mL<sup>-1</sup>) within 3–5 h directly from blood.<sup>[94]</sup> While, to the best of our knowledge, there is no commercially available PCR-based assay providing resistance detection in *Candida* species from clinical specimens, these assays can still facilitate treatment decisions as they allow identification of fungal pathogens (e.g., *Candida*

*krusei*) that feature intrinsic drug resistance to some antifungal agents.<sup>[96]</sup> We envision that these tests will be refined, and also the detection of resistance markers will be available in the near future.

### 6.3. Whole Genome Sequencing

A more holistic approach that does not only unravel resistance-conferring mutations in a single gene but instead analyzes the whole genome of a pathogen is termed whole genome sequencing (WGS).<sup>[97]</sup> Figure 7 illustrates a general schematic of such genomic approaches for antimicrobial resistance detection. In such assays, the pathogenic microbes (bacteria or fungi) are isolated from clinical specimens; subsequently, the genomic DNA is cut into short fragments that are amplified and sequenced. Finally, a specialized software is used to assemble the sequencing results enabling detailed analysis and the detection of resistance genes and mutations.<sup>[11]</sup> WGS principally enables concurrent species identification, strain typing, and comprehensive detection of resistance-conferring genes and mutations.<sup>[98]</sup> Concerning AMR detection in fungal pathogens, WGS has been successfully applied to confirm numerous SNPs linked to resistance toward azoles, echinocandins, and 5-flucytosine in *C. glabrata*.<sup>[99]</sup> However, in the routine clinical praxis, the practicability of WGS is currently still limited as it is costly, slow (several days turnaround time), and requires complex and sophisticated software for data analysis and interpretation.<sup>[97,98,100,101]</sup> Furthermore, a standardized and open-access database with all known resistance genes and mutations for the entirety of pathogenic microorganisms is still lacking, as emphasized by the EUCAST.<sup>[98,102]</sup>

For a more comprehensive overview of genotypic AMR approaches, we would like to refer the reader to the recent articles of Boolchandani et al.<sup>[86]</sup> and van Belkum et al.<sup>[38]</sup> A more specific insight into nucleic acid-based and molecular strategies for resistance detection in fungi is presented by Sanguinetti and Posteraro,<sup>[17]</sup> and Kidd et al.<sup>[103]</sup> in their review articles. Rath et al. provide an overview of commercially available PCR assays for *Aspergillus* species identification and resistance detection.<sup>[90]</sup> To summarize, genotypic AMR techniques have a great potential to expedite the treatment of severe fungal infections by directing the physicians on which drugs should be avoided.<sup>[36]</sup>

### 6.4. RNA-Based Resistance and Susceptibility Detection—The Transcriptomic Approach

Molecular detection of antimicrobial resistance is not limited to proteome and DNA analyses, and messenger RNA (mRNA) profiling is emerging as a tool for resistance detection in microbial pathogens.<sup>[101,104,105]</sup> These methods are based on monitoring the expression signature of mRNA transcripts (transcriptome analysis by RNA sequencing) and leverage the fact that susceptible and resistant microorganisms have discernible mRNA profiles upon antibiotic exposure, allowing their classification into resistant or susceptible categories.

As an example, the GoPhAST-R assay<sup>[101]</sup> allowed unravelling the susceptibility of five different bacterial species for

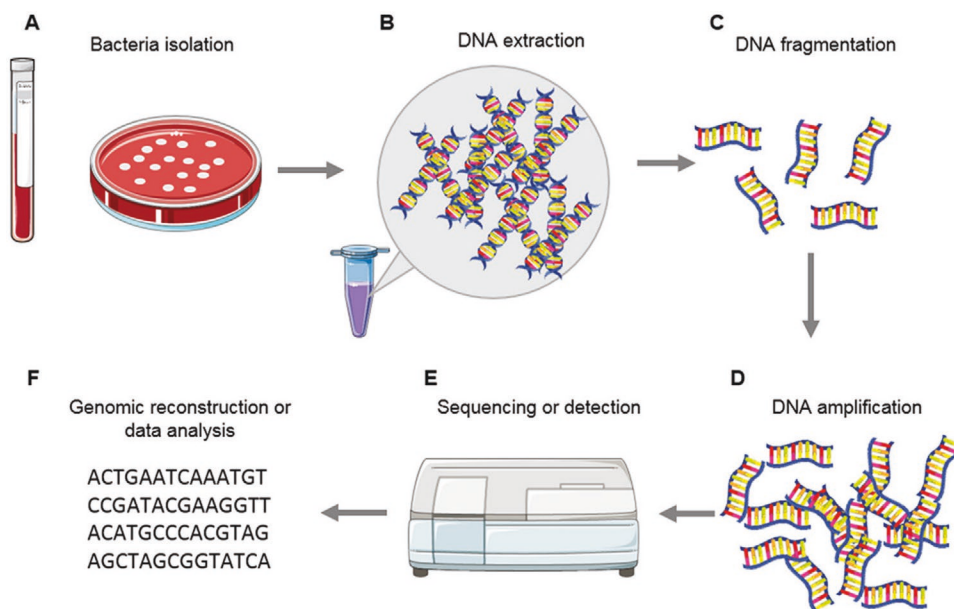


**Figure 7.** Workflow depicting genomic approaches for antimicrobial resistance detection in pathogenic microorganisms. A) Bacteria or fungi are isolated from clinical specimens. B) Subsequently, the cells are lysed, and the genomic DNA is extracted. C) Then, the DNA is cut into short fragments, and these fragments are D) amplified and E) sequenced. F) Finally, specialized software analyses and interprets the sequencing results and assembles the genome. Reproduced with permission.<sup>[11]</sup> Copyright 2018, American Chemical Society.

three clinically relevant antibiotics within 4 h, and its feasibility for direct analysis of positive blood cultures was demonstrated. Additionally, the GoPhAST-R assay allows analyzing the sequence of mRNAs to unveil essential resistance genes in the investigated pathogens. Combining this genotypic information with the phenotypic mRNA expression data enabled the classification of bacteria into ‘resistant or susceptible’ with 94–99% accuracy.<sup>[101]</sup> These transcriptomic approaches have been only demonstrated for bacterial pathogens, but it should be principally feasible to extend them also to fungal pathogens. Thus, we envision that such assays can become of great importance in the future and provide a novel way to detect antifungal susceptibility and resistance in fungal species.

## 7. The Potential of Microfluidics for AFST

Microfluidics has revolutionized the field of fungi research by enabling parallelization and high-throughput<sup>[106–108]</sup> processing of different fungal species, as single cells or populations,<sup>[107,109–112]</sup> while miniaturizing the experimental setup and reducing the required sample volume.<sup>[106]</sup> **Table 3** summarizes the main advantages that microfluidics-based techniques offer with respect to applications in fungal pathogen diagnostics.

Microfluidic systems also have the potential to integrate all steps (cell isolation from body fluids, detection and identification, and susceptibility testing) in a typical clinical flow, as schematically illustrated in **Figure 8**, and to simplify the current complex and lengthy procedures. For example, let us consider the case of candidemia, where the first functional microfluidic unit would allow *Candida* cell isolation from blood and fungal cell concentration. Subsequently, the resulting suspension could be directly processed by the ‘identification unit’. The latter can

include adapted conventional identification schemes (as discussed in Section 2) or more sophisticated devices, such as biosensors. Finally, a phenotypic AFST will be performed, and MIC values will be determined. While such integrated systems do not yet exist, we envision that in the near future, such schemes will be developed and successfully demonstrated for potential clinical applications. The following section describes emerging microfluidic-based techniques for each of the essential units (namely isolation, detection and identification, and phenotypic AFST) required. Specifically, we focus on microfluidic-based techniques for yeast pathogens, such as *Candida* and *Cryptococcus*.

### 7.1. Step 1: Isolation and Concentration of Fungal Pathogens from Blood

Several microfluidic approaches for isolation and concentration of fungal cells from blood rely on their morphological difference, namely cell size, and shape, from white blood cells (WBCs).<sup>[119,120]</sup> For example, inertial focusing of lysed blood in a spiral-shaped polydimethylsiloxane (PDMS) device (see **Figure 9A-i**) was used to separate *Candida* cells from WBCs and focus them into designated outlets as shown in **Figure 9A-ii**.<sup>[119]</sup> However, only ≈45% of *C. albicans* cells were actually focused into the correct outlet from lysed blood. This effect was ascribed to the higher viscosity of blood compared to a buffer solution used to establish the system.<sup>[119]</sup> Furthermore, the separation performance was less efficient for other *Candida* species (*C. glabrata*, *C. parapsilosis*, and *C. tropicalis*),<sup>[119]</sup> underscoring that such inertial focusing devices must be individually adapted for different-sized species.

Another approach is based on viscoelastic separation and concentration of *C. albicans* from WBCs using a hyaluronic acid solution as a viscoelastic fluid.<sup>[120]</sup> Lysed blood spiked with

**Table 3.** Advantages of microfluidics for fungal pathogen diagnostic applications.

Advantage	Explanation	Ref.
Miniaturization	Miniaturization reduces the required sample and reagent volumes, as well as device size benefitting potential point-of-care applications	[106,113,114]
Parallelization and high-throughput	Fabrication of numerous microfluidic channels or the creation of microdroplets allows for parallelization and high-throughput screening	[106–108]
Integration of different unit operations	Integration of different unit operations (e.g., cell isolation and manipulation, species identification) into a single microfluidic device has been successfully demonstrated	[113,115]
Single-cell analysis	Microfluidic systems have been coupled with microscopy and imaging techniques for single-cell detection and analysis, reducing the absolute number of required cells	[107,113,115]
Controlled microenvironment	Microfluidic systems allow precise control over the microenvironment of cells and thus, are predestined to reveal the effect of the cellular environment on the cell's behavior	[117,118]

*C. albicans* cells and hyaluronic acid (at a concentration of 0.1%) was continuously introduced into the microfluidic device, as illustrated in Figure 9B-i. The larger WBCs (9–15 μm diameter) migrated toward the channel walls, and the smaller *Candida* cells (3 μm diameter) were focused in the microfluidic channel's center (see Figure 9B-ii depicting randomly distributed cells in the inlet and separated cell streams toward the outlets). Approximately 99% of yeast cells and 96% of WBCs were directed into their allocated outlet; furthermore, the microfluidic device allowed a 92-fold cell concentration using two sequential concentration processes.<sup>[120]</sup>

Even without being integrated into a microfluidic lab-on-a-chip device, as described above, these microfluidic cell isolation and concentration units can improve fungal pathogen diagnostics. Preconcentrating cells can help to reach sufficient cell numbers (gene copies) for successful PCR detection and save time in automated blood culture systems as higher cell numbers shorten the time to growth detection.<sup>[119,121]</sup> Furthermore, PCR assays' sensitivity can be improved by removing WBCs (before DNA extraction) as their excess DNA can inhibit PCR reactions applied to blood samples.<sup>[120,122]</sup> Finally, microfluidic processing could serve as an alternative to traditional centrifugation minimizing cell damage due to centrifugal forces.<sup>[123,124]</sup> Still, the applicability of such devices for processing 'real' clin-

ical samples preceding PCR, blood culture, or AFST analysis should be demonstrated in the future.

## 7.2. Step 2: Microfluidics for Fungal Pathogen Detection and Identification

One approach for microfluidic detection and identification includes functionalizing microfluidic channels with species-specific capture probes such as antibodies.<sup>[125]</sup> Asghar et al. have created a microfluidic device with three channels and anti-*C. albicans* antibodies were immobilized onto the channels' bottom via protein G-based surface chemistry, as depicted in Figure 10A-i,A-ii, respectively. Green fluorescent protein (GFP)-expressing *C. albicans* at a concentration range of 10–10<sup>5</sup> CFU mL<sup>-1</sup> were detected within 2 h (compared to days with conventional agar-based methods). This labeled proof-of-concept assay is only applicable for artificially derived GFP expressing yeasts; still, for wild-type strains, this approach could be potentially extended by employing fluorescently labeled antibodies or peptide nucleic acid-based fluorescence in situ hybridization.<sup>[125,126]</sup>

While only a handful of works demonstrated microfluidic-assisted identification of fungal species, there are numerous biosensing systems for fungal pathogens detection<sup>[127–130]</sup> which

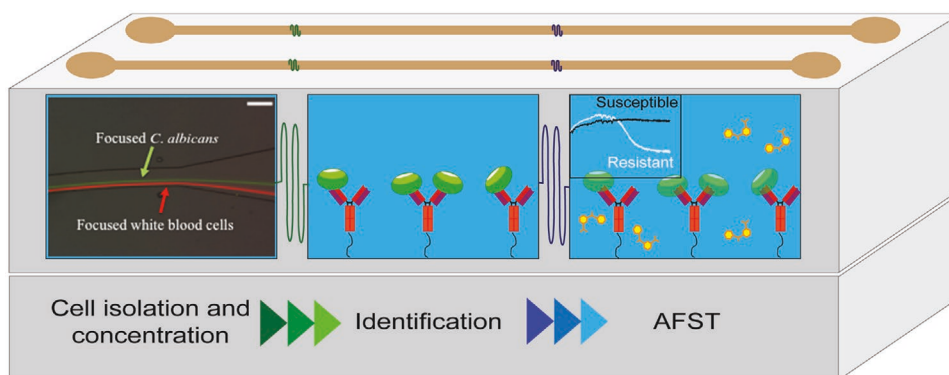


**Figure 8.** Ideal microfluidic lab-on-a-chip system for integrated cell isolation, detection, and identification, as well as phenotypic AFST of fungal pathogens from the blood. First, the *Candida* cells are separated from WBCs in lysed blood and concentrated before transferred to the “identification unit.” This identification step is, for example, achieved by adapted conventional identification schemes or biosensors using species-specific capture probes such as antibodies. The subsequent introduction of antifungals potentially allows a phenotypic AFST and a determination of MIC values. The image depicting *C. albicans* and white blood cells focused within a microfluidic device is adapted with permission under the terms of the Creative Commons CC BY license.<sup>[119]</sup> Copyright 2019, the Authors. Published by Frontiers Media S.A.

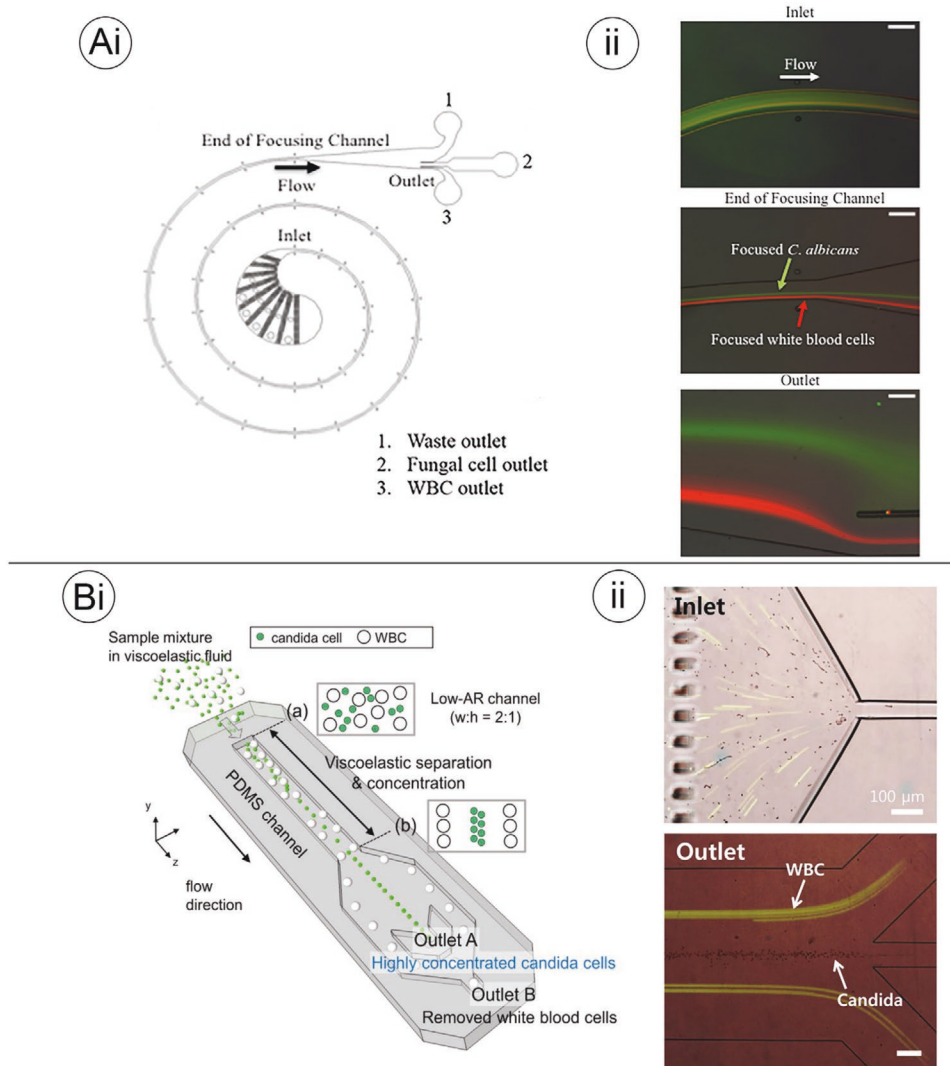


**Figure 9.** Microfluidic tools for isolation and concentration of *Candida* species. A-i) Schematic of a spiral-shaped microfluidic device for isolation and concentration of *Candida* cells from WBCs by inertial focusing. A-ii) *Candida* cells and WBCs are focused into separate streams as they flow through the device; cells are stained for clarity with fluorescein isothiocyanate (*Candida*) and calcein (WBCs). Adapted with permission under the terms of the Creative Commons CC BY license.<sup>[119]</sup> Copyright 2019, the Authors. Published by Frontiers Media S.A. B-i) Schematic of a PDMS-based microfluidic channel for size-dependent viscoelastic separation of *C. albicans* and WBCs. B-ii) Comparison of randomly distributed cells at the inlet and segregated *Candida* and WBC streams at the outlet. Reproduced with permission under the terms of the Creative Commons CC BY license.<sup>[120]</sup> Copyright 2019, the Authors. Published by Springer Nature.

have not yet been coupled with microfluidics. For example, immunosensors such as antibody-functionalized surface plasmon resonance (SPR)<sup>[129]</sup> and electrochemical impedance spectroscopy (EIS)<sup>[130]</sup> biosensors were employed for *Candida* cell detection. Thus, we envision that, in the future, the integration of these biosensors with available microfluidic devices<sup>[131]</sup> can be readily realized to advance the field.

### 7.3. Step 3: Phenotypic AFST

There are several microfluidic-assisted phenotypic AFST assays reported<sup>[60,108,132]</sup>; yet, some of these were only used for qualitative antifungals screening with no MIC determination.

For example, a highly parallelized microfluidic system was developed for the screening of small molecule compounds that enhance the antifungal effect of amphotericin B against *C. albicans*.<sup>[108]</sup> In this assay, *C. albicans* cells expressing GFP only when alive were introduced into the microchannels, as shown in Figure 10B.<sup>[108]</sup> The cells were incubated in a liquid growth medium until the growing yeast cells filled in-line the microchannels and adhered to their surface. Subsequently, mixtures of amphotericin B and various small molecule compounds were introduced for 1 h, and fluorescence microscopy was applied to identify remaining fluorescent persister cells that were still alive.<sup>[108]</sup> From a library of around 50 000 compounds, 10 small molecules were identified whose addition to amphotericin B solution increased the antifungal effect.

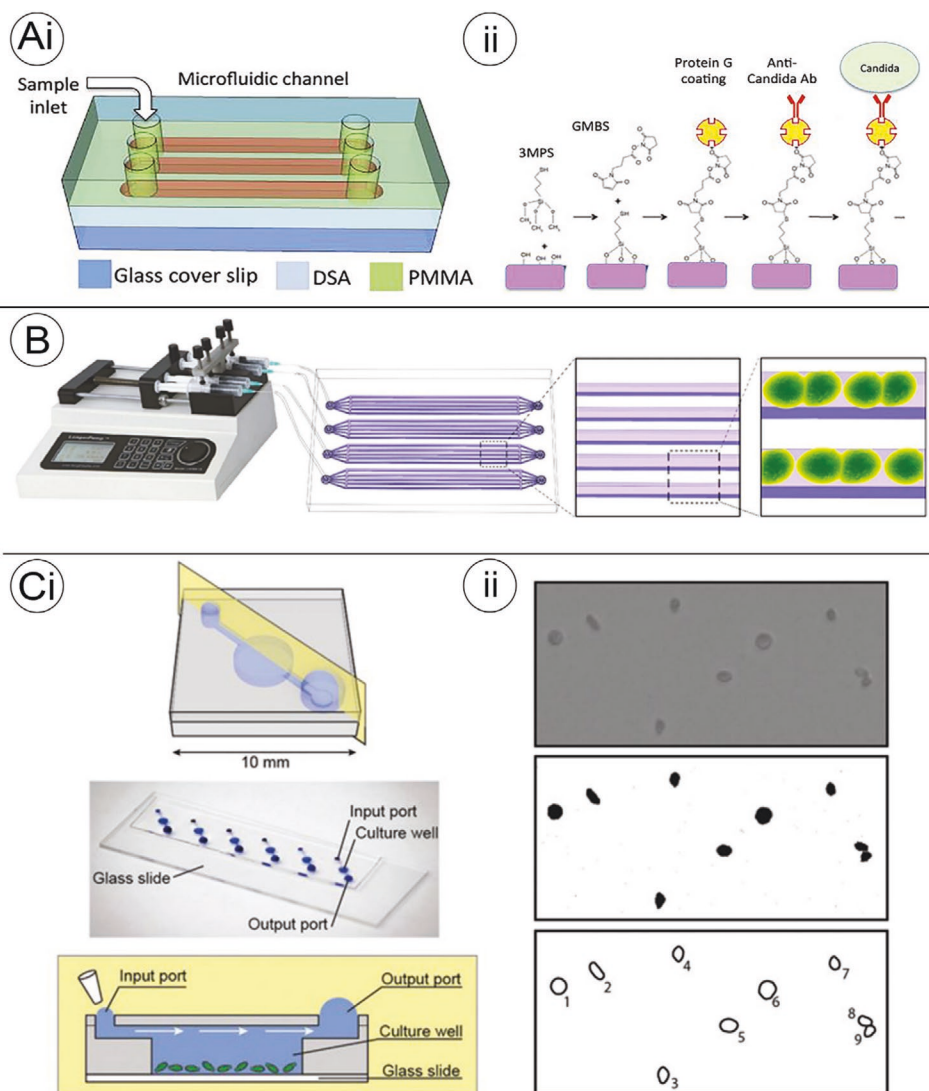


**Figure 10.** Microfluidic systems for fungi identification and phenotypic antifungal drug screening. A-i) Schematic of the microfluidic channel consisting of polymethyl methacrylate attached to a glass cover by a double-sided adhesive layer. A-ii) Functionalization of the glass slide with anti-*C. albicans* antibodies is achieved by using protein G-based surface chemistry and allows detection of bound *C. albicans* cells by fluorescence microscopy. Adapted with permission.<sup>[125]</sup> Copyright 2019, American Chemical Society. B) A microfluidic chip consisting of microchannels is used for high-throughput screening of antifungal drugs against *C. albicans*. Adapted with permission under the terms of the Creative Commons CC BY license.<sup>[108]</sup> Copyright 2019, the Authors. Published by Springer Nature. C-i) Schematic of the cell culture platform for *C. neoformans*. C-ii) Analyzing the germination of *C. neoformans* in the microfluidic device is performed by image processing and analysis. Adapted with permission.<sup>[132]</sup> Copyright 2016, Oxford University Press.

Another approach combined a PDMS-based microfluidic platform and an image processing unit to study the effects of two clinically relevant antifungals (amphotericin B and fluconazole) on germination and growth of *Cryptococcus neoformans* (*C. neoformans*).<sup>[132]</sup> Spore or yeast cells were seeded into microfluidic culture wells, exposed to the antifungal-containing growth medium at inhibitory drug concentrations, and incubated; see Figure 10C-i for image and schematic of the microfluidic cell culture device. Subsequently, the cells were imaged by light microscopy, and an image processing algorithm allowed to detect and analyze cells, as shown in Figure 10C-ii. This algorithm classified the cells into either spores or yeast, based on shape, cell area, and aspect ratio; vegetative growth was also assessed by

measuring the number of cells in an image frame. Interestingly, both antifungals inhibited the yeast cell's vegetative growth but did not impair the germination process.<sup>[132]</sup> This method has the potential to be expanded for the identification and assessment of novel antifungal drugs targeting the germination process and could be extended to other species such as *Aspergilli* by adapting the image processing algorithm.

To the best of our knowledge, only the above-described optical on-chip assay in which *A. niger* conidia are introduced onto photonic silicon chips through microfluidic channels (see Section 5.5) demonstrated the employment of a microfluidic platform for AFST, including MIC determination. Other microfluidic AFST approaches, as presented in this section, will still need

to demonstrate their applicability for a more quantitative AFST, including MIC determination for usage in clinical applications.

While microfluidic approaches specifically for AFST and MIC determination are still rare, microfluidic devices have been more frequently employed for AST of bacteria and have enabled MIC determination or differentiation between “resistant” and “susceptible” in a couple of hours. For example, Churski et al. have described a microdroplet system based on reducing resazurin to resorufin by living cells’ metabolisms.<sup>[133]</sup> Avesar et al. further extended this principle to perform AST of small numbers of bacteria confined within nanoliter arrays allowing to reveal susceptibility within  $\approx 5$  h.<sup>[134]</sup> Baltekin et al. could even assess antibiotic activity by direct single-cell imaging and classify *E. coli* bacteria as susceptible or resistant within 30 min.<sup>[116]</sup> Although still in its infancy, the successful application of microfluidic systems for AST of bacteria emphasizes the potential use of microfluidics for point-of-care AFST.

## 8. Conclusion

The most crucial parameter in developing novel AFST methods is the assay time, which allows to promptly initiate a patient-tailored therapy, thus improving antifungal therapy outcomes and preventing the spread of antifungal resistance.<sup>[23,135,136]</sup> Yet, the development of rapid phenotypic growth-based AFST methods is particularly challenging as, in most cases, fungi are relatively slow-growing species, especially when compared to bacteria.<sup>[137]</sup> Thus, the main conclusion of this review is that despite the significant progress made over the last decade, the overall assay time for sample collection to AFST result is still too lengthy to provide a meaningful clinical advantage with respect to reference phenotypic techniques which require several days for completion.<sup>[12,16]</sup> For example, novel phenotypic approaches, such as fluorescence microscopy or flow cytometry (discussed in Section 5) reduce only the AFST assay time to a couple of hours,<sup>[61,63]</sup> but their preceding lengthy clinical workflow will remain unchanged (requiring typically 2–6 days). Therefore, the added value of nonculture molecular approaches, such as genotypic AMR detection methods which allow for both species identification and detection of resistance-conferring mutations within hours,<sup>[33,93]</sup> is superior to currently available phenotypic techniques. In practice, these genotypic detection schemes are rarely performed in clinical settings, especially as these methods only reveal resistance in selected cases and not susceptibility, and as such only guide physicians on which drugs should be avoided.<sup>[36]</sup>

We believe that only holistic solutions for the entire workflow (including cell isolation and concentration, species identification, and AFST) are likely to unravel the “time bottleneck” of fungal phenotypic disease diagnostics. This review reveals that the advancement of microfluidic techniques, in which integration of different functional units for cell isolation, identification, and phenotypic AFST is accomplished, will be a game changer and will also allow for parallelization and high-throughput screening<sup>[106–108]</sup>. We envision that in the near future, such holistic, integrated microfluidic schemes will be developed and successfully demonstrated for potential clinical applications to simplify and expedite the current complex and lengthy procedures.

The emergence and global spread of fungal pathogens further accelerated by the COVID-19 pandemic<sup>[138,139]</sup> necessitate a joint effort of health organizations, scientists from different disciplines, and clinicians to combat this neglected forefront of fungal pathogens pathogen diagnosis and monitoring.

## Acknowledgements

The authors acknowledge the financial support from the German Research Foundation (DFG) via the grant SCHE 279/32-1 and the Lower Saxony Ministry for Science and Culture, Research Cooperation Lower Saxony–Israel. E.S. is grateful for the support of the Israeli Innovation Authority (via Kamin Project 65025) and J.B. acknowledges the support of the Emmy Noether Programme (346772917).

## Conflict of Interest

The authors declare no conflict of interest.

## Keywords

diagnostics, drug resistance, fungal pathogens, microfluidics, rapid antifungal susceptibility testing

Received: June 26, 2021

Revised: September 5, 2021

Published online: September 23, 2021

- [1] D. Sanglard, *Front. Med.* **2016**, *3*, 11.
- [2] G. D. Brown, D. W. Denning, N. A. R. Gow, S. M. Levitz, M. G. Netea, T. C. White, *Sci. Transl. Med.* **2012**, *4*, 165rv13.
- [3] D. S. Perlin, R. Rautemaa-Richardson, A. Alastruey-Izquierdo, *Lancet Infect. Dis.* **2017**, *17*, e383.
- [4] Centers for Disease Control and Prevention at the U.S. Department of Health and Human Services, Antibiotic Resistance Threats in the United States **2019**, <https://www.cdc.gov/drugresistance/pdf/threats-report/2019-ar-threats-report-508.pdf> (accessed: May 2021).
- [5] H. Du, J. Bing, T. Hu, C. L. Ennis, C. J. Nobile, G. Huang, *PLoS Pathog.* **2020**, *16*, e1008921.
- [6] A. L. Colombo, J. N. de Almeida Júnior, M. A. Slavin, S. C.-A. Chen, T. C. Sorrell, *Lancet Infect. Dis.* **2017**, *17*, e344.
- [7] A. H. Limper, A. Adenis, T. Le, T. S. Harrison, *Lancet Infect. Dis.* **2017**, *17*, e334.
- [8] D. W. Denning, M. J. Bromley, *Science* **2015**, *347*, 1414.
- [9] S. Doron, L. E. Davidson, *Mayo Clin. Proc.* **2011**, *86*, 1113.
- [10] P. Morency-Potvin, D. N. Schwartz, R. A. Weinstein, *Clin. Microbiol. Rev.* **2017**, *30*, 381.
- [11] H. Leonard, R. Colodner, S. Halachmi, E. Segal, *ACS Sens.* **2018**, *3*, 2202.
- [12] M. J. Arendrup, J. Meletiadis, J. Mouton, K. Lagrou, P. Hamal, J. Guinea, EUCAST Definitive Document E. DEF 7.3.2., [https://www.eucast.org/fileadmin/src/media/PDFs/EUCAST\\_files/AFST/Files/EUCAST\\_E\\_Def\\_7.3.2\\_Yeast\\_testing\\_definitive\\_revised\\_2020.pdf](https://www.eucast.org/fileadmin/src/media/PDFs/EUCAST_files/AFST/Files/EUCAST_E_Def_7.3.2_Yeast_testing_definitive_revised_2020.pdf) (accessed: May 2021).
- [13] European Committee on Antimicrobial Susceptibility Testing, Breakpoint Tables for Interpretation of MICs for Antifungal Agents Version 10.0, [https://www.eucast.org/fileadmin/src/media/PDFs/EUCAST\\_files/AFST/Clinical\\_breakpoints/AFST\\_BP\\_v10.0\\_200204\\_updatd\\_links\\_200924.pdf](https://www.eucast.org/fileadmin/src/media/PDFs/EUCAST_files/AFST/Clinical_breakpoints/AFST_BP_v10.0_200204_updatd_links_200924.pdf) (accessed: May 2021).

- [14] M. Arvanitis, T. Anagnostou, B. B. Fuchs, A. M. Caliendo, E. Mylonakis, *Clin. Microbiol. Rev.* **2014**, *27*, 490.
- [15] Clinical and Laboratory Standards Institute, Reference Method for Broth Dilution Antifungal Susceptibility Testing of Yeasts, 4th ed. (Approved Standard M27), <https://clsi.org/standards/products/microbiology/documents/m27/> (accessed: September 2021).
- [16] M. J. Arendrup, J. Meletiadis, J. Mouton, K. Lagrou, P. Hamal, J. Guinea, EUCAST Definitive Document E. DEF 9.3.1., [https://www.eucast.org/fileadmin/src/media/PDFs/EUCAST\\_files/AFST/Files/EUCAST\\_E\\_Def\\_9.3.2\\_Mould\\_testing\\_definitive\\_revised\\_2020.pdf](https://www.eucast.org/fileadmin/src/media/PDFs/EUCAST_files/AFST/Files/EUCAST_E_Def_9.3.2_Mould_testing_definitive_revised_2020.pdf) (accessed: May 2021).
- [17] M. Sanguinetti, B. Posteraro, *Clin. Microbiol. Infect.* **2017**, *23*, 931.
- [18] E. L. Berkow, S. R. Lockhart, L. Ostrosky-Zeichner, *Clin. Microbiol. Rev.* **2020**, *33*, e00069.
- [19] M. Ruhnke, G. Behre, D. Buchheidt, M. Christopeit, A. Hamprecht, W. Heinz, C.-P. Heussel, M. Horger, O. Kurzai, M. Karthaus, J. Löffler, G. Maschmeyer, O. Penack, C. Rieger, V. Rickerts, J. Ritter, M. Schmidt-Hieber, N. Schuelper, S. Schwartz, A. Ullmann, J. J. Vehreschild, M. von Lilienfeld-Toal, T. Weber, H. H. Wolf, *Mycoses* **2018**, *61*, 796.
- [20] C. Lass-Flörl, *Med. Mycol.* **2019**, *57*, S155.
- [21] K. H. Neppelenbroek, R. S. Seó, V. M. Urban, S. Silva, L. N. Dovigo, J. H. Jorge, N. H. Campanha, *Oral Dis* **2014**, *20*, 329.
- [22] M. Sanguinetti, B. Posteraro, C. Beigelman-Aubry, F. Lamoth, V. Dunet, M. Slavin, M. D. Richardson, *J. Antimicrob. Chemother.* **2019**, *74*, ii27.
- [23] S. Arikan, *Med. Mycol.* **2007**, *45*, 569.
- [24] bioMérieux SA, Etest Application Guide, [https://www.biomerieuxusa.com/sites/subsidiary\\_us/files/supplementary\\_inserts\\_-\\_16273\\_-\\_b\\_-\\_en\\_-\\_eag\\_-\\_etest\\_application\\_guide-3.pdf](https://www.biomerieuxusa.com/sites/subsidiary_us/files/supplementary_inserts_-_16273_-_b_-_en_-_eag_-_etest_application_guide-3.pdf) (accessed: May 2021).
- [25] G. Li, J. Sun, S. Pan, W. Li, S. Zhang, Y. Wang, X. Sun, H. Xu, L. Ming, *Front. Cell. Infect. Microbiol.* **2019**, *9*, 285.
- [26] E.-L. Ericson, L. Klingspor, M. Ullberg, V. Ozenci, *Diagn. Microbiol. Infect. Dis.* **2012**, *73*, 153.
- [27] A. B. Guzel, M. Ilkit, T. Akar, R. Burgut, S. C. Demir, *Med. Mycol.* **2011**, *49*, 16.
- [28] P. Staib, J. Morschhäuser, *Mycoses* **2007**, *50*, 1.
- [29] bioMérieux SA, Etest Reading Guide, [https://www.ilexmedical.com/files/ETEST\\_RG.pdf](https://www.ilexmedical.com/files/ETEST_RG.pdf) (accessed: May 2021).
- [30] Clinical and Laboratory Standards Institute, Method for Antifungal Disk Diffusion Susceptibility Testing of Yeasts, 3rd ed. (Approved Guideline Document M44), <https://clsi.org/standards/products/microbiology/documents/m44/> (accessed: September 2021).
- [31] B. Lamy, *Clin. Microbiol. Infect.* **2019**, *25*, 268.
- [32] N. Cobos-Trigueros, A. J. Kaasch, A. Soriano, J.-L. Torres, A. Vergara, L. Morata, Y. Zboromyrska, C. D. La Calle, I. Alejo, C. Hernández, C. Cardozo, F. Marco, A. Del Río, M. Almela, J. Mensa, J. A. Martínez, *J. Clin. Microbiol.* **2014**, *52*, 3082.
- [33] J. D. Bard, F. Lee, *Clin. Microbiol. Newsl.* **2018**, *40*, 87.
- [34] E. Eraso, I. H. Sahand, M. Villar-Vidal, C. Marcos, M. Dolores Moragues, L. Madariaga, J. Pontón, G. Quindós, *Med. Mycol.* **2006**, *44*, 611.
- [35] A. Espinel-Ingroff, *J. Clin. Microbiol.* **2003**, *41*, 403.
- [36] C. D. Doern, *J. Clin. Microbiol.* **2018**, *56*.
- [37] A. van Belkum, T. T. Bachmann, G. Lüdke, J. G. Lisby, G. Kahlmeter, A. Mohess, K. Becker, J. P. Hays, N. Woodford, K. Mitsakakis, J. Moran-Gilad, J. Vila, H. Peter, J. H. Rex, W. M. Dunne, *Nat. Rev. Microbiol.* **2019**, *17*, 51.
- [38] A. van Belkum, C.-A. D. Burnham, J. W. A. Rossen, F. Mallard, O. Rochas, W. M. Dunne, *Nat. Rev. Microbiol.* **2020**, *18*, 299.
- [39] C. J. Utz, S. Shadomy, *J. Infect. Dis.* **1977**, *135*, 970.
- [40] G. Wagner, S. Shadomy, L. D. Paxton, A. Espinel-Ingroff, *Antimicrob. Agents Chemother.* **1975**, *8*, 107.
- [41] Clinical and Laboratory Standards Institute, Reference Method for Broth Dilution Antifungal Susceptibility Testing of Filamentous Fungi, 3rd ed. (Approved Guideline Document M38), <https://clsi.org/standards/products/microbiology/documents/m38/> (accessed: September 2021).
- [42] Clinical and Laboratory Standards Institute, Method for Antifungal Disk Diffusion Susceptibility Testing of Nondermatophyte Filamentous Fungi, 3rd ed. (Approved Guideline Document M51-A), <https://clsi.org/standards/products/microbiology/documents/m51/> (accessed: September 2021).
- [43] J. Guinea, P. E. Verweij, J. Meletiadis, J. W. Mouton, F. Barchiesi, M. C. Arendrup, *Clin. Microbiol. Infect.* **2019**, *25*, 681.
- [44] J. B. Buil, H. A. L. van der Lee, A. J. M. M. Rijs, J. Zoll, J. A. M. F. Hovestadt, W. J. G. Melchers, P. E. Verweij, *Antimicrob. Agents Chemother.* **2017**, *61*.
- [45] M. C. Arendrup, P. E. Verweij, J. W. Mouton, K. Lagrou, J. Meletiadis, *J. Antimicrob. Chemother.* **2017**, *72*, 3325.
- [46] E. Borghi, R. Iatta, R. Sciota, C. Biassoni, T. Cuna, M. T. Montagna, G. Morace, *J. Clin. Microbiol.* **2010**, *48*, 3153.
- [47] M. Cuenca-Estrella, A. Gomez-Lopez, A. Alastruey-Izquierdo, L. Bernal-Martinez, I. Cuesta, M. J. Buitrago, J. L. Rodriguez-Tudela, *J. Clin. Microbiol.* **2010**, *48*, 1782.
- [48] Thermo Fisher Scientific, Thermo Scientific Sensititre Plate Guide for Antimicrobial Susceptibility Testing, <https://www.thermofisher.com/document-connect/document-connect.html?url=https%3A%2F%2Fassets.thermofisher.com%2FTFS-Assets%2FMBD%2Fbrochures%2FSensititre-Plate-Guide-Booklet-EN.pdf&title=U2Vuc2l0aXRyZSBQbGF0ZSBHdWlkZQ==> (accessed: May 2021).
- [49] C. Castro, M. C. Serrano, B. Flores, A. Espinel-Ingroff, E. Martín-Mazuelos, *J. Clin. Microbiol.* **2004**, *42*, 4358.
- [50] M. A. Pfaller, A. Espinel-Ingroff, R. N. Jones, *J. Clin. Microbiol.* **2004**, *42*, 4577.
- [51] H. C. Chang, J. J. Chang, S. H. Chan, A. H. Huang, T. L. Wu, M. C. Lin, T. C. Chang, *J. Clin. Microbiol.* **2001**, *39*, 1328.
- [52] M. Cuenca-Estrella, A. Gomez-Lopez, E. Mellado, J. L. Rodriguez-Tudela, *Clin. Microbiol. Infect.* **2005**, *11*, 486.
- [53] A. Espinel-Ingroff, A. Rezusta, *J. Clin. Microbiol.* **2002**, *40*, 2101.
- [54] A. Espinel-Ingroff, B. Arthington-Skaggs, N. Iqbal, D. Ellis, M. A. Pfaller, S. Messer, M. Rinaldi, A. Fothergill, D. L. Gibbs, A. Wang, *J. Clin. Microbiol.* **2007**, *45*, 1811.
- [55] S. Chaturvedi, S. S. Rajkumar, X. Li, G. J. Hurteau, M. Shtutman, V. Chaturvedi, *PLoS One* **2011**, *6*, e17032.
- [56] M. A. Pfaller, S. A. Messer, A. Karlsson, A. Bolmström, *J. Clin. Microbiol.* **1998**, *36*, 2586.
- [57] S. N. Rampersad, *Sensors* **2012**, *12*, 12347.
- [58] E. A. Idelevich, C. M. Grunewald, J. Wüllenweber, K. Becker, *PLoS One* **2014**, *9*, e114834.
- [59] M. A. Pfaller, D. J. Diekema, G. W. Procop, M. G. Rinaldi, *J. Clin. Microbiol.* **2007**, *45*, 3522.
- [60] C. Heuer, H. Leonard, N. Nitzan, A. Lavy-Alperovitch, N. Massad-Ivanir, T. Scheper, E. Segal, *ACS Infect. Dis.* **2020**.
- [61] C. J. Ingham, S. Boonstra, S. Levels, M. de Lange, J. F. Meis, P. M. Schneeberger, *PLoS One* **2012**, *7*, e33818.
- [62] C. Marinach, A. Alanio, M. Palous, S. Kwasek, A. Fekkar, J.-Y. Brossas, S. Brun, G. Snounou, C. Hennequin, D. Sanglard, A. Detry, J.-L. Golmard, D. Mazier, *Proteomics* **2009**, *9*, 4627.
- [63] L. A. Vale-Silva, V. Buchta, *Mycoses* **2006**, *49*, 261.
- [64] E. M. Maiolo, U. Furustrand Tafin, O. Borens, A. Trampuz, *Antimicrob. Agents Chemother.* **2014**, *58*, 2709.
- [65] G. Vrioni, C. Tsiamis, G. Oikonomidis, K. Theodoridou, V. Kapsimali, A. Tsakris, *Ann. Transl. Med.* **2018**, *6*, 240.
- [66] M. Welker, A. van Belkum, *Front. Microbiol.* **2019**, *10*, 2711.
- [67] A. van Belkum, M. Welker, D. Pincus, J. P. Charrier, V. Girard, *Ann. Lab. Med.* **2017**, *37*, 475.

- [68] C. Wensch, K. F. Linnau, B. Parschalk, K. Zedtwitz-Liebenstein, A. Georgopoulos, *J. Clin. Microbiol.* **1997**, *35*, 5.
- [69] L. A. Vale-Silva, P. Pinto, V. Lopes, H. Ramos, E. Pinto, *Eur. J. Clin. Microbiol. Infect. Dis.* **2012**, *31*, 941.
- [70] R.-J. Bleichrodt, N. D. Read, *Fungal Biol. Rev.* **2019**, *33*, 1.
- [71] U. Furustrand Tafin, M. Clauss, P. M. Hauser, J. Bille, J. F. Meis, A. Trampuz, *Clin. Microbiol. Infect.* **2012**, *18*, E241.
- [72] U. Furustrand Tafin, J. F. Meis, A. Trampuz, *Antimicrob. Agents Chemother.* **2013**, *57*, 5704.
- [73] S. A. Balkum, W. M. Dunne, *J. Clin. Microbiol.* **2013**, *51*, 2018.
- [74] E. de Carolis, A. Vella, A. R. Florio, P. Posteraro, D. S. Perlin, M. Sanguinetti, B. Posteraro, *J. Clin. Microbiol.* **2012**, *50*, 2479.
- [75] A. Vella, E. de Carolis, L. Vaccaro, P. Posteraro, D. S. Perlin, M. Kostrzewa, B. Posteraro, M. Sanguinetti, *J. Clin. Microbiol.* **2013**, *51*, 2964.
- [76] L. Green, B. Petersen, L. Steimel, P. Haeber, W. Current, *J. Clin. Microbiol.* **1994**, *32*, 1088.
- [77] K.-O. Söderström, L.-M. Parvinen, M. Parvinen, *Experientia* **1977**, *33*, 265.
- [78] S. A. Balajee, K. A. Marr, *J. Clin. Microbiol.* **2002**, *40*, 2741.
- [79] A. Bhasin, D. N. Little, *J. Mater. Civ. Eng.* **2009**, *21*, 235.
- [80] C. J. Ingham, P. M. Schneeberger, *PLoS One* **2012**, *7*, e35478.
- [81] C. J. Ingham, A. Sprenkels, J. Bomer, D. Molenaar, A. van den Berg, J. E. T. van Hylckama Vlieg, W. M. de Vos, *Proc. Natl. Acad. Sci. U. S. A.* **2007**, *104*, 18217.
- [82] M. J. Henry-Stanley, R. M. Garni, C. L. Wells, *J. Microbiol. Methods* **2004**, *59*, 289.
- [83] H. Leonard, S. Halachmi, N. Ben-Dov, O. Nativ, E. Segal, *ACS Nano* **2017**, *11*, 6167.
- [84] N. Massad-Ivanir, Y. Mirsky, A. Nahor, E. Edrei, L. M. Bonanno-Young, N. Ben Dov, A. Sa'ar, E. Segal, *Analyst* **2014**, *139*, 3885.
- [85] H. Leonard, C. Heuer, D. Weizmann, N. Massad-Ivanir, S. Halachmi, R. Colodner, E. Segal, in *Frontiers in Biological Detection: From Nanosensors to Systems XI* (Eds: A. Danielli, B. L. Miller, S. M Weiss), SPIE, Bellingham WA **2019**, p. 3.
- [86] M. Boolchandani, A. W. D'Souza, G. Dantas, *Nat. Rev. Genet.* **2019**, *20*, 356.
- [87] C. D. Pham, C. B. Bolden, R. J. Kuykendall, S. R. Lockhart, *J. Clin. Microbiol.* **2014**, *52*, 790.
- [88] Y. Zhao, Y. Nagasaki, M. Kordalewska, E. G. Press, R. K. Shields, M. H. Nguyen, C. J. Clancy, D. S. Perlin, *Antimicrob. Agents Chemother.* **2016**, *60*, 6573.
- [89] C. Dudiuk, S. Gamarra, F. Leonardeli, C. Jimenez-Ortigosa, R. G. Vitale, J. Afeltra, D. S. Perlin, G. Garcia-Effron, *J. Clin. Microbiol.* **2014**, *52*, 2609.
- [90] P.-M. Rath, J. Steinmann, *Front. Microbiol.* **2018**, *9*, 740.
- [91] E. Dannaoui, F. Gabriel, M. Gaboyard, G. Lagardere, L. Audebert, G. Quesne, S. Godichaud, P. E. Verweij, I. Accoceberry, M.-E. Bougnoux, *J. Clin. Microbiol.* **2017**, *55*, 3210.
- [92] PathoNostics B.V., AsperGenius Instructions for Use Version 3.1E, received upon request from PathoNostics B.V., Maastricht, the Netherlands in March **2021**.
- [93] P. L. White, R. B. Posso, R. A. Barnes, *J. Clin. Microbiol.* **2015**, *53*, 2115.
- [94] E. Mylonakis, C. J. Clancy, L. Ostrosky-Zeichner, K. W. Garey, G. J. Alangaden, J. A. Vazquez, J. S. Groeger, M. A. Judson, Y.-M. Vinagre, S. O. Heard, F. N. Zervou, I. M. Zacharioudakis, D. P. Kontoyiannis, P. G. Pappas, *Clin. Infect. Dis.* **2015**, *60*, 892.
- [95] F. Korber, I. Zeller, M. Grünstäudl, B. Willinger, P. Apfalter, A. M. Hirschl, A. Makristathis, *Wien. Klein. Wochenschr.* **2017**, *129*, 427.
- [96] M. C. Arendrup, T. F. Patterson, *J. Infect. Dis.* **2017**, *216*, S445.
- [97] M. Su, S. W. Satola, T. D. Read, *J. Clin. Microbiol.* **2019**, *57*.
- [98] A. Vasala, V. P. Hytönen, O. H. Laitinen, *Front. Cell. Infect. Microbiol.* **2020**, *10*, 308.
- [99] C. Biswas, S. C.-A. Chen, C. Halliday, E. Martinez, R. J. Rockett, Q. Wang, V. J. Timms, R. Dhakal, R. Sadsad, K. J. Kennedy, G. Playford, D. J. Marriott, M. A. Slavin, T. C. Sorrell, V. Sintchenko, *J. Visualized Exp.* **2017**, *130*, e56714.
- [100] S. Quainoo, J. P. M. Coolen, S. A. F. T. van Hijum, M. A. Huynen, W. J. G. Melchers, W. van Schaik, H. F. L. Wertheim, *Clin. Microbiol. Rev.* **2017**, *30*, 1015.
- [101] R. P. Bhattacharyya, N. Bandyopadhyay, P. Ma, S. S. Son, J. Liu, L. L. He, L. Wu, R. Khafizov, R. Boykin, G. C. Cerqueira, A. Pironi, R. F. Rudy, M. M. Patel, R. Yang, J. Skerry, E. Nazarian, K. A. Musser, J. Taylor, V. M. Pierce, A. M. Earl, L. A. Cosimi, N. Shores, J. Beechem, J. Livny, D. T. Hung, *Nat. Med.* **2019**, *25*, 1858.
- [102] M. J. Ellington, O. Ekelund, F. M. Aarestrup, R. Canton, M. Doumith, C. Giske, H. Grundman, H. Hasman, M. T. G. Holden, K. L. Hopkins, J. Iredell, G. Kahlmeter, C. U. Köser, A. MacGowan, D. Mevius, M. Mulvey, T. Naas, T. Peto, J.-M. Rolain, Ø. Samuelsen, N. Woodford, *Clin. Microbiol. Infect.* **2017**, *23*, 2.
- [103] S. E. Kidd, S. C.-A. Chen, W. Meyer, C. L. Halliday, *Front. Microbiol.* **2019**, *10*, 2903.
- [104] A. K. Barczak, J. E. Gomez, B. B. Kaufmann, E. R. Hinson, L. Cosimi, M. L. Borowsky, A. B. Onderdonk, S. A. Stanley, D. Kaur, K. F. Bryant, D. M. Kriple, A. Sloutsky, D. T. Hung, *Proc. Natl. Acad. Sci. U. S. A.* **2012**, *109*, 6217.
- [105] X. Yang, M. M. Hashemi, N. Andini, M. M. Li, S. Kuang, K. C. Carroll, T.-H. Wang, S. Yang, *J. Antimicrob. Chemother.* **2020**, *75*, 1747.
- [106] W. Zhou, J. Le, Y. Chen, Y. Cai, Z. Hong, Y. Chai, *TrAC* **2019**, *112*, 175.
- [107] T. Beneyton, I. P. M. Wijaya, P. Postros, M. Najah, P. Leblond, A. Couvent, E. Mayot, A. D. Griffiths, A. Drevelle, *Sci. Rep.* **2016**, *6*, 27223.
- [108] Le Qiang, J. Guo, Y. Han, J. Jiang, X. Su, H. Liu, Q. Qi, L. Han, *Sci. Rep.* **2019**, *9*, 8087.
- [109] K. K. Lee, L. Labiscsak, C. H. Ahn, C. I. Hong, *Fungal Genet. Biol.* **2016**, *94*, 11.
- [110] T. Geng, E. L. Bredeweg, C. J. Szymanski, B. Liu, S. E. Baker, G. Orr, J. E. Evans, R. T. Kelly, *Sci. Rep.* **2015**, *5*, 16111.
- [111] F. Ellett, J. Jorgensen, G. H. Frydman, C. N. Jones, D. Irimia, *PLoS Pathog.* **2017**, *13*, e1006154.
- [112] K. L. Hanson, D. V. Nicolau, L. Filippini, L. Wang, A. P. Lee, *Small* **2006**, *2*, 1212.
- [113] Z. A. Khan, M. F. Siddiqui, S. Park, *Biotechnol. Lett.* **2019**, *41*, 221.
- [114] K. Zhang, S. Qin, S. Wu, Y. Liang, J. Li, *Chem. Sci.* **2020**, *11*, 6352.
- [115] I.-F. Cheng, H.-C. Chang, D. Hou, H.-C. Chang, *Biomicrofluidics* **2007**, *1*, 021503.
- [116] Ö. Baltekin, A. Boucharin, E. Tano, D. I. Andersson, J. Elf, *Proc. Natl. Acad. Sci. U. S. A.* **2017**, *114*, 9170.
- [117] E. W. K. Young, D. J. Beebe, *Chem. Soc. Rev.* **2010**, *39*, 1036.
- [118] J. Aranda Hernandez, C. Heuer, J. Bahnmann, N. Szita, in *Advances in Biochemical Engineering/Biotechnology*, Springer, Berlin **2021**.
- [119] B. B. Fuchs, S. Eatemadpour, J. M. Martel-Foley, S. Stott, M. Toner, E. Mylonakis, *Front. Cell. Infect. Microbiol.* **2019**, *9*, 27.
- [120] J. Nam, W. S. Jang, H. Da Hong, C. S. Lim, *Sci. Rep.* **2019**, *9*, 3067.
- [121] B. J. George, L. L. Horvath, D. R. Hospenthal, *J. Clin. Microbiol.* **2005**, *43*, 433.
- [122] W. A. Al-Soud, P. Rådström, *J. Clin. Microbiol.* **2001**, *39*, 485.
- [123] J. M. Martel, K. C. Smith, M. Dlamini, K. Pletcher, J. Yang, M. Karabacak, D. A. Haber, R. Kapur, M. Toner, *Sci. Rep.* **2015**, *5*, 11300.
- [124] B. W. Peterson, P. K. Sharma, H. C. van der Mei, H. J. Busscher, *Appl. Environ. Microbiol.* **2012**, *78*, 120.



- [125] W. Asghar, M. Sher, N. S. Khan, J. M. Vyas, U. Demirci, *ACS Omega* **2019**, *4*, 7474.
- [126] D. M. Harris, D. J. Hata, *Ann. Clin. Microbiol. Antimicrob.* **2013**, *12*, 2.
- [127] H. Muramatsu, K. Kajiwara, E. Tamiya, I. Karube, *Anal. Chim. Acta* **1986**, *188*, 257.
- [128] S. R. Sá, A. G. Silva Junior, R. G. Lima-Neto, C. A. S. Andrade, M. D. L. Oliveira, *Talanta* **2020**, *220*, 121375.
- [129] S. Yodmongkol, S. Thaweboon, B. Thaweboon, C. Puttharugsa, B. Sutapun, R. Amarith, A. Somboonkaew, T. Srihirin, *Jpn. J. Appl. Phys.* **2016**, *55*, 02BE03.
- [130] D. Kwasny, S. E. Tehrani, C. Almeida, I. Schjødt, M. Dimaki, W. E. Svendsen, *Sensors* **2018**, *18*, 2214.
- [131] D.-S. Wang, S.-K. Fan, *Sensors* **2016**, *16*, 1175.
- [132] L. J. Barkal, N. M. Walsh, M. R. Botts, D. J. Beebe, C. M. Hull, *Integr. Biol.* **2016**, *8*, 603.
- [133] K. Churski, T. S. Kaminski, S. Jakiela, W. Kamysz, W. Baranska-Rybak, D. B. Weibel, P. Garstecki, *Lab Chip* **2012**, *12*, 1629.
- [134] J. Avesar, D. Rosenfeld, M. Truman-Rosentsvit, T. Ben-Arye, Y. Geffen, M. Bercovici, S. Levenberg, *Proc. Natl. Acad. Sci. U. S. A.* **2017**, *114*, E5787.
- [135] Centers for Disease Control and Prevention at the U.S. Department of Health and Human Services, CDC Actions to Prevent the Spread of Antifungal Resistance, <https://www.cdc.gov/fungal/pdf/cdc-antifungal-resistance-508.pdf> (accessed: May 2021).
- [136] M. A. Knoll, H. Ulmer, C. Lass-Flörl, *J. Fungi* **2021**, *7*, 63.
- [137] J. Rousk, E. Bååth, *FEMS Microbiol. Ecol.* **2011**, *78*, 17.
- [138] M. Hoenigl, *Clin. Infect. Dis.* **2020**, ciaa1342.
- [139] Centers for Disease Control and Prevention at the U.S. Department of Health and Human Services, Fungal Diseases and COVID-19, <https://www.cdc.gov/fungal/covid-fungal.html> (accessed: June 2021).



**Christopher Heuer** received his M.Sc. in Life Science from Leibniz University Hannover (LUH). He is currently a Ph.D. student at both the Institute of Technical Chemistry at LUH and at the Faculty of Biotechnology and Food Engineering at the Technion–Israel Institute of Technology, pursuing a dual doctorate. His research focuses on the employment of photonic silicon-based optical sensors for fungal pathogen diagnostics.



**Janina Bahnemann** studied Life Science at Leibniz University Hannover (LUH) and received her Ph.D. from the Institute of Bioprocess and Biosystems Engineering at the Hamburg University of Technology in 2014. In 2015, she joined the Institute for Environmental and Applied Sciences at the California Institute of Technology (Caltech) as a postdoctoral researcher. Since 2017, she has been a junior research group leader (funded by the DFG's Emmy Noether Program) at the Institute of Technical Chemistry at LUH. Her research focuses on cell culture and microsystems engineering, high-resolution 3D printing technology, and the development of lab-on-a-chip-based biosensors.



**Thomas Scheper** is head of the Institute of Technical Chemistry at the Leibniz University of Hannover. His research activities are in the area of bioprocess engineering, mammalian cell cultivation technology, and tissue engineering/regenerative medicine. He is cooperating with many industrial partners to use intelligent bioanalytics and biosensors for an effective optimization, control and documentation of biotechnological production processes. Additionally, biosensors based on aptamer technology are developed in his research team for bed-side monitoring in medicine.



**Ester Segal** is a Full Professor of Biotechnology and Food Engineering at the Technion–Israel Institute of Technology. She received her Ph.D. in Chemical Engineering from the Technion in 2004 and later trained at the University of California–San Diego, where she was a Rothschild postdoctoral fellow. Since 2007, she heads the Technion’s Lab of Multifunctional Nanomaterials. Her research focuses on the broad interface between nanomaterials science and biotechnology, including the basic study of structure–property relationships of nanomaterials and application of this knowledge in development of functional materials systems for biosensing and diagnostics.

### 3.2 3D-Printing in Biotechnology

This section is reproduced from the following review article:

## “3D Printing in Biotechnology - An Insight into Miniaturized and Microfluidic Systems for Applications from Cell Culture to Bioanalytics”

Christopher Heuer, John-Alexander Preuß, Taieb Habib, Anton Enders and Janina Bahnemann

*Engineering in Life Sciences, 22, 744–759 (2022)*

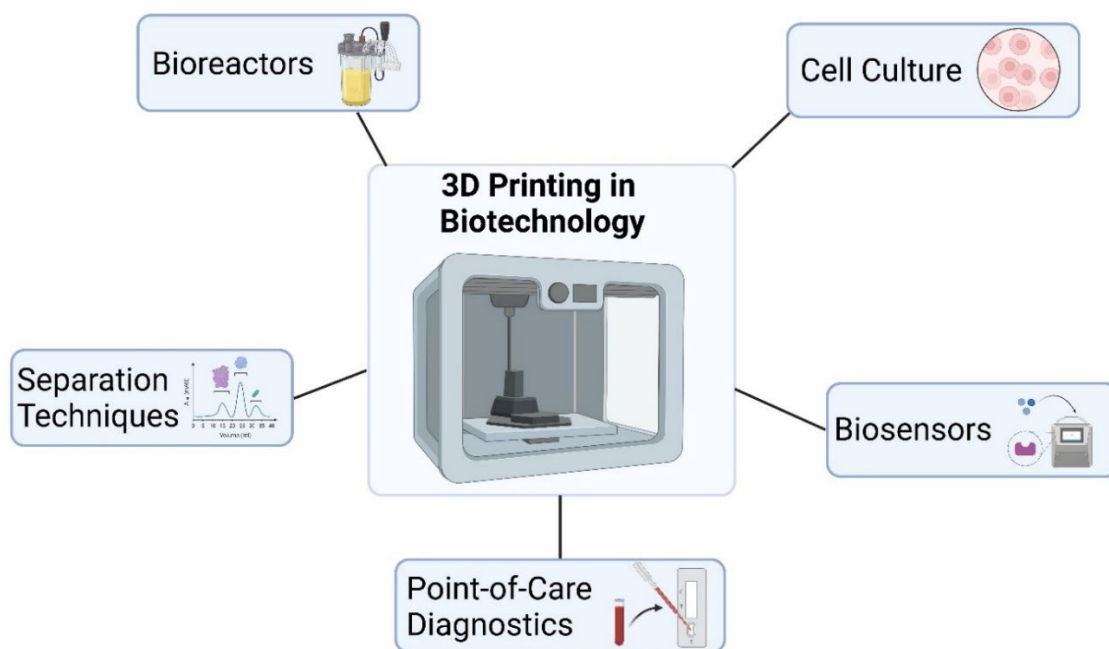


**Figure 2** Graphical abstract of the review article “3D Printing in Biotechnology - An Insight into Miniaturized and Microfluidic Systems for Applications from Cell Culture to Bioanalytics”. This figure was created with biorender.com.

## REVIEW

# 3D printing in biotechnology—An insight into miniaturized and microfluidic systems for applications from cell culture to bioanalytics

Christopher Heuer<sup>1</sup>  | John-Alexander Preuß<sup>1</sup> | Taieb Habib<sup>1</sup> | Anton Enders<sup>1</sup> | Janina Bahnemann<sup>1,2</sup>

<sup>1</sup> Institute of Technical Chemistry, Leibniz University Hannover, Hannover, Germany

<sup>2</sup> Cell Culture Technology, Faculty of Technology, Bielefeld University, Bielefeld, Germany

## Correspondence

Janina Bahnemann, Institute of Technical Chemistry, Leibniz University Hannover, Hannover, Germany.  
Email: [jbahnemann@iftc.uni-hannover.de](mailto:jbahnemann@iftc.uni-hannover.de)

## Abstract

Since its invention in the 1980s, 3D printing has evolved into a versatile technique for the additive manufacturing of diverse objects and tools, using various materials. The relative flexibility, straightforwardness, and ability to enable rapid prototyping are tremendous advantages offered by this technique compared to conventional methods for miniaturized and microfluidic systems fabrication (such as soft lithography). The development of 3D printers exhibiting high printer resolution has enabled the fabrication of accurate miniaturized and microfluidic systems—which have, in turn, substantially reduced both device sizes and required sample volumes. Moreover, the continuing development of translucent, heat resistant, and biocompatible materials will make 3D printing more and more useful for applications in biotechnology in the coming years. Today, a wide variety of 3D-printed objects in biotechnology—ranging from miniaturized cultivation chambers to microfluidic lab-on-a-chip devices for diagnostics—are already being deployed in labs across the world. This review explains the 3D printing technologies that are currently used to fabricate such miniaturized microfluidic devices, and also seeks to offer some insight into recent developments demonstrating the use of these tools for biotechnological applications such as cell culture, separation techniques, and biosensors.

## KEYWORDS

3D printing, biosensors, cell culture, microfluidics, miniaturization

**Abbreviations:** CAD, computer-aided design; DLP, digital light processing; FDM, fused deposition modeling; MJP, MultiJet printing; OD, optical density; PDMS, polydimethylsiloxane; PSi, porous silicon; *S. cerevisiae*, *Saccharomyces cerevisiae*; SLA, stereolithography; SPE, screen printed electrode

This is an open access article under the terms of the [Creative Commons Attribution-NonCommercial](https://creativecommons.org/licenses/by-nc/4.0/) License, which permits use, distribution and reproduction in any medium, provided the original work is properly cited and is not used for commercial purposes.

© 2021 The Authors. *Engineering in Life Sciences* published by Wiley-VCH GmbH

## 1 | INTRODUCTION

In recent years, additive manufacturing techniques—also known collectively as 3D printing—have become widely recognized as a very promising technology, with the potential to revolutionize the biotechnology field. 3D printing was initially developed by Charles (Chuck) W. Hull in 1984, and it was subsequently patented in 1986 as a system that could produce three-dimensional objects in an additive manner, layer by layer [1–3]. Since that time, this young technology has already experienced several major breakthroughs: First, the term 3D printing now describes a variety of different manufacturing methods, the most commonly known and widely used being stereolithography (SLA) [1]; fused deposition modeling (FDM) [4]; selective laser sintering (SLS) [5]; and various inkjet-based techniques, including MultiJet printing (MJP) [6]. Each of these methods has its own specific relative advantages and disadvantages—resulting in specific areas of preferred applications for all of them. SLA, for example, enables the production of the finest structures compared to the other technologies [7, 8]. By contrast, FDM printers offer significantly higher accessibility due to their relatively low acquisition cost [9]. In addition, FDM printers can use a wide range of biocompatible thermoplastic polymers, which further expands their potential range of applications [10–12].

Second, the operation of modern 3D printers has become very straightforward, and no longer requires any substantial expertise or training: simply put, computer-aided design (CAD) software is used to create a 3D design, which can then be transferred directly to the printer for manufacturing. The ability to create complex 3D structures in a simple and flexible fashion sets this technology apart from more conventional methods for constructing miniaturized and microfluidic systems fabrication—such as soft lithography with polydimethylsiloxane (PDMS), which requires a unique master mold for each design [13].

Third, key features (such as printing resolution and speed) have also significantly improved over the years. For instance, while the first commercially available 3D printer (SLA-1) took an entire day to print even simple prototypes [3], modern 3D printers can print structures with dimensions of as low as 20–30  $\mu\text{m}$  within just a few hours [14]. Collectively, these technological advancements in the field of 3D printing now enable advanced modern 3D printer systems to create rapid prototyping systems through which researchers can test varying experimental parameters before fabricating miniaturized microfluidic systems. Furthermore, concurrent advances in material sciences have led to the development of a wide and ever-growing array of printing materials with various useful properties, such as translucence, heat resistance, and biocompatibility [15–17]—making this technology more and

more attractive for researchers working within the biotechnology field.

This review aims to explain additive manufacturing techniques relevant to biotechnology applications, and give an insight into some of the many opportunities that modern 3D printing techniques have to offer. We focus on miniaturized and microfluidic 3D-printed devices made from plastic polymers for utilization in microbial and mammalian cell culture and bioanalytics (e.g. chromatography, electrophoresis, biosensors, etc.) and highlight relevant examples mainly drawn from the last 5 years.

## 2 | 3D PRINTING TECHNIQUES

The fundamental insight underlying the concept of 3D printing is to imagine that all three-dimensional objects are the total sum of their various 2D elements—which can be built up upon each other, layer by layer. Accordingly, if a CAD model of the desired object is sliced into a finite number of 2D layers (dependent on the resolution of the 3D printer), those layers can then be used to inform a 3D printer how to assemble the entire object, layer by layer [18, 19]. A popular file format to be loaded in the slicing software is Standard Tessellation Language (.STL), which describes an object's surface geometry as a number of triangles [87].

In the literature, several 3D printing techniques (all with different comparative advantages and disadvantages) have been described for the manufacturing of microfluidic and miniaturized devices using various materials. SLA was the first established and patented technique: in this approach, a liquid photopolymer is precisely cured at a designated location using a laser (see Figure 1A) [20]. A stage or carrier plate is immersed in a bath containing this photopolymer and a photoinitiator, and its Z position can be moved stepwise to define the printing height of each layer. Since a laser must cure every spot, the printer's resolution is limited by the minimum pixel size of the laser beam [20]. SLA offers both the best resolution and lowest surface roughness of all the 3D printing techniques surveyed in this chapter. Channel dimensions below 30  $\mu\text{m}$  have been reported in the literature [21]. A further refinement aimed at improving the low printing throughput of SLA was the development of digital light processing (DLP), which offers the ability to cure all relevant spots of a layer in parallel [22]. SLA and DLP do not require additional support materials, but the photopolymer solution needs to be removed after the printing procedure. In addition to commercialized materials, various self-defined formulations of biocompatible and transparent materials such as polyethylene glycol diacrylate can also be employed as printing materials using these techniques [21, 23]. However, it should be

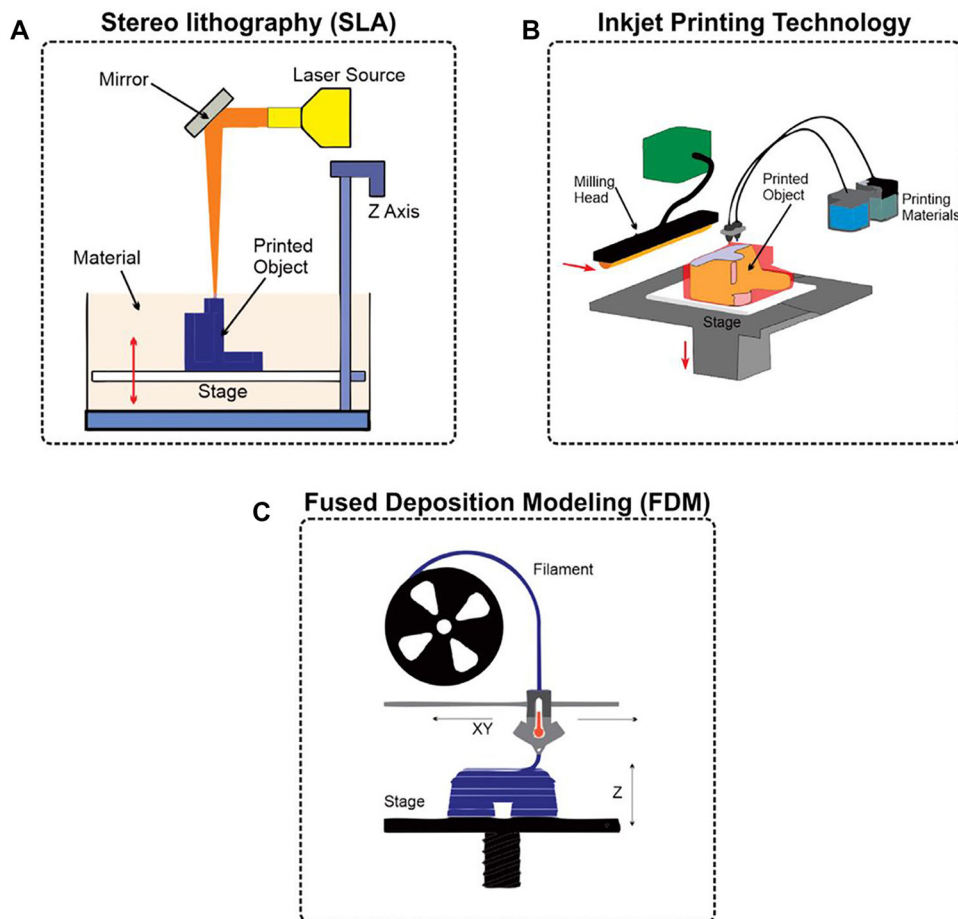


**FIGURE 1** Principles of 3D printing techniques. (A) In stereolithography (SLA) a movable stage is immersed in a bath containing a photopolymer and a photoinitiator. A laser is used to cure the polymer material at designated positions. (B) During inkjet-based printing, main and support materials are dropwise applied onto a stage, and the main material is cured using UV light. A milling head or leveling blade is used to smooth the surface after a layer is finished. (C) Fused deposition modeling (FDM) uses filaments of thermoplastic polymers that are heated and subsequently applied layer by layer to create the 3D object. Adapted with permission from [45]. Copyright 2018, the authors. Published under Creative Commons Attribution 4.0 International license (CC BY 4.0)

noted that residual non-reacted photoinitiators can impair biocompatibility, and that the light absorptive properties of the photopolymer might affect the printing resolution [20].

Inkjet-based techniques such as MJP and PolyJet printing (these actually constitute the same technology issued by different manufacturers) are a popular alternative since they utilize a high degree of automation and also result in a high-quality end product [20]. In this technology, main and support material are applied dropwise through printheads consisting of an array of nozzles (see Figure 1B). The main material is usually a proprietary acrylate, which is then cured using UV light [22, 24, 25], while the support material enables the fabrication of overhanging and complex 3D structures by filling cavities and hollows such as microfluidic channels—although this support material must ultimately be removed after the printing procedure is completed [25, 26]. Different commercial suppliers offer numerous materials with different proper-

ties (e.g. rigid, flexible, transparent, biocompatible, high-temperature resistant [15, 27, 28]). Unfortunately, the exact formulation of these commercialized materials is often not publicly available, and, as a result, the bioactivity of any such material must first be investigated carefully prior to use, as some of these materials may release potentially non-biocompatible leachables [20]. In addition, since all materials are applied dropwise, the overall resolution depends on the droplet size [22]—although this still permits the fabrication of channel dimensions in the range of hundreds of micrometers and below [29–32].

Last but not least, FDM is the cheapest technique for 3D printing of miniaturized devices. This technology belongs to the extrusion-based methods, as a printhead heats thermoplastic filaments above the melting point and then applies them onto a surface to let them cool (see Figure 1C) [20]. Instead of an external support material being used to fill cavities, fragile support structures are themselves

printed—which facilitates the creation of overhanging structures. The main advantages of FDM are the free choice of material (e.g. acrylonitrile butadiene styrene (ABS) [33], polyethylene terephthalate glycol (PETG) [18], polylactide acid (PLA) [18, 34, 35], polyurethane [36], etc.), the ability to use multiple materials within a single 3D-printed object, and the option to intervene in the printing process [18, 37, 38]. The main disadvantages posed by this technique are the usage of heat-sensitive materials (thermoplastics), the risk of potential fluid leakage due to an incomplete infill of the filamentous structures, and the difficulty of printing integrated channels [39]. This method also has the highest roughness and the lowest printing resolution out of all of the techniques surveyed in this paper [22, 40]. Nonetheless, even using FDM, channel dimensions down to 40  $\mu\text{m}$  have still been reported [36]—although channel dimensions in the range of hundreds of micrometers are far more common [34, 35, 41].

It should be emphasized that the 3D printing technology and material have to be selected carefully and with the specific goals of a given project in mind, since there is no universal material that is best suited (or even appropriate) for all conceivable applications. For usage in biotechnology, desired material properties that must be carefully considered include biocompatibility, gas permeability, and the option to be sterilized. In FDM, commonly used materials such as ABS and PLA are biocompatible—but the fabrication of transparent devices and integrated microfluidic channels can be challenging [13, 42]. Some materials, such as the commonly used PLA, are heat-sensitive and thus not suited for heat steam sterilization; however, heat-resistant alternatives for FDM exist. Photocurable materials such as polyacrylates (typically used in SLA and inkjet-based techniques) are better suited to create transparent devices, the development of integrated microfluidic channels is more straightforward, and heat steam sterilizable materials are also available [13, 27, 42]. However, researchers should bear in mind that photopolymers may have cytotoxic properties, and comprehensive biocompatibility studies for many commercially available materials are often nonexistent [13, 20]. Nevertheless, there are also examples of such biocompatible resins used in SLA and inkjet-based techniques [15, 43].

It is also dangerous to attempt to generalize about the biocompatibility of any 3D printing material. For example, Rimington et al. have demonstrated that the same 3D printing material had varied cell-specific effects in terms of proliferation and differentiation for different cell types [44]; Siller et al. have demonstrated that even post-processing can have a significant effect on the biocompatibility [15]. This underscores, once again, that the material used for any given project must be selected, taking into account both the cell type(s) and the application(s) in question.

In terms of gas permeability, however, it can generally be stated that 3D-printed plastic materials used in SLA, inkjet-based techniques, and FDM tend to have relatively poor gas permeability [13]. For further reading, we would refer the reader to the excellent review article of Bhattacharjee et al. who give a detailed overview of various properties of plastic materials used in SLA, FDM, and inkjet-based 3D printing technologies [13].

### 3 | 3D-PRINTED DEVICES FOR MICROBIAL AND CELL CULTURE

Due to the wide availability of biocompatible materials, 3D printing allows for the fabrication of microbioreactors, cultivation vessels, and other devices for microbial and mammalian cell culture applications. Various studies have now demonstrated the biocompatibility of diverse materials that are compatible with different 3D printing techniques [15, 43, 46]. For instance, Siller et al. have comprehensively studied the biocompatibility of polyacrylate materials used in inkjet-based 3D printers for the cultivation of mesenchymal stem cells (MSCs) according to EN ISO 10993-12 (2012). The viability of cells was measured by various assays (Cell Titer Blue assay, lactate dehydrogenase assay, flow cytometry, real-time live-cell imaging) and found to be unaffected by the polyacrylate materials themselves [15, 47]. However, post-processing and sterilization/disinfection procedures were found to exert significant effects on cell growth and viability [15].

#### 3.1 | Microbioreactors for microbial cultivation

Miniaturization is one of the most significant advantages offered by microbioreactors during bioprocess optimization. These systems significantly reduce the required volumes of cell culture media—thereby enabling researchers to run several experiments at varying conditions in parallel, while also conducting them in a highly space-efficient manner. Furthermore, 3D printing facilitates rapid prototyping of microbioreactors at a comparatively low price, since adapting the CAD file permits simple reactor design adjustments. One example of such a miniaturized system was presented by Panjan et al. who developed a microbioreactor (1 mL internal volume) fabricated by SLA procedure to cultivate *Saccharomyces cerevisiae* (*S. cerevisiae*) with integrated optical density (OD) and real-time glucose monitoring [48]. Figure 2A-i depicts the reactor design consisting of its main cultivation chamber, including a connection port for glucose biosensor integration, an inlet and outlet for liquids, and a gas outlet on top

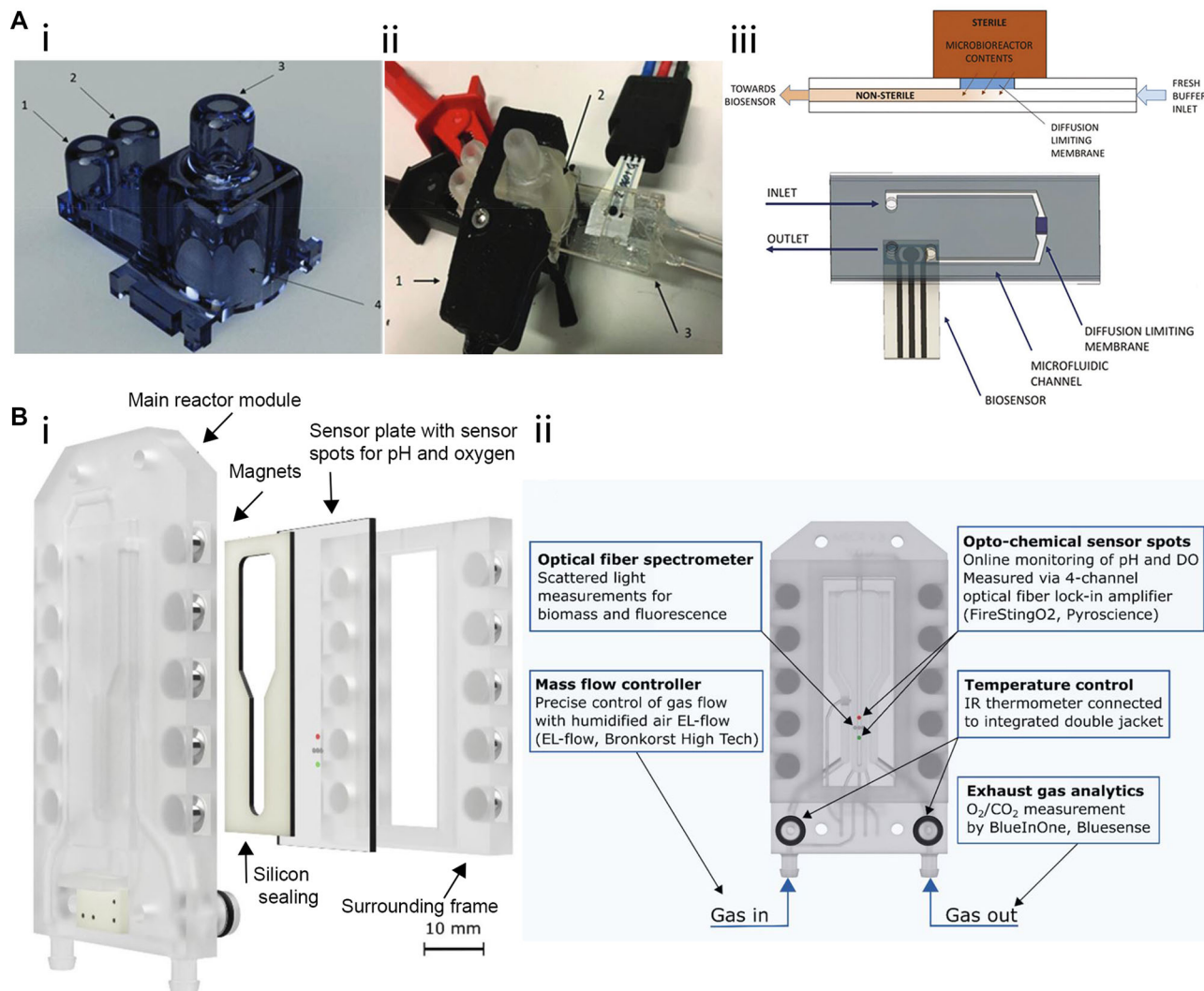


**FIGURE 2** 3D-printed microbioreactors for microbial cultivation. (A-i) 3D-printed microbioreactor consisting of (1) inlet (2) outlet (3) gas outlet and (4) the main reactor chamber with biosensor integration port. (A-ii) In the experimental setup, a (1) OD sensor is clipped onto the (2) reactor chamber, and the (3) glucose biosensor is integrated. (A-iii) Sterile integration of the glucose biosensors guaranteed by separating the microbioreactor and the biosensing unit with a diffusion limiting membrane. Adapted with permission from [48]. Copyright 2018, the Royal Society of Chemistry. Published under Creative Commons Attribution-NonCommercial 3.0 Unported license (CC BY-NC 3.0). (B-i) Exploded view of the micro bubble column reactor consisting of the main reactor module, sensor plate within a surrounding frame, and silicon sealing being held together by magnets. (B-ii) Schematic of the reactor depicting the position of microsensor spots for process analysis, gassing in-, and outlet as well as the connectors for temperature control. Adapted with permission from [49]. Copyright 2021, the authors. Published under Creative Commons Attribution 4.0 International license (CC BY 4.0)

of the reactor. Placing two small polytetrafluoroethylene (PTFE)-covered magnetic balls inside the microbioreactor enabled magnetically mediated mixing during the cultivation process. Figure 2A-ii depicts the experimental setup, which included a clipped-on OD sensor and an integrated electrochemical glucose oxidase biosensor. Integration of such biosensors for process control in microbioreactors is particularly challenging since the sterility of the system needs to be guaranteed. In the presented work, this challenge was overcome by connecting the reactor chamber to a microfluidic channel via a diffusion limiting

membrane (see Figure 2A-iii). This membrane prevented contamination, while still allowing glucose slowly to pass through (i.e. from the reactor to the non-sterile microfluidic channel) and be flushed towards the biosensor. As a proof-of-concept, this microbioreactor system successfully monitored *S. cerevisiae* growth and glucose consumption in real-time over a cultivation period of 8 h.

In another article, Frey et al. reported the development of a customized 3D-printed micro bubble column reactor system (fabricated by MultiJet printing) and demonstrated its successful integration with various microsensors for



bioprocess control during the cultivation of *S. cerevisiae* [49]. In this system, gassing occurred from the reactor bottom, causing air bubbles to rise through the reactor chamber. Fluids (e.g. culture medium) in the microreactor were thereby agitated, preventing concentration and temperature gradients without using stirrers. Figure 2B-i depicts an exploded view of the microreactor components: The main reactor module sets the shape of the device and provides channels for temperature and gas transfer control. The sensor plate containing microsensing elements, a surrounding frame, and silicon sealing creates the reactor volume by being tied to the main reactor module with magnets. Furthermore, the overall system is clamped together, using a connector clip and screws, in order to avoid leakage. The sensor provides a rapid heat and mass transfer due to the small reactor volume (550  $\mu\text{L}$ ), online monitoring of process parameters (biomass, dissolved oxygen, pH), and exhaust gas analysis ( $\text{O}_2$ ,  $\text{CO}_2$ ). Figure 2B-ii depicts a schematic of the reactor detailing the position of microsensor spots for process analysis, gassing in, and outlet, as well as the connectors for temperature control. During an *S. cerevisiae* cultivation over a 16 h period, the process parameters were successfully monitored. In terms of the growth rate, the 3D-printed micro bubble column reactor achieved similar values ( $0.403 \pm 0.02 \text{ h}^{-1}$  at  $20 \text{ g L}^{-1}$  glucose) compared to conventional systems such as a 2.5 L stirred-tank bioreactor in batch mode ( $0.4 \text{ h}^{-1}$  at  $30 \text{ g L}^{-1}$  glucose) [50].

### 3.2 | Applications in mammalian cell culture

Microbioreactors also hold great promise for application in the field of mammalian cell culture; for example, Quian et al. have recently fabricated miniaturized 3D-printed spinning bioreactors to generate and culture forebrain-specific organoids derived from human-induced pluripotent stem cells [51]. These organoids are small organ-like cell structures that can be artificially produced from embryonic, adult, and induced pluripotent stem cells, and as such they are highly useful for disease modeling and drug testing since they resemble “real” organs much more closely than conventional monolayer cultures [51, 52]. Their microbioreactors were created by fitting a 3D-printed cover consisting of 12 spinning shafts and interconnecting gears (created by FDM) onto a standard 12-well plate (see Figure 3A). The gears were driven by a single electric motor, allowing the researchers to sustain organoids in suspension under gentle spinning conditions and thereby preventing aggregation and increasing cell viability compared to static cultures. Miniaturization of the system enables studying organoid generation and performing drug screen-

ing and disease modeling under different conditions at lower volumes—which reduces the cost of running experiments compared to deploying larger spinning flasks. As a proof-of-concept application, the forebrain-organoid platform was employed for disease modeling of Zika virus exposure.

Other works have also demonstrated (for example) the usefulness of microfluidic on-chip platforms as blood-brain barrier models [53], microbioreactors for tissue engineering [54], and cultivation chambers for studying angiogenesis (formation of new blood vessels) [55]. These examples underscore the tremendous applicability of 3D printing across a wide variety of cultivation devices and applications.

Aside from the employment of 3D printing technology to fabricate microbioreactors or cultivation devices, additive manufacturing techniques have also been utilized to manufacture other mammalian cell culture-related 3D-printed tools. For example, Alessandri et al. have developed a microfluidic co-extrusion device that enables the production of hydrogel microcapsules to cultivate and differentiate human neuronal stem cells [56]. Production of these hydrogel microcapsules could potentially be used to create a 3D culture system for high-throughput screening, since a massive amount of these stem cell-containing microcapsules can be produced automatically at once. This 3D-printed tool was created by a DLP printer and consists of three inlets (Figure 3B-i) which separately guided fluids into three individual conical layers (Figure 3B-ii), where the outer layers surrounded the inner ones. Three syringe pumps then introduced an alginate solution into the outer layer, an intermediate buffer solution into the middle layer, and the cell suspension supplemented with matrigel (to support stem cell growth) into the inner layer. At the nozzle of the 3D-printed devices, the fluids conjoined and formed droplets with cells encapsulated in them, which were then collected into a calcium gelatination bath (see Figure 3B-iii for the 3-way co-extrusion procedure and production of the hydrogel microcapsules). Neuronal stem cell differentiation into neurons was successfully achieved by culturing the encapsulated cells in a mitogen-free differentiation medium for 13 days; viability was found to be high ( $\sim 98\%$ ), as revealed by 4',6-diamidino-2-phenylindole (DAPI) immunofluorescence.

In a recent project reported by Lavrentieva et al. a 3D-printed device made from polyacrylate material using MultiJet technology was employed to create stiffness gradient hydrogels. These hydrogels are capturing increasing interest in the field of mechanobiology for studying the influence of mechanical cell-matrix (e.g. extracellular matrix) interactions [57]. Reproducible fabrication of these stiffness gradient hydrogels helps researchers to experimentally identify the optimal mechanical conditions for 3D cell

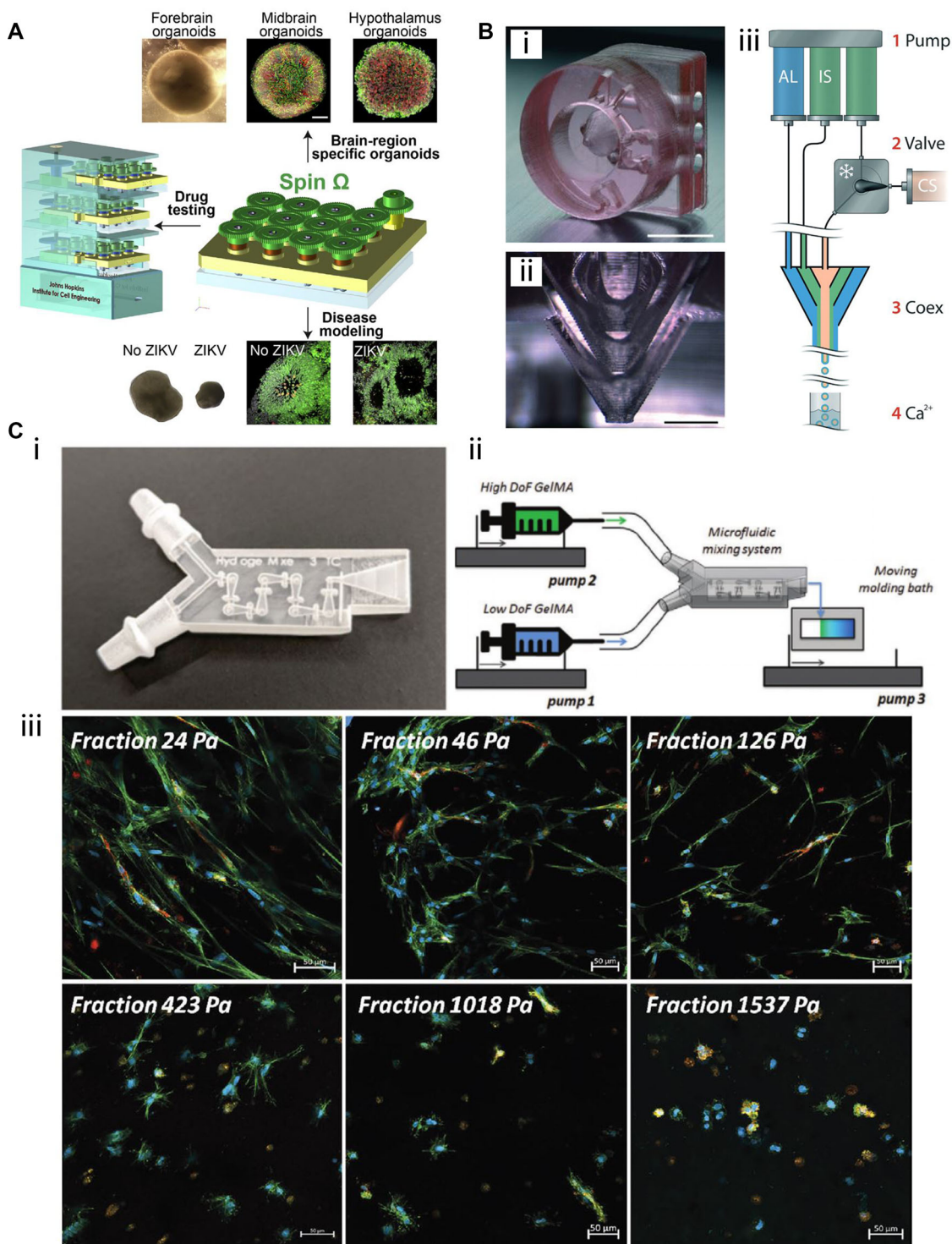


**FIGURE 3** 3D-printed devices for mammalian cell culture applications. (A) Microbioreactors for forebrain-specific organoid generation and zika virus disease modeling. Reproduced with permission from [51]. Copyright 2016, Elsevier. (B-i) A 3D-printed co-extrusion device with three inlets and (B-ii) three separate conical layers conjoining to form a nozzle is employed to (B-iii) encapsulate human neuronal stem cells into hydrogel microcapsules for high-throughput differentiation. Adapted with permission from [56]. Copyright 2016, the Royal Society of Chemistry. (C-i) A 3D-printed microfluidic mixing device is used to (C-ii) create stiffness gradient hydrogels and (C-iii) study their mechanical influence on cell spreading using various fluorescence dyes for staining. Adapted with permission from [57]. Copyright 2020, the authors. Published under Creative Commons Attribution 4.0 International license (CC BY 4.0)

culture with respect to changes in morphology and cell spreading. In the presented approach, two syringes were connected to the 3D-printed tool, and the gradient was created by pumping hydrogels with high and low crosslinker amounts at varying flow rates into the device. An integrated HC-mixer (as previously described [25]) facilitated homogenous mixing before hydrogels were cast onto a moving molding bath (see Figure 3C-i for a micrograph of the 3D-printed device and Figure 3C-ii for the hydrogel fabrication procedure). Human adipose tissue-derived mesenchymal stem cells (hAD-MSCs) and human umbilical cord vein endothelial cells (HUVECs) cells were then encapsulated into the hydrogel and cultivated for 7 days. These cells were subsequently visualized via staining and fluorescence microscopy (see Figure 3C-iii), and the results demonstrated that cell spreading was increasingly hindered along the gradient with higher stiffness.

3D printing has also been employed to create spiral-shaped inertial focusing devices with potential use for cell culture applications [58]. Such tools are traditionally fabricated via soft lithography (PDMS) or micromilling procedures [58, 59] and were, for instance, demonstrated to isolate T and B cells from blood [60] or isolate single stem cells from stem cell clusters [61]. Such tools have also been used for cell retention integrated into miniature auto-perfusion bioreactors, and as such they can greatly contribute to bioprocess applications [62].

Here, once again, 3D printing offers an alternative to conventional methods that require cleanroom procedures (photolithography/ soft lithography) or are subtractive approaches (micromilling) [58]. Figure 4A depicts an example of a 3D-printed inertial focusing device that can be used to separate bacteria cells using antibody-modified magnetic nanoparticle clusters. In this system, single bacteria are focused near the outer wall of the channel, while larger clusters of bacteria attached to the magnetic nanoparticles are focused towards the inner channel wall (see Figure 4B) and transferred to their respective outlets [63]. The presented device potentially enables the separation of specific bacterial species by choosing the appropriate antibodies.

While 3D-printed inertial focusing devices for bioprocess applications are still rare, we believe that these tools will increasingly be employed for such operations in the future. For example, Enders et al. have shown that these 3D-printed spiral cell separator devices can be used for cell retention to enable continuous cultivation processes [64]. Such systems could also potentially be used to concentrate cells with the aim to improve the transient transfection of mammalian cell lines used for protein production.

We note in passing that 3D printing has mainly been employed for tissue engineering applications by printing scaffolds from various materials and bioprinting (printing

of biomaterials and living cells). Because this review aims to explain the application of 3D-printed miniaturized and microfluidic devices made from plastic materials, we do not dwell on 3D printing for tissue engineering; nevertheless, we would refer any interested readers to the review articles of Tamay et al. [65] and Zaszczynska et al. [66].

## 4 | 3D-PRINTED DEVICES FOR BIOANALYTICS

Bioanalytical methods such as chromatography and electrophoresis are routinely used in biotechnology laboratories to separate and detect nucleic acids and proteins. Biosensors are widely applied to detect various target molecules using appropriate biosensing schemes (e.g. optical, electrochemical, mechanical, etc.) and concepts. Once again, 3D printing offers substantial benefits across all of these applications—including system miniaturization that reduces fluid consumption, and required space and results in lowered experimental cost and greater parallelization opportunities. Moreover, 3D printing also enables rapid prototyping of different experimental setups in a flexible and customized fashion. For example, in terms of biosensor integration into 3D-printed microfluidic systems, parameters such as channel dimensions and geometries, and device size can all be quickly adjusted to fit shifting experimental requirements.

### 4.1 | Chromatography and electrophoresis

One advantage of 3D printing for chromatography applications is the ability to miniaturize systems, which can be used to combine numerous columns within a single 3D-printed device or miniaturize very long chromatographic columns within one microfluidic lab-on-a-chip tool [67, 68]. One example of such a miniaturized chromatographic system was given by Lucklum et al. who developed stacked spiral miniature 3D gas chromatography columns for potential use in a portable ethylene sensor system during fruits transport and storage [69].

Moreover, the ability of 3D printing to manufacture complex 3D structures enables the production of customized and tailored column beds. While conventional beds are often made out of porous materials with inhomogeneous structures, they can be directly manufactured via 3D printing in an ordered fashion with specific geometries to improve the separation performance [67, 70]. Simon and Dimartino were one of the first to manufacture an ion-exchange adsorber with a DLP printer in a single step, using a customized printing material [71, 72], thereby

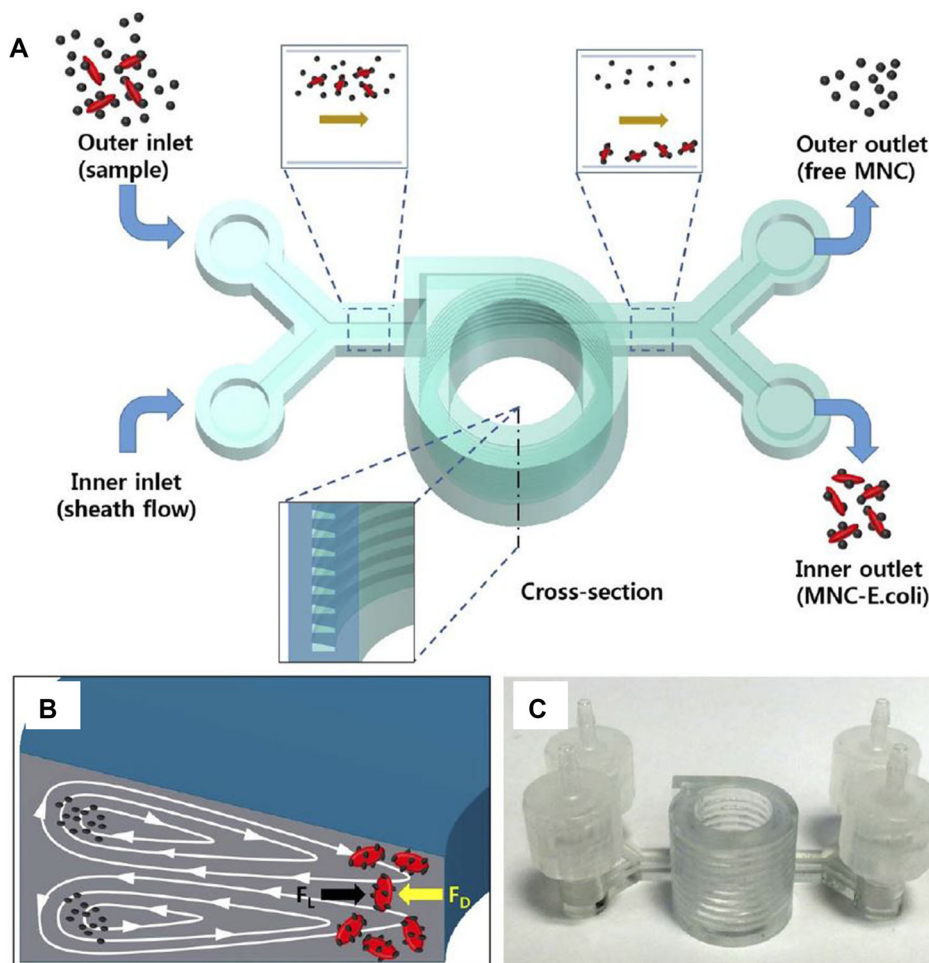


**FIGURE 4** 3D-printed microfluidic inertial focusing device for bacteria separation (A) Schematic of the 3D-printed spiral-shaped inertial focusing device. Bacteria and antibody-modified magnetic nanoparticle clusters (MNC) are introduced into the system. (B) Single bacteria are focused near the outer wall of the channel, while bacteria attached to the antibody-modified magnetic nanoparticles are focused close to the inner channel wall, enabling separation into designated outlets. (C) Photograph of the 3D-printed tool. Reproduced with permission from [63]. Copyright 2015, the authors. Published under a Creative Commons Attribution-NonCommercial-NoDerivs 4.0 International License

enabling the fabrication of columns with such ordered bed morphology (see Figure 5A). This system was used to separate BSA and myoglobin and purify C-phycoyanin, a bacterial pigment-protein with potential uses in medicine and biotechnology by means of anion exchange chromatography [72].

Although the feature size of the adsorbers bed channels was reportedly larger than in commercial resins ( $200\ \mu\text{m}$  compared to  $50\ \mu\text{m}$ ), the separation performance was similar. The authors claim that the improvement of 3D printing resolution within the next few years will likely continue to enhance the comparative performance of these 3D-printed bed columns in comparison to more conventional packaging [72].

With respect to the bed structure design, the ability of 3D printing for rapid prototyping also offers tremendous benefits. For example, different bed structures with various sizes or geometries can potentially be created and

expeditiously tested for their separation performances. Figure 5B shows a collection of ordered beds with different geometries (such as spheres, tetrahedra, and triangular bipyramids) that are designed, printed, and characterized in various configurations according to their shape, position, orientation, and plate height. Experimental validations of computations predictions regarding such permutations can be achieved through rapid prototyping of these structures via 3D printing [73].

For the future, we envision integrated and continuous chromatographic units in biotechnological applications. For instance, culture broth from a bioprocess could continuously be forwarded through a chromatographic separation unit for preparative or analytic purposes. The role of 3D printing would be to help achieve the simplification of interfacing across all units. A single 3D-printed microfluidic chip could potentially supersede complex tubing connections, integrate valves for pseudo-continuous

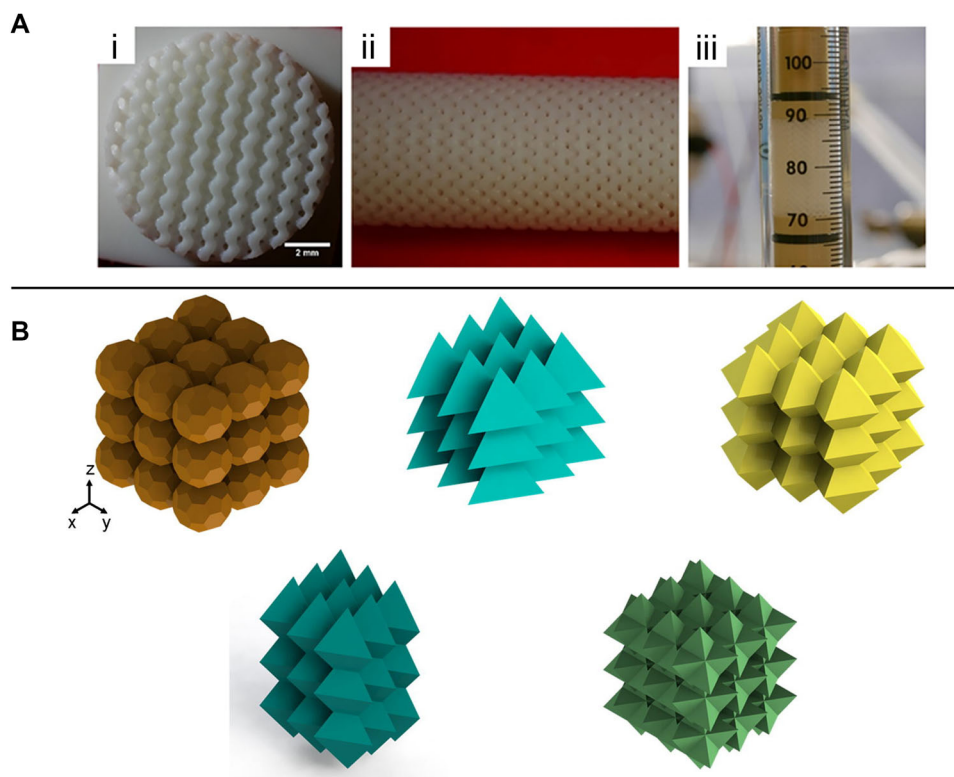


**FIGURE 5** (A) 3D-printed anion exchange column with (i-ii) an ordered bed morphology. These ordered cylindrical structures are termed Schoen gyroid structures. (iii) Integration of the 3D-printed structure in a glass column. Adapted with permission from [72]. Copyright 2020, the authors. Published under Creative Commons Attribution 4.0 International license (CC BY 4.0). (B) Bed geometries designed and printed via 3D printing. These structures were experimentally investigated regarding their plate height to confirm computational predictions. Adapted with permission from [73]. Copyright 2017, Elsevier

sample injection. Using customized 3D-printed threads, this interface could integrate any commercialized or self-designed (3D-printed) columns or follow-up analytics (e.g. mass spectrometry) into a single miniaturized and tightly arranged platform. One particularly tantalizing example of how 3D printing can facilitate the integration of high-performance liquid chromatography (HPLC) into a customized and more complex setting was given by Wang et al. in 2017. An end front sample preparation application was developed, which included both microflow injection ( $\mu$ FI) and peak focusing. For the  $\mu$ FI, a 3D-printed multiway valve controlled the access of sample, eluent, and washing buffer towards HPLC, 3D-printed microsolid phase extraction (3D- $\mu$ SPE) unit, and waste. The 3D- $\mu$ SPE accomplished peak focusing using polyaniline-decorated magnetic nanoparticles and antimicrobial substances have been detected with a 16-25 fold increase of efficiency in saliva and urine samples [74].

An example of a 3D-printed gel electrophoretic chip (created by MultiJet technology) that proved useful for DNA separation was recently given by Adamski et al. in their work. Figure 6A-i depicts a schematic of this device, which consists of two crossed microfluidic channels where

the shorter channel is used to introduce the DNA sample (fluorescently labeled 50 to 800 bp DNA ladder fragments) and transfer it to the longer separation channel, which is filled with electrophoresis gel [75]. The introduced fluorescently labeled DNA fragments (Figure 6A-ii) are then driven through the channel by applying a voltage and separated (Figure 6A-iii and iv). Fluorescence is used to detect the labeled and separated DNA fragment at a designated spot (Figure 6A-v and vi). According to the authors of that publication, this device is the first 3D-printed tool ever reported as being successfully used for gel electrophoretic DNA separation. Notably, this device can also be rapidly fabricated (3 h printing) at a relatively low cost (<1€).

3D printing has additionally been employed to create free-flow electrophoresis systems [33, 76, 77]. This electrophoretic technique separates the analytes in a liquid phase continuously, and does not require a gel-like matrix of the sort utilized in agarose gel electrophoresis and sodium dodecyl sulfate-polyacrylamide gel electrophoresis (SDS-PAGE) for DNA and protein separation, respectively [78]. For example, Preuss et al. have developed a 3D-printed free-flow electrophoresis device with a simple design that can be fabricated from a polyacrylate

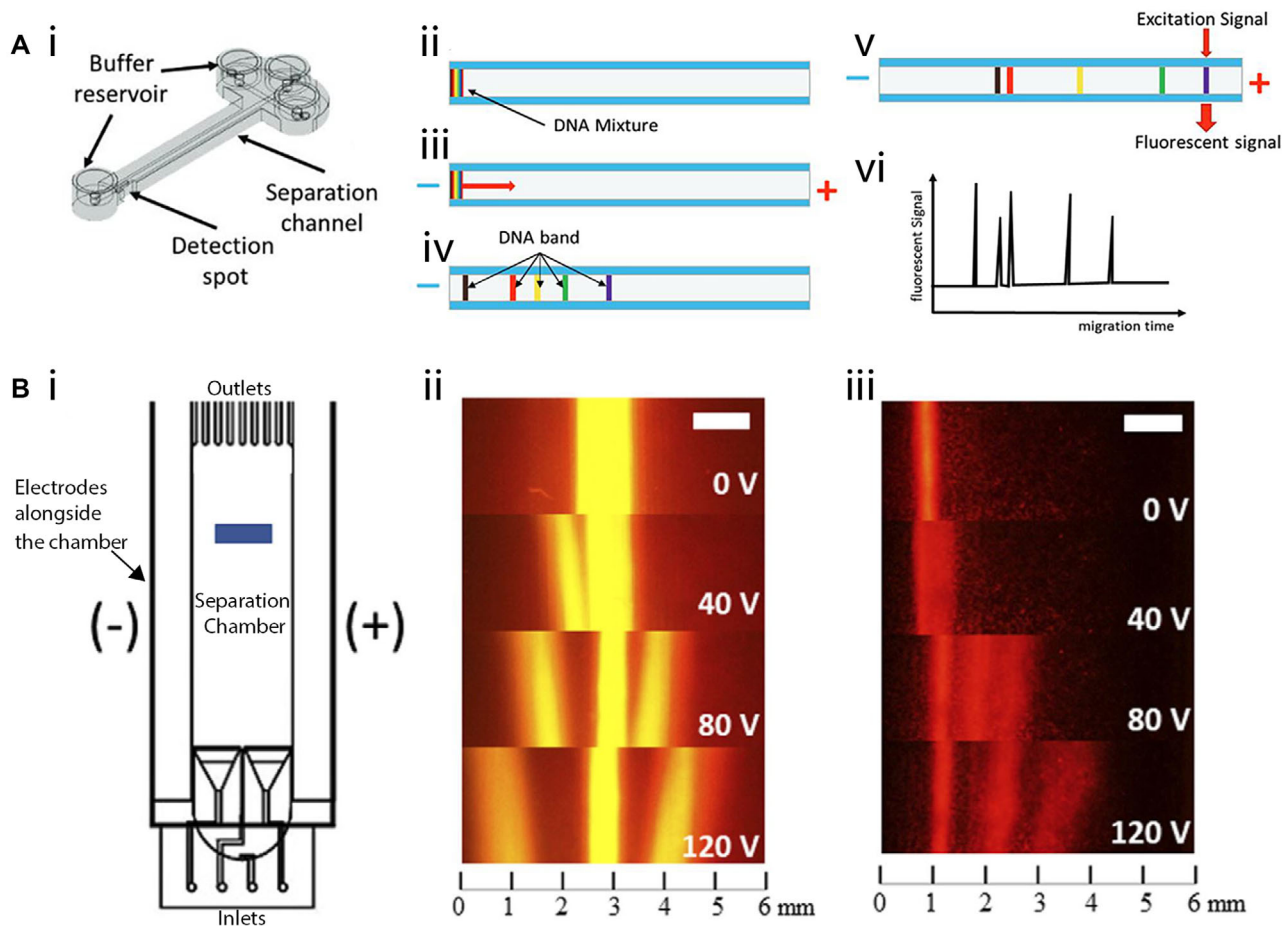


**FIGURE 6** 3D-printed electrophoretic devices. (A-i) Schematic of the 3D-printed device for gel electrophoretic separation of DNA. (ii-iv) Fluorescently-labeled DNA fragments introduced into the separation channel are driven through the channel by applying voltage and separated. (v-vi) Fluorescence is used to detect the fragments. Reproduced with permission from [75]. Copyright 2016, the authors. Published under Attribution-NonCommercial-NoDerivatives 4.0 International license (CC BY-NC-ND 4.0) (B-i) Schematic of the 3D-printed free-flow electrophoretic system used to (ii) separate fluorescence dyes and (iii) fluorescently-labeled amino acids. Adapted with permission from [76]. Copyright 2020, the authors. Published under Creative Commons Attribution 4.0 International license (CC BY 4.0)

material using the MultiJet printing technology [76]. This free-flow electrophoresis system consists of inlets for buffer and sample, a separation chamber, and outlets that guide the separate fractions into designated collection wells (see Figure 6B-i). Alongside the device, two platinum wires (functioning as electrodes) are installed and separated from the separation chamber using a polycarbonate membrane. The principle of this free-flow electrophoresis technique is straightforward: Applying a voltage creates a positive pole on one side of the separation chamber and a negative pole on the other side, allowing researchers to separate differently charged molecules. In this proof-of-concept study, the fluorescence dyes rhodamine B, pyronine Y, and sulforhodamine B (Figure 6B-ii), and the fluorescently-labeled amino acids arginine, glycine, and glutamate (Figure 6B-iii) could be successfully segregated.

## 4.2 | Biosensors and point-of-care diagnostics

Various biosensor systems designed to detect diverse target molecules such as DNA [79], proteins [80], carbohydrates [81, 82], and bacteria [26] have also been successfully integrated into 3D-printed systems. The integration of optical and electrochemical biosensors into microfluidic and miniaturized 3D-printed systems has been an area of increasing interest in recent years [83]. An example of such an optical biosensor was presented by Arshavsky-Graham et al. who deployed a photonic porous silicon (PSi) chip as the transducing element and integrated the chip into a 3D-printed system (see Figure 7A-i) [80]. These PSi-chips consist of a porous nanostructure that is preferential for capture probe (e.g. aptamers, antibodies) immobilization due to its high surface area [84]. Molecule binding

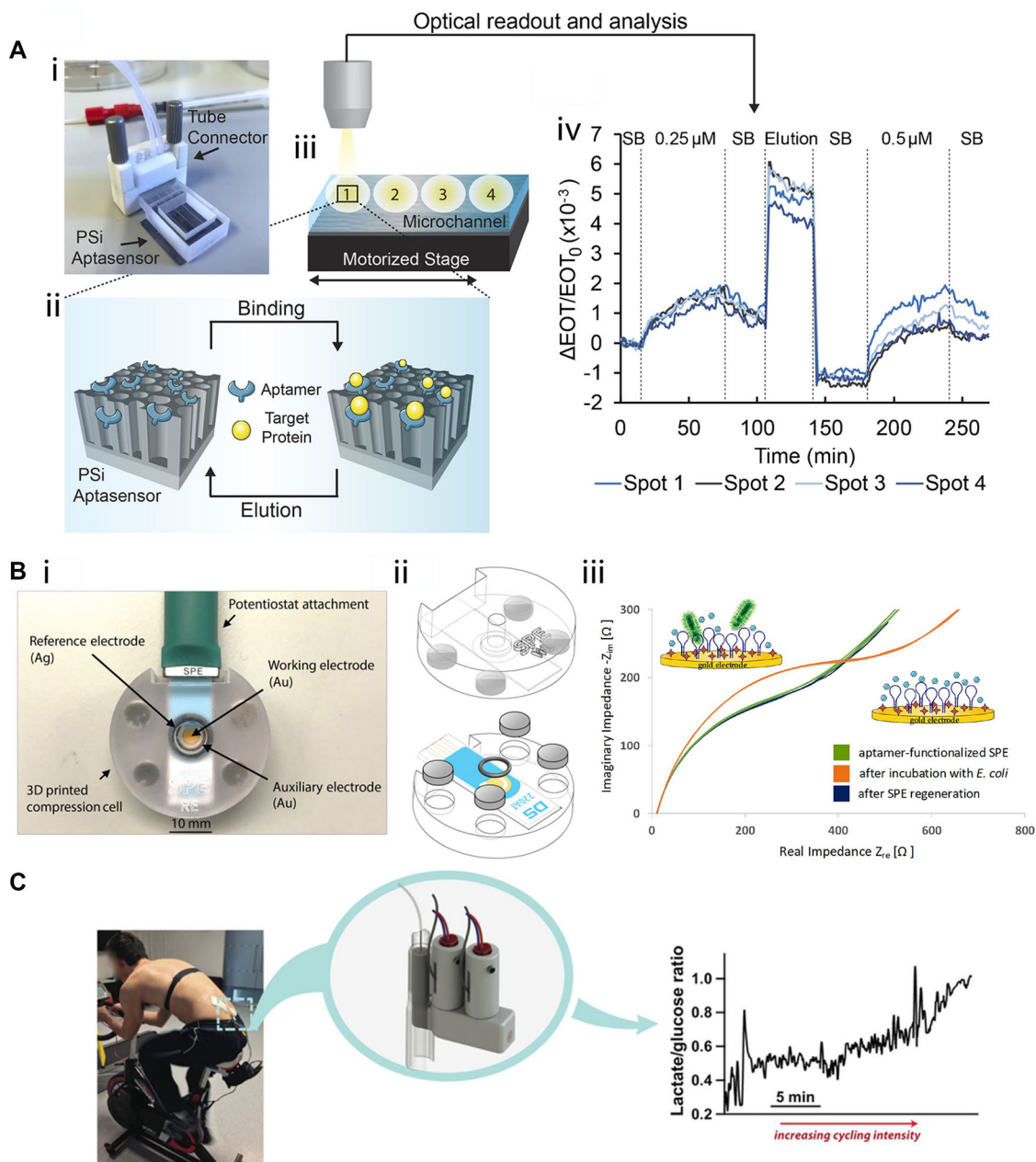


**FIGURE 7** 3D printing for biosensing applications. (A-i) Photograph of the 3D-printed device with integrated photonic PSI-chips. (A-ii) The chip's silicon nanostructure is functionalized with aptamers specific for target proteins exhibiting a histidine-tag. (A-iii) Measurements are conducted at different spots along the microfluidic channel, and optical readout and analysis are performed to (A-iv) monitor target molecule binding by tracking changes in the refractive index within the porous layer. Reproduced with permission from [80]. Copyright 2021, the authors. Published under Creative Commons Attribution 4.0 International license (CC BY 4.0). (B-i) Photograph of the impedance-based biosensor for *E. coli* detection in which (B-ii) the SPE is placed between two 3D-printed parts. The system is held together by disc magnets and sealed by using an o-ring. (B-ii) Presence of *E. coli* cells onto the aptamer-decorated SPE gold surface is detected by monitoring changes in the impedance signal. Adapted with permission from [26]. Copyright 2020, the authors. Published under Creative Commons Attribution 4.0 International license (CC BY 4.0). (C) Microdialysis probes and lactate and glucose biosensors are integrated into a 3D-printed system to analyze lactate and glucose levels in subcutaneous tissue during a cycling exercise. Reproduced with permission from [85]. Copyright 2015, American Chemical Society. Published under Creative Commons Attribution 4.0 International license (CC BY 4.0)

(Figure 7A-ii) to these capture probes can be monitored in a label-free manner by illuminating the chips (Figure 7A-iii) and recording unique reflectance spectra using a spectrometer. The reflectance spectra are then analyzed to monitor refractive index changes within the porous nanostructure caused by target molecules binding to the respective capture probe (see Figure 7A-iv). In the presented work, the P*Si*-chip was integrated by bonding the 3D-printed device (created by MultiJet printing) with microfluidic channels open to their bottom onto the chip's surface using an optical adhesive. Subsequently, the nanostructured silicon surface was functionalized using an established aptamer binding to histidine-tags in proteins. Optical readout and analysis were also enabled by the translucent properties of the 3D-printed material. Both the selectivity and sensitivity of this 3D-printed microfluidic biosensing system were superior to the previously used system; moreover, biosensor regeneration was also demonstrated using an imidazole-containing buffer to elute the target molecule from the sensor surface. In general, this same concept can be applied for various target molecules simply by employing designated aptamers or other capture probes.

In another work, Siller et al. similarly demonstrated how an electrochemical impedance spectroscopy (EIS) biosensor for bacteria detection could be integrated into a 3D-printed system using the same printing technology [26]. Figure 7B-i and -ii both illustrate the 3D-printed device, which consisted of a screen-printed electrode (SPE) placed between two 3D-printed parts held together by magnets. The upper part contained a cavity, allowing the addition of defined volumes of buffer or bacteria suspension onto the electrode. The gold surface of the SPE was functionalized with aptamers specific for *Escherichia coli* to facilitate the detection of this bacterial species by EIS measurements (Figure 7B-iii) at cell densities between  $10^5$  and  $10^8$  cells mL<sup>-1</sup>. In contrast, a different bacterium, *Enterococcus faecalis*, remained undetectable even at high concentrations ( $10^8$  cells mL<sup>-1</sup>), demonstrating the system's selectivity. This project also highlights one of the particular strengths of this approach: design flexibility. The static system (described above) was adjusted to create a flow cell by integrating inlets and outlets, enabling automated control of the fluid flow and introducing defined volumes (e.g. washing buffer and sample suspensions) by connecting the flow cell to pumps. For instance, this system could be used to adjust concentrations automatically, run concentration gradients, or switch between dynamic (flow) and static (without flow) states. Moreover, a micromixer was also integrated, enabling homogenous mixing of fluids before being introduced onto the SPE surface.

3D printing has even been applied to fabricate systems that can potentially be used as wearable biosensors. For example, Gowers et al. have reported their success-

ful integration of microdialysis probes, as well as glucose and lactate biosensors, into a 3D-printed system [85]. Their device was attached directly to the human body, and facilitated the measurement of lactate and glucose levels in the subcutaneous tissue during cycling exercises, as shown in Figure 7C. Tracking both of these biomarkers is of particular interest for sports- and fitness-related monitoring, since lactate is produced during intense exercise when there is not sufficient oxygen in the tissues and aerobic metabolism cannot provide enough energy for the body [85]. The described biosensor system demonstrates a concrete step towards point-of-care applications which would potentially permit individual physicians to perform monitoring and diagnostics on individual patients without relying on centralized laboratories. Indeed, 3D printing has already been used for various applications in this realm—including blood plasma separation, concentration and detection of bacteria from blood, or diagnosis of drug-resistant bacteria [86], underscoring yet again the tremendous versatility of this technology.

## 5 | CONCLUDING REMARKS

In this review, we have sought to offer some insights into promising recent developments of 3D printing technology for the fabrication of miniaturized and microfluidic tools in the biotechnology field. Various devices for different applications—ranging from cell culture to biosensors and diagnostics—have already been realized in labs across the world, thanks to the ever-increasing variety of available materials and printing technologies. Compared to soft lithography using PDMS, 3D printing allows for the relatively automated and straightforward fabrication of devices, within a single step and without the requirement for a master mold or cleanroom procedures.

Having said that, some technological barriers do continue to limit the widespread adoption of 3D printing for microfluidic systems—and, to date, no 3D printing technology and material have managed to successfully package and duplicate all the beneficial properties realized through PDMS (e.g. very high resolution, biocompatibility, gas permeability, optical clarity, and flexibility) [13]. Nevertheless, the authors firmly believe that the principle obstructions which currently impede widespread adoption of this technology can, and will, be substantially overcome within the next few years. Only the future will reveal if 3D printing remains a technique primarily used for experiment-specific rapid prototyping, or if 3D printing will finally enable rapid manufacturing of customized 3D-printed tools for market-wide applications such as cell culture, biosensors, or point-of-care diagnostics—but



there is unquestionably room for great optimism about the promise of this young and rapidly advancing technology.

## ACKNOWLEDGMENTS

The authors acknowledge the financial support through the Emmy Noether Programme (346772917).

Open access funding enabled and organized by Projekt DEAL.

## CONFLICT OF INTEREST

The authors declare no conflict of interest.

## DATA AVAILABILITY STATEMENT

Data sharing not applicable – no new data generated.

## ORCID

Christopher Heuer  <https://orcid.org/0000-0002-3694-0008>

## REFERENCES

- Hull, C. W. Apparatus for Production of Three-Dimensional Objects by Stereolithography. US Patent US4575330A; 1984.
- Hull, C. On stereolithography. *Virtual Phys. Prototyp.* 2012, 7, 177.
- Hull, C. W. The birth of 3D printing. *Res. Technol. Manag.* 2015, 58, 25–29.
- Crump, S. S. Apparatus and Method for Creating Three-Dimensional Objects. US Patent US5121329A; 1989.
- Deckard, C. R. Apparatus for Producing Parts by Selective Sintering. US Patent US5597589A; 1986.
- Sachs, E. M., Haggerty, J. S., Cima, M. J., Williams, P. A. *Three-Dimensional Printing Techniques*. US Patent US5204055A; 1989.
- Gong, H., Bickham, B. P., Woolley, A. T. and Nordin, G. P., Custom 3D printer and resin for 18  $\mu\text{m}$  x 20  $\mu\text{m}$  microfluidic flow channels. *Lab Chip* 2017, 17, 2899–2909.
- Bhanvadia, A. A., Farley, R. T., Noh, Y. and Nishida, T., High-resolution stereolithography using a static liquid constrained interface. *Commun. Mater.* 2021, 2, 1–7.
- Takagishi, K. and Umez, S., Development of the improving process for the 3D printed structure. *Sci. Rep.* 2017, 7, 1–10.
- Mazzanti, V., Malagutti, L. and Mollica, F., FDM 3D printing of polymers containing natural fillers: a review of their mechanical properties. *Polymers.* 2019, 11, 1094.
- Šafka, J., Ackermann, M., Bobek, J., Seidl, M., et al. Use of composite materials for FDM 3D print technology. *Mater. Sci. Forum* 2016, 862, 174–181.
- Chen, M. Y., Skewes, J., Daley, R., Woodruff, M. A., et al. Three-dimensional printing versus conventional machining in the creation of a meatal urethral dilator: development and mechanical testing. *Biomed. Eng. Online* 2020, 19, 1–11.
- Bhattacharjee, N., Urrios, A., Kang, S. and Folch, A., The upcoming 3D-printing revolution in microfluidics. *Lab Chip* 2016, 16, 1720–1742.
- Beauchamp, M. J., Nordin, G. P. and Woolley, A. T., Moving from millifluidic to truly microfluidic sub-100- $\mu\text{m}$  cross-section 3D printed devices. *Anal. Bioanal. Chem.* 2017, 409, 4311–4319.
- Siller, I. G., Enders, A., Steinwedel, T., Epping, N. - M., et al. Real-time live-cell imaging technology enables high-throughput screening to verify in vitro biocompatibility of 3D printed materials. *Materials.* 2019, 12, 2125.
- Gross, B. C., Erkal, J. L., Lockwood, S. Y., Chen, C., et al. Evaluation of 3D printing and its potential impact on biotechnology and the chemical sciences. *Anal. Chem.* 2014, 86, 3240–3253.
- Krujatz, F., Lode, A., Seidel, J., Bley, T., et al. Additive Biotech—Chances, challenges, and recent applications of additive manufacturing technologies in biotechnology. *N. Biotechnol.* 2017, 39, 222–231.
- Romanov, V., Samuel, R., Chaharlang, M., Jafek, A. R., et al. FDM 3D printing of high-pressure, heat-resistant, transparent microfluidic devices. *Anal. Chem.* 2018, 90, 10450–10456.
- He, Y., Wu, Y., Fu, J. Z., Gao, Q., et al. Developments of 3D printing microfluidics and applications in chemistry and biology: a review. *Electroanalysis* 2016, 28, 1658–1678.
- Au, A. K., Huynh, W., Horowitz, L. F. and Folch, A., 3D-printed microfluidics. *Angew. Chem. Int. Ed.* 2016, 55, 3862–3881.
- Kuo, A. P., Bhattacharjee, N., Lee, Y. S., Castro, K., et al. High-precision stereolithography of biomicrofluidic devices. *Adv. Mater. Technol.* 2019, 4, 11.
- Mehta, V. and Rath, S. N. 3D printed microfluidic devices: a review focused on four fundamental manufacturing approaches and implications on the field of healthcare. *Bio-Design Manuf.* 2021, 4, 311–343.
- Urrios, A., Parra-Cabrera, C., Bhattacharjee, N., Gonzalez-Suarez, A. M., et al. 3D-printing of transparent bio-microfluidic devices in PEG-DA. *Lab Chip* 2016, 16, 2287–2294.
- Samper, I. C., Gowers, S. A. N., Rogers, M. L., Murray, D. R. K., et al. 3D printed microfluidic device for online detection of neurochemical changes with high temporal resolution in human brain microdialysate. *Lab Chip* 2019, 19, 2038–2048.
- Enders, A., Siller, I. G., Urmann, K., Hoffmann, M. R., et al. 3D printed microfluidic mixers—a comparative study on mixing unit performances. *Small* 2019, 15, 9.
- Siller, I. G., Preuss, J. A., Urmann, K., Hoffmann, M. R., et al. 3D-printed flow cells for aptamer-based impedimetric detection of *E. coli* Crooks Strain. *Sensors* 2020, 20, 16.
- Stratasys, Our materials. <https://www.stratasys.com/materials/search>, accessed June 2021.
- 3D Systems Inc. What are the Benefits of MultiJet Printing?. 3D Systems Inc.; [https://www.3dsystems.com/resources/information-guides/multi-jet-printing/mjp?smtNoRedir=1&\\_ga=2.164098874.461882064.1624609672-2059785067.1603350887](https://www.3dsystems.com/resources/information-guides/multi-jet-printing/mjp?smtNoRedir=1&_ga=2.164098874.461882064.1624609672-2059785067.1603350887), accessed June 2021.
- Ukita, Y., Takamura, Y. and Utsumi, Y., Direct digital manufacturing of autonomous centrifugal microfluidic device. *Jpn. J. Appl. Phys.* 2016, 55, 6.
- Sochol, R. D., Sweet, E., Glick, C. C., Venkatesh, S., et al. 3D printed microfluidic circuitry via multijet-based additive manufacturing. *Lab Chip* 2016, 16, 668–678.
- Walczak, R. and Adamski, K., Inkjet 3D printing of microfluidic structures—on the selection of the printer towards printing your own microfluidic chips. *J. Micromech. Microeng.* 2015, 25, 11.
- Yin, P. J., Zhao, L., Chen, Z. Z., Jiao, Z. Q., et al. Simulation and practice of particle inertial focusing in 3D-printed serpentine microfluidic chips via commercial 3D-printers. *Soft Matter* 2020, 16, 3096–3105.

33. Anciaux, S. K., Geiger, M. and Bowser, M. T., 3D printed micro free-flow electrophoresis device. *Anal. Chem.* 2016, 88, 7675–7682.
34. Bressan, L. P., Adamo, C. B., Quero, R. F., de Jesus, D. P., et al. A simple procedure to produce FDM-based 3D-printed microfluidic devices with an integrated PMMA optical window. *Anal. Methods* 2019, 11, 1014–1020.
35. Zeraatkar, M., Filippini, D. and Percoco, G., On the impact of the fabrication method on the performance of 3D printed mixers. *Micromachines* 2019, 10, 10.
36. Nelson, M. D., Ramkumar, N. and Gale, B. K., Flexible, transparent, sub-100  $\mu\text{m}$  microfluidic channels with fused deposition modeling 3D-printed thermoplastic polyurethane. *J. Micromech. Microeng.* 2019, 29, 8.
37. Li, F., Smejkal, P., Macdonald, N. P., Guijt, R. M., et al. One-step fabrication of a microfluidic device with an integrated membrane and embedded reagents by multimaterial 3D printing. *Anal. Chem.* 2017, 89, 4701–4707.
38. Ruiz, C., Kadimisetty, K., Yin, K., Mauk, M. G., et al. Fabrication of hard-soft microfluidic devices using hybrid 3D printing. *Micromachines* 2020, 11, 11.
39. Salentijn, G. I. J., Oomen, P. E., Grajewski, M. and Verpoorte, E., Fused deposition modeling 3d printing for (bio)analytical device fabrication: procedures, materials, and applications. *Anal. Chem.* 2017, 89, 7053–7061.
40. Macdonald, N. P., Cabot, J. M., Smejkal, P., Guijt, R. M., et al. Comparing microfluidic performance of three-dimensional (3D) printing platforms. *Anal. Chem.* 2017, 89, 3858–3866.
41. Kotz, F., Mader, M., Dellen, N., Risch, P., et al. Fused deposition modeling of microfluidic chips in polymethylmethacrylate. *Micromachines* 2020, 11, 12.
42. Quero, R. F., da Silveira, G. D., da Silva, J. A. F., da Jesus, D. P. Understanding and improving FDM 3D printing to fabricate high-resolution and optically transparent microfluidic devices. *Lab Chip* 2021.21:3715–3729.
43. Piironen, K., Haapala, M., Talman, V., Järvinen, P., et al. Lab on a chip cell adhesion and proliferation on common 3D printing materials used in stereolithography of microfluidic devices. *Lab Chip* 2020, 20, 2372–2382.
44. Rimington, R. P., Capel, A. J., Player, D. J., Bibb, R. J., et al. Feasibility and biocompatibility of 3D-printed photopolymerized and laser sintered polymers for neuronal, myogenic, and hepatic cell types. *Macromol. Biosci.* 2018, 18, 1800113.
45. Gul, J. Z., Sajid, M., Rehman, M. M., Siddiqui, G. U., et al. 3D printing for soft robotics - a review. *Sci. Technol. Adv. Mater.* 2018, 19, 243–262.
46. Gulyas, M., Csiszer, M., Mehes, E. and Czirik, A., Software tools for cell culture-related 3D printed structures. *PLoS One* 2018, 13, e0203203.
47. Siller, I. G., Enders, A., Gellermann, P., Winkler, S., et al. Characterization of a customized 3D-printed cell culture system using clear, translucent acrylate that enables optical online monitoring. *Biomed. Mater.* 2020, 15, 55007.
48. Panjan, P., Virtanen, V. and Sesay, A. M., Towards microbioprocess control: an inexpensive 3D printed microbioreactor with integrated online real-time glucose monitoring. *Analyst* 2018, 143, 3926–3933.
49. Frey, L. J., Vorländer, D., Ostsieker, H., Rasch, D., et al. 3D-printed micro bubble column reactor with integrated microsensors for biotechnological applications: from design to evaluation. *Sci. Rep.* 2021, 11, 7276.
50. Kuhlmann, W., Meyer, H. D., Bellgardt, K. H. and Schügerl, K., On-line analysis of yeast growth and alcohol production. *J. Biotechnol.* 1984, 1, 171–185.
51. Qian, X., Nguyen, H. N., Song, M. M., Hadiono, C., et al. Brain-region-specific organoids using mini-bioreactors for modeling ZIKV exposure. *Cell* 2016, 165, 1238–1254.
52. Drost, J. and Clevers, H., Organoids in cancer research. *Nat. Rev. Cancer* 2018, 18, 407–418.
53. Wang, Y. I., Abaci, H. E. and Shuler, M. L., Microfluidic blood-brain barrier model provides in vivo-like barrier properties for drug permeability screening. *Biotechnol. Bioeng.* 2017, 114, 184–194.
54. Gensler, M., Leikeim, A., Möllmann, M., Komma, M., et al. 3D printing of bioreactors in tissue engineering: a generalised approach. *PLoS One* 2020, 15, e0242615.
55. Siller, I. G., Epping, N. M., Lavrentieva, A., Scheper, T., et al. Customizable 3D-printed (Co)cultivation systems for in vitro study of angiogenesis. *Materials.* 2020, 13, 1–17.
56. Alessandri, K., Feyeux, M., Gurchenkov, B., Delgado, C., et al. A 3D printed microfluidic device for production of functionalized hydrogel microcapsules for culture and differentiation of human Neuronal Stem Cells (hNSC). *Lab Chip* 2016, 16, 1593–1604.
57. Lavrentieva, A., Fleischhammer, T., Enders, A., Pirmahboub, H., et al. Fabrication of stiffness gradients of GelMA hydrogels using a 3D printed micromixer. *Macromol. Biosci.* 2020, 20, 2000107.
58. Razavi Bazaz, S., Rouhi, O., Raoufi, M. A., Ejeian, F., et al. 3D printing of inertial microfluidic devices. *Sci. Rep.* 2020, 10, 14.
59. Aranda Hernandez, J., Heuer, C., Bahnemann, J., Szita, N. Microfluidic Devices as Process Development Tools for Cellular Therapy Manufacturing. In: *Advances in Biochemical Engineering/Biotechnology*; 2021.
60. Chiu, P. L., Chang, C. H., Lin, Y. L., Tsou, P. H., et al. Rapid and safe isolation of human peripheral blood B and T lymphocytes through spiral microfluidic channels. *Sci. Rep.* 2019, 9, 1–10.
61. Nathamgari, S. S. P., Dong, B., Zhou, F., Kang, W., et al. Isolating single cells in a neurosphere assay using inertial microfluidics. *Lab Chip* 2015, 15, 4591–4597.
62. Yin, L., Au, W. Y., Yu, C. C., Kwon, T., et al. Miniature auto-perfusion bioreactor system with spiral microfluidic cell retention device. *Biotechnol. Bioeng.* 2021, 118, 1951–1961.
63. Lee, W., Kwon, D., Choi, W., Jung, G. Y., et al. 3D-Printed microfluidic device for the detection of pathogenic bacteria using size-based separation in helical channel with trapezoid cross-section. *Sci. Rep.* 2015, 5, 1–7.
64. Enders, A., Preuss, J. - A., Bahnemann, J., 3D printed microfluidic spiral separation device for continuous, pulsation-free and controllable CHO cell retention. *Micromachines* 2021, 12, 1060.
65. Tamay, D. G., Dursun Usal, T., Alagoz, A. S., Yucel, D., et al. 3D and 4D printing of polymers for tissue engineering applications. *Front. Bioeng. Biotechnol.* 2019, 0, 164.
66. Zaszczynska, A., Moczulska-Heljak, M., Grady, A., Sajkiewicz, P., *Advances in 3d printing for tissue engineering. Materials* 2021, 14, 3149.
67. Salmean, C. and Dimartino, S., 3D-printed stationary phases with ordered morphology: state of the art and future development in liquid chromatography. *Chromatographia* 2019, 82, 443–463.

68. Kalsoom, U., Nesterenko, P. N. and Paull, B., Current and future impact of 3D printing on the separation sciences. *Trends Anal. Chem.* 2018, 105, 492–502.
69. Lucklum, F., Janssen, S., Lang, W. and Vellekoop, M. J., Miniature 3D gas chromatography columns with integrated fluidic connectors using high-resolution stereolithography fabrication. *Procedia Eng.*, 2015, 120, 703–706.
70. Schure, M. R., Maier, R. S., How does column packing microstructure affect column efficiency in liquid chromatography? *J. Chromatogr. A* 2006, 1126, 58–69.
71. Simon, U. and Dimartino, S., Direct 3D printing of monolithic ion exchange adsorbers. *J. Chromatogr. A* 2019, 1587, 119–128.
72. Simon, U., Scorza, L. C. T., Teworte, S., McCormick, A. J., et al. Demonstration of protein capture and separation using three-dimensional printed anion exchange monoliths fabricated in one-step. *J. Sep. Sci.* 2021, 44, 1078–1088.
73. Nawada, S., Dimartino, S. and Fee, C., Dispersion behavior of 3D-printed columns with homogeneous microstructures comprising differing element shapes. *Chem. Eng. Sci.* 2017, 164, 90–98.
74. Wang, H., Cocovi-Solberg, D. J., Hu, B. and Miró, M., 3D-printed microflow injection analysis platform for online magnetic nanoparticle sorptive extraction of antimicrobials in biological specimens as a front end to liquid chromatographic assays. *Anal. Chem.* 2017, 89, 12541–12549.
75. Adamski, K., Kubicki, W. and Walczak, R., 3D printed electrophoretic lab-on-chip for DNA separation. *Procedia Eng.* 2016, 168, 1454–1457.
76. Preuss, J., Nguyen, G. N., Berk, V. and Bahnemann, J., Miniaturized free-flow electrophoresis: production, optimization, and application using 3D printing technology. *Electrophoresis* 2021, 42, 305–314.
77. Barbaresco, F., Cocuzza, M., Pirri, C. F. and Marasso, S. L., Application of a micro free-flow electrophoresis 3d printed lab-on-a-chip for micro-nanoparticles analysis. *Nanomaterials* 2020, 10, 1277.
78. Islinger, M., Eckerskorn, C. and Völkl, A., Free-flow electrophoresis in the proteomic era: a technique in flux. *Electrophoresis* 2010, 31, 1754–1763.
79. Loo, A. H., Chua, C. K., Pumera, M., DNA biosensing with 3D printing technology. *Analyst* 2017, 142, 279–283.
80. Arshavsky-Graham, S., Enders, A., Ackerman, S., Bahnemann, J., et al. 3D-printed microfluidics integrated with optical nanostructured porous aptasensors for protein detection. *Microchim. Acta* 2021, 188, 1–12.
81. Nesaei, S., Song, Y., Wang, Y., Ruan, X., et al. Micro additive manufacturing of glucose biosensors: a feasibility study. *Anal. Chim. Acta* 2018, 1043, 142–149.
82. Cardoso, R. M., Silva, P. R. L., Lima, A. P., Rocha, D. P., et al. 3D-Printed graphene/polylactic acid electrode for bioanalysis: biosensing of glucose and simultaneous determination of uric acid and nitrite in biological fluids. *Sens. Actuators, B Chem.* 2020, 307, 127621.
83. Muñoz, J., Pumera, M., 3D-printed biosensors for electrochemical and optical applications. *TrAC - Trends Anal. Chem.* 2020, 128, 115933.
84. Arshavsky-Graham, S., Massad-Ivanir, N., Segal, E., Weiss, S., Porous silicon-based photonic biosensors: current status and emerging applications. *Anal. Chem.* 2019, 91, 441–467.
85. Gowers, S. A. N., Curto, V. F., Seneci, C. A., Wang, C., et al. 3D printed microfluidic device with integrated biosensors for online analysis of subcutaneous human microdialysate. *Anal. Chem.* 2015, 87, 7763–7770.
86. Chan, H. N., Tan, M. J. A., Wu, H. Point-of-care testing: applications of 3D printing. *Lab Chip* 2017, 17, 2713–2739.
87. Hällgren S., Pejryd L., Ekengren J. 3D Data Export for Additive Manufacturing - Improving Geometric Accuracy. *Procedia CIRP.* 2016;50:518–523.

**How to cite this article:** Heuer, C., Preuß, J.-A., Habib, T., Enders, A., Bahnemann, J. 3D printing in biotechnology—An insight into miniaturized and microfluidic systems for applications from cell culture to bioanalytics. *Eng Life Sci.* 2022;22: 744–759. <https://doi.org/10.1002/elsc.202100081>

### 3.3 Silicon Diffraction Gratings as Optical Sensors

Microstructured photonic silicon chips consisting of diffraction gratings have been recently applied to optically track the behaviour of microorganisms on micropatterned surfaces in real-time.<sup>28,32,33</sup> These diffraction gratings consist of microwell or micropillar patterns and are fabricated by conventional photolithography and reactive ion etching processes.<sup>28,32</sup> The diffraction gratings act as a multiple slit with a specific slit width and periodicity that reflects light into a set of diffraction orders (as schematically presented in Figure 3A-i) and create 2D diffraction patterns, as shown in Figure 3 A-ii. These patterns can be described as follows:<sup>34,35</sup>

$$I(\theta) \propto I_1 I_2 I_3 \quad (1)$$

and

$$I(\theta) \propto \left(\frac{\sin K}{K}\right)^2 \left(\frac{\sin 2NK}{\sin 2K}\right)^2 \cos^2\left(\frac{\psi_0}{2}\right) \quad (2)$$

Where  $I$  is the intensity of the reflected light,  $K$  equals  $\left(\frac{d\pi}{2\lambda}\right) \sin\theta$ ,  $\lambda$  is the wavelength,  $\theta$  the diffraction angle,  $d$  the grating period, and  $N$  the number of illuminated pores or pillars. The phase shift between the light reflected from the top and bottom of the periodic microstructure is described by  $\psi_0 = \left(\frac{2\pi}{\lambda}\right)\delta$  with  $\delta$  being the optical path difference (OPD). This OPD is the extra distance a light beam travels that is reflected from the bottom of the microstructure. As Figure 3B demonstrates, the OPD is the sum of the distances AB, which is  $L$  (the height of the microstructure), BC described by  $d/2 \sin\theta$  and CD given by  $L \cos\theta$ . Thus, the OPD can be expressed with the following equation:

$$OPD = L + \frac{d}{2} \sin\theta + L \cos\theta \quad (3)$$

When the diffraction angle  $\theta$  is 0 the OPD equals:

$$OPD = 2L \quad (4)$$

This yields:  $OPD = 2nL$  when the microstructure is filled with a medium with the refractive index  $n$ . The  $2nL$  parameter is also referred to as the effective optical thickness (EOT) of the silicon microstructure. The diffraction pattern of the latter structures is described by the following equation when  $\theta$  is 0:

$$I(\theta = 0) = \cos^2\left(\frac{\psi_0}{2}\right) \quad (5)$$

And thus:<sup>34</sup>

$$I(\theta = 0) = \cos^2\left(\frac{2\pi nL}{\lambda}\right) \quad (6)$$

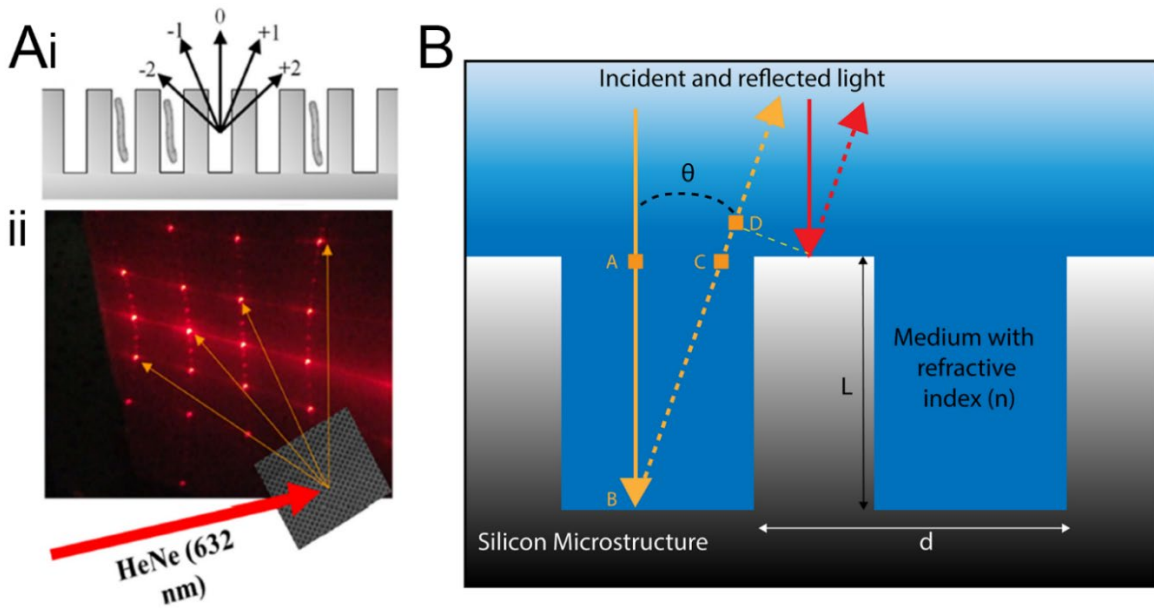


**Figure 3** Optical properties of Si diffraction gratings. (A-i) The diffraction gratings reflect light into a set of diffraction orders, and (A-ii) create a 2D diffraction pattern when illuminated with a laser (here exemplarily for a HeNe laser at 632 nm). Images adapted with permission from Mirsky *et al.*<sup>35</sup> (B) Schematic of a silicon diffraction grating. The light is reflected from the top and bottom of the microstructure. Image created according to Leonard *et al.*<sup>34</sup>

When photonic silicon chips consisting of such diffraction gratings are illuminated by a white light source positioned perpendicularly to the chip surface (Figure 4A), and the zero-order ( $\theta = 0$ ) reflected light is recorded, characteristic reflectance spectra are obtained, see Figure 4B-i. These spectra exhibit typical interference fringes as the light is partially reflected from the top and bottom of the Si microstructure. Fast Fourier transform (FFT) frequency analysis of the reflectance spectra yields a single peak where the peak position corresponds to the  $2nL$  ( $n$  = refractive index within the microstructure and  $L$  = depth or height of

the microstructure) and the peak height corresponds to the intensity of the reflected light as depicted in Figure 4B-ii. The  $2nL$  can be used to detect and monitor microbial growth within the microstructure by an optical assay, termed PRISM; for example, bacteria growing within the structure increase the refractive index  $n$  and thus the  $2nL$  parameter. Also, the intensity signal can be used to monitor microbial growth on top of the structure by intensity-based PRISM (referred to as iPRISM) as the cells scatter light and reduce the intensity signal.

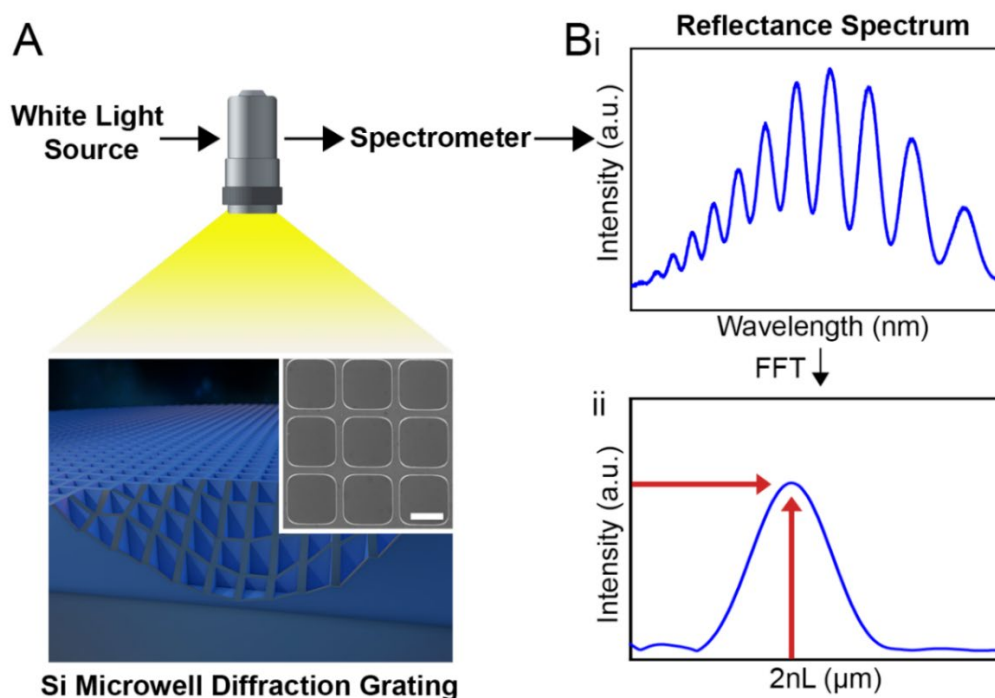


**Figure 4** Principle of photonic silicon chips consisting of microwell diffraction gratings. (A) The photonic silicon chips are illuminated by a white light source, and a spectrometer records the zero-order reflected light. The insert shows a scanning electron micrograph of the microwell structure (scale bar corresponds to  $4\ \mu\text{m}$ ). (B-i) The resulting reflectance spectra exhibit interference fringes as the top and bottom of the microstructure partially reflect the light. (B-ii) The reflectance spectra are analyzed by fast Fourier transform (FFT), and in the resulting single peaks, the peak height corresponds to the intensity of the reflected light and the peak position to the  $2nL$  value. The lens in figure part A was obtained with permission from biorender.com.

This principle was first harnessed by Massad-Ivanir *et al.*, who trapped bacteria within microwells with appropriate dimensions and detected the bacteria by measuring shifts in  $2nL$  (increase) and intensity (decrease).<sup>32</sup> These photonic silicon chips were later employed for the AST of bacteria; the PRISM assay monitored the behaviour of bacteria in the presence of clinically relevant antibiotics at varying concentrations by tracking changes in the  $2nL$  value.<sup>28</sup> Bacteria growth was associated with an increase in the  $2nL$ , while inhibitory effects at high antibiotic concentration resulted in largely unchanged  $2nL$  values. MIC values could be expeditiously determined after 2 – 3 h as compared to 8 h by state-of-the-art methods and mostly agreed with reference values.<sup>28</sup>

## 4 Experimental

This experimental section is reproduced from the research articles that constitute this thesis.

### Materials and Microorganisms

Materials: Glutaraldehyde, calcofluor white, Roswell Park Memorial Institute medium (RPMI 1640), cation-adjusted Muller Hinton broth (CAMHB), propidium iodide, D-glucose, amphotericin B, anidulafungin, ciprofloxacin, chloramphenicol and voriconazole were supplied by Sigma-Aldrich, Israel. Also, ethylenediaminetetraacetic acid (EDTA) and tris(hydroxymethyl)aminomethane hydrochloride (Tris HCl) were obtained from Sigma-Aldrich, Israel.

Absolute ethanol, all buffer salts (NaCl, KCl, KH<sub>2</sub>PO<sub>4</sub>, Na<sub>2</sub>HPO<sub>4</sub>) and NaOH were purchased from Merck, Germany. Isopropanol and acetone were supplied by Gadot, Israel. Potato dextrose agar (PDA), potato dextrose broth (PDB), bacto agar, yeast extract, Luria-Bertani (LB) broth and casein hydrolysate were purchased from Difco, USA. 3-(*N*-morpholino)propanesulfonic acid (MOPS) was supplied by Chem-Impex International, Inc., USA, and Sabouraud dextrose agar (SDA) plates were purchased from Novamed Ltd., Israel. Detergent Fairy Ultra Plus was obtained from Procter and Gamble (Cincinnati, USA), gentamicin sulfate from AppliChem GmbH, Germany, Pelikan ink 156372 (designated blue dye) from Pelikan Group GmbH, Germany, and paraffin oil of low viscosity from Carl Roth GmbH + Co. K.G., Germany.

Sodium dodecyl sulfate (SDS) was supplied by Thermo Scientific, USA, Zirconia/Silica beads were obtained from Biospec Products, Inc., USA, and all polymerase chain reaction (PCR) reagents were purchased from Takara, Japan. DNA staining dye (SimplySafe™ dye) was obtained from EURx, Poland and the DNA gel extraction kit (AccuPrep Gel Purification Kit) from Bioneer, South Korea. VisiJet® M2S-HT90 3D printing material and wax support material VisiJet® M2 SUP were purchased from 3D Systems Inc., USA. UV-curable glue (Norland Optical Adhesive 72) was obtained from Norland Products Inc., USA, and UV-curable lacquer (luxaprint® shellac) was purchased from DETAX GmbH, Germany.

Microorganisms: *E. coli* K12 and *Serratia marcescens* (*S. marcescens*) were generously provided by Prof. Sima Yaron (Department of Biotechnology and Food Engineering, Technion – Israel Institute of Technology). *C. auris* DSM 21092 was obtained from the German Collection of Microorganisms and Cell Culture (DSMZ), Germany and *Saccharomyces cerevisiae* (*S. cerevisiae*) NCYC 1024 from the National Collection of Yeast Cultures, United Kingdom. *A. niger* was isolated from a contaminated onion and identified as described in the upcoming sections.

### Preparation of Solutions and Media

All aqueous solutions and media were prepared in Milli-Q water (18.2 MΩ cm). Phosphate buffered saline (PBS) was composed of 137 mM NaCl, 2.7 mM KCl, 1.8 mM KH<sub>2</sub>PO<sub>4</sub>, and 10 mM Na<sub>2</sub>HPO<sub>4</sub>. RPMI 1640

## Experimental

2 % G medium (RPMI 1640 medium supplemented with 2 % D-glucose) was constituted of 10.4 g L<sup>-1</sup> RPMI 1640, 34.5 g L<sup>-1</sup> MOPS and 18 g L<sup>-1</sup> D-glucose and adjusted to pH 7.0 with 1 M NaOH. PDA was prepared by suspending 39 g L<sup>-1</sup> PDA powder in water, and LB agar was made from 25 g L<sup>-1</sup> LB broth and 15 g L<sup>-1</sup> bacto agar. 1 % PDA contained 10 g L<sup>-1</sup> PDA and 15 g L<sup>-1</sup> bacto agar, and water agar was made from 20 g L<sup>-1</sup> bacto agar. Potato dextrose yeast extract casein hydrolysate medium (PDYC) was composed of 24 g L<sup>-1</sup> potato dextrose broth, 2 g L<sup>-1</sup> yeast extract and 1.2 g L<sup>-1</sup> casein hydrolysate. CAMHB medium was prepared according to the manufacturer's instructions. DNA extraction buffer was constituted of 200 mM Tris HCl, 0.5 % SDS, 25 mM EDTA and 250 mM NaCl. All media and buffer were heat-steam sterilized at 121 °C for 30 min or sterile-filtered prior to use.

### Preparation of Bacterial and Yeast Cultures

Bacterial (*E. coli*) and yeast (*C. auris*; *S. cerevisiae*) cultures were stored as cryo cultures at -80 °C. Prior to AST experiments, the cells were subcultured onto LB agar (bacteria) or PDA (yeast), and incubated at 37 °C or 30 °C for 16 – 18 h. Colonies from these agar plates were directly used to obtain the cell suspensions used in BMD (~ 10<sup>5</sup> cells mL<sup>-1</sup> for both bacteria and yeast) and (i)PRISM experiments (turbidity standard: McFarland 0.5 for bacteria and McFarland 2.0 for yeast). A McFarland standard of 0.5 corresponded to ~ 10<sup>8</sup> bacteria mL<sup>-1</sup>, and a McFarland standard of 2.0 is equivalent to ~ 10<sup>7</sup> yeasts mL<sup>-1</sup>.

### *Aspergillus niger*

Isolation: The fungus was isolated from a contaminated onion into 1 % PDA and incubated in darkness for 10 days at 25 °C. Conidia from the mature culture were re-cultured by streaking onto SDA plates supplemented with chloramphenicol to eliminate bacterial contamination and incubated as described above. For the preparation of mono-conidial cultures, conidia were re-cultured onto water agar and incubated overnight (18 h) at 25 °C. Single germinating conidia were removed by micromanipulation under a light microscope and transferred to 1 % PDA. All tests were performed with a single mono-conidial culture isolate, designated HCN 18, in order to limit possible genetic variability. Species identification of isolate HCN 18 was carried out by sequencing the internal transcribed spacer (ITS) regions.

Identification by ITS regions: *A. niger* isolate HCN 18 was grown overnight at room temperature in liquid PDYC medium in a petri dish without shaking. For DNA extraction, two full spatulas of the mycelium were transferred to a clean tube with 100 µL Zirconia/Silica beads and 500 µL DNA extraction buffer and mixed for one minute on a vortex mixer (Scientific Industries, Inc., USA). The sample was incubated for 30 min at room temperature and centrifuged for 10 min at 4 °C and 12500 rpm (Centrifuge 5417R, Eppendorf AG, Germany). The supernatant was transferred to a clean tube, and an equal volume of isopropanol was added. The sample was incubated for 20 minutes at -20 °C and afterwards centrifuged at 13000 rpm for 2 min.



## Experimental

Subsequently, the supernatant was discarded, and the resulting pellet was washed with 1 mL 70 % ethanol, followed by centrifugation at 13000 rpm for 2 min. The supernatant was rejected again, and the pellet was left for drying for around 1 h and resuspended in 50  $\mu\text{L}$  of sterile water. The concentration of the genomic DNA was determined by using a Nanodrop One device (Thermo Scientific, USA), resulting in a concentration of 56.4 ng  $\mu\text{L}^{-1}$  with an A260:A280 ratio of 1.85.

Species identification of isolate HCN 18 was carried out by sequencing the ITS1 and ITS2 internal transcribed spacer regions by using the primers ITS1F (5'-CTTGGTCATTTAGAGGAAGTAA-3') and ITS4 (5'-TCCTCCGCTTATTGATATGC-3'). PCR amplification reaction mixtures contained 1 x PCR buffer, 0.2 mM premixed dNTPs, 1.25 U of Takara Taq<sup>TM</sup> Polymerase, 1  $\mu\text{M}$  ITS1F and ITS4 primers and 50 ng genomic DNA in a total volume of 25  $\mu\text{L}$ . For non-template control, the PCR reaction mixture contained all the components mentioned above but no genomic *Aspergillus* DNA. PCR amplification was carried out in a biometra TGradient Thermocycler (Analytik Jena, Germany) using an initial denaturation step at 94 °C for 2 min, followed by 29 cycles at 94 °C for 30 s, 55 °C for 30 s and 72 °C for 30 s, with a final extension for 2 min at 72 °C. Successful amplification was confirmed after standard electrophoresis in a 1 % agarose gel by visualizing the PCR product under UV light by using the SimplySafe<sup>TM</sup> dye. The PCR fragment was extracted from the gel by using a DNA gel extraction kit and sent to Hylabs (Israel) for sequencing by using an ABI 3730xl DNA Analyzer (Thermo Scientific, USA). Sequence alignment was done using the nucleotide BLAST search algorithm BLASTn, at the NCBI website (<https://blast.ncbi.nlm.nih.gov/Blast.cgi>). The species was identified as *A. niger* (NCBI Accession number: MK182796.1).

Culture preparation: *A. niger* cultures were refreshed every two weeks onto 1 % PDA and maintained at 4 °C until use. Prior to iPRISM experiments, the cultures were transferred onto SDA plates containing chloramphenicol. Because *A. niger* showed the fastest growth at 30 °C, the fungal cultures were subsequently incubated at 30 °C, and after 2 – 5 days, sufficient sporulation for AFST experiments was reached. Conidial density was quantified by using a hemocytometer (Neubauer improved cell counting chamber) and adjusted to 10<sup>5</sup> cells mL<sup>-1</sup> for subsequent AFST experiments.

### **Fabrication and Preparation of Photonic Silicon Chips**

Silicon chips with microwell gratings (3 or 4  $\mu\text{m}$  well width with a depth of  $\sim$  4  $\mu\text{m}$ ) were fabricated by standard lithography or laser writing and reactive ion etching techniques at the Micro- and Nano-Fabrication and Printing Unit (Technion). The resulting wafers were coated with a photoresist to protect their microstructure while dicing the wafer into 5 x 5 mm chips using an automated dicing saw (DAD3350, Disco, Japan). The photonic silicon chips were washed with acetone to remove the photoresist and oxidized for 1 h at 800 °C in a furnace (Lindberg/Blue M 1200 °C Split-Hinge, Thermo Scientific, USA).

## Experimental

### **Photonic Silicon Chips Characterization**

Optical microscopy: The photonic silicon chips were examined immediately after experiments by using an optical light microscope (Axio Scope A1, Carl Zeiss, Germany) to identify fungal growth and ensure no bacterial contamination occurred.

Scanning electron microscopy: High-resolution scanning electron microscopy (HR-SEM) was performed using a Zeiss Ultra Plus high-resolution scanning microscope. Before HR-SEM experiments, the samples were fixated using 2.5 % glutaraldehyde in PBS, washed with water, dehydrated through a dilution series in ethanol with increasing ethanol concentrations 10 % - 50 % - 70 % - absolute ethanol), and gently dried under a stream of nitrogen. Focused ion beam (FIB)-cross-sectional SEM images were obtained using a Dual Beam Helios NanoLab G3 instrument (FEI, USA). A platinum deposition was performed prior to observation.

Confocal microscopy: Confocal laser scanning microscopy (CLSM) using an LSM 700 (Carl Zeiss, Germany) was performed on samples stained by Calcofluor white and a drop of 10 % potassium hydroxide; Excitation wavelength was 405 nm, and images were rendered by Zen software (Carl Zeiss, Germany). Confocal laser scanning microscopy was also performed on samples where cells were stained with 20  $\mu\text{g mL}^{-1}$  propidium iodide after fixation in glutaraldehyde. The photoluminescence of the photonic silicon chips and fluorescence emitted by the propidium iodide-stained yeast cells were detected using 405 nm (Si photoluminescence) and 555 nm (propidium iodide) laser excitation wavelengths.

### **iPRISM/ PRISM Assay in the Aluminum Flow Cell**

A custom-made aluminium chamber with seven injection and outlet channels was used to fix and separate the photonic silicon chips during the (i)PRISM assays. Each injection channel was connected by tubing to a syringe injection port and allowed for the injection of the cell suspensions. The chamber was controlled by a motorized linear stage (Thorlabs, Inc, USA). The photonic chips were placed in a small square cavity in each channel and were separated from each other and fixed on the surface of the chamber by a rubber gasket. The system was further sealed before the experiments with an acrylic piece and by tightening the lid of the aluminium housing.

Before each experiment, the system was sterilized with 70 % ethanol and sterile water, followed by the introduction of only growth medium to allow devices, temperature, and medium to equilibrate. Subsequently, 500  $\mu\text{L}$  of the microbial suspensions were introduced into the heat controlled (30 °C or 37 °C) channels. For *A. niger*, the antifungals were introduced after 15 min, while for *C. auris*, the cell suspensions were introduced together with the antifungal. The reflectance signal of the zero-order reflected light was continuously recorded during the experiment.

## Experimental

### iPRISM/ PRISM Data Acquisition and Analysis

A bifurcated fiber optic equipped with a 74 series collimating lens was positioned perpendicularly to the photonic silicon chips, illuminating them via an HL-2000 white light source, and the reflected light was recorded by a USB4000 CCD spectrometer (all Ocean Optics, USA). The position of the chamber was controlled by a motorized stage (Thorlabs, USA) and LabView (National Instruments, USA). Wavelength in the range from 450 – 900 nm was inverted into wavenumber ( $\text{cm}^{-1}$ ) and interpolated with a cubic spline before FFT frequency analysis was performed on the obtained spectra. The resulting peak after FFT was identified by determining the maximum peak position, where the height of the detected peak directly corresponds to the intensity of the reflected light and the peak position to the  $2nL$  value ( $n$  = refractive index within the medium and  $L$  = depth or height of the microstructure). The intensity and  $2nL$  values were plotted versus time. For AFST of *A. niger*, the introduction time of the antifungal is referred to as time 0. The per cent changes of the intensity ( $\Delta I$ ) were calculated as follows:

$\Delta I (\%) = \frac{I - I_0}{I_0} \times 100 \%$ ; where  $I$  is the intensity at a given time, and  $I_0$  is the intensity at time 0. For *C.*

*auris*, the per cent changes of the intensity  $\Delta I (\%)$  and  $\Delta 2nL (\%)$  were calculated as follows:

$\Delta I (\%) = \frac{I - I_0}{I_0} \times 100 \%$  and  $\Delta 2nL (\%) = \frac{2nL - 2nL_0}{2nL_0} \times 100 \%$ ; where  $I_0$  and  $2nL_0$  refer to the values of  $2nL$  and intensity at  $t = 0$  min (introduction of cell suspensions together with the antifungal). For data analysis in AFST experiments,  $I_0$  and  $2nL_0$  were replaced by  $I_{90}$  and  $2nL_{90}$  ( $t = 90$  min) as the reference time point because occasionally, the signals were unstable at the beginning of the assay, ascribed to the high number of introduced cells.

### 3D Printing and Post Processing of the Gradient Generator

The computer-aided design (CAD) model was created using SolidWorks 2020 (Dassault Systèmes SolidWorks Corp, Waltham, MA, USA). The model was saved as an STL file for printing purposes and as an SAT file for simulations. All files are provided in the supplementary information of the associated article (<https://pubs.rsc.org/en/content/articlelanding/2022/LC/D2LC00640E>). The models were printed using a high-resolution 3D printer (ProJet® MJP 2500 Plus, 3D Systems, USA) with an xyz resolution of 32, 28 and 32  $\mu\text{m}$ , respectively. The printed device was removed from the printing platform after incubation at  $-18$  °C for 10 min. Afterwards, all pieces were placed in EasyClean units from 3D Systems (water vapour bath and hot paraffin oil bath at 65 °C) to remove the wax support material. The interior structures were flushed at least three times with hot paraffin oil using a syringe. In order to remove oil residues, the parts were then submerged in an ultrasonic bath (Elma Elmasonic S30, Schmidbauer GmbH, Germany) with water and detergent at 50 °C for at least three times. Subsequently, the device was cleaned with deionized water and dried at 70 °C for 1 hour.

## Experimental

### **Gradient Generator Simulation Studies and Experimental Characterization**

The functionality of the gradient generator design was tested by running a computational fluid dynamics (CFD) simulation using COMSOL® Multiphysics 5.5 (COMSOL Inc., Sweden). General simulation settings were chosen according to Enders et al.<sup>36</sup> As physical properties, a density of  $1 \text{ g cm}^{-3}$  and a dynamic viscosity of  $10^{-3} \text{ kg m}^{-1} \text{ s}^{-1}$  were selected for water. For inlet A, the concentration of a fictive substance with a diffusion constant of  $10^{-9} \text{ m}^2 \text{ s}^{-1}$  was set to  $1 \text{ mol m}^{-3}$ , while the concentration of inlet B was defined as  $0 \text{ mol m}^{-3}$ . In order to simulate the performance of the designed device, the inflows at inlet A and inlet B were defined as  $323 \text{ } \mu\text{L min}^{-1}$  and  $677.3 \text{ } \mu\text{L min}^{-1}$ , respectively.

The source fluids – blue dye (ink; 1:30 diluted), glucose ( $6 \text{ g L}^{-1}$ ), and ciprofloxacin ( $1 \text{ mg L}^{-1}$ ) – were introduced into the device by a syringe pump into inlet A at a flow rate of  $323 \text{ } \mu\text{L min}^{-1}$ , while the sink fluid water was introduced by a second syringe pump into inlet B at a flow rate of  $677.3 \text{ } \mu\text{L min}^{-1}$ . After 5 min, the first fractions were collected from the six outlets, the pumps were stopped, and the solutions were transferred into a 96-well plate or reaction tubes. Next, the pumps were started again, and after 30 s, a second batch was collected. This procedure was repeated again for the collection of a third batch from every outlet. The dye was quantified at 600 nm (NanoDrop™ 2000 spectrophotometer, Thermo Fisher Scientific GmbH, Germany), the glucose concentration was measured using a Cedex BioAnalyzer (Roche Diagnostics Deutschland GmbH, Germany), and ciprofloxacin was quantified via a fluorescence assay ( $\lambda_{\text{ex}} 272 \text{ nm}$ ,  $\lambda_{\text{em}} 421 \text{ nm}$ ; Varioskan Flash, Thermo Scientific, USA). For every source fluid, a different gradient generator device was used. The photograph of the dye-water gradient was obtained using a VHX-6000 digital microscope (Keyence Deutschland GmbH, Germany).

### **Photonic Silicon Chip Integration into the Gradient Generator**

Silicon chips with microwells (width of approx.  $4 \text{ } \mu\text{m}$  and depth of approx.  $4 \text{ } \mu\text{m}$ ) were integrated into the 3D-printed microfluidic gradient generator device as follows: The chips (diced into  $5 \times 5 \text{ mm}$ ) were individually placed into the square-shaped cavities ( $5.1 \times 5.1 \text{ mm}$ ) of the gradient generator. UV-curable glue was carefully applied to the chip backside of the photonic silicon sensor and allowed to cure for 30 min under UV light at  $365 \text{ nm}$  with  $1.5 \text{ mW cm}^{-2}$  (VL-6.LC UV lamp 365/254 nm 6 W, Vilber Lourmat, France) to seal the system leakage-free. In order to improve the optical properties, UV-curable lacquer was applied into rectangular depressions on top of the 3D-printed surfaces above the integrated photonic silicon chips and cured for 5 min under UV light using the same conditions as for the UV-curable adhesive.

### **Gradient Generator-Based PRISM Assay**

The gradient generator device with integrated photonic silicon chips was placed onto a heat-controlled aluminium sub-structure ( $37 \text{ } ^\circ\text{C}$ ) and connected via a 3D-printed adapter to a motorized linear stage (Thorlabs, Inc., USA) for movement control. 70 % ethanol was used to disinfect the system before growth

## Experimental

medium (CAMHB) was introduced – allowing devices, temperature, and medium to equilibrate. Subsequently, suspensions of *E. coli* (McFarland 0.5) and 1 mg L<sup>-1</sup> ciprofloxacin (source fluid) and *E. coli* (McFarland 0.5) without antibiotic (sink fluid) were introduced for 5 min. The outlets were then closed (using silicone tubing and Luer adapters), and the bacteria were given 10 min to settle within the microstructure before the optical assay (PRISM) was initiated. The 2nL values were plotted versus time to monitor bacterial growth. The percent changes of 2nL were calculated as follows:

$$\Delta 2nL (\%) = \frac{2nL - 2nL_0}{2nL_0} \times 100 \%$$
; where 2nL is the 2nL value at a given time, and 2nL<sub>0</sub> corresponds to the 2nL when the PRISM assay was started.

### Broth Microdilution

Standard broth microdilution: BMD was performed according to the European Committee for Antimicrobial Susceptibility Testing (EUCAST) AFST protocols for conidia-forming moulds<sup>19</sup> and yeast cells.<sup>16</sup> For MIC determination, fungal growth was visually observed after 24 h (*C. auris*) and 48 h (*A. niger*) and also confirmed by absorbance measurements at 530 nm and 600 nm, respectively (Varioskan Flash, Thermo Scientific, USA). The MIC for *A. niger* was defined as the lowest antifungal concentration at which no growth was visible. For *C. auris*, the MIC was set as the lowest concentration of a drug that resulted in ≥ 50 % growth inhibition (anidulafungin) and ≥ 90 % growth inhibition (amphotericin B) compared to the untreated drug-free control. The only adjustment compared to the EUCAST protocol was decreasing the incubation temperature to 30 °C if not otherwise described. Gold standard BMD of bacteria (*E. coli* and *S. marcescens*) was performed using the protocols that are recommended by EUCAST, namely ISO 20776-1:2020 standard for bacteria.<sup>37</sup>

For bacterial species, the MIC was determined visually after 18 h incubation at 37 °C supported by absorbance measurements at 600 nm (Varioskan Flash, Thermo Scientific, USA) and defined as the lowest antibiotic concentration at which no growth was visible.

Gradient generator-enabled broth microdilution: The gradient generator was heat-steam sterilized and used to create the two-fold antimicrobial dilutions series, which was collected from the outlets of the device. Accordingly, the source fluids ciprofloxacin (1 mg L<sup>-1</sup>), gentamicin (1 mg L<sup>-1</sup>), and voriconazole (0.25 mg L<sup>-1</sup>) in growth medium were diluted by the sink fluid (CAMHB or RPMI 2 % G medium) to obtain the desired two-fold dilutions. Broth microdilution (BMD) was performed as described above for the following pathogen drug combinations: *E. coli* and gentamicin, *S. marcescens* and ciprofloxacin, and *C. auris* and voriconazole.

## 5 Results

This section consists of three papers, published in peer-reviewed journals. The papers are listed in the order in which they appear in this thesis:

**5.1 C. Heuer\***, H. Leonard\*, N. Nitzan, A. Lavy-Alperovitch, N. Massad-Ivanir, T. Scheper and E. Segal, Antifungal Susceptibility Testing of *Aspergillus niger* on Silicon Microwells by Intensity-Based Reflectometric Interference Spectroscopy, *ACS infectious diseases*, 2020, **6**, 2560–2566. (\*equal contribution)

**5.2 C. Heuer**, X. Jiang, G. Ron, O. Ternyak, T. Scheper, J. Bahnemann and E. Segal, Photonic Si Microwell Architectures for Rapid Antifungal Susceptibility Determination of *Candida auris*, *Chemical Communications*, 2024.

**5.3 C. Heuer\***, J.-A. Preuss\*, M. Buttkewitz, T. Scheper, E. Segal and J. Bahnemann, A 3D-printed microfluidic gradient generator with integrated photonic silicon sensors for rapid antimicrobial susceptibility testing, *Lab on a chip*, 2022, **22**, 4950–4961. (\*equal contribution)

First, the article “*Antifungal Susceptibility Testing of Aspergillus niger on Silicon Microwells by Intensity-Based Reflectometric Interference Spectroscopy*” describes for the first time the application of photonic silicon chips for rapid AFST, where the opportunistic pathogenic mould *A. niger* is used as a model fungus. Previous work has established the use of photonic silicon chips for the AST of bacteria only.<sup>28</sup> Fungi are different from bacteria in many aspects, including their morphology, size, and reproduction mechanism, and *Aspergillus* was selected as a relevant model, representing filamentous fungi. Moreover, the conventional gold standard AFST assay for *Aspergillus* is BMD, which is lengthy (48 – 72 h), and automated state-of-the-art AFST methods (e.g., Vitek2) are not yet available.<sup>14,19</sup> Realizing these differences, we have adapted the chip structure to accommodate the large fungal conidia within the periodic microwells. In addition, we have established an intensity-based PRISM (iPRISM), where the amplitude of the white light reflectance is used rather than the EOT (2nL). Fungal growth at varying concentrations of clinically-relevant antifungals is detected by monitoring intensity changes in the white light reflectance from the photonic silicon chips allowing expeditious MIC determination within 10 – 12 h.

Next, in the article “*Photonic Si Microwell Architectures for Rapid Antifungal Susceptibility Determination in Candida auris*”, the iPRISM assay is extended to the emerging pathogenic yeast *C. auris*. This yeast is well known for its morbidity and multi-drug resistance, with some isolates exhibiting drug resistance to all types of available antifungal medication (pan-resistance).<sup>38</sup> In gold standard BMD and the automated Vitek2, the AFST of yeast species is only completed within 24 h and 12 – 18 h, respectively.<sup>16,20,21</sup> In the extended iPRISM assay, the microwells dimensions are enlarged to fit the majority of the yeast cells in the

## Results

individual wells. The growth is monitored at varying antifungal concentrations by tracking intensity changes, and MIC values are expeditiously determined within 6 h. Moreover, this article gives the first incidence that photonic silicon chips can be used to differentiate yeast and bacteria by their varying growth patterns, as can be detected by also tracking the 2nL signal using PRISM.

As explained in the literature survey, holistic and miniaturized A(F)ST approaches that successfully integrate and automate the various required steps (*e.g.*, generation of antimicrobial dilution series, cell inoculum, sensing, and MIC determination) are considered vital for point-of-care susceptibility testing.<sup>14,31</sup> The article “*A 3D-printed microfluidic gradient generator with integrated photonic silicon sensors for rapid antimicrobial susceptibility testing*” demonstrates the use of 3D printing for the fabrication of a microfluidic gradient generator. This device automatically generates the desired two-fold antimicrobial dilution series in one step by adjusting the flow rate and channel length ratios and is first established for gold standard BMD of different pathogen-drug combinations. Next, the device is interfaced with photonic silicon chips to provide an assay for integrated and automated AST with the potential to be used as a point-of-care test. Using *E. coli* and ciprofloxacin as a model pathogen-drug combination, MIC values can be determined within 90 minutes compared to 8 – 24 h for bacterial species in current clinical procedures.<sup>28,39</sup>

## 5.1 Antifungal Susceptibility Testing of *Aspergillus niger*

This section is reproduced from the research article “*Antifungal Susceptibility Testing of Aspergillus niger on Silicon Microwells by Intensity-Based Reflectometric Interference Spectroscopy*”, published in the peer-reviewed journal *ACS Infectious Diseases*.

# “Antifungal Susceptibility Testing of *Aspergillus niger* on Silicon Microwells by Intensity-Based Reflectometric Interference Spectroscopy”

Christopher Heuer\*, Heidi Leonard\*, Nadav Nitzan, Ariella Lavy-Alperovitch, Naama Massad-Ivanir, Thomas Scheper and Ester Segal  
(\* equal contribution)

*ACS infectious diseases*, 6, 2560–2566 (2020)

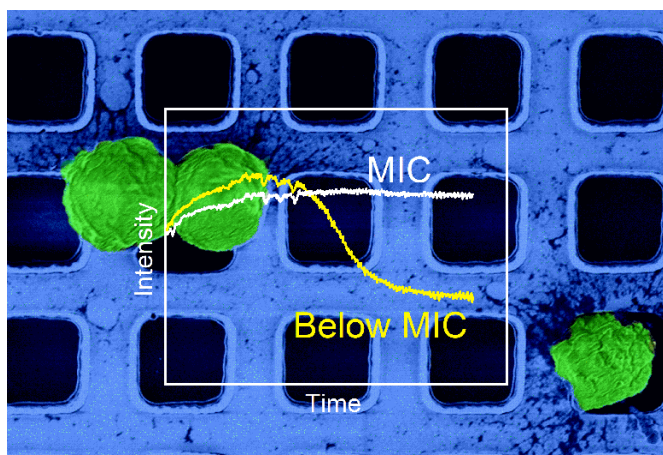


**Figure 5** Graphical abstract of the research article “Antifungal Susceptibility Testing of *Aspergillus niger* on Silicon Microwells by Intensity-Based Reflectometric Interference Spectroscopy”.

The article addresses the first research aim and presents for the first time the iPRISM assay for a rapid, label-free and phenotypic AFST of the filamentous fungi *A. niger*. This fungal mould species can cause opportunistic infections in humans with a weak immune system and was reported as a cause of fungal coinfections in COVID-19 patients.<sup>40</sup> In the presented optical iPRISM assay, photonic silicon chips consisting of periodic arrays of microwell diffraction gratings were developed as sensors that provide a



## Results

microstructured surface for *A. niger* colonization and an optical transducer element for sensitive fungal growth monitoring. The individual wells (width:  $\sim 3 \mu\text{m}$ , depth:  $\sim 4 \mu\text{m}$ ) of this microstructure were designed to confine *A. niger* conidia from a suspension in growth medium within the wells. Subsequent germination and hyphae formation at this solid-liquid interface were optically tracked in real-time by detecting intensity changes in the white light reflectance from the photonic silicon chips.

Next, fungal growth was monitored in the presence of two clinically-relevant antifungal agents with distinct mechanisms (voriconazole: inhibition of cell membrane biosynthesis and amphotericin B: cell membrane destruction) to determine the MIC values for both drugs. The obtained MICs agreed with values published by EUCAST - the European society for susceptibility testing standardization - and could successfully be determined within 10 and 12 h, respectively. Thus, the iPRISM provides an expeditious alternative to the gold standard BMD, which extends to 48 h for filamentous fungi.

In the following article, “*Antifungal Susceptibility Testing of Aspergillus niger on Silicon Microwells by Intensity-Based Reflectometric Interference Spectroscopy*”, the results are presented and discussed in detail.

# Antifungal Susceptibility Testing of *Aspergillus niger* on Silicon Microwells by Intensity-Based Reflectometric Interference Spectroscopy

Christopher Heuer,<sup>1</sup> Heidi Leonard,<sup>1</sup> Nadav Nitzan, Ariella Lavy-Alperovitch, Naama Massad-Ivanir, Thomas Scheper, and Ester Segal\*



Cite This: *ACS Infect. Dis.* 2020, 6, 2560–2566



Read Online

ACCESS |



Metrics & More



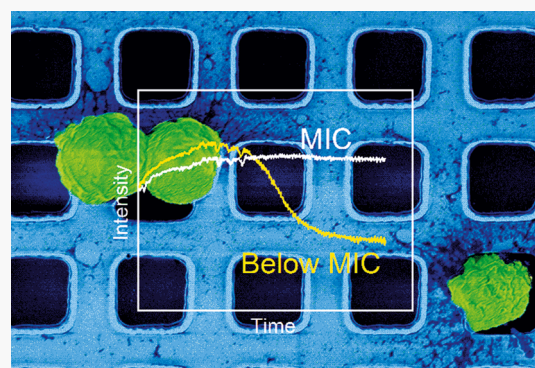
Article Recommendations



Supporting Information

**ABSTRACT:** There is a demonstrated and paramount need for rapid, reliable infectious disease diagnostics, particularly those for invasive fungal infections. Current clinical determinations for an appropriate antifungal therapy can take up to 3 days using current antifungal susceptibility testing methods, a time-to-readout that can prove detrimental for immunocompromised patients and promote the spread of antifungal resistant pathogens. Herein, we demonstrate the application of intensity-based reflectometric interference spectroscopic measurements (termed iPRISM) on microstructured silicon sensors for use as a rapid, phenotypic antifungal susceptibility test. This diagnostic platform optically tracks morphological changes of fungi corresponding to conidia growth and hyphal colonization at a solid–liquid interface in real time. Using *Aspergillus niger* as a model fungal pathogen, we can determine the minimal inhibitory concentration of clinically relevant antifungals within 12 h. This assay allows for expedited detection of fungal growth and provides a label-free alternative to broth microdilution and agar diffusion methods, with the potential to be used for point-of-care diagnostics.

**KEYWORDS:** *Aspergillus niger*, antifungal susceptibility testing, fungal resistance, sensor, optical sensor



Pathogenic fungi are a rising cause of disease and pose a threat to immunocompromised individuals.<sup>1</sup> Particularly, *Candida* species, pathogenic *Aspergilli*, and *Cryptococci* account for invasive fungal infections in humans,<sup>2,3</sup> resulting in ~1.4 million deaths (annually) ascribed to fungal infection.<sup>4</sup> Because of acquired antimicrobial resistance, species identification alone is not sufficient to target effective therapy for fungal infections.<sup>5</sup> Thus, antifungal susceptibility testing (AFST) is critical to direct the proper choice of treatment in a timely manner.<sup>6,7</sup> Classical AFST methods include broth microdilution (BMD) testing, the suggested reference method (by the Clinical & Laboratory Standards Institute – CLSI or the European Committee on Antimicrobial Susceptibility Testing – EUCAST), as well as agar diffusion methods, such as the Etest (bioMérieux SA). These methods are labor-intensive and time-consuming (up to 72 h),<sup>6,8</sup> and automated tests (e.g., Vitek2, bioMérieux SA) are only available for a limited spectrum of microorganisms.<sup>9</sup> Thus, accelerating AFST is of great importance to improve the clinical outcome of antifungal therapy and abate the emergence of antifungal resistance.<sup>1</sup>

New approaches for molecular identification of fungal pathogens and rapid AFST include mass spectrometry (MS)<sup>10</sup> and nucleic acid-based diagnostics.<sup>6</sup> However, high equipment acquisition costs as well as insufficient validation

and multiplexing ability limit the use of MS for AFST.<sup>10</sup> For genomic AFST, the main disadvantage is its inability to reveal the phenotypical behavior of a pathogen.<sup>11</sup> Therefore, research efforts are directed toward developing novel phenotypic AFST methods such as flow cytometry,<sup>12</sup> colorimetric redox indicators,<sup>13</sup> and isothermal microcalorimetry.<sup>14</sup> Furthermore, microfluidic systems have recently been applied to study fungal growth and assess the activity of antimicrobials.<sup>15,16</sup> However, some of these new techniques rely on sophisticated and expensive equipment, have a limited microorganism spectrum, or do not effectively accelerate the determination of the minimum inhibitory concentration (MIC) values.

Previously, phase-shift reflectometric interference spectroscopic measurements (PRISM) were demonstrated to monitor antibiotic susceptibility and the behavior of bacteria, colonizing within silicon microstructured arrays.<sup>17,18</sup> In this work, we

Received: April 23, 2020

Published: September 15, 2020



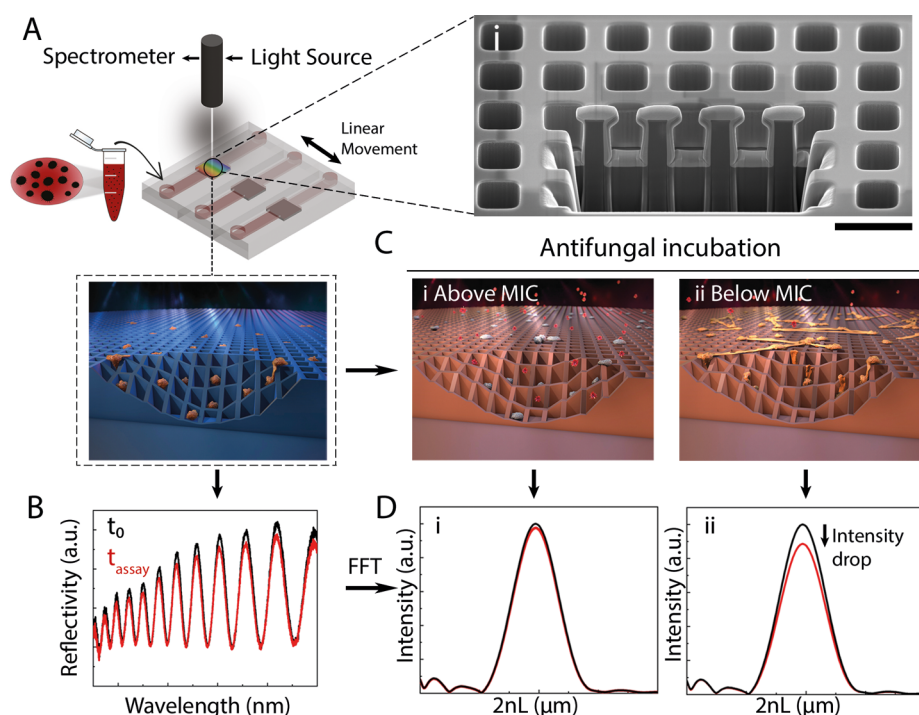


**Figure 1.** iPRISM AFST concept: Schematic representation of optical monitoring of *A. niger* growth and responses to antifungals by iPRISM. (A) Photonic silicon chips of microwell arrays entrap *Aspergillus* conidia from a conidia suspension while illuminated with a white light source. (A-i) Representative cross-sectioned HR-SEM of the photonic chip (scale bar represents 5  $\mu\text{m}$ ). (B) The resulting reflectance spectra are recorded and analyzed in real time, allowing for label-free monitoring of fungal growth and responses to antifungals. (C) After allowing the conidia to settle within the silicon microwells, antifungals are introduced (C-i), resulting in growth inhibition at concentrations above the MIC or (C-ii) unimpeded growth at subinhibitory antifungal concentrations. (D-i) After applying frequency analysis, growth inhibition corresponds to unchanged intensity values, while (D-ii) fungal growth on top of the microwells results in a reduction of the intensity of the reflected light.

demonstrate an easy-to-perform platform that allows the growth of *Aspergillus niger* (*A. niger*) to be tracked in real time. Due to the different behavior and morphology of filamentous fungi compared to bacteria, herein, we apply intensity-based PRISM, referred to as iPRISM, as a tool for rapid and label-free, phenotypic AFST using the fungal species *A. niger* as a model microorganism.

## RESULTS AND DISCUSSION

iPRISM relies on the capture of fungal conidia within silicon microwells and the subsequent monitoring of fungal growth in real time by intensity-based reflectometric interference spectroscopic measurements, as depicted in Figure 1. Assays are performed in a series of temperature-controlled microfluidic channels, each containing an injection port and a waste outlet. Photonic silicon chips consisting of diffraction gratings, specifically periodic arrays of microwells with a width of  $\sim 3 \mu\text{m}$  and depth of  $\sim 4 \mu\text{m}$  (see scanning electron micrograph in Figure 1A-i), are individually fixed in the center of the flow channels and illuminated by a white light source positioned normal to the photonic silicon chip (Figure 1A). The resulting reflectance spectrum of the zero-order diffraction exhibits interference fringes (Figure 1B), as the incident light is partially reflected by the top and the bottom of the microwells.<sup>17</sup> The application of frequency analysis results in a single peak where the peak position corresponds to  $2nL$  ( $n$  represents the refractive index of the medium within the arrays, and  $L$  represents the height of the microstructures; see Figure S1) and the peak amplitude or intensity ( $I$ ) corresponds to the intensity of the reflected light (Figure 1D-i,ii). The antifungal

agent is introduced, and fungal growth is monitored in real time by tracking the intensity changes ( $\Delta I$ ) during AFST experiments.

iPRISM is performed in two steps: Initially, *Aspergillus* conidia suspensions at a designated concentration are introduced into the microfluidic channels and allowed to incubate on the silicon microtopologies for 15 min (Figure 1A). Subsequently, the antifungal (at varying concentrations) is introduced into the channels, and the fungal response is optically monitored by iPRISM. If the conidia germinate and hyphal growth occurs on top of the microwells (see Figure 1C-ii), the intensity of the reflected light decreases over time (Figure 1D-ii), while inhibition of growth and cell death (see Figure 1C-i) result in unchanged intensity values (Figure 1D-i).

*A. niger* suspensions ( $10^5$  conidia  $\text{mL}^{-1}$ ) were introduced into the channels, and growth was monitored by iPRISM. The latter concentration corresponds to the suggested seeding concentration by EUCAST protocols for AFST of conidia-forming molds, including *Aspergillus* species.<sup>8</sup> Figure 2A presents an iPRISM curve, where the values of  $\Delta I$  (%) are tracked in real time, depicting a continuous decrease in intensity over a time scale of 15 h, while for the reference channel (containing just growth medium), the signal is unchanged (see also Figure S2A, in which averaged iPRISM results and the corresponding standard deviation values are presented). The decrease in the signal is ascribed to germination and hyphal growth, which were verified by confocal laser scanning microscopy (CLSM) of *A. niger* stained with Calcofluor White after 15 min, 4, 5, 6, and 15 h of on-chip incubation at 30  $^\circ\text{C}$  (Figure 2A-i-v). Germination is visible

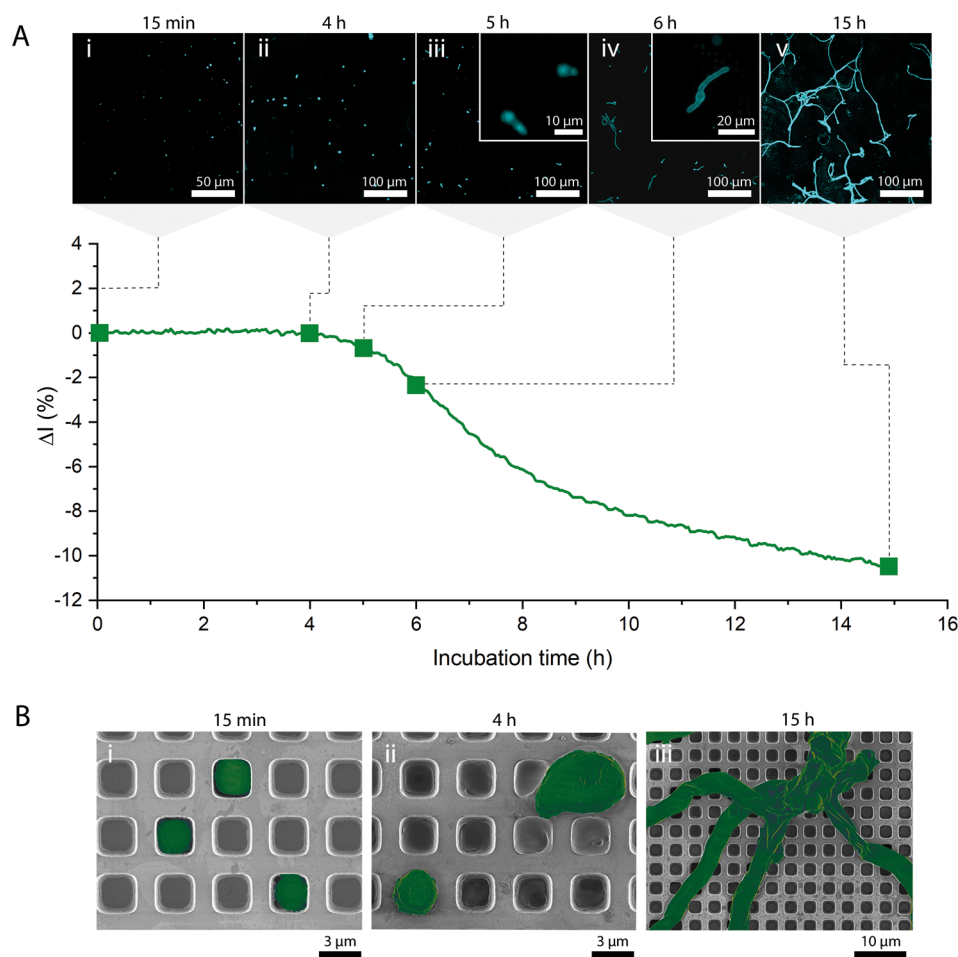


**Figure 2.** iPRISM of *A. niger*, at a concentration of  $10^5$  conidia  $\text{mL}^{-1}$ , on photonic silicon chips. (A) Real-time iPRISM curve, where  $\Delta I$  values were recorded over a time period of 15 h with corresponding false-colored CLSM images following Calcofluor White staining after (A-i) 15 min, (A-ii) 4 h, (A-iii) 5 h, (A-iv) 6 h, and (A-v) 15 h of incubation. Note that Figure S2 provides averaged iPRISM results, including standard deviation values, for a concentration of  $10^5$  conidia  $\text{mL}^{-1}$ . (B) Corresponding HR-SEM images: (i) The *A. niger* conidia are entrapped inside the microwell at  $t = 15$  min. (ii) The conidia swell and break out from the microwells at  $t = 4$  h. (iii) *A. niger* spreading over the chip surface after 15 h of incubation. Fungi are false-colored green for clarity.

after around 5 h (Figure 2A-iii), and further growth corresponds to a distinct reduction in signal intensity after 6 h (Figure 2A-iv) and 15 h (Figure 2A-v). Germination is a process required for vegetative growth of hyphae in which the extension of the cytoplasm and the disintegration of the outer conidial wall allows the nascent germ tube to emerge.<sup>19</sup> In previous works, it was reported that distinct germ tube formation of *A. niger* conidia was visible after 6 h, which is in good agreement to our findings.<sup>20</sup>

The confocal images of the photonic silicon chips during the first 4 h of incubation show that the conidia swell. The latter is an essential step, prior to germination, where the conidia uptake liquid and their size increases.<sup>19</sup> To verify this behavior and rule out staining procedure artifacts, the chips were studied by high resolution scanning electron microscopy (HR-SEM). Figure 2B-i shows that, in the beginning of the assay, most of the conidia, which are spherical with a typical diameter of  $\sim 3 \mu\text{m}$ , are entrapped within the microwells. The proportion of conidia seeded per well is typically between 2 and 5 conidia per 100 microwells at a seeding concentration of  $10^5$  conidia  $\text{mL}^{-1}$  (see a representative HR-SEM image in Figure S3). Over time, the confined conidia swell and break out from the microwells, as depicted in Figure 2B-ii, and after 15 h, the hyphae grow on

top of the microwells and cover the chip (Figure 2B-iii). The latter further supports the observed significant decrease in intensity with time.

iPRISM at a lower initial conidia concentration of  $10^4$  conidia  $\text{mL}^{-1}$ , which may be of potential clinical relevancy, results in unchanged intensity as depicted in Figure S2A. Optical microscopy studies reveal that the conidia germinate and form few germ tubes on the chip (Figure S2B). Yet, the iPRISM assay is not sensitive enough to detect these local morphological changes. It should be noted that there are microfluidic methods that allow for more sensitive detection of germination and fungal growth; however, these techniques require sophisticated single-cell microscopy, or the use of fluorescent labeling.<sup>21</sup> Higher conidia concentrations, such as  $10^6$  conidia  $\text{mL}^{-1}$ , are found to cause unstable intensity values immediately after introduction (Figure S2A). This effect is ascribed to the high number of cells that are settling onto the silicon surface. Furthermore, the germination at  $10^6$  conidia  $\text{mL}^{-1}$  is clearly inhibited (Figure S2B), likely due to the presence of a self-inhibitor. The latter was shown by Barrios-Gonzalez et al.<sup>22</sup> to decrease the germination rate of *A. niger* at concentrations above  $10^6$  conidia  $\text{mL}^{-1}$ . Moreover, the overall observed intensity decrease for  $10^6$  cells  $\text{mL}^{-1}$  is less

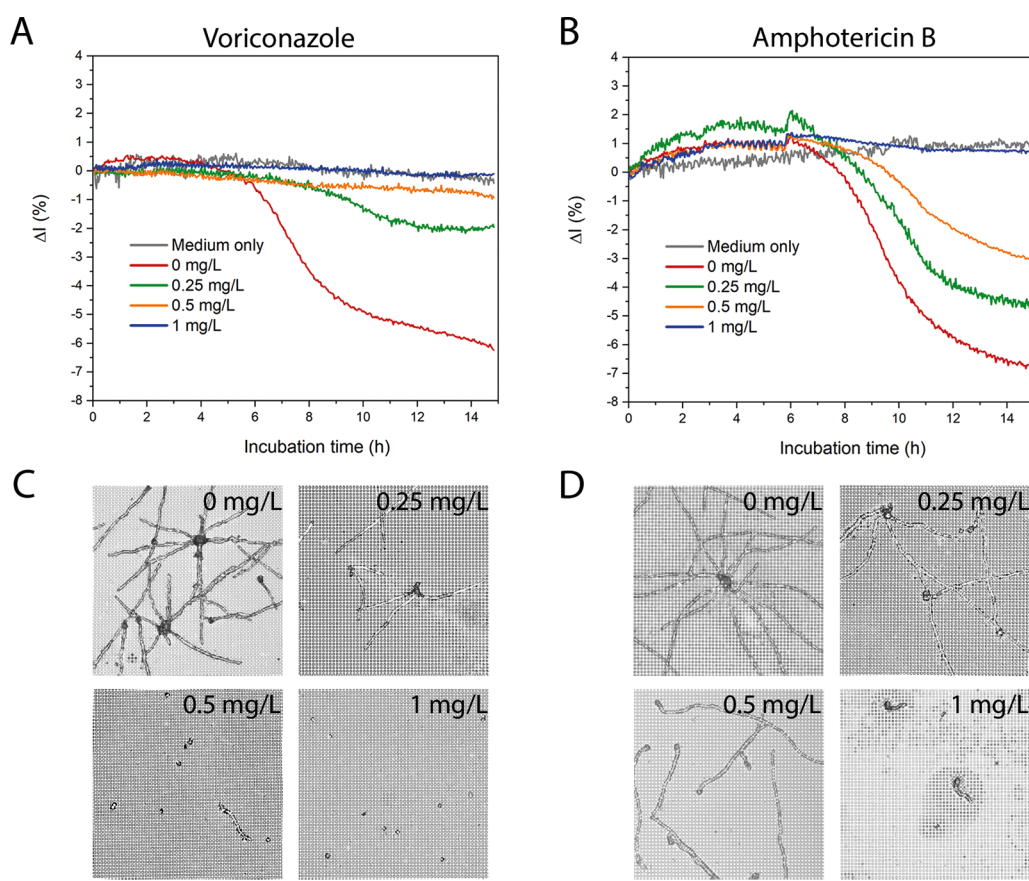


**Figure 3.** *A. niger* iPRISM AFST. iPRISM curves, displaying  $\Delta I$  (%) over time, upon exposure to varying concentrations of the antifungal drugs: (A) voriconazole and (B) amphotericin B. Corresponding optical microscope images of photonic silicon chips after 15 h, revealing the behavior of the fungi upon exposure to different concentrations of (C) voriconazole and (D) amphotericin B. Scale bar represents 50  $\mu\text{m}$ .

pronounced in comparison to  $10^5$  cells  $\text{mL}^{-1}$  (slope values of  $-0.82 \Delta I$  (%)  $\text{h}^{-1}$  vs  $-0.18 \Delta I$  (%)  $\text{h}^{-1}$ , respectively). Therefore, we have adhered to the EUCAST protocol, and all subsequent experiments were performed with conidial seeding concentrations of  $10^5$  conidia  $\text{mL}^{-1}$ .

For the determination of MIC values by iPRISM, *A. niger* conidia were exposed to various concentrations of the clinically relevant antifungals: voriconazole and amphotericin B (Figure 3). Voriconazole is the recommended antimicrobial agent for the treatment of invasive aspergillosis,<sup>23</sup> and it inhibits the biosynthesis of the fungal cell membrane component ergosterol.<sup>24</sup> Amphotericin B is used as a second-line treatment, and the drug interacts with ergosterol in the cell membrane, resulting in cell death.<sup>25</sup> Figure 3 presents iPRISM curves for *A. niger* upon exposure to varying concentrations of voriconazole (Figure 3A) and amphotericin B (Figure 3B). For both drugs, increased concentrations result in moderate intensity changes in comparison to the untreated fungi. For example, when using  $1 \text{ mg L}^{-1}$  voriconazole, the intensity remains constant throughout the experiment, whereas a characteristic decrease of  $\sim 6\%$  is detected in the absence of the drug. This behavior is ascribed to complete growth inhibition of the fungi in the presence of increasing concentrations of the antifungal agent. Indeed, optical microscopy images (Figure 3C) reveal that, at a voriconazole concentration of  $1 \text{ mg L}^{-1}$ , no germination is observed, while at lower drug concentrations, some germination occurs, and few germ tubes are visible on the surface of the chip. A similar

behavior is observed upon exposure to amphotericin B, and at a concentration of  $1 \text{ mg L}^{-1}$ , only minor germination is observed after 15 h (Figure 3D).

In standard methods for AFST, such as BMD or E-test, the MIC is defined as the lowest concentration of a drug that inhibits the visible growth of a microorganism.<sup>8</sup> In the iPRISM assay, we suggest designating the MIC as the lowest concentration of an antifungal agent at which no reduction of the intensity value  $\Delta I$  (%) occurs, while at subinhibitory concentrations, a decline of intensity should be visible to some extent. As such, the iPRISM MIC values were determined to be 0.5 and  $1 \text{ mg L}^{-1}$  for voriconazole and amphotericin B, respectively. Figure S4 presents averaged iPRISM curves and the respective standard deviations of triplicate experiments using different chips. The statistical analysis of these results demonstrates that MIC values for amphotericin B and voriconazole can be determined within 10 and 12 h, respectively. Note that the obtained Zprime score values are negative (Table S1), indicating a low signal-to-noise ratio. This may emphasize the general challenge to define a specific MIC value for a drug–strain combination due to possible inter- and intralaboratory variation in antimicrobial susceptibility testing (AST).<sup>26</sup> This variation is also recognized by EUCAST quality control documents stating that repeated testing of quality control strains should yield individual MIC values randomly distributed within the recommended ranges.<sup>27</sup> Thus, the iPRISM method significantly accelerates the MIC determination in comparison to the gold-standard microbiological

technique BMD, in which the MIC is determined only after 48 h.<sup>8</sup>

The iPRISM MIC values for the two antifungal drugs are compared to MIC values determined by the BMD testing, which is standardized by both EUCAST and CLSI (Table 1).

**Table 1. Comparison of MIC Values as Determined by iPRISM and BMD for Voriconazole and Amphotericin B**

antifungal agent	iPRISM		BMD	
	MIC (mg L <sup>-1</sup> )	time (h)	MIC (mg L <sup>-1</sup> )	time (h)
voriconazole	0.5	12	0.5	48
amphotericin B	1	10	0.25	48

The iPRISM and BMD MIC values for voriconazole are the same, while for amphotericin B, the iPRISM MIC is higher than the BMD value. Yet, the iPRISM MIC values for both voriconazole and amphotericin B comply with the EUCAST MIC distribution for these antifungals.<sup>28,29</sup> It should be kept in mind that differences in MIC values between methods are common in both AFST and AST.<sup>7</sup> We have previously shown that MIC values of *E. coli* grown on silicon gratings are slightly higher in comparison to values determined by BMD.<sup>18</sup> The main reason for these discrepancies is likely due to the different growth environments provided for the fungi, where the BMD analyzes fungal growth in a liquid medium and the iPRISM detects changes occurring on the surface of the silicon grating. Thus, it is possible that the microtopologies provide a surface with which the *A. niger* can interact.

A proof-of-concept for a rapid and label-free assay for phenotypic AFST testing of filamentous fungi is demonstrated. The fungi are colonized on a microstructured photonic chip, which also serves as the optical transducer element. Fungal growth is monitored in real time by detecting changes in the reflectivity spectra collected from the photonic silicon chip and are correlated to characteristic morphology changes of the fungi. This approach is employed to study the behavior of *A. niger* upon exposure to clinically relevant antifungals, specifically voriconazole and amphotericin B. Using the iPRISM assay, distinct differentiation between growth and no growth and determination of MIC values can be achieved within <12 h for *A. niger*. Thus, iPRISM is significantly faster than classical methods used for filamentous fungi. Furthermore, the MIC values determined by iPRISM are in agreement with standardized BMD results for *A. niger*. Nevertheless, it should be noted that MIC determination for slower-growing strains may take longer compared to the model species in this work. Also, the agreement of MIC values for other fungi–drug combinations to reference methods should be validated in the future.

While this platform was demonstrated for *A. niger*, iPRISM can potentially be used as a tool for monitoring other microorganisms, such as *Candida* and *Cryptococcus* species due to its simple principle of detection. Thus, current and future research in our group focus on demonstrating iPRISM applicability for AFST of yeast, owing to their different morphology compared to *Aspergillus* species.

## METHODS

**Materials.** Glutaraldehyde, Calcofluor White, Roswell Park Memorial Institute medium (RPMI 1640), D-glucose, amphotericin B, and voriconazole were supplied by Sigma-Aldrich, Israel. Absolute ethanol, dimethyl sulfoxide (DMSO),

and all buffer salts were purchased from Merck, Germany. Isopropanol and acetone were supplied by Gadot, Israel. Potato Dextrose Agar (PDA), Potato Dextrose Broth (PDB), Bacto agar, yeast extract, and casein hydrolysate were purchased from Difco, USA. 3-(*N*-Morpholino)-propanesulfonic acid (MOPS) was supplied by Chem-Impex International, Inc., USA. Sabouraud Dextrose Agar (SDA) plates were purchased from Novamed Ltd., Israel.

**Preparation of Solutions and Media.** All aqueous solutions and media were prepared in Milli-Q water (18.2 MΩ cm). Phosphate buffered saline (PBS) was composed of 137 mM NaCl, 2.7 mM KCl, 1.8 mM KH<sub>2</sub>PO<sub>4</sub>, and 10 mM Na<sub>2</sub>HPO<sub>4</sub>. RPMI 1640 2% G medium (RPMI 1640 medium supplemented with 2% D-glucose; referred to as growth medium) comprised 10.4 g L<sup>-1</sup> RPMI 1640, 34.5 g L<sup>-1</sup> MOPS, and 18 g L<sup>-1</sup> glucose. 1% PDA contained 10 g L<sup>-1</sup> PDA and 15 g L<sup>-1</sup> Bacto agar; water agar contained 20 g L<sup>-1</sup> Bacto agar. All media and buffer were autoclaved or sterile filtered prior to use.

***Aspergillus niger* Isolate.** The fungi were isolated from a contaminated onion into 1% PDA and incubated in darkness for 10 days at 25 °C. Conidia from the mature culture were recultured by streaking onto SDA plates supplemented with chloramphenicol to eliminate bacterial contamination and incubated as described above. For preparation of monoconidial cultures, conidia were recultured onto water agar and incubated overnight (18 h) at 25 °C. Single germinating conidia were removed by micromanipulation under a light microscope and transferred to 1% PDA. All tests were performed with a single monoconidial culture isolate, designated HCN 18, in order to limit possible genetic variability. Species identification of isolate HCN 18 was carried out by sequencing the internal transcribed spacer regions (ITS1 and ITS2; see the Supporting Information for the sequence (Table S2) and protocol), and the isolate was identified as *A. niger*.

**Preparation of Fungal Cultures.** Fungal cultures were refreshed every 2 weeks onto 1% PDA and maintained at 4 °C until used. Prior to iPRISM experiments, the cultures were transferred onto SDA plates containing chloramphenicol. Because *A. niger* showed the fastest growth at 30 °C, the fungal cultures were subsequently incubated at 30 °C, and after 2–5 days, sufficient sporulation for AFST experiments was reached. Conidial density was quantified by using a hemocytometer (Neubauer improved cell counting chamber).

**Fabrication and Preparation of Photonic Silicon Chips.** Silicon chips with microwell gratings were fabricated by standard lithography and reactive ion etching techniques at the Micro- and Nano-Fabrication and Printing Unit (Technion). The resulting wafers were coated with photoresist to protect their microstructure while dicing the wafer into 5 × 5 mm chips using an automated dicing saw (DAD3350, Disco, Japan). The photonic silicon chips were washed with acetone to remove the photoresist and oxidized for 1 h at 800 °C in a furnace (Lindberg/Blue M 1200 °C Split-Hinge, Thermo Scientific, USA).

**iPRISM Assay.** A custom-made, aluminum chamber with seven injection and outlet channels was used to fix and separate the photonic silicon chips during the iPRISM assays. Each injection channel was connected by tubing to a syringe injection port, and the injection of the conidia suspensions was allowed. The chamber was controlled by a motorized linear stage (Thorlabs, Inc., USA). The photonic chips were placed

in a small square cavity in each channel and were separated from each other and fixed on the surface of the chamber by a rubber gasket. The system was further sealed before the experiments by an acrylic piece and by tightening the lid of the aluminum housing. Before each experiment, the system was sterilized with 70% ethanol and sterile water followed by introduction of only growth medium to allow devices, temperature, and medium to equilibrate. Subsequently, 500  $\mu\text{L}$  of the conidia suspension was introduced, and after 15 min, the antifungals were introduced, while the reflectance signal was continuously recorded during the experiment.

**Data Acquisition and Analysis.** A bifurcated fiber optic (Ocean Optics, USA) equipped with a collimating lens was positioned normal to the photonic silicon chips, illuminating them via a white light source. The reflected light was recorded by a USB4000 CCD spectrometer (Ocean Optics, USA). The position of the chamber was controlled by a motorized stage (Thorlabs, USA) and LabView (National Instruments, USA). Frequency analysis was performed on acquired spectra in the range between 450 and 900 nm. The resulting peak after fast Fourier transform (FFT) was identified by determining the maximum peak position, where the height of the detected peak directly corresponds to the intensity of the reflected light. The intensity values were plotted versus time. For AFST, the introduction time of the antifungal is referred to as time 0. The percent changes of the intensity ( $\Delta I$ ) were calculated as follows:  $\Delta I (\%) = \frac{I - I_0}{I_0} \times 100\%$ , where  $I$  is the intensity at a given time and  $I_0$  is the intensity at time 0.

**Characterization of Photonic Silicon Chips.** The chips were examined immediately after experiments by using an optical light microscope (Axio Scope A1, Carl Zeiss, Germany) to identify fungal growth and ensure no bacterial contamination occurred.

High-resolution scanning electron microscopy (HR-SEM) was performed using a Zeiss Ultra Plus high-resolution scanning microscope. Samples were fixated using 2.5% glutaraldehyde in PBS, washed with water, and dehydrated through a dilution series in ethanol with increasing concentration from 10% to absolute ethanol.

Focused ion beam (FIB)-cross-sectional SEM images were obtained using a Dual Beam Helios NanoLab G3 instrument (FEI, USA). Platinum deposition was performed prior to observation.

Confocal laser scanning microscopy (CLSM; LSM 700, Carl Zeiss, Germany) was performed on samples stained by Calcofluor White and a drop of 10% potassium hydroxide; the excitation wavelength was 405 nm, and images were rendered by Zen software (Carl Zeiss, Germany).

**Broth Microdilution.** BMD was performed according to the EUCAST AFST protocol for conidia forming molds.<sup>8</sup> Fungal growth was visually observed after 48 h and also confirmed by optical density measurements (600 nm,  $n = 5$ , Varioskan Flash, Thermo Scientific, USA). The only adjustment we made to the EUCAST protocol was decreasing the incubation temperature to 30 °C.

## ■ ASSOCIATED CONTENT

### Supporting Information

The Supporting Information is available free of charge at <https://pubs.acs.org/doi/10.1021/acsinfecdis.0c00234>.

Figure S1, schematic of the silicon microstructure; Figure S2, iPRISM assay for different cell concen-

trations; Figure S3, representative seeding proportion; Figure S4, iPRISM for AFST in triplicates; Table S1, ZPrime Score for voriconazole and amphotericin B at different time points; Table S2, ITS sequencing result; protocol for DNA extraction and sequencing of the ITS regions (PDF)

## ■ AUTHOR INFORMATION

### Corresponding Author

Ester Segal – Department of Biotechnology and Food Engineering, Technion – Israel Institute of Technology, Haifa 3200003, Israel; [orcid.org/0000-0001-9472-754X](https://orcid.org/0000-0001-9472-754X); Email: [esegal@technion.ac.il](mailto:esegal@technion.ac.il)

### Authors

Christopher Heuer – Department of Biotechnology and Food Engineering, Technion – Israel Institute of Technology, Haifa 3200003, Israel; Institute of Technical Chemistry, Leibniz University Hannover, 30167 Hannover, Germany

Heidi Leonard – Department of Biotechnology and Food Engineering, Technion – Israel Institute of Technology, Haifa 3200003, Israel; [orcid.org/0000-0003-2461-6822](https://orcid.org/0000-0003-2461-6822)

Nadav Nitzan – Department of Biotechnology and Food Engineering, Technion – Israel Institute of Technology, Haifa 3200003, Israel

Ariella Lavy-Alperovitch – Department of Biology, Technion – Israel Institute of Technology, Haifa 3200003, Israel

Naama Massad-Ivanir – Department of Biotechnology and Food Engineering, Technion – Israel Institute of Technology, Haifa 3200003, Israel; [orcid.org/0000-0001-8964-9997](https://orcid.org/0000-0001-8964-9997)

Thomas Scheper – Institute of Technical Chemistry, Leibniz University Hannover, 30167 Hannover, Germany

Complete contact information is available at: <https://pubs.acs.org/10.1021/acsinfecdis.0c00234>

### Author Contributions

<sup>†</sup>C.H. and H.L. contributed equally. E.S., H.L., N.N., and C.H. conceptualized the study. A.L.-A., N.M.-I., H.L., and C.H. performed the experiments. E.S., H.L., T.S., and C.H. wrote the manuscript. All authors commented, revised, and approved the final version of the paper.

### Notes

The authors declare no competing financial interest.

## ■ ACKNOWLEDGMENTS

This work was partially supported by the Israel Innovation Authority (Kamin program). C.H. acknowledges financial aid from the Leibniz Universitätsgesellschaft and the Technion. We thank Dima Peselev and Orna Ternyak (MNFPU, Technion) for the microfabrication of the photonic chips and Omer Sabach for his artwork depicting the microfluidic channels (Figure 1A).

## ■ REFERENCES

- (1) Srinivasan, A., Lopez-Ribot, J. L., and Ramasubramanian, A. K. (2014) Overcoming Antifungal Resistance. *Drug Discovery Today: Technol.* 11, 65–71.
- (2) Garber, G. (2001) An Overview of Fungal Infections. *Drugs* 61, 1–12.
- (3) Montoya, M. C., Moye-Rowley, W. S., and Krysan, D. J. (2019) *Candida auris* the Canary in the Mine of Antifungal Drug Resistance. *ACS Infect. Dis.* 5, 1487–1492.

- (4) Sanglard, D. (2016) Emerging Threats in Antifungal-Resistant Fungal Pathogens. *Front. Med.* 3, 11–11a.
- (5) Ingham, C. J., Boonstra, S., Levels, S., de Lange, M., Meis, J. F., and Schneeberger, P. M. (2012) Rapid Susceptibility Testing and Microcolony Analysis of *Candida* Spp. Cultured and Imaged on Porous Aluminum Oxide. *PLoS One* 7 (3), No. e33818.
- (6) Sanguinetti, M., and Posteraro, B. (2017) New Approaches for Antifungal Susceptibility Testing. *Clin. Microbiol. Infect.* 23 (12), 931–934.
- (7) Leonard, H., Colodner, R., Halachmi, S., and Segal, E. (2018) Recent Advances in the Race to Design a Rapid Diagnostic Test for Antimicrobial Resistance. *ACS Sens* 3 (11), 2202–2217.
- (8) Arendrup, M. C., Meletiadis, J., Mouton, J. W., Lagrou, K., Hamal, P., and Guinea, J., and the Subcommittee on Antifungal Susceptibility Testing (AFST) of the ESCMID European Committee for Antimicrobial Susceptibility Testing. (2017) *EUCAST Definitive Document E.DEF 9.3.1*.
- (9) van Belkum, A., and Dunne, W. M. (2013) Next-Generation Antimicrobial Susceptibility Testing. *J. Clin. Microbiol.* 51 (7), 2018–2024.
- (10) van Belkum, A., Welker, M., Pincus, D., Charrier, J. P., and Girard, V. (2017) Matrix-Assisted Laser Desorption Ionization Time-of-Flight Mass Spectrometry in Clinical Microbiology: What Are the Current Issues? *Ann. Lab. Med.* 37 (6), 475–483.
- (11) Wickes, B. L., and Wiederhold, N. P. (2018) Molecular Diagnostics in Medical Mycology. *Nat. Commun.* 9 (1), 5135.
- (12) Bleichrodt, R.-J., and Read, N. D. (2019) Flow Cytometry and FACS Applied to Filamentous Fungi. *Fungal Biol. Rev.* 33 (1), 1–15.
- (13) Leong, C., Buttafuoco, A., Glatz, M., and Bosshard, P. P. (2017) Antifungal Susceptibility Testing of *Malassezia* Spp. with an Optimized Colorimetric Broth Microdilution Method. *J. Clin. Microbiol.* 55 (6), 1883.
- (14) Furustrand Tafin, U., Orasch, C., and Trampuz, A. (2013) Activity of Antifungal Combinations against *Aspergillus* Species Evaluated by Isothermal Microcalorimetry. *Diagn. Microbiol. Infect. Dis.* 77 (1), 31–36.
- (15) Ellett, F., Jorgensen, J., Frydman, G. H., Jones, C. N., and Irimia, D. (2017) Neutrophil Interactions Stimulate Evasive Hyphal Branching by *Aspergillus fumigatus*. *PLoS Pathog.* 13 (1), No. e1006154.
- (16) Cermak, N., Olcum, S., Delgado, F., Wasserman, S., Payer, K., Murakami, M., Knudsen, S., Kimmerling, R., Stevens, M., Kikuchi, Y., Sandikci, A., Ogawa, M., Agache, V., Baleras, F., Weinstock, D. M., and Manalis, S. R. (2016) High-throughput measurement of single-cell growth rates using serial microfluidic mass sensor arrays. *Nat. Biotechnol.* 34, 1052–1059.
- (17) Massad-Ivanir, N., Mirsky, Y., Nahor, A., Edrei, E., Bonanno-Young, L. M., Ben Dov, N., Sa'ar, A., and Segal, E. (2014) Trap and Track: Designing Self-Reporting Porous Si Photonic Crystals for Rapid Bacteria Detection. *Analyst* 139 (16), 3885–3894.
- (18) Leonard, H., Halachmi, S., Ben-Dov, N., Nativ, O., and Segal, E. (2017) Unraveling Antimicrobial Susceptibility of Bacterial Networks on Micropillar Architectures Using Intrinsic Phase-Shift Spectroscopy. *ACS Nano* 11 (6), 6167–6177.
- (19) Tsukahara, T. (1968) Electron microscopy of swelling and germinating conidiospores of *Aspergillus niger*. *Med. Mycol.* 6 (3), 185–191.
- (20) Anderson, J. G., and Smith, J. E. (1971) The Production of Conidiophores and Conidia by Newly Germinated Conidia of *Aspergillus niger* (Microcycle Conidiation). *J. Gen. Microbiol.* 69, 185–197.
- (21) Zhou, W., Le, J., Chen, Y., Cai, Y., Hong, Z., and Chai, Y. (2019) Recent Advances in Microfluidic Devices for Bacteria and Fungus Research. *TrAC, Trends Anal. Chem.* 112, 175–195.
- (22) Barrios-Gonzalez, J., Martinez, C., Aguilera, A., and Raimbault, M. (1989) Germination of concentrated suspensions of spores from *Aspergillus niger*. *Biotechnol. Lett.* 11, 551–554.
- (23) Maertens, J. A., Raad, I. I., Marr, K. A., Patterson, T. F., Kontoyannis, D. P., Cornely, O. A., Bow, E. J., Rahav, G., Neofytos, D., Aoun, M., Baddley, J. W., Giladi, M., Heinz, W. J., Herbrecht, R., Hope, W., Karthaus, M., Lee, D.-G., Lortholary, O., Morrison, V. A., Oren, I., Selleslag, D., Shoham, S., Thompson, G. R., Lee, M., Maher, R. M., Schmitt-Hoffmann, A.-H., Zeiher, B., and Ullmann, A. J. (2016) Isavuconazole versus Voriconazole for Primary Treatment of Invasive Mould Disease Caused by *Aspergillus* and Other Filamentous Fungi (SECURE): A Phase 3, Randomised-Controlled, Non-Inferiority Trial. *Lancet* 387 (10020), 760–769.
- (24) Johnson, L. B., and Kauffman, C. A. (2003) Voriconazole: A New Triazole Antifungal Agent. *Clin. Infect. Dis.* 36 (5), 630–637.
- (25) Gray, K. C., Palacios, D. S., Dailey, I., Endo, M. M., Uno, B. E., Wilcock, B. C., and Burke, M. D. (2012) Amphotericin Primarily Kills Yeast by Simply Binding Ergosterol. *Proc. Natl. Acad. Sci. U. S. A.* 109 (7), 2234.
- (26) Mouton, J. W., Meletiadis, J., Voss, A., and Turnidge, J. (2018) Variation of MIC measurements: the contribution of strain and laboratory variability to measurement precision. *J. Antimicrob. Chemother.* 73, 2374–2379.
- (27) European Committee on Antimicrobial Susceptibility Testing (2020) *Routine and extended internal quality control for MIC determination and agar dilution for yeasts and moulds as recommended by EUCAST, version 4.0*, <http://www.eucast.org>.
- (28) European Committee on Antimicrobial Susceptibility Testing (2012) *Voriconazole and Aspergillus spp.: Rationale for the clinical breakpoints, version 1.0*, <http://www.eucast.org>.
- (29) European Committee on Antimicrobial Susceptibility Testing (2012) *Amphotericin B and Aspergillus spp.: Rationale for the clinical breakpoints, version 1.0*, <http://www.eucast.org>.



## **Supporting information:** Antifungal susceptibility testing of *Aspergillus niger* on silicon microwells by intensity-based reflectometric interference spectroscopy

*Christopher Heuer*<sup>†‡⊥</sup>, *Heidi Leonard*<sup>†⊥</sup>, *Nadav Nitzan*<sup>†</sup>, *Ariella Lavy-Alperovitch*<sup>§</sup>, *Naama Massad-Ivanir*<sup>†</sup>, *Thomas Scheper*<sup>‡</sup>, *Ester Segal*<sup>†\*</sup>

<sup>†</sup> Department of Biotechnology and Food Engineering, <sup>§</sup> Department of Biology, Technion – Israel Institute of Technology, Haifa, 3200003, Israel,

<sup>‡</sup> Institute of Technical Chemistry, Leibniz Universität Hannover, 30167 Hannover, Germany.

<sup>⊥</sup> Equal contribution

\* Corresponding Author, Email: [esegal@technion.ac.il](mailto:esegal@technion.ac.il)

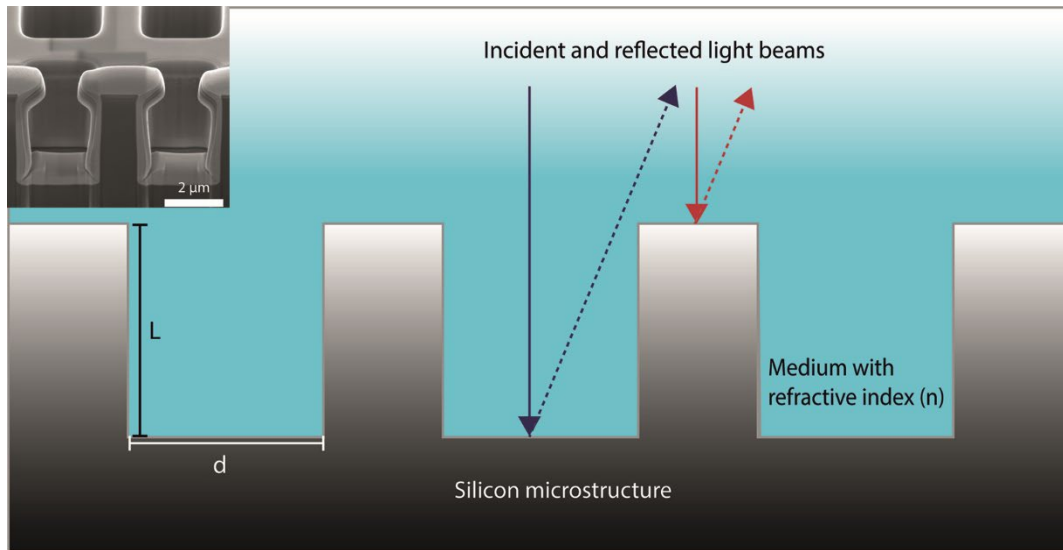


**Figure S1.** Microstructure and reflectance from a photonic silicon chip. Schematic illustration of the photonic gratings and a characteristic cross-sectional SEM image (inset). The grating is composed of silicon and the filling medium is typically a conidia suspension with a refractive index of  $n$  (conidia are not shown in this drawing).  $L$  represents the height of the microtopology and  $d$  is its width. Incident light hits both the bottom of the matrix (blue rays) and the top of the structures (red rays). The optical path difference (OPD) is the product of  $2L$  and the refractive index of the filling medium.

## Results

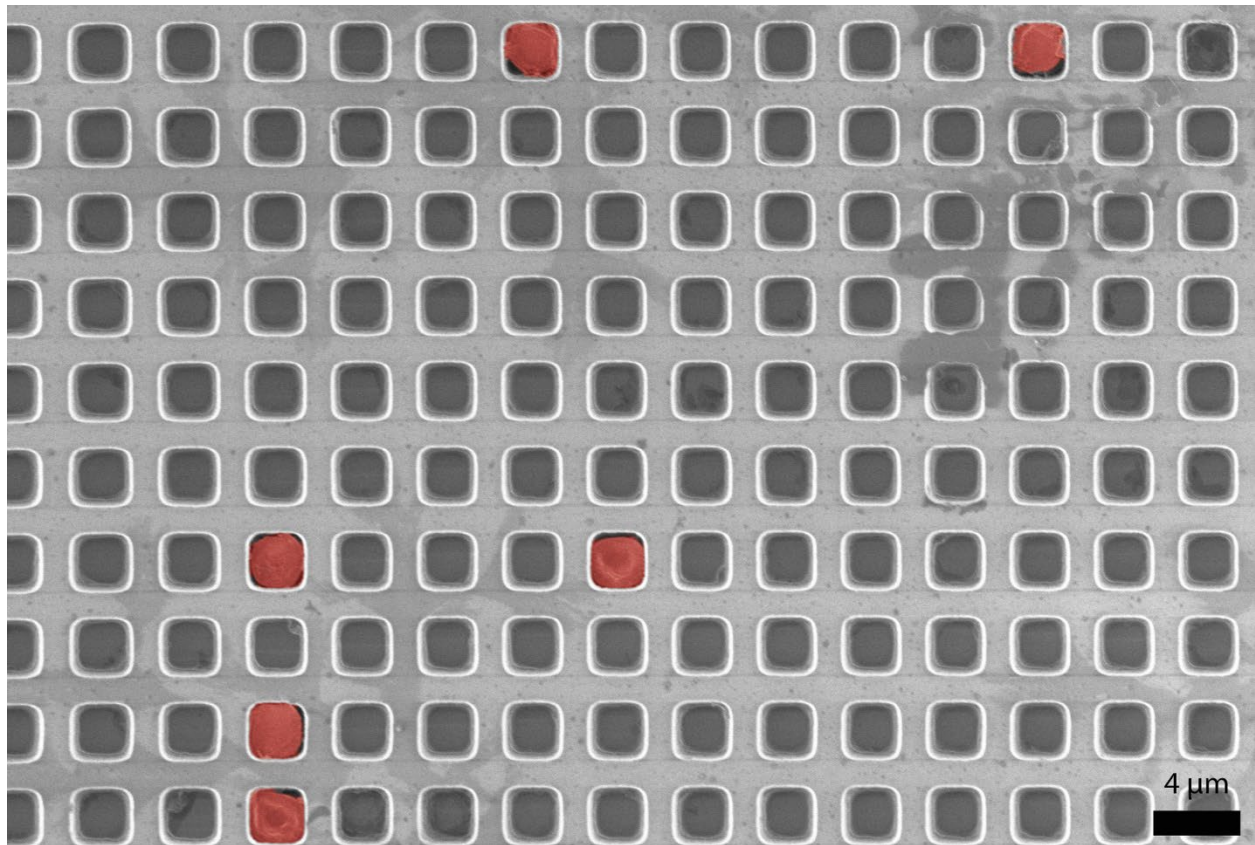


**Figure S2.** The proportion of conidia seeded per well. A representative high-resolution scanning electron microscopy image with six conidia (false-colored for clarity) confined within a total of 150 microwells. A typical proportion of conidia seeded per well is 2-5 conidia per 100 microwells.

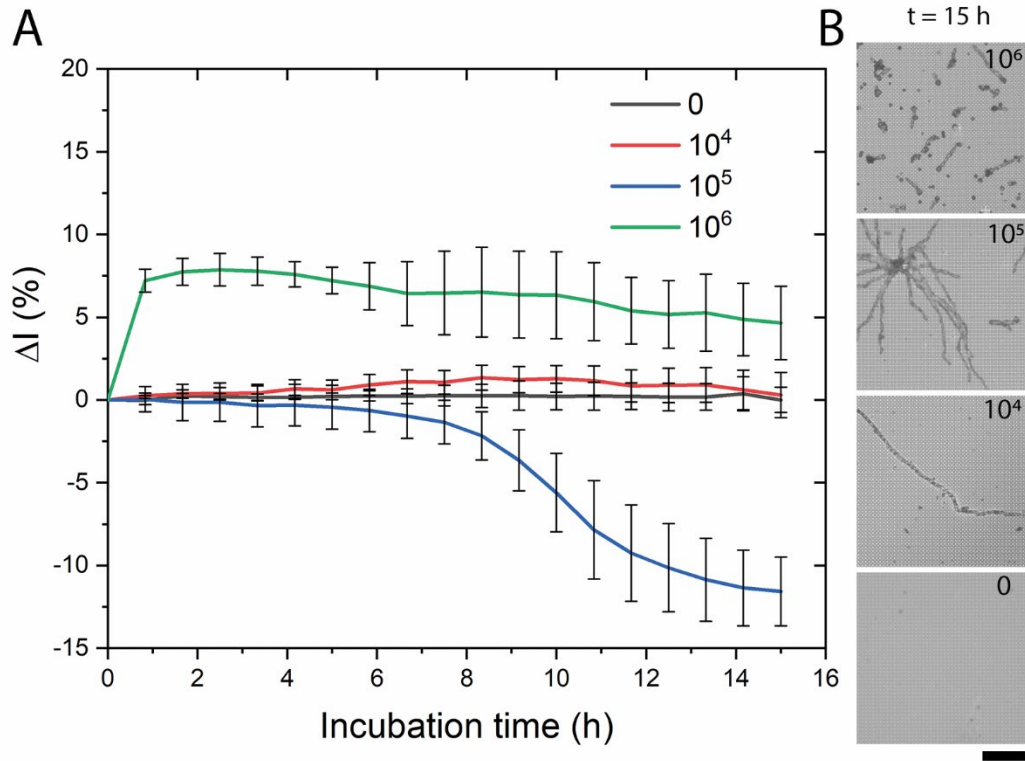


**Figure S3.** iPRISM for monitoring the growth of *Aspergillus niger* at different initial conidia concentrations. (A)  $\Delta I$  (%) over time for conidial seeding suspensions of 0,  $10^4$ ,  $10^5$  and  $10^6$  conidia  $\text{mL}^{-1}$ ; Average and standard deviation for triplicates ( $n=3$ ) were calculated every 50 min. (B) Optical microscope images of *Aspergillus niger* fixed after 15 h of incubation with conidial seeding suspensions of 0,  $10^4$ ,  $10^5$  and  $10^6$  conidia  $\text{mL}^{-1}$ . Black scale bar represents 50  $\mu\text{m}$ .

## Results

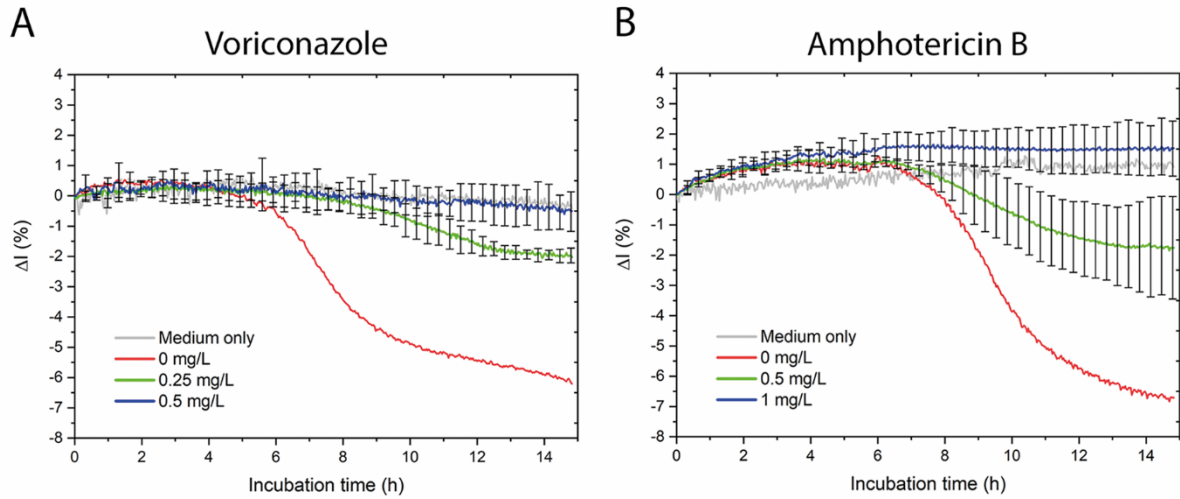


**Figure S4.** Comparison of the MIC and the highest subinhibitory concentration of voriconazole and amphotericin B against *Aspergillus niger* in triplicate ( $n=3$ ). (A) Comparison of the MIC ( $0.5 \text{ mg L}^{-1}$ ) and highest subinhibitory concentration ( $0.25 \text{ mg L}^{-1}$ ) of voriconazole against *Aspergillus niger* according to Figure 3A. (B) Comparison of MIC ( $1 \text{ mg L}^{-1}$ ) and highest subinhibitory concentration ( $0.5 \text{ mg L}^{-1}$ ) of amphotericin B against *Aspergillus niger* according to Figure 3B. T-tests were performed for both drugs after 8, 10 and 12 h of incubation and in the end of the assay ( $\sim 15$  h), showing that the intensity signal for the MIC and the highest subinhibitory concentration are significantly different ( $p < 0.05$ ) for voriconazole and amphotericin B after 12 and 10 h, respectively.

## Results

The ZPrime Score (Z'), based on Zhang et al.<sup>1</sup>, is calculated using the following equation:

$$Z' = 1 - \frac{3 * (\sigma_{MIC} + \sigma_{sub MIC})}{|\mu_{MIC} - \mu_{sub MIC}|}$$

$\sigma_{MIC}$  and  $\sigma_{sub MIC}$  are the standard deviations of the MIC and the first subinhibitory concentration.  $\mu_{MIC}$  and  $\mu_{sub MIC}$  represent the mean (n = 3) of the MIC and the first subinhibitory concentration. The calculated values for voriconazole and amphotericin B are presented in Table S1 using the data in Figure S4.

**Table S1.** ZPrime Score after 10 h, 12h and in the end of the assay (~15 h) for voriconazole and amphotericin B.

<b>Time (h)</b>	<b>ZPrime Score voriconazole</b>	<b>ZPrime Score amphotericin B</b>
<b>10</b>	-3.45	-1.4
<b>12</b>	-0.89	-0.99
<b>15</b>	-0.52	-1.37

**Table S2.** Sequencing result for the forward primer ITSF1.

DNA sequence	
5'	-
TTCCGTAGGTGAACCTGCGGNGGATCATTACCGAGTGCGGGTCCTTTGGGCCCCAACCTCCC	
ATCCGTG	
TCTATTGTACCCTGTTGCTTCGGCGGGCCCGCCGCTTGTCGGCCGCCGGGGGGGCGCCTCT	
GCCCCCGGGCCCGTGCCC	
GCCGGAGACCCCAACACGAACACTGTCTGAAAGCGTGCAGTCTGAGTTGATTGAATGCAA	
TCAGTTAAACTTTCAACAA	
TGGATCTCTTGGTTCCGGCATCGATGAAGAACGCAGCGAAATGCGATAACTAATGTGAAT	
TGCAGAATTCAGTGAATCAT	
CGAGTCTTTGAACGCACATTGCGCCCCCTGGTATTCCGGGGGGCATGCCTGTCCGAGCGTC	
ATTGCTGCCCTCAAGCCCG	
GCTTGTGTGTTGGGTCGCCGTCCCCCTCTCCGGGGGGACGGGCCCGAAAGGCAGCGGCGG	
CACCGCGTCCGATCCTCGAG	
CGTATGGGGCTTTGTCACATGCTCTGTAGGATTGGCCGGCGCCTGCCGACGTTTTCCAACC	
ATTCTTTCCAGGTTGACCT	
CGGATCAGGTAGGGATAACCGCTGAACTTAAGCATATCAATAAGCGGGAGGAA - 3'	

**Protocol for species identification by Internal transcribed spacer (ITS) regions:**

**DNA extraction.** *Aspergillus niger* isolate HCN 18 was grown overnight at room temperature in liquid potato dextrose yeast extract casein hydrolysate medium (PDYC, 24 g L<sup>-1</sup> potato dextrose broth, 2 g L<sup>-1</sup> yeast extract and 1.2 g L<sup>-1</sup> casein hydrolysate, all Difco, USA) in a petri dish without

## Results

shaking. For DNA extraction two full spatulas of the mycelium were transferred to a clean tube with 100  $\mu$ L Zirconia/Silica beads (Biospec Products, Inc., USA) and 500  $\mu$ L DNA extraction buffer (200 mM tris(hydroxymethyl)aminomethane hydrochloride (Tris HCl, Sigma Aldrich, Israel), 0,5 % sodium dodecyl sulfate (SDS, Thermo Scientific, USA), 25 mM ethylenediaminetetraacetic acid (EDTA, Sigma Aldrich, Israel), 250 mM NaCl (Merck, Germany) and mixed for one minute on a vortex mixer (Scientific Industries, Inc., USA). The sample was incubated for 30 min at room temperature and centrifuged for 10 min at 4 °C and 12500 rpm (Centrifuge 5417R, Eppendorf AG, Germany). The supernatant was transferred to a clean tube, and an equal volume of isopropanol was added. The sample was incubated for 20 minutes at -20 °C and afterward centrifuged at 13000 rpm for 2 min. Subsequently, the supernatant was discarded, and the resulting pellet was washed with 1 mL 70 % ethanol followed by centrifugation at 13000 rpm for 2 min. The supernatant was rejected again, and the pellet was left for drying for around 1 h and resuspended in 50  $\mu$ L of sterile double distilled water. The concentration of the genomic DNA was determined by using a Nanodrop one (Thermo Scientific, USA) resulting in a concentration of 56.4 ng/ $\mu$ L with an A260:A280 ratio of 1.85.

**PCR Amplification of ITS.** Species identification of isolate HCN 18 was carried out by sequencing the ITS1 and ITS2 internal transcribed spacer regions by using the primers ITS1F (5'-CTTGGTCATTTAGAGGAAGTAA-3') and ITS4 (5'-TCCTCCGCTTATTGATATGC-3').<sup>2</sup> PCR amplification reaction mixtures contained 1 x PCR buffer, 0.2 mM premixed dNTP's, 1.25 U of Takara Taq™ Polymerase (all Takara, Japan), 1  $\mu$ M ITS1F and ITS4 primers and 50 ng genomic DNA in a total volume of 25  $\mu$ L. For non-template control the PCR reaction mixture contained all the components as mentioned above but no genomic *Aspergillus* DNA. PCR amplification was carried out in a biometra TGradient Thermocycler (Analytik Jena, Germany)



## Results

using an initial denaturation step at 94 °C for 2 min, followed by 29 cycles at 94 °C for 30 s, 55 °C for 30 s and 72 °C for 30 s, with a final extension for 2 min at 72 °C. Successful amplification was confirmed after standard electrophoresis in a 1 % agarose gel by visualizing the PCR product under UV light by using the SimplySafe™ dye (EURx, Poland). The PCR fragment was extracted from the gel by using a DNA gel extraction kit (AccuPrep Gel Purification Kit, Bioneer, South Korea) and sent to Hylabs (Israel) for sequencing by using an ABI 3730xl DNA Analyzer (Thermo Scientific, USA). Sequence alignment was done using the nucleotide-nucleotide BLAST search algorithm BLASTn, at the NCBI website (<https://blast.ncbi.nlm.nih.gov/Blast.cgi>). The species was identified as *Aspergillus niger* (NCBI Accession number: MK182796.1).

## REFERENCES

- (1) Zhang; Chung; Oldenburg. A Simple Statistical Parameter for Use in Evaluation and Validation of High Throughput Screening Assays. *Journal of biomolecular screening* **1999**, *4*, 67–73
- (2) White, T. J.; Bruns, T.; Lee, S.; Taylor, J. Amplification and Direct Sequencing of Fungal Ribosomal RNA Genes for Phylogenetics. *PCR Protoc. Guide Methods Appl.* **1990**, *18* (1), 315–322.

## 5.2 Photonic Si Microwell Architectures for Rapid Antifungal Susceptibility Determination of *Candida auris*

This section is reproduced from the research article “*Photonic Si Microwell Architectures for Rapid Antifungal Susceptibility Determination of Candida auris*”, published in the peer-reviewed journal *Chemical Communications*.

### “Photonic Si Microwell Architectures for Rapid Antifungal Susceptibility Determination of *Candida auris*”

Christopher Heuer, Xin Jiang, Gali Ron, Orna Ternyak, Thomas Scheper, Janina Bahnemann and Ester Segal

*Chemical Communications* (2024)

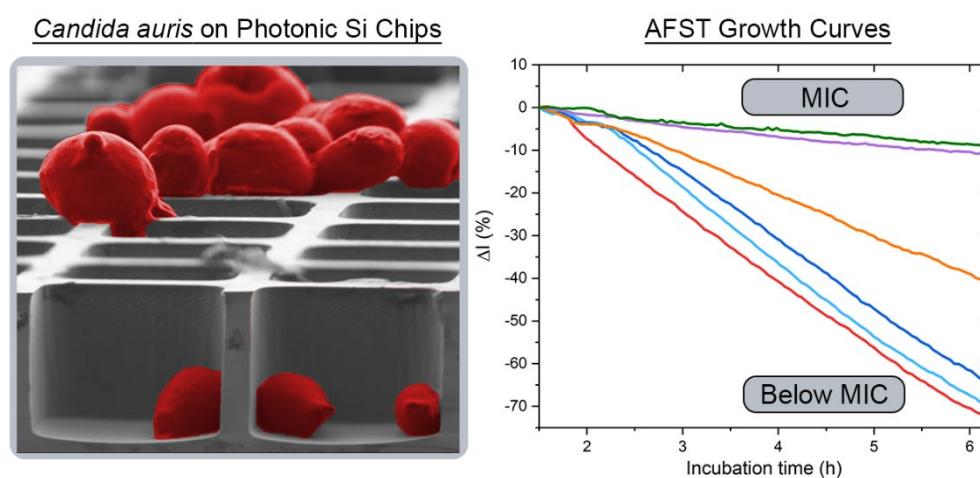


**Figure 6** Graphical abstract of the research article “Photonic Si Microwell Architectures for Rapid Antifungal Susceptibility Determination in *Candida auris*”.

The article addresses the second research aim and explains how the iPRISM assay is extended and employed for a rapid AFST of the emerging yeast pathogen *C. auris*. This fungal species is recognized for its morbidity and mortality in hospitalized patients and is considered an urgent global threat to healthcare settings as clinical isolates of this species frequently develop antifungal resistance.<sup>13,38,41,42</sup>

In this work, the microwell structure has been rationally designed and enlarged (width:  $\sim 4 \mu\text{m}$ , depth:  $\sim 4 \mu\text{m}$ ) as compared to the previous study to allow confinement of the *C. auris* cells within the

## Results

microstructure. For iPRISM-based AFST, the yeast cells were exposed to varying concentrations of two clinically-relevant antifungals (anidulafungin: inhibition of cell wall synthesis and amphotericin B: cell membrane damage), and growth was monitored by detecting intensity changes. MIC determination was feasible within 3.5 and 6 h for anidulafungin and amphotericin B, respectively, and thus, iPRISM accelerates the AFST by >18 h as compared to the standard BMD, which typically requires 24 h.

Besides observing intensity changes, a second parameter – namely the  $2nL$  ( $n$  = refractive index of a medium within the microstructure;  $L$  = height of the microstructure) was tracked by PRISM. Strong fungal growth where the yeast cells formed dense aggregates on top of the microstructure caused a decrease in this parameter, different from previous studies dealing with bacterial species where their colonization within the microwells typically leads to a  $2nL$  increase. These findings emphasize that photonic silicon chips can potentially be used to identify or differentiate between microorganisms by their distinct growth behaviours, which can be correlated to characteristic  $2nL$  changes. Such a feature could be beneficial for the current clinical AST/AFST workflow, where species identification is a prerequisite that precedes susceptibility testing.

In the following article, “*Photonic Si Microwell Architectures for Rapid Antifungal Susceptibility Determination in Candida auris*”, the results are presented and discussed in detail.



Cite this: DOI: 10.1039/d3cc04446g

 Received 7th September 2023,  
Accepted 18th December 2023

DOI: 10.1039/d3cc04446g

rsc.li/chemcomm

## Photonic Si microwell architectures for rapid antifungal susceptibility determination of *Candida auris*†

 Christopher Heuer,<sup>id abc</sup> Xin Jiang,<sup>id a</sup> Gali Ron,<sup>a</sup> Orna Ternyak,<sup>d</sup>  
Thomas Scheper,<sup>b</sup> Janina Bahnmann<sup>id c</sup> and Ester Segal<sup>id \*a</sup>

**We present the application of a photonic silicon chip-based optical sensor system for expeditious and phenotypic antifungal susceptibility testing. This label-free diagnostic assay optically monitors the growth of *Candida auris* at varying antifungal concentrations on a microwell-structured silicon chip in real-time, and antifungal susceptibility is detected within 6 h, four times faster than in the current gold standard method.**

In recent years, multidrug-resistant fungal pathogens have emerged as a global health threat, with high mortality rates resulting in over 1.6 million deaths annually.<sup>1,2</sup> The severity of this situation is underscored by the World Health Organization's first-ever fungal priority pathogens list published in 2022, aiming to guide public health strategies against pathogenic fungi.<sup>3</sup> The excessive use of antifungals, together with climate change, accelerates the emergence and evolution of resistant fungal pathogens.<sup>4,5</sup> The spread of fungal infections in the last three years is mainly ascribed to the increasing number of immunocompromised and vulnerable patients,<sup>3</sup> which is closely linked to the COVID-19 pandemic.<sup>6</sup> The yeast *Candida auris* (*C. auris*), well known for its pathogenicity and associated morbidity, is now classified as an urgent threat by the United States Centers for Disease Control and Prevention.<sup>7</sup> *C. auris* is not only difficult to eradicate from clinical settings but is often multidrug-resistant, with some isolates being recognized as pan-resistant (resistant to antifungals of all drug classes).<sup>3,8</sup> Thus, there is a paramount need for diagnostic methods that can expeditiously determine the correct antifungal prescription,

improving therapy outcomes and minimizing the spread of resistance.<sup>9</sup> Specifically, antifungal susceptibility testing (AFST), in which pathogenic fungi are exposed to varying antifungals at increasing concentrations, and the minimum inhibitory concentration (MIC) is determined, can help physicians to guide treatment decisions.<sup>10</sup> However, current AFST methods, like agar-based tests or the gold standard broth microdilution (BMD), are lengthy and require > 24 h.<sup>10</sup> Also, commercially available state-of-the-art automated methods such as the Vitek2 (bioMérieux) typically provide results only within 12–18 h,<sup>11,12</sup> a limited set of antifungals is available, and MIC values have not always been accurately determined.<sup>13</sup> Thus, there is an urgent clinical need for rapid and reliable novel AFST methods for *Candida* species.

Herein, we present the use of a photonic silicon chip with microwell diffraction gratings that serves as a sensitive sensor for label-free fungal growth monitoring by detecting changes in white light reflectance. Such silicon-based materials are characterized by their biocompatibility and have been widely employed for diagnostic, therapeutic and biosensing applications.<sup>14–16</sup> Specifically, we have previously shown that photonic silicon chips, with different dimensions and microtopologies,<sup>17</sup> can be used for rapid susceptibility testing of the bacterial species *Escherichia coli* (*E. coli*) within 90 minutes<sup>18–20</sup> and the mould *Aspergillus niger* (*A. niger*) within 10–12 h<sup>21</sup> using phase-shift reflectometric interference spectroscopic measurements (PRISM) and intensity-based PRISM (iPRISM) tests. In these optical assays, the photonic silicon chips are individually fixated into heat-controlled microfluidic channels, and suspensions of yeast cells in growth medium are introduced into these channels (see Fig. 1A). The chips consist of arrays of microwells (width: ~4 μm and depth: ~4 μm) that were specifically designed to fit the majority of *C. auris* cells (having spherical to oval shape with characteristic dimensions of 2–3 × 2.5–5 μm<sup>22</sup>) within the individual wells, see Fig. 1B-i for cross-section and top view (insert) scanning electron microscopy (SEM) images. Yet, *C. auris* can also form cell aggregates which are mainly found on top of the microwells. Continuous reflectance measurements are used to obtain characteristic spectra (Fig. 1B-ii), which are further processed by Fast Fourier

<sup>a</sup> Department of Biotechnology and Food Engineering, Technion – Israel Institute of Technology, Haifa, 3200003, Israel. E-mail: esegal@technion.ac.il

<sup>b</sup> Institute of Technical Chemistry, Leibniz University Hannover, Hannover 30167, Germany

<sup>c</sup> Institute of Physics, University of Augsburg, Augsburg 86159, Germany

<sup>d</sup> Micro- and Nanofabrication and Printing Unit, Technion – Israel Institute of Technology, Haifa, 3200003, Israel

† Electronic supplementary information (ESI) available. See DOI: <https://doi.org/10.1039/d3cc04446g>



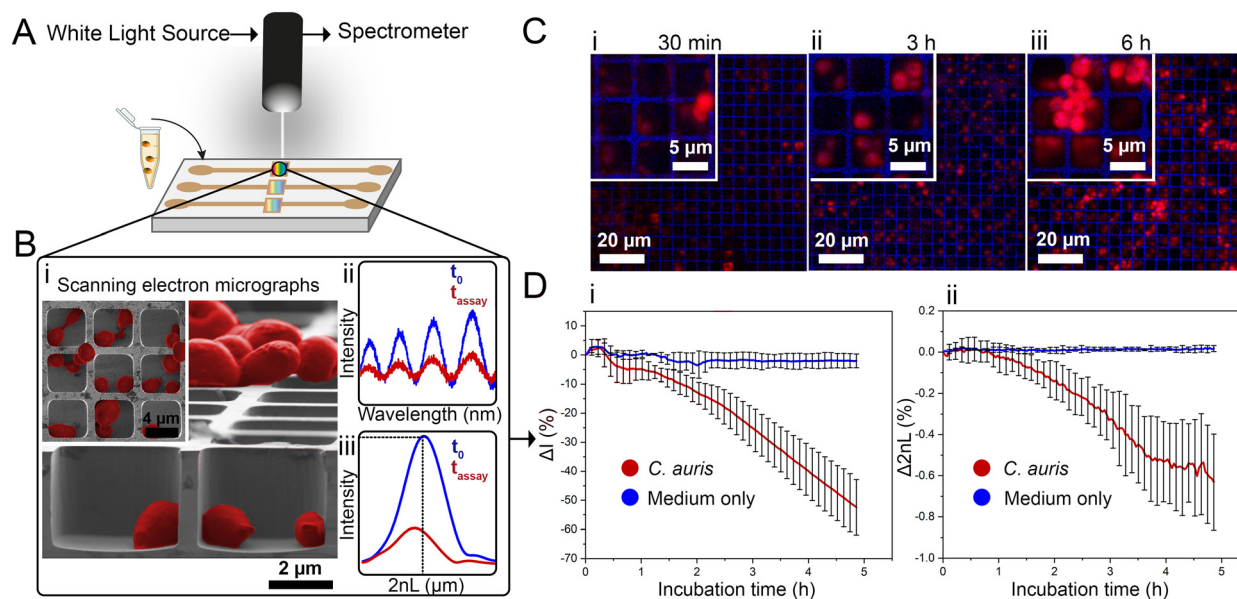


**Fig. 1** iPRISM concept for *C. auris* growth monitoring. (A) Suspensions of *C. auris* cells in growth medium (RPMI) are introduced onto a photonic silicon chip, having a periodic microwell array structure, fixated within microfluidic channels (channels height  $\sim 1$  mm allowing for cells suspensions, growth medium and antifungal solution to flow on top of the microwells). The chip microstructure is specifically designed to (B-i) accommodate *C. auris* cells within the microwells as demonstrated by top view and cross section (insert) SEM micrographs. Cells are false-coloured in red for clarity. A white light source is positioned normal to the chips and illuminates the sensor elements, while the reflected light is continuously recorded. (B-ii) The resulting reflectance spectra show characteristic interference fringes, as the incident light is reflected from the top and bottom interfaces of the microwell arrays. The latter spectra are recorded and transformed into (B-iii) single peaks by frequency analysis. The amplitude of the peak corresponds to the intensity of the reflected light and the peak position correlates to the  $2nL$ . (C) Confocal laser scanning microscopy after cell staining with propidium iodide reveals *C. auris* cells (initial cell density: McFarland 2.0) growing within and on top of the silicon microstructure resulting in characteristic growth curves with a continuous averaged ( $n = 3$ ) decrease of the (D-i) intensity and (D-ii)  $2nL$  signals. Error bars depict standard deviations.

Transform (FFT) frequency analysis. The latter results in a single peak (Fig. 1B-iii), where the peak amplitude corresponds to the intensity of the reflected light and the peak position corresponds to  $2nL$  ( $n$  refers to the refractive index of a medium within the grating and  $L$  is the microwells' depth). Please also refer to Fig. S1 (ESI $\dagger$ ) and to our previous works<sup>19,23,24</sup> for a detailed explanation of the involved optical principles.

Monitoring both parameters over time allows tracking *C. auris* growth in a label-free manner in real-time. Fig. 1D depicts growth curves (intensity and  $2nL$ ) for *C. auris* suspensions at McFarland value of 2.0 (which corresponds to  $\sim 10^7$  cells  $\text{mL}^{-1}$ , as routinely used for AFST of *Candida* species by commercial automated systems such as the Vitek2;<sup>12</sup> for experimental details and further discussion on *C. auris* cell density see the ESI $\dagger$ , Fig. S2). For both parameters, a general trend of decreasing signals (intensity slope:  $-10.8 \Delta I (\%) \text{h}^{-1}$  and  $2nL$  slope:  $-0.13 \Delta 2nL (\%) \text{h}^{-1}$ ) is observed (see Fig. 1D-i and ii). The major decrease in the intensity signal is ascribed to *C. auris* cells growing on the microstructured silicon surface<sup>19,23</sup> and Fig. S3 (ESI $\dagger$ ) depicts the correlation between cell concentrations and the obtained intensity signal (Fig. S4 (ESI $\dagger$ ) presents the corresponding raw reflectance spectra). Fig. 1C shows corresponding confocal laser scanning micrographs of *C. auris* at different time points (30 min, 3 h, 6 h), demonstrating that at the beginning of the assay, most cells reside within the microwells. Whereas at later times, the cells tend to grow out of the wells and are found on the top of the microstructure, as also

revealed by SEM studies presented in Fig. S5 (ESI $\dagger$ ). Moreover, similar behaviour is also observed for a second yeast species – the industrial-relevant *Saccharomyces cerevisiae* where a characteristic reduction in both intensity and  $2nL$  signals is obtained, see Fig. S6 (ESI $\dagger$ ).

While the observed intensity decrease is in agreement with our previous studies, where varying microorganisms were grown on microstructured silicon gratings,<sup>17,19,21</sup> the obtained trend of  $2nL$  reduction (Fig. 1D-ii) is different from the typical behaviour we have observed for bacteria.<sup>19,21</sup> In general, we found that bacterial cells tend to reside and proliferate within the microwell structure (see Fig. S7, ESI $\dagger$ ) and, as such, induce an increase in the  $2nL$  value over time. The latter is ascribed to an increase in the average refractive index within the microstructure.<sup>17–19</sup> We were expecting a similar behaviour for *C. auris*, as most cells are found to reside in the wells at the beginning of the assay. Yet, within 6 h *C. auris* forms dense cell aggregates on the top of the microstructure, as depicted in the electron micrographs included in Fig. S5 (ESI $\dagger$ ). To further investigate this behaviour, *C. auris* was studied in a growth medium designated for bacteria (CAMHB), where growth is observed to be impaired compared to that in RPMI (designated for yeasts). The slope of the intensity signal is found to be five times lower in CAMHB, while the  $2nL$  slope is mainly unchanged, see Fig. S8 (ESI $\dagger$ ). Moreover, SEM studies show that *C. auris* do not form aggregates on top of the silicon microstructure in CAMHB, as also depicted in Fig. S8 (ESI $\dagger$ ).



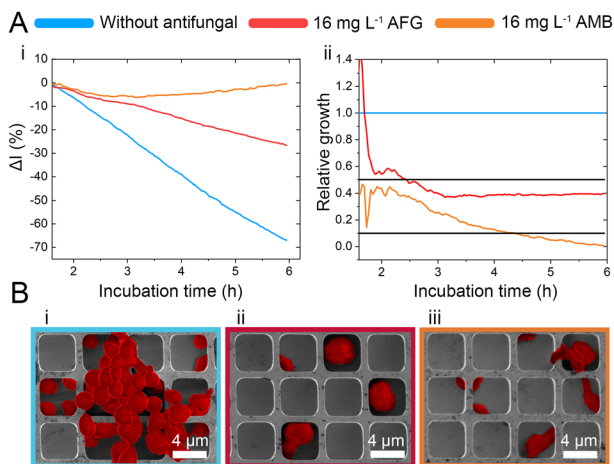


**Fig. 2** iPRISM "overkill" experiments. (A-i) iPRISM growth curves for unhindered growth and *C. auris* exposed to 16 mg L<sup>-1</sup> anidulafungin (AFG) and amphotericin B (AMB), respectively. These growth curves are transformed into relative growth where the unhindered growth is defined as 100% (1.0) growth. Black threshold lines indicate 50% (0.5) and 10% (0.1) growth. (B-i to B-iii) Scanning electron microscopy images reveal how *C. auris* behaves on the microstructure in the absence and presence of high antifungal concentrations. Cells are false-coloured in red for clarity.

This may suggest that the cells emerging from the wells and forming dense cell clusters on the top of the microstructure potentially impede light interference from the chip, resulting in a reduction of the  $2nL$  signal. However, this phenomenon should be further investigated as we also observed it in the case of biofilm formation by the bacterial pathogen *Pseudomonas aeruginosa*.<sup>17</sup> Herein, we will mainly focus on monitoring the intensity changes for sensitive growth detection at varying antifungal concentrations, following the iPRISM assay principle.<sup>21</sup> The iPRISM concept for AFST of *C. auris* was first established with high antibiotic concentrations (see Fig. 2) of two clinically relevant antifungal agents with different modes of action, namely anidulafungin (echinocandin: inhibition of cell wall biosynthesis)<sup>25</sup> and amphotericin B (polyene: cell membrane damage).<sup>26,27</sup> The tested concentrations of these drugs (both 16 mg L<sup>-1</sup>) are at the upper range of the recommended concentrations for AFST of *Candida* species according to BMD protocols by the European Society of Antimicrobial Susceptibility Testing (EUCAST).<sup>28</sup> Thus, fungal growth is inhibited at these concentrations (Fig. 2A-i), and the relative growth compared to the drug-free control falls below the 50% (anidulafungin) and 10% (amphotericin B) growth values, as depicted in Fig. 2A-ii. The latter values also serve as the MIC threshold for these respective antifungals (anidulafungin MIC: lowest drug concentration with  $\geq 50\%$  growth inhibition and amphotericin B MIC: lowest drug concentration with  $\geq 90\%$  growth inhibition) according to EUCAST.<sup>28</sup> Scanning electron micrographs (Fig. 2Bi-iii) reveal that in the absence of an antifungal drug, *C. auris* grow in dense networks within and on top of the silicon microstructure, while when exposed to an antifungal, fewer cells are observed on the chip surface (Fig. 2B-ii and iii). Moreover, cells exposed to anidulafungin (Fig. 2B-ii) appear round and swollen – characteristic of morphological changes induced by this type of antifungal agent.<sup>29</sup> In the case of amphotericin B,

cells exhibit a deformed appearance, which is ascribed to cell membrane damage (Fig. 2B-iii).<sup>30</sup>

*C. auris* cells were grown at various concentrations of anidulafungin and amphotericin B in order to determine MIC values, and Fig. 3 depicts the corresponding relative growth curves. Increased concentrations of both antifungal agents result in reduced growth compared to the untreated control. According to the MIC definitions (as explained above), the iPRISM MIC values are 0.25 mg L<sup>-1</sup> for both drugs. Statistical analysis of iPRISM results obtained from different chips (as shown in Fig. S9, ESI<sup>†</sup>) reveals that MIC value determination is feasible within 3.5 h and 6 h for anidulafungin and amphotericin B, respectively. Thus, the iPRISM platform provides a significantly reduced assay time compared to the gold-standard BMD (time: 24 h) and the commercially available Vitek2 system (time: 12–18 h).<sup>11,12,28</sup> Please also refer to Fig. S11 (ESI<sup>†</sup>), demonstrating that standard BMD-based MIC

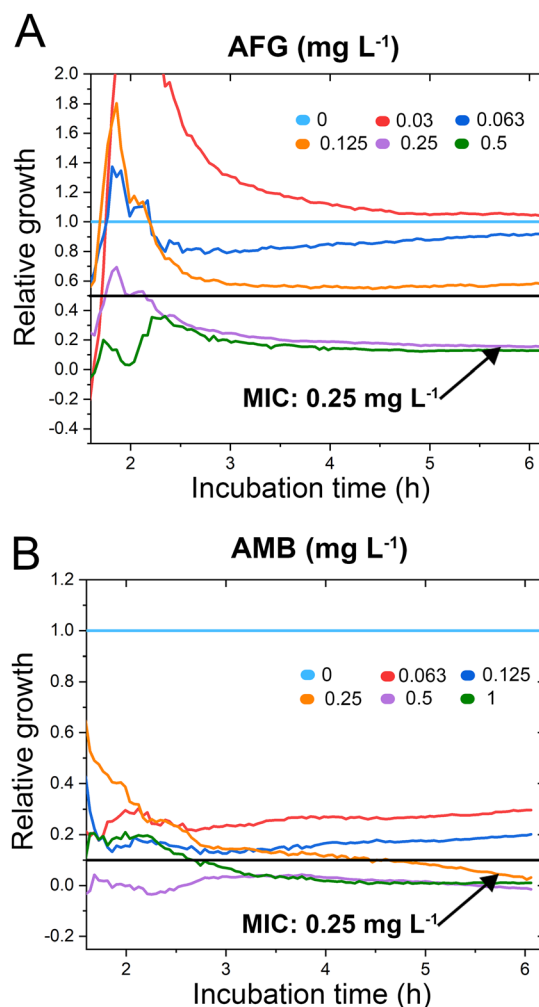


**Fig. 3** *C. auris* iPRISM AFST. Relative growth of *C. auris* at varying concentrations of (A) anidulafungin (AFG) and (B) amphotericin B (AMB). The underlying intensity changes and also the corresponding  $2nL$  growth curves are presented in Fig. S10 (ESI<sup>†</sup>), demonstrating that the intensity is superior in its quantitative sensitivity for growth at varying antifungal concentrations while the  $2nL$  is still sensitive qualitatively.



value determination (*C. auris* and amphotericin B) can be reduced to 19 h using continuous microplate reader measurements and statistical analysis. Thus, the presented iPRISM assay still provides a significantly faster MIC determination.

To test the accuracy of the obtained MIC values, we compare the latter concentrations to the outcome of gold standard BMD performed according to EUCAST protocols, see Table S1 in the ESI.† The iPRISM MIC values for anidulafungin (0.25 mg L<sup>-1</sup> vs. 0.0625 mg L<sup>-1</sup>) and amphotericin B (0.25 mg L<sup>-1</sup> vs. 0.125–0.25 mg L<sup>-1</sup>) are one to two dilutions higher than the BMD value. Such a difference between two dilutions is considered as an essential agreement.<sup>31</sup> Furthermore, the obtained MIC values do not exceed the tentative epidemiological cut-off values (ECOFFs) determined by different approaches (Table S1, ESI†).<sup>32</sup> As such, for both drugs, this *C. auris* isolate is correctly classified into the wild-type population without acquired drug resistance. It should be noted that MIC value deviations between different methods and protocols are often encountered in susceptibility testing.<sup>33</sup> As previously observed, MIC values determined by (i)PRISM for *E. coli*<sup>18,19</sup> and *A. niger*<sup>21</sup> tend to be higher in comparison to BMD MICs. These deviations are mainly ascribed to the different assay procedures. While in the BMD, the fungal cells are suspended and grow in a liquid medium, in the iPRISM assay, the behaviour of the cell-silicon substrate interface is monitored.

A diagnostic platform for rapid and phenotypic AFST of *C. auris* as a model yeast pathogen is shown, demonstrating and extending the applicability of this label-free assay to a wide variety of clinically relevant species (bacteria, filamentous fungi, yeast). The yeast cells grow on a microstructured silicon surface that also serves as a sensitive sensing element allowing the detection of changes in the white light reflectivity. The latter changes are correlated to fungal growth and used to study the behaviour of *C. auris* upon exposure to anidulafungin and amphotericin B – two clinically relevant antifungals from two distinct antifungal classes. MIC values for these antifungals can be obtained within 6 h and agree with values determined by classical BMD. Thus, iPRISM provides a novel method for AFST of *Candida* species that is significantly faster (time reduction: ≥18 h) than gold standard methods.

This work was supported by the Israel Science Foundation (grant No. 2458/21). We also acknowledge funding by the German Research Foundation (DFG) via the Emmy Noether program (project ID346772917), and grant SCHE 279/32-2, as well as by the VolkswagenStiftung via the program “Niedersächsisches Vorab: Research Cooperation Lower Saxony—Israel”. The authors thank the staff of the Micro- and Nanofabrication and Printing Unit (MNFPU) at the Technion for the fabrication of the photonic silicon chips.

## Conflicts of interest

There are no conflicts to declare.

## References

- 1 K. Benedict, M. Richardson, S. Vallabhaneni, B. R. Jackson and T. Chiller, *Lancet Infect. Dis.*, 2017, **17**, e403–e411.
- 2 A. Rokas, *Nat. Microbiol.*, 2022, **7**, 607–619.
- 3 WHO fungal priority pathogens list to guide research, development and public health action, <https://www.who.int/publications/i/item/978924006024>, (accessed March 2023).
- 4 U. Hofer, *Nat. Rev. Microbiol.*, 2019, **17**, 588.
- 5 N. A. R. Gow, C. Johnson, J. Berman, A. T. Coste, C. A. Cuomo, D. S. Perlin, T. Bicanic, T. S. Harrison, N. Wiederhold, M. Bromley, T. Chiller and K. Edgar, *Nat. Commun.*, 2022, **13**, 5352.
- 6 CDC special report 2022: COVID-19 U.S. impact on antimicrobial resistance.
- 7 CDC report: antibiotic resistance threats in the United States 2019.
- 8 B. O'Brien, J. Liang, S. Chaturvedi, J. L. Jacobs and V. Chaturvedi, *Lancet Microbe*, 2020, **1**, e193–e194.
- 9 D. S. Perlin, R. Rautemaa-Richardson and A. Alastruey-Izquierdo, *Lancet Infect. Dis.*, 2017, **17**, e383–e392.
- 10 C. Heuer, J. Bahnmann, T. Scheper and E. Segal, *Small methods*, 2021, **5**, 2100713.
- 11 M. Cuenca-Estrella, A. Gomez-Lopez, A. Alastruey-Izquierdo, L. Bernal-Martinez, I. Cuesta, M. J. Buitrago and J. L. Rodriguez-Tudela, *J. Clin. Microbiol.*, 2010, **48**, 1782.
- 12 E. Borghi, R. Iatta, R. Sciota, C. Biassoni, T. Cuna, M. T. Montagna and G. Morace, *J. Clin. Microbiol.*, 2010, **48**, 3153–3157.
- 13 S. Kathuria, P. K. Singh, C. Sharma, A. Prakash, A. Masih, A. Kumar, J. F. Meis and A. Chowdhary, *J. Clin. Microbiol.*, 2015, **53**, 1823–1830.
- 14 Y. Chen, M. Alba, T. Tieu, Z. Tong, R. Singh Minhas, D. Rudd, N. H. Voelcker, A. Cifuentes-Rius and R. Elnathan, *Adv. NanoBiomed Res.*, 2021, **1**, 2100002.
- 15 T. Tieu, M. Alba, R. Elnathan, A. Cifuentes-Rius and N. H. Voelcker, *Adv. Ther.*, 2018, **2**, 1800095.
- 16 C. Pacholski, *Sensors*, 2013, **13**, 4694–4713.
- 17 H. Leonard, X. Jiang, S. Arshavsky-Graham, L. Holtzman, Y. Haimov, D. Weizman, S. Halachmi and E. Segal, *Nanoscale Horiz.*, 2022, **7**, 729–742.
- 18 C. Heuer, J.-A. Preuss, M. Buttkewitz, T. Scheper, E. Segal and J. Bahnmann, *Lab Chip*, 2022, **22**, 4950–4961.
- 19 H. Leonard, S. Halachmi, N. Ben-Dov, O. Nativ and E. Segal, *ACS Nano*, 2017, **11**, 6167–6177.
- 20 X. Jiang, T. Borkum, S. Shprits, J. Boen, S. Arshavsky-Graham, B. Rofman, M. Strauss, R. Colodner, J. Sulam, S. Halachmi, H. Leonard and E. Segal, *Adv. Sci.*, 2023, e2303285.
- 21 C. Heuer, H. Leonard, N. Nitzan, A. Lavy-Alperovitch, N. Massad-Ivanir, T. Scheper and E. Segal, *ACS Infect. Dis.*, 2020, **6**, 2560–2566.
- 22 J. Osei Sekyere, *MicrobiologyOpen*, 2018, **7**, e00578.
- 23 Y. Mirsky, A. Nahor, E. Edrei, N. Massad-Ivanir, L. M. Bonanno-Young, E. Segal and A. Sa'ar, *Appl. Phys. Lett.*, 2013, **103**, 033702.
- 24 N. Massad-Ivanir, Y. Mirsky, A. Nahor, E. Edrei, L. M. Bonanno-Young, N. Ben Dor, A. Sa'ar and E. Segal, *Analyst*, 2014, **139**, 3885–3894.
- 25 J. A. Vazquez and J. D. Sobel, *Clin. Infect. Dis.*, 2006, **43**, 215.
- 26 A. Zumbuehl, D. Jeannerat, S. E. Martin, M. Sohrmann, P. Stano, T. Vigassy, D. D. Clark, S. L. Hussey, M. Peter, B. R. Peterson, E. Pretsch, P. Walde and E. M. Carreira, *Angew. Chem.*, 2004, **116**, 5293–5297.
- 27 S. L. Regen, *JACS Au*, 2021, **1**, 3–7.
- 28 EUCAST DEFINITIVE DOCUMENT E.DEF 7.3.2 Method for the determination of broth dilution minimum inhibitory concentrations of antifungal agents for yeasts.
- 29 N. Yagüe, L. Gómez-Delgado, M. Á. Curto, V. S. D. Carvalho, M. B. Moreno, P. Pérez, J. C. Ribas and J. C. G. Cortés, *Pharmaceuticals*, 2021, **14**, 1332.
- 30 E. Grella, A. Zdybicka-Barabas, B. Pawlikowska-Pawlega, M. Cytrynska, M. Włodarczyk, W. Grudzinski, R. Luchowski and W. I. Gruszecki, *Sci. Rep.*, 2019, **9**, 17029.
- 31 N. P. Wiederhold, *Open Forum Infect. Dis.*, 2021, **8**, ofab444.
- 32 M. C. Arendrup, A. Prakash, J. Meletiadis, C. Sharma and A. Chowdhary, *Antimicrob. Agents Chemother.*, 2017, **61**, e00485-17.
- 33 C. B. Terwee, L. D. Roorda, J. Dekker, S. M. Bierma-Zeinstra, G. Peat, K. P. Jordan, P. Croft and H. C. W. de Vet, *J. Clin. Epidemiol.*, 2010, **63**, 524–534.



## Supplementary Information

### Photonic Si Microwell Architectures for Rapid Antifungal Susceptibility Determination of *Candida auris*

Christopher Heuer<sup>a,b,c</sup>, Xin Jiang<sup>a</sup>, Gali Ron<sup>a</sup>, Orna Ternyak<sup>d</sup>, Thomas Scheper<sup>b</sup>, Janina Bahnemann<sup>c</sup> and Ester Segal<sup>a\*</sup>

a Department of Biotechnology and Food Engineering, Technion – Israel Institute of Technology, 320003 Haifa, Israel, \*email: esegal@tecchnion.ac.il

b Institute of Technical Chemistry, Leibniz University Hannover, 30167 Hannover, Germany

c Institute of Physics, University of Augsburg, 86159 Augsburg, Germany

d Micro- and NanoFabrication and Printing Unit, Technion – Israel Institute of Technology, Haifa, 3200003, Israel

### Experimental Procedures

**Materials, Media and Microbial Strains.** Glutaraldehyde, Roswell Park Memorial Institute medium (RPMI 1640), Cation-adjusted Muller Hinton broth (CAMHB), D-glucose, anidulafungin, amphotericin B and propidium iodide were supplied by Sigma-Aldrich, Israel. Absolute ethanol and all buffer salts (NaCl, KCl, KH<sub>2</sub>PO<sub>4</sub>, Na<sub>2</sub>HPO<sub>4</sub>.) and NaOH were purchased from Merck, Germany. 3-(N-morpholino)propanesulfonic acid (MOPS) was supplied by Chem-Impex International, Inc., USA. Potato Dextrose Agar (PDA) and Bacto agar were purchased from Difco, USA.

All aqueous solutions and media were prepared in Milli-Q water (18.2 MΩ cm). Phosphate buffered saline (PBS) was composed of 137 mM NaCl, 2.7 mM KCl, 1.8 mM KH<sub>2</sub>PO<sub>4</sub>, and 10 mM Na<sub>2</sub>HPO<sub>4</sub>. RPMI 1640 2 % G medium (RPMI 1640 medium supplemented with 2 % D-glucose; referred to as growth medium) was constituted of 10.4 g L<sup>-1</sup> RPMI 1640, 34.5 g L<sup>-1</sup> MOPS and 18 g L<sup>-1</sup> glucose, adjusted to pH 7.0 with 1 M NaOH and sterile filtered before use. PDA was prepared by suspending 39 g L<sup>-1</sup> PDA powder in water, followed by steam sterilization at 121 °C for 30 min before pouring the plates. CAMHB was prepared according to the manufacturer's instructions and supplemented with 15 g L<sup>-1</sup> Bacto agar for agar plate preparation. *Candida auris* (*C. auris*) DSM 21092 was obtained from the German Collection of Microorganisms and Cell Culture (DSMZ), Germany and *Saccharomyces cerevisiae* (*S. cerevisiae*) NCYC 1024 from the National Collection of Yeast Cultures, United Kingdom. *Escherichia coli* (*E. coli*) K12 was generously provided by Prof. Sima Yaron (Department of Biotechnology and Food Engineering – Technion)

**Preparation of Microbial Cultures.** All microbial cultures were stored at -80 °C. The yeasts *C. auris* and *S. cerevisiae* were refreshed on PDA and incubated for 16 - 18 h at 30 °C before cell suspensions in growth medium for antifungal susceptibility testing (AFST) experiments were directly prepared from these fresh agar plates. For iPRISM experiments, the cell suspension was adjusted corresponding to a turbidity standard of McFarland 2.0 (~10<sup>7</sup> cells mL<sup>-1</sup>), and for broth microdilution (BMD), cell suspensions with a cell density of ~10<sup>5</sup> cells mL<sup>-1</sup> were prepared. *E. coli* was refreshed on MHB agar plates and grown for 16 h at 37 °C. The bacterial cells were resuspended in MHB and adjusted to a cell density corresponding to a turbidity standard of McFarland 0.5 (~10<sup>8</sup> cells mL<sup>-1</sup>) before PRISM experiments were performed at 37 °C.

**Fabrication and preparation of photonic silicon chips.** Silicon chips with microwell gratings (dimensions: width of ~ 4 μm and depth of ~ 4 μm) were fabricated by laser writing and reactive ion etching techniques at the Micro- and Nano-Fabrication and Printing Unit (Technion) and cut into chips of 5 x 5 mm, as previously described.<sup>1</sup>

**(i)PRISM Assay.** A custom-made, aluminium flow cell was assembled as explained in our previous work<sup>2</sup> and controlled by a motorized linear stage (Thorlabs, Inc, USA) and LabView (National Instruments, USA) for incremental movement. Before each experiment, the system was rinsed with 70 % ethanol, and sterile water before growth medium was introduced to allow the medium, temperature (30 °C) and device to equilibrate. Afterwards, 500 μL of the yeast cell suspensions (McFarland 2.0) at varying antifungal concentrations were introduced while the zero-order reflected light was continuously recorded as follows. A 74-series collimating lens connected to a bifurcated fibre optic was arranged perpendicularly to the photonic silicon chips,



## Results

illuminating them via an HL-2000 white light source, and the reflected light was recorded by a USB4000 CCD spectrometer (all Ocean Optics, USA). Fast Fourier transform (FFT) frequency analysis was performed on acquired reflectivity spectra in a range between 450 to 900 nm, and the resulting single peak was identified by determining the maximum peak position, where the height of the detected peak directly corresponds to the intensity of the reflected light and the peak position to the  $2nL$  value ( $n$  = refractive index of the medium within the grating and  $L$  = depth of the microstructure). The intensity and  $2nL$  values were plotted versus time, and the per cent changes of the intensity  $\Delta I$  (%) and  $\Delta 2nL$  (%) were calculated as follows:  $\Delta I$  (%) =  $\frac{I - I_0}{I_0} \times 100$  % and  $\Delta 2nL$  (%) =  $\frac{2nL - 2nL_0}{2nL_0} \times 100$  %, where  $I_0$  and  $2nL_0$  refer to the values of  $2nL$  and intensity at  $t = 0$  min (introduction of cell suspensions). For AFST experiments,  $I_0$  and  $2nL_0$  were replaced by  $I_{90}$  and  $2nL_{90}$  ( $t = 90$  min) as occasionally the signals were unstable at the beginning of the assay, ascribed to the high number of introduced cells.

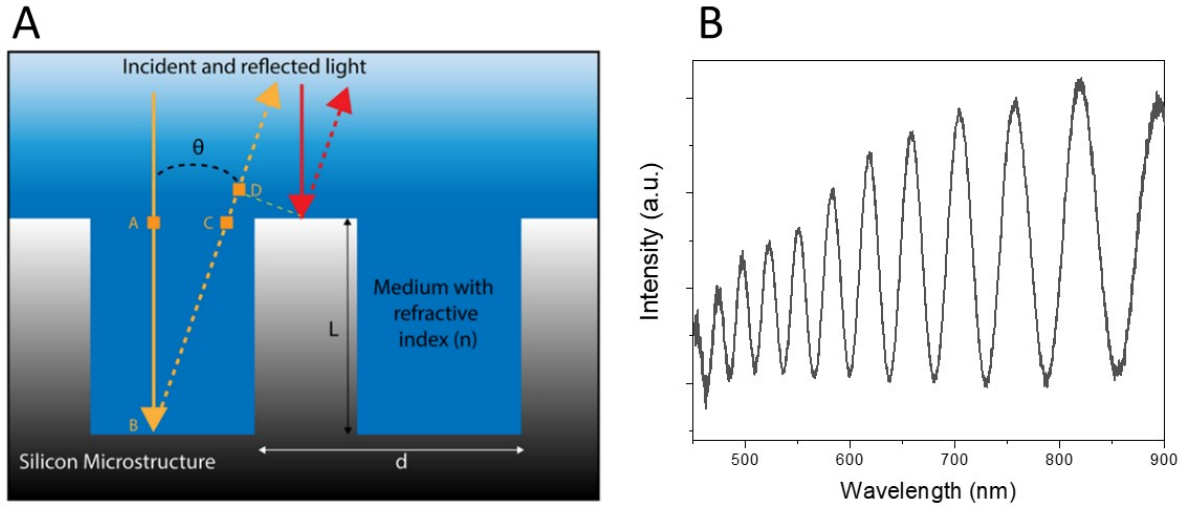
**Photonic Silicon Chips Characterization.** High-resolution scanning electron microscopy (HR-SEM) was performed using a Zeiss Ultra Plus high-resolution scanning microscope (Carl Zeiss, Germany). After sensing experiments, samples were fixated using 2.5 % glutaraldehyde in PBS and stored for at least 24 h at 7 °C. Subsequently, the chips were washed with water, dehydrated through a dilution series in ethanol (10 % - 50 % - 70 % - absolute ethanol) and gently dried under a stream of nitrogen before being observed using the scanning electron microscope.

Confocal laser scanning microscopy was performed using an LSM 700 confocal laser scanning microscope (Carl Zeiss, Germany) on samples where cells were stained with 20  $\mu\text{g mL}^{-1}$  propidium iodide after fixation in glutaraldehyde. The photoluminescence of the photonic silicon chips and fluorescence emitted by the propidium iodide-stained yeast cells were detected using 405 nm (Si photoluminescence) and 555 nm (propidium iodide) laser excitation wavelengths.

**Broth Microdilution AFST.** Broth microdilution (BMD) was performed based on the AFST protocol for yeasts of the European Committee for Antimicrobial Susceptibility Testing (EUCAST).<sup>3</sup> Briefly, two-fold dilution series of the antifungals anidulafungin and amphotericin B were prepared in growth medium and tested against a cell suspension (standardized cell density:  $10^5$  cells  $\text{mL}^{-1}$ ) of *C. auris* in a 96-well plate. Fungal growth was observed after incubation for 24 h at 30 °C by absorbance measurements (530 nm,  $n = 3$  for every tested concentration, Varioskan Flash, Thermo Scientific, USA). According to the EUCAST protocols, the MIC was defined as the lowest concentration of a drug that results in  $\geq 50$  % growth inhibition (anidulafungin) and  $\geq 90$  % growth inhibition (amphotericin B) compared to the untreated drug-free control.

## Supporting Data

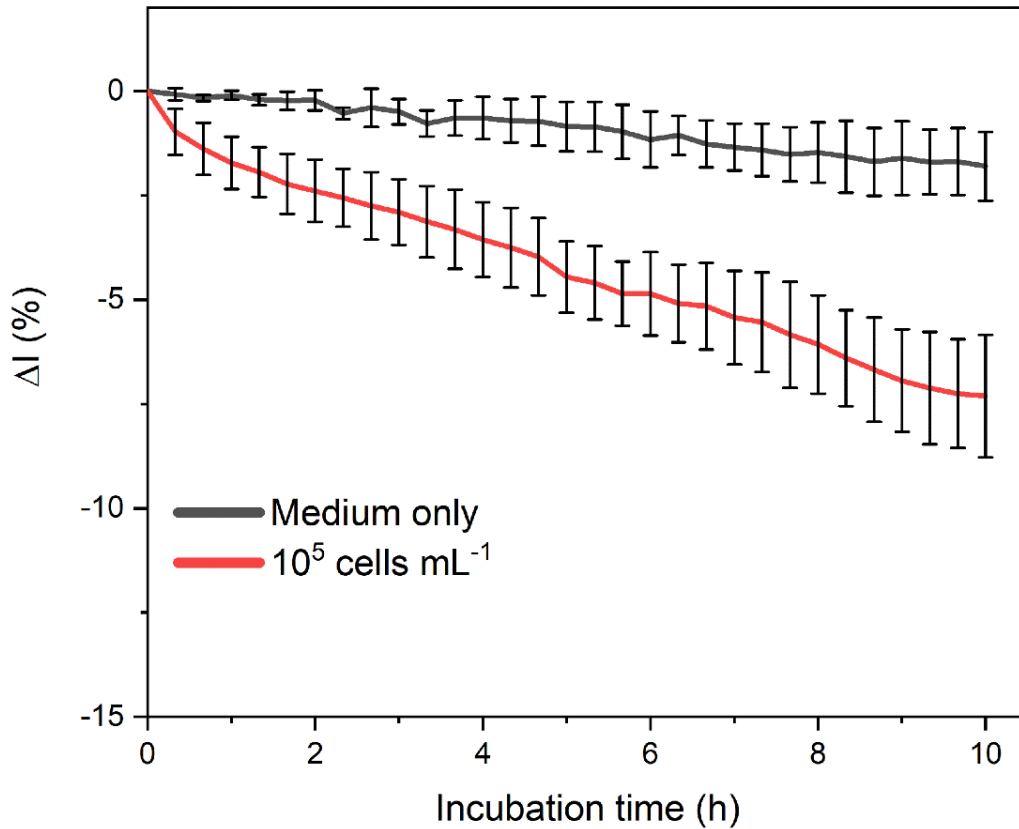
Figure S1A depicts a schematic illustration of the cross-section of the silicon microwell structure. The incident light is partially reflected from the bottom (orange arrow) and top (red arrow) interfaces of the silicon microwell grating, and the resulting reflectance spectra of the zero-order diffraction exhibit characteristic interference fringes (Figure S1B). The interference spectra are transformed into the corresponding single peaks by frequency analysis, allowing the monitoring of the reflected light intensity and the  $2nL$  value, as explained in the main article (Figure 1).



**Figure S1.** Microstructure and reflectance spectrum obtained from a photonic silicon chip. (A) Schematic illustration of the photonic silicon microwell gratings.  $L$  represents the height of the microstructure, and  $d$  is its width. Incident light hits both the bottom (orange arrow) and the top (red arrows) of the structure and is reflected from both interfaces. (B) The reflected light interferes, and the resulting reflectance spectra show characteristic interference fringes.

## Results

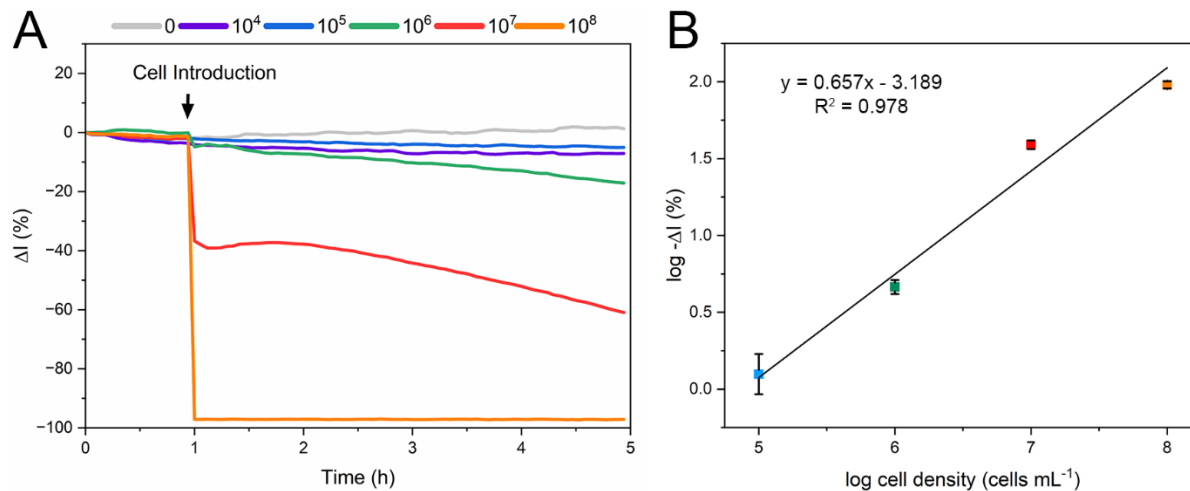
iPRISM for antifungal susceptibility testing (AFST) of *C. auris* was performed with cell suspensions at McFarland 2.0 ( $\sim 10^7$  cells mL<sup>-1</sup>; see Figure 1). The latter cell density is routinely used for AFST of *Candida* species by commercially available automated systems such as the Vitek2<sup>4</sup> and also expedites growth detection as compared to lower cell densities used in gold standard BMD ( $\sim 10^5$  cells mL<sup>-1</sup>) procedures.<sup>3</sup> Figure S2 demonstrates that at  $10^5$  cells mL<sup>-1</sup>, growth detection in the iPRISM assay is feasible, slope:  $-0.73 \Delta I (\%) h^{-1}$ . Yet, growth detection is clearly expedited at McFarland 2.0 with a slope of  $-10.8 \Delta I (\%) h^{-1}$  (Figure 1).



**Figure S2.** Averaged ( $n = 3$ ) iPRISM growth curves for *C. auris* at an initial cell density of  $10^5$  cells mL<sup>-1</sup> and medium only. Error bars show standard deviations of these triplicate measurements.

## Results

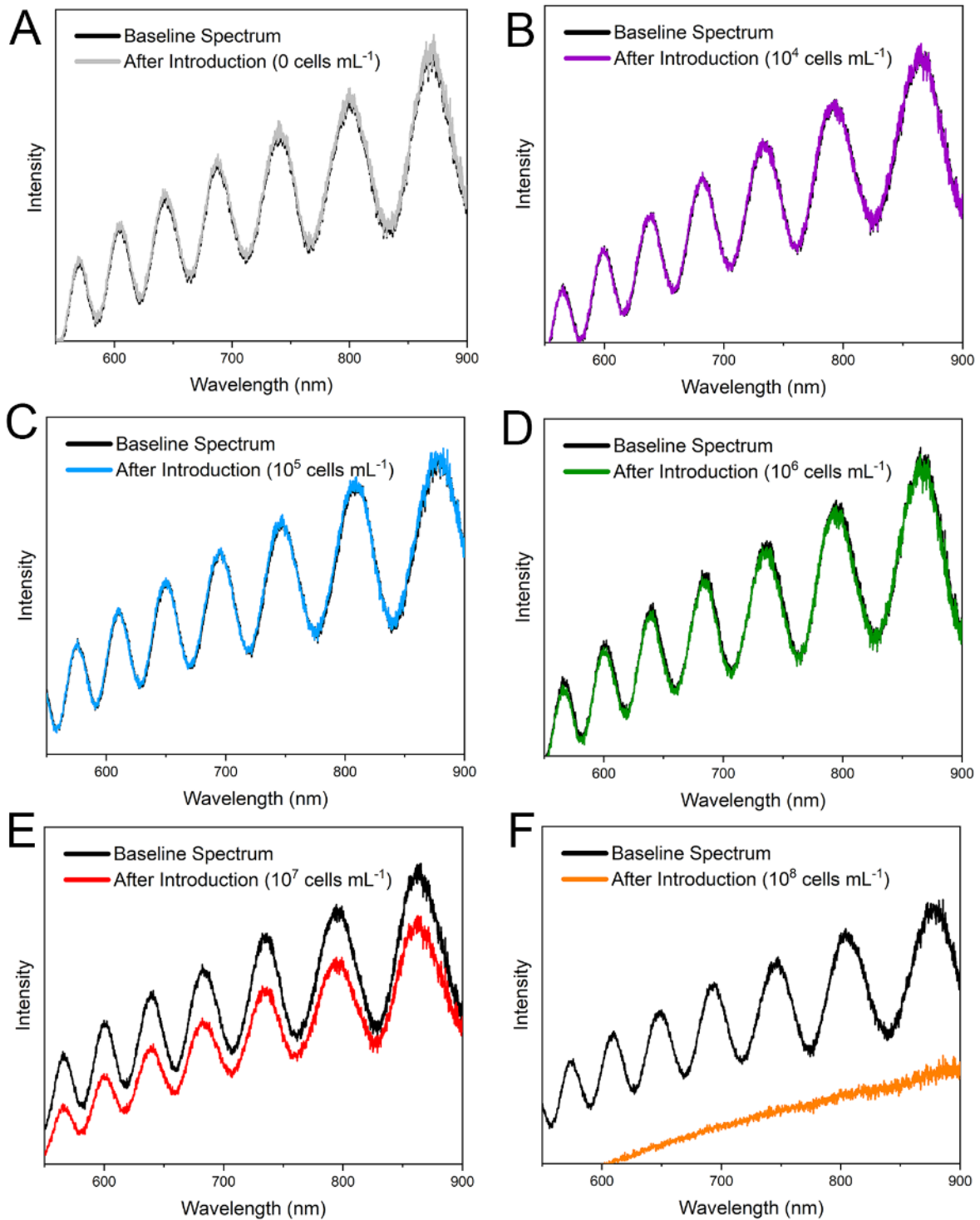
Figure S3 shows the intensity change caused by the introduction of *C. auris* suspensions of different cell densities. Figure S3A depicts characteristic iPRISM curves, where the change in intensity  $\Delta I$  (%) is plotted over time, following the introduction of *C. auris* suspensions of different cell densities, and Figure S3B summarizes the respective average  $-\Delta I$  (%) in a log-log scale at a concentration range from  $10^5$  –  $10^8$  cells  $\text{mL}^{-1}$ . The decrease in light intensity is ascribed to light scattering induced by microbial cells, as described previously.<sup>5</sup>



**Figure S3.** Intensity changes after the introduction of *C. auris* suspensions of different cell density values compared to the baseline values plotted over time. (B) A calibration curve (log-log scale) showing the average  $-\Delta I$  (%) changes caused by the introduction of different *C. auris* cell concentrations ( $n = 3$ ). Error bars show standard deviation.

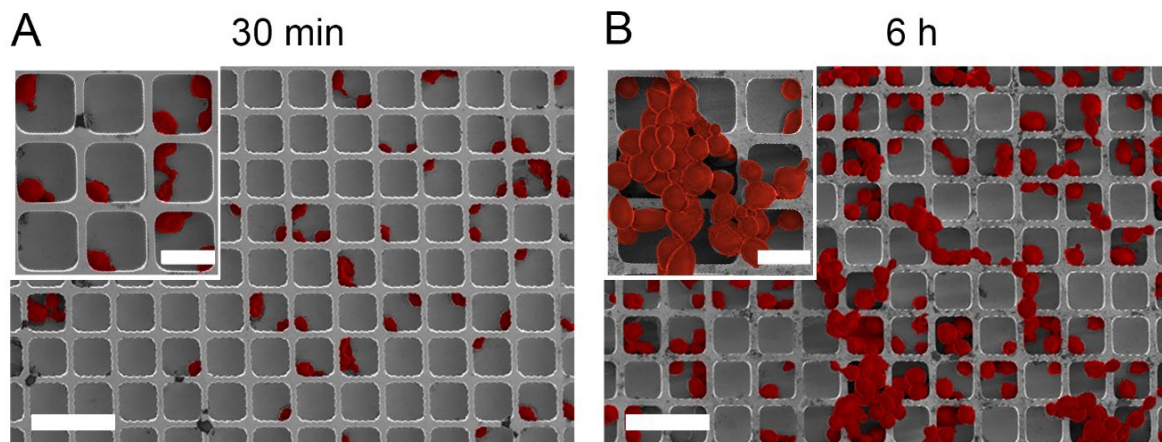
## Results

Figure S4 presents the raw reflectance spectra before and after the introduction of a concentration range from  $10^4$ – $10^8$  cell  $\text{mL}^{-1}$ .



**Figure S4.** Change of the reflectance spectra after introduction of *C. auris* suspensions of different cell density values.

## Results



**Figure S5.** Scanning electron micrographs of *C. auris* (inoculum: McFarland 2.0) growing on the photonic silicon chips for (A) 30 min and (B) 6h, respectively. Scale bars correspond to 10  $\mu\text{m}$  and 4  $\mu\text{m}$  (inserts). Yeast cells were false-coloured in red for clarity.

## Results

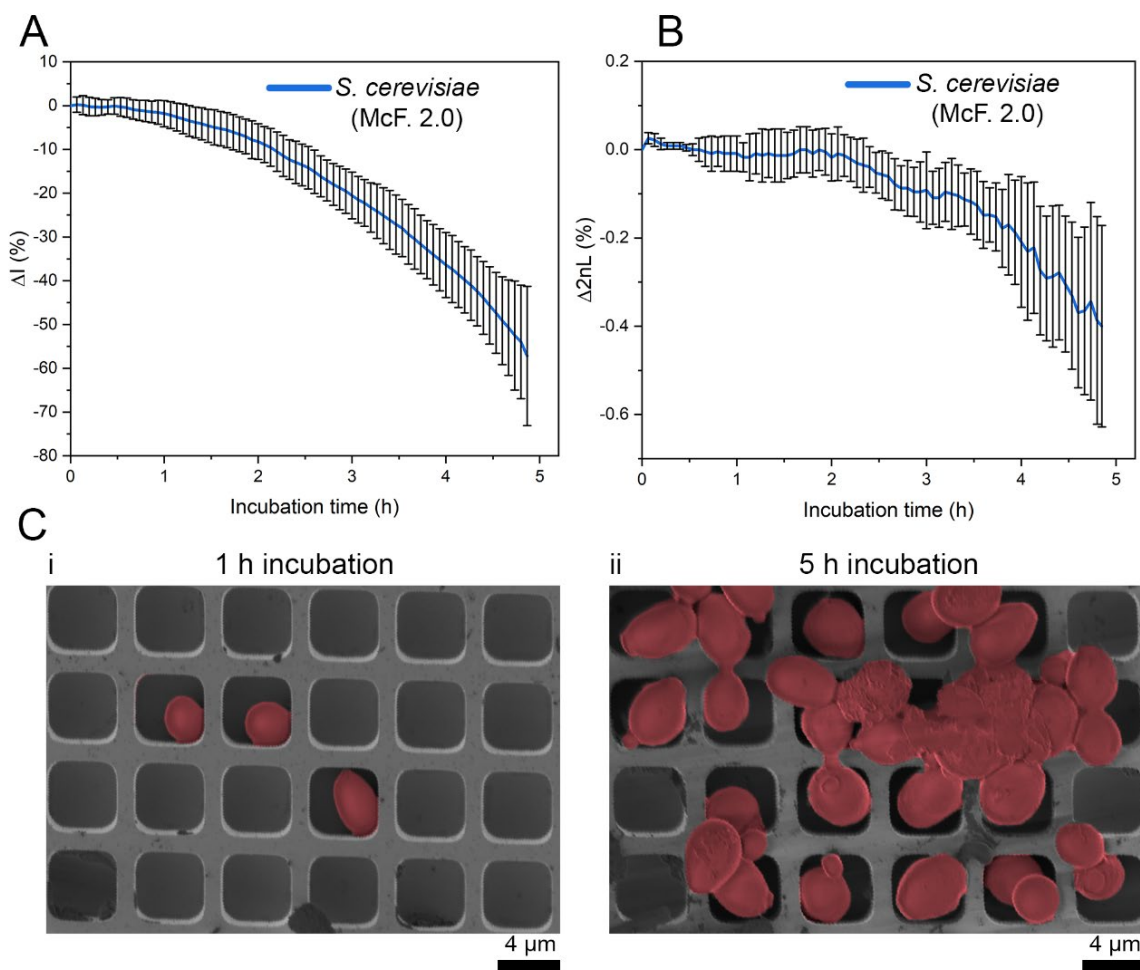


**Figure S6.** Averaged *S. cerevisiae* (i)PRISM growth curves ( $n = 3$ ) for (A) intensity (slope:  $-11.4 \Delta I (\%) h^{-1}$ ) and (B) 2nL (slope:  $-0.08 \Delta 2nL (\%) h^{-1}$ ) changes. The error bars show the standard deviation of the triplicate measurements. (C) Corresponding scanning electron micrographs after (C-i) 1h and (C-ii) 5 h of incubation. The yeast cells were false-coloured in red for clarity.

## Results

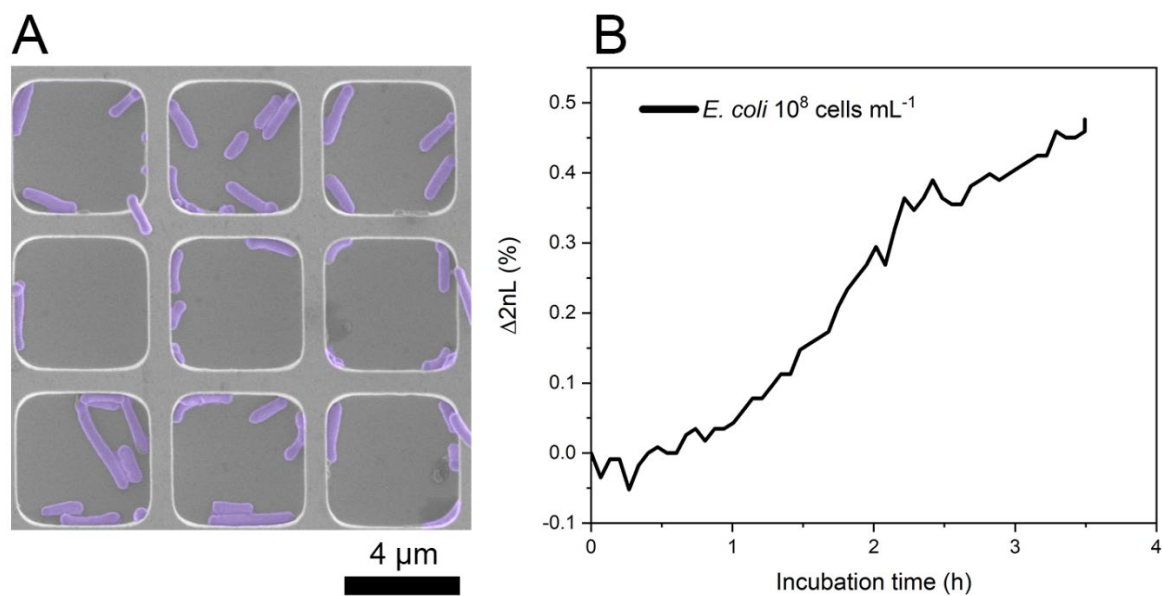


**Figure S7.** The bacterial species *E. coli* on photonic Si microwell chips. (A) A scanning electron micrograph demonstrates that most *E. coli* cells with a typical length of 1 – 2  $\mu\text{m}$  reside within the microwell structure. The cells were false-coloured for clarity. (B) Bacterial proliferation within the microwells typically results in a 2nL increase ascribed to the increased refractive index within the microstructure due to bacterial growth.



## Results

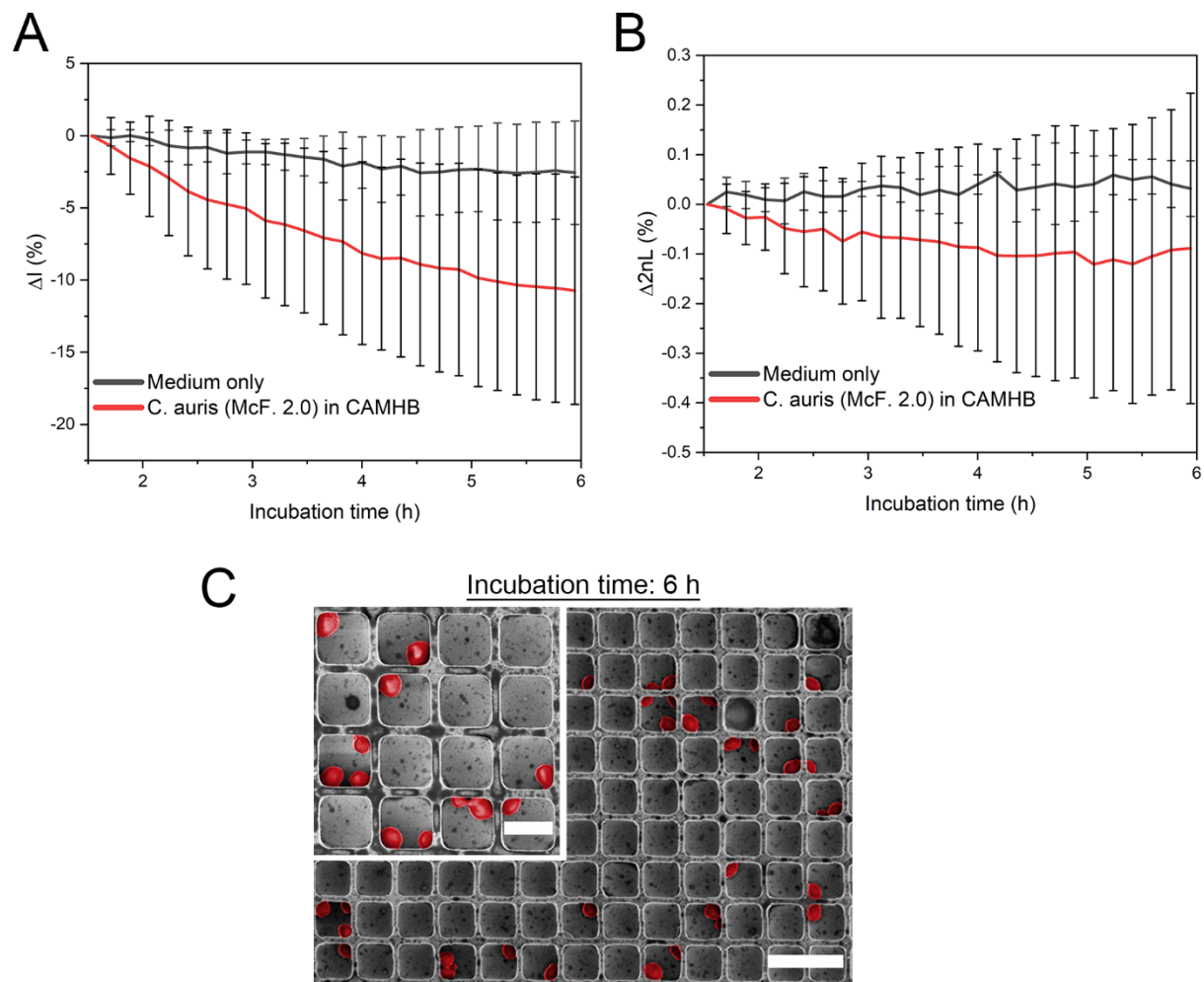


**Figure S8.** *C. auris* growing in cation-adjusted Muller Hinton Broth (CAMHB), a medium designated for antimicrobial susceptibility testing of bacteria. Averaged (i)PRISM growth curves for (A) intensity (slope:  $-1.8 \Delta I$  (%)  $h^{-1}$ ) and (B) 2nL (slope:  $-0.015 \Delta 2nL$  (%)  $h^{-1}$ ) signals of *C. auris* growing in CAMHB ( $n > 10$ ) and growth medium only as control ( $n = 3$ ). Error bars depict standard deviation. (C) Scanning electron micrographs after 6 h of incubation. The scale bars correspond to 10  $\mu m$  and 4  $\mu m$  (insert). Cells are false-coloured in red for clarity.

## Results

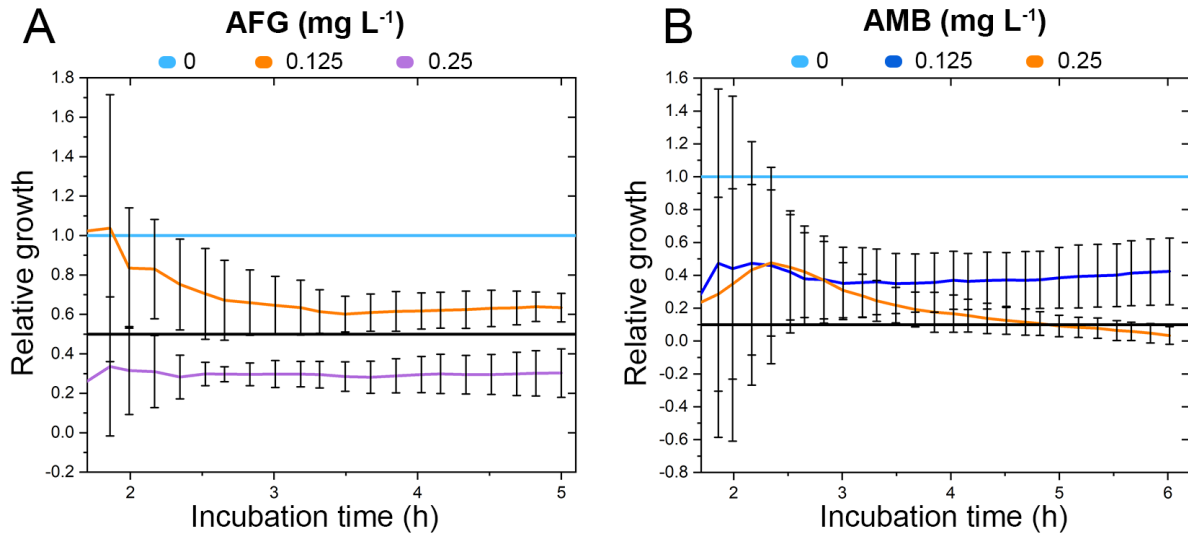


**Figure S9.** Relative growth was determined by iPRISM for the MIC, and the highest subinhibitory concentration for (A) anidulafungin (AFG) and (B) amphotericin B (AMB) against *C. auris* ( $n=3$ ); error bars indicate standard deviations. The MIC can be determined within 3.5 h for anidulafungin and 6 h for amphotericin B as at these time points, the growth at the MIC and the highest subinhibitory concentration are significantly different (two-tailed t-test;  $p < 0.05$ ). Also, here all MIC growth curves fall below the MIC threshold (black lines) of 50 % (0.5) growth (anidulafungin) and 10 % (0.1) growth (amphotericin B).

Results

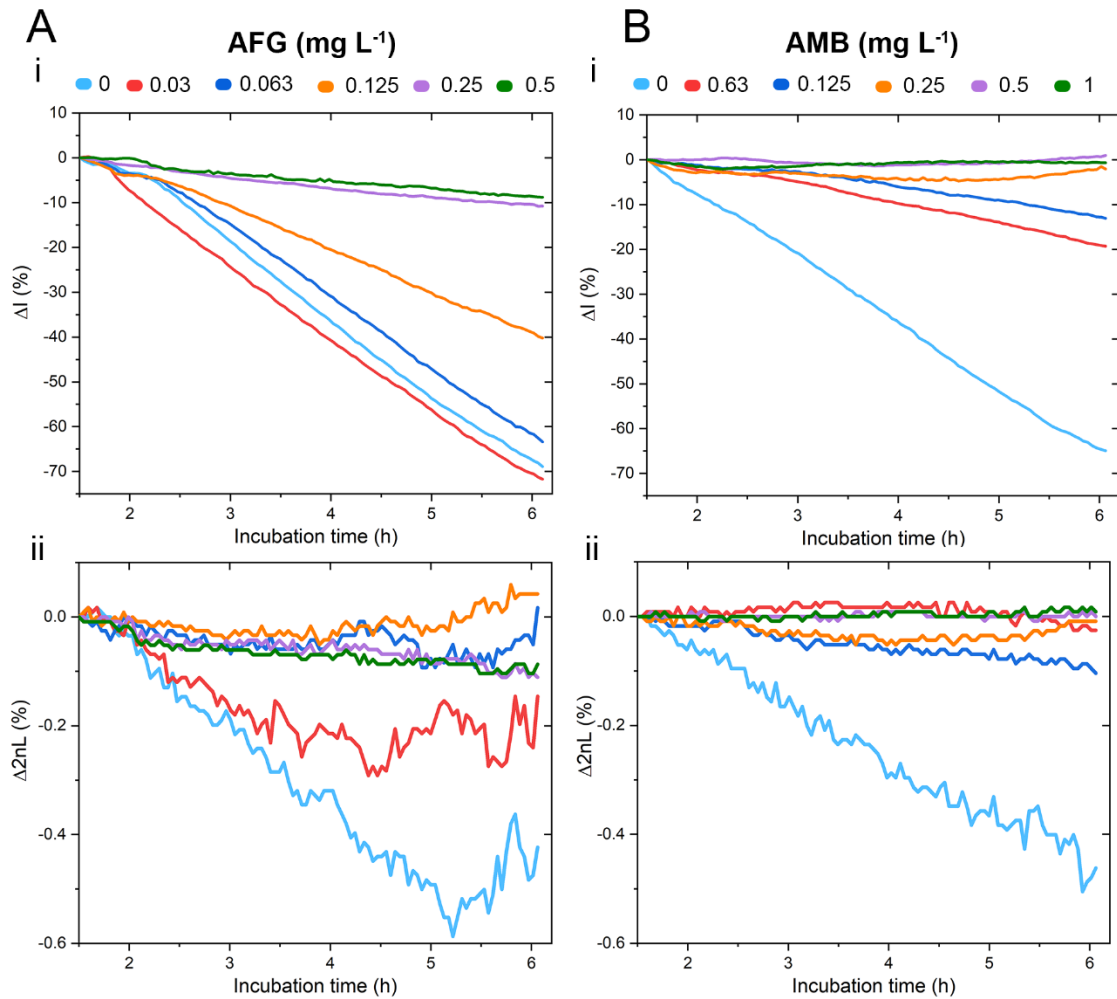


**Figure S10.** Growth curves for *C. auris* at varying antifungal concentrations by monitoring intensity and 2nL changes. (A-i) Intensity and (A-ii) 2nL changes for *C. auris* growing at varying anidulafungin concentrations. (B-i) Intensity and (B-ii) 2nL changes for *C. auris* exposed to different amphotericin B concentrations.

## Results

Figure S11 shows the growth curves obtained by a standard BMD assay for *C. auris* and amphotericin B, continuously monitored using a microplate reader. The MIC is determined to be 0.25 mg L<sup>-1</sup> as this concentration causes a > 90 % growth inhibition compared to the untreated no-drug control. The MIC (0.25 mg L<sup>-1</sup>) and the lowest subinhibitory concentration (0.125 mg L<sup>-1</sup>) are statistically different after 19 h (two-tailed t-test,  $p < 0.05$ ). Thus, the MIC can be determined within 19 h - an assay time which is still significantly longer than for the iPRISM assay (MIC determination within 6 h).

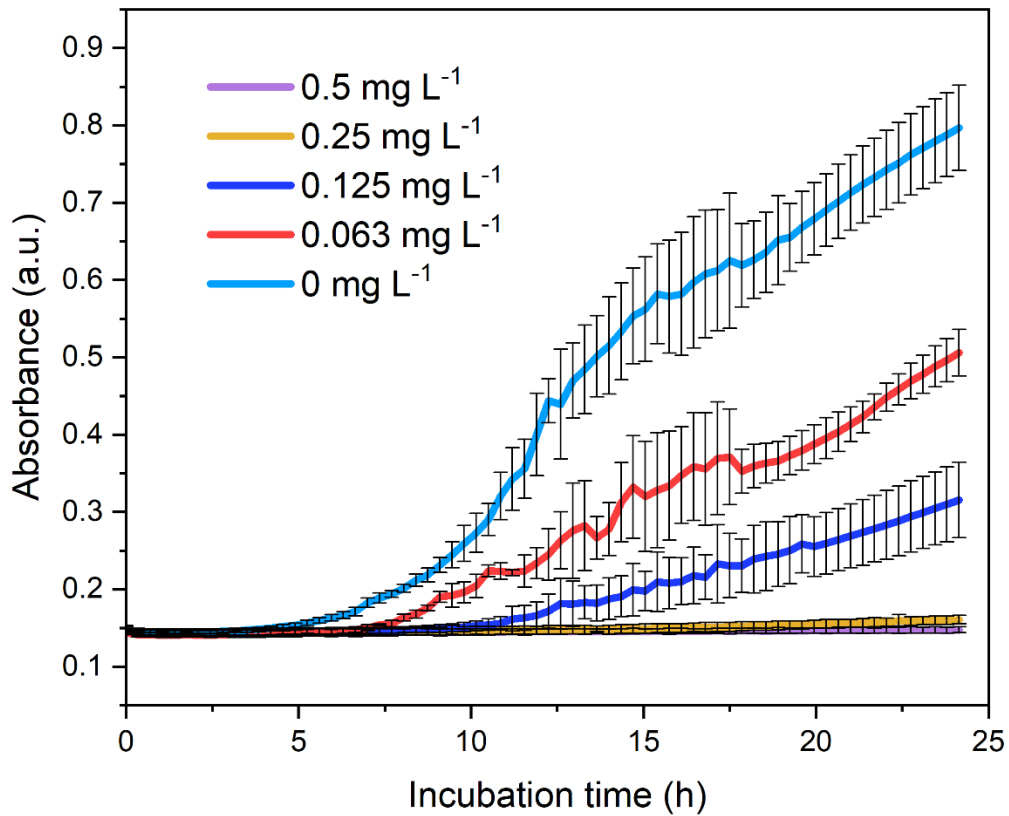


**Figure S11.** Continuous microplate reader measurements ( $n = 3$ ) for a standard BMD with *C. auris* and different amphotericin B concentrations over an incubation time of 24 h. Error bars indicate the standard deviation of the triplicate measurements.

## Results

**Table S1.** MIC value comparison for anidulafungin (AFG) and amphotericin B (AMB) obtained by iPRISM and gold standard BMD methods, including respective tentative epidemiological cut-off values (ECOFFs).

Antifungal	iPRISM		BMD		ECOFFs (mg L <sup>-1</sup> )
	MIC (mg L <sup>-1</sup> )	Time (h)	MIC (mg L <sup>-1</sup> )	Time (h)	
AFG	0.25	3.5	0.0625 mg L <sup>-1</sup>	24	0.25 - 2 <sup>6</sup>
AMB	0.25	6	0.125 - 0.25 mg L <sup>-1</sup>	24	1 - 2 <sup>6</sup>

## References

- 1 C. Heuer, J.-A. Preuss, M. Buttkewitz, T. Scheper, E. Segal and J. Bahnemann, *Lab Chip*, 2022, **22**, 4950–4961.
- 2 H. Leonard, S. Halachmi, N. Ben-Dov, O. Nativ and E. Segal, *ACS Nano*, 2017, **11**, 6167–6177.
- 3 EUCAST DEFINITIVE DOCUMENT E.DEF 7.3.2 Method for the determination of broth dilution minimum inhibitory concentrations of antifungal agents for yeasts,  
[https://www.eucast.org/fileadmin/src/media/PDFs/EUCAST\\_files/AFST/Files/EUCAST\\_E\\_Def\\_7.3.2\\_Yeast\\_testing\\_definitive\\_revised\\_2020.pdf](https://www.eucast.org/fileadmin/src/media/PDFs/EUCAST_files/AFST/Files/EUCAST_E_Def_7.3.2_Yeast_testing_definitive_revised_2020.pdf), (accessed March 2023).
- 4 E. Borghi, R. Iatta, R. Sciota, C. Biassoni, T. Cuna, M. T. Montagna and G. Morace, *J. Clin. Microbiol.*, 2010, **48**, 3153–3157.
- 5 N. Massad-Ivanir, Y. Mirsky, A. Nahor, E. Edrei, L. M. Bonanno-Young, N. Ben Dov, A. Sa'arb and E. Segal, *Analyst*, 2014, **139**, 3885–3894.
- 6 M. C. Arendrup, A. Prakash, J. Meletiadiis, C. Sharma and A. Chowdhary, *Antimicrob. Agents Chemother.*, 2017, **61**.

### 5.3 A 3D-Printed Microfluidic Gradient Generator with Integrated Photonic Silicon Sensors for Rapid Antimicrobial Susceptibility Testing

This section is reproduced from the research article “A 3D-Printed Microfluidic Gradient Generator with Integrated Photonic Silicon Sensors for Rapid Antimicrobial Susceptibility Testing”, published in the peer-reviewed journal *Lab on a Chip*.

## “A 3D-Printed Microfluidic Gradient Generator with Integrated Photonic Silicon Sensors for Rapid Antimicrobial Susceptibility Testing”

Christopher Heuer\*, John-Alexander Preuß\*, Marc Buttkewitz, Thomas Scheper, Ester Segal and Janina Bahnemann  
(\* equal contribution)

*Lab on a chip*, 22, 4950–4961 (2022)

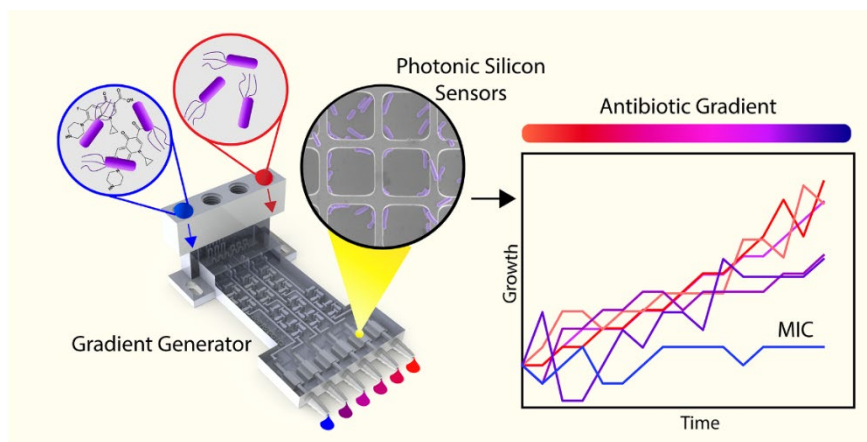


**Figure 7** Graphical abstract of the research article “A 3D-Printed Microfluidic Gradient Generator with Integrated Photonic Silicon Sensors for Rapid Antimicrobial Susceptibility Testing”.

The article addresses the third research objective and presents an integrated system for rapid automated AST, which can potentially be employed in point-of-care settings. The system includes a 3D-printed microfluidic gradient generator which is interfaced with photonic chips that encompass the sensing element. This gradient generator was fabricated from a heat-resistant and biocompatible material and automatically

## Results

generates the desired two-fold antimicrobial dilution series in one step by adjusting the flow rate and channel length ratios. The device and its accuracy were carefully characterized using different fluids (ink, glucose, ciprofloxacin), and for all fluids, precise two-fold dilution series were obtained. Next, the gradient generator was established for gold standard BMD of different pathogen drug combinations (*C. auris* and voriconazole, *E. coli* and gentamicin, *S. marcescens* and ciprofloxacin) by collecting the respective antimicrobial concentrations from the outlets of the generator. The attained MICs from this gradient generator enabled BMD agreed with the values from a manually prepared BMD, demonstrating that the gradient generator and its function did not impair the outcome of such standard AST. Finally, the device was interfaced with the optical transducer element by integrating the photonic silicon chips into the gradient generator for automated optical AST using PRISM (detecting 2nL changes). The application of the silicon chip integrated gradient generator was demonstrated for the bacterial pathogen *E. coli* and the antibiotic ciprofloxacin and MIC value determination was feasible within 90 minutes compared to 8 – 24 h in current clinical procedures for bacterial pathogens.

In the following article, “*A 3D-Printed Microfluidic Gradient Generator with Integrated Photonic Silicon Sensors for Rapid Antimicrobial Susceptibility Testing*”, the results are presented and discussed in detail.


 Cite this: *Lab Chip*, 2022, 22, 4950

## A 3D-printed microfluidic gradient generator with integrated photonic silicon sensors for rapid antimicrobial susceptibility testing†

 Christopher Heuer, <sup>‡,a,c</sup> John-Alexander Preuss, <sup>‡,a,b</sup> Marc Buttkewitz, <sup>a</sup> Thomas Scheper, <sup>a</sup> Ester Segal <sup>\*c</sup> and Janina Bahnemann <sup>\*a,b</sup>

With antimicrobial resistance becoming a major threat to healthcare settings around the world, there is a paramount need for rapid point-of-care antimicrobial susceptibility testing (AST) diagnostics. Unfortunately, most currently available clinical AST tools are lengthy, laborious, or are simply inappropriate for point-of-care testing. Herein, we design a 3D-printed microfluidic gradient generator that automatically produces two-fold dilution series of clinically relevant antimicrobials. We first establish the compatibility of these generators for classical AST (*i.e.*, broth microdilution) and then extend their application to include a complete on-chip label-free and phenotypic AST. This is accomplished by the integration of photonic silicon chips, which provide a preferential surface for microbial colonization and allow optical tracking of bacterial behavior and growth at a solid-liquid interface in real-time by phase shift reflectometric interference spectroscopic measurements (PRISM). Using *Escherichia coli* and ciprofloxacin as a model pathogen-drug combination, we successfully determine the minimum inhibitory concentration within less than 90 minutes. This gradient generator-based PRISM assay provides an integrated AST device that is viable for convenient point-of-care testing and offers a promising and most importantly, rapid alternative to current clinical practices, which extend to 8–24 h.

 Received 12th July 2022,  
 Accepted 27th October 2022

DOI: 10.1039/d2lc00640e

[rsc.li/loc](https://rsc.li/loc)

### Introduction

The emergence of antimicrobial resistance in bacterial and fungal pathogens caused by the extensive use and misuse of antimicrobials has led to the emergence of ‘superbugs’ and a global health crisis.<sup>1,2</sup> According to a recent study by the antimicrobial resistance collaborators, ~1.3 million deaths were directly attributed to antimicrobial resistance in 2019<sup>3</sup> and by 2050, antimicrobial-resistant infections could even come to surpass cancer as the leading cause of mortality.<sup>4</sup> This concerning situation is only further exacerbated by the lack of a robust pipeline for developing new antimicrobials – which underscores the pressing need for proper antimicrobial stewardship (especially efforts to curb the excessive use of antimicrobials and the spread of drug resistance by

encouraging physicians to prescribe suitable antimicrobials only when needed).<sup>5,6</sup> An essential part of effective antimicrobial stewardship is clinical antimicrobial susceptibility testing (AST). In these assays, pathogens are exposed to a panel of antimicrobials at varying concentrations so that the minimum inhibitory concentration (MIC) can be determined. This value is typically defined as the lowest drug concentration that inhibits the pathogens' growth and helps physicians to differentiate between resistant and susceptible isolates and choose the adequate antimicrobial for treatment.<sup>13–15</sup> Yet gold-standard reference AST techniques, such as broth microdilution (BMD) and agar-based methods in which growth can be determined by absorbance measurements<sup>16</sup> or visually,<sup>17,18</sup> are labor-intensive procedures with long ( $\geq 16$  h) wait times and are not well-suited for point-of-care (PoC) purposes.<sup>16–19</sup>

To overcome these limitations, extensive research is directed towards the development of microfluidic devices for miniaturized and rapid AST assays<sup>20,21</sup> using various sensing approaches (*e.g.*, chromogenic agar,<sup>22</sup> oxygen consumption,<sup>23,24</sup> membrane integrity,<sup>25</sup> single-cell imaging,<sup>26</sup> or metabolic activity/metabolite analysis<sup>27–29</sup>). However, in most studies, the total assay time (including sample preparation and time readout) is still in the range of several hours, and sample preparation should be further

<sup>a</sup> Institute of Technical Chemistry, Leibniz University Hannover, 30167 Hannover, Germany

<sup>b</sup> Institute of Physics, University of Augsburg, 86159 Augsburg, Germany.  
 E-mail: Janina.bahnemann@uni-a.de

<sup>c</sup> Department of Biotechnology and Food Engineering, Technion – Israel Institute of Technology, 320003 Haifa, Israel. E-mail: esegal@technion.ac.il

 † Electronic supplementary information (ESI) available. See DOI: <https://doi.org/10.1039/d2lc00640e>

‡ Christopher Heuer and John-Alexander Preuss contributed equally to this work.





simplified.<sup>20</sup> To answer these challenges and make AST procedures more appropriate for deployment at PoC, the integration of microfluidic gradient generators (GG) in AST systems is suggested.<sup>7–12,30–32</sup> These GG devices are designed to establish a desired antimicrobial dilution series – combining advantages of automation, and minimized sample and reagents consumption. The automatically generated concentrations are then collected and used for BMD testing, or the AST procedure is performed within the microfluidic system. Yet, existing microfluidic GG AST systems still suffer from different shortcomings; for example, in diffusion-based assays, the diffusion behavior of each antimicrobial agent must be well known to accurately predict the specific concentration in the area of interest.<sup>30,31</sup> By contrast, convective gradient generators allow a high control of the respective concentration without a precise determination of the antimicrobials' diffusive behavior. Yet, tree-like gradient generators (based on a cascade of divisions and reunions with an additional branch at every level) that represent the standard system of such convective gradient generators are often constrained by a maximal flow rate (as thorough mixing is required between each reunion and division).<sup>33</sup> Moreover, reported convective GG AST systems only apply non-clinically relevant linear concentration gradients,<sup>7,8,10</sup> require inconvenient off-chip testing after antimicrobial solution collection,<sup>8,11</sup> need to be coupled with sophisticated microscopy analysis,<sup>7,10</sup> or provide AST results within  $\geq 8$  h<sup>8,9</sup> which in a clinical setting often corresponds to next-day results only.<sup>13</sup> See Table 1 for a summary of previously reported relevant convective GG devices for AST.

In this work, we build a 3D-printed GG system for creating clinically relevant two-fold dilution series of antimicrobials and integrate it with an on-chip phenotypic AST, allowing for an automatic rapid susceptibility determination (within <90 min). The microfluidic GG principle relies on adjusting the channel length ratios of parallel channels<sup>33</sup> and flow rate ratios to generate defined concentrations in one step. The device is fabricated from a biocompatible and heat-resistant<sup>34</sup> polyacrylate material by high-resolution 3D printing – a technique that enables the manufacturing of microfluidic

devices and has accordingly assumed increasing importance in many biotechnology-related fields, ranging from diagnostics to cell culture.<sup>35–39</sup> Compared to standard fabrication processes such as polydimethylsiloxane-based soft-lithography,<sup>10,12,40</sup> 3D printing offers rapid prototyping of complex structures in a single step,<sup>38,41</sup> the use of various and versatile materials,<sup>34,40,42</sup> and does not require sophisticated microfabrication facilities.<sup>12,38</sup> The functionality of the GG is first established off-chip, see Fig. 1A, for various clinically relevant microorganisms (bacterial and fungal) using the gold standard BMD assay. In these tests, two-fold serial dilutions of antimicrobials are prepared in a liquid growth medium and inoculated with a predefined and standardized cell number. Next, we interface the gradient generator with an array of photonic silicon chips (Fig. 1B-i), consisting of microwell diffraction gratings, which provide a preferential surface for microbial colonization and act as an optical transducer element and previously enabled real-time and rapid AST of *Escherichia coli* (*E. coli*) in 2–3 h and *Aspergillus niger* (*A. niger*) in 10–12 h.<sup>43,44</sup> In this label-free PRISM (phase shift reflectometric interference spectroscopic measurement) method, continuous reflectivity measurements (Fig. 1B-ii) track bacterial growth in the presence of different antibiotic concentrations within the microwell structure of photonic silicon chips. After applying frequency analysis, single peaks are obtained (Fig. 1B-v and -vi) where the peak position corresponds to  $2nL$  ( $n$  is the refractive index of the medium within the grating and  $L$  represents the height of the microstructures). At antibiotic concentrations  $\geq$  MIC (Fig. 1B-iii), bacterial growth is inhibited and the  $2nL$  value remains largely unchanged (Fig. 1B-v), whereas uninhibited bacterial growth (Fig. 1B-iv) results in an increase of the  $2nL$  due to refractive index changes (Fig. 1B-vi). Susceptibility and corresponding MIC values are determined by the extent of antimicrobial-hindered bacterial growth within the grating by monitoring the  $2nL$  value over time (Fig. 1B-vii). The resulting integrated platform, combining the microfluidic GG device and PRISM sensors, allows for rapid (90 min) phenotypic AST in a label-free format, which is highly applicable in PoC settings.

**Table 1** Relevant convective microfluidic GG systems for AST assays previously reported in the literature. The gradient generator devices are ordered according to their reported assay time, from the lengthiest to the most expeditious

Principle	Gradient	Flow rate ( $\mu\text{L min}^{-1}$ )	AST method	Label	Assay time (h)	Ref.
Tree-like	Linear	0.167	Fluorescence imaging of stained biofilm	Yes	>24	7
One-step inlet position	Linear	2280	Off-chip turbidity	No	Overnight	8
Vacuum driven	Exponential (two-fold dilution)	No data	Fluorescence detection (resazurin-based redox indicator)	Yes	8	9
Acoustic waves	Linear	3.3	Time-lapse microscopy (covered area)	No	5.5	10
3D tree-like	Symmetric gradient of 3 fluids	1000	Off-chip fluorescence detection (resazurin-based redox indicator)	Yes	5	11
Tree-like	Exponential (two-fold dilution)	1.5	Microscopy (cell counting)	No	3	12
One-step parallel channels	Exponential (two-fold dilution)	1000	PRISM	No	$\leq 1.5$	This study



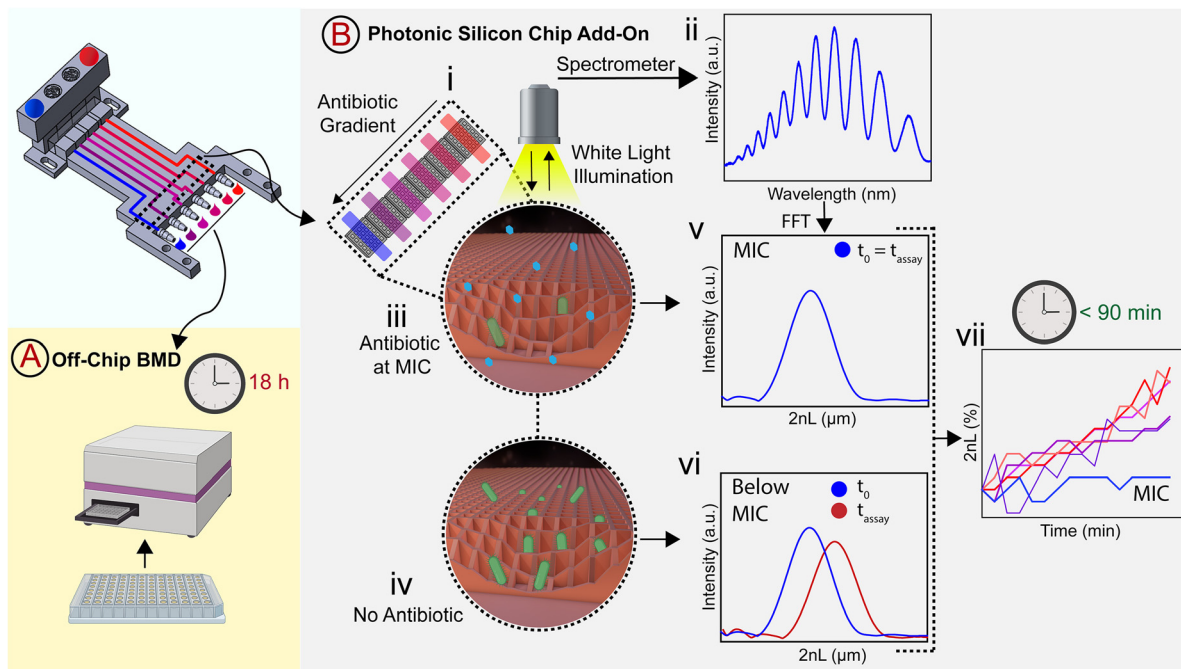


**Fig. 1** (A) First, the functionality of the GG device is established by the gold-standard BMD method. The GG is used to generate two-fold dilutions of antimicrobials that are tested in a 96 well plate against three different microorganisms (*E. coli*, *S. marcescens*, and *C. auris*). The MIC is determined after incubation by absorbance measurements or visually. (B-i) Second, the integration of photonic silicon chips consisting of microwell diffraction gratings for rapid optical AST (PRISM) is demonstrated. (B-ii) Illumination of the photonic silicon chips by a white light source results in characteristic reflectivity spectra exhibiting interference fringes as light is partially reflected from the top and bottom surfaces of the silicon microwell diffraction grating. These reflectivity spectra are recorded and analysed in real time, enabling label-free monitoring of bacterial growth in the presence of varying antibiotic concentrations generated by the GG device. (B-iii) Bacterial growth is inhibited at antibiotic concentrations  $\geq$  MIC, while at (B-iv) subinhibitory concentrations, the bacteria grow and proliferate within the microwells. To monitor this bacterial behaviour, the reflectivity spectrum (at each time point) is analysed by frequency analysis (FFT), yielding a single peak where the peak position corresponds to the  $2nL$  value ( $n$  = refractive index within the microwells;  $L$  = height of the microstructure). When bacterial growth is inhibited, (B-v) this  $2nL$  value remains unchanged, while (B-vi) it increases when bacteria grow inside the microwells and induce changes in the average refractive index values. (B-vii) The  $2nL$  is monitored in real-time and used to track bacterial growth at varying antimicrobial concentrations to determine the MIC value within less than 90 min.

## Experimental

### Materials, media, and microbial strains

VisiJet® M2S-HT90 3D printing material and wax support material VisiJet® M2 SUP were purchased from 3D Systems Inc. (SC, USA). Cation-adjusted Muller Hinton broth (CAMHB), Roswell Park Memorial Institute medium (RPMI 1640), 3-(*N*-morpholino)propanesulfonic acid (MOPS), glutaraldehyde,  $D$ -glucose, voriconazole, and ciprofloxacin were supplied by Sigma-Aldrich, Israel. All buffer salts were obtained from Merck, Germany. Potato dextrose agar (PDA), bacto agar, and Luria-Bertani (LB) broth were supplied by Becton Dickinson (Difco, USA). Absolute ethanol was purchased from Gadot, Israel. Detergent fairy ultra plus was purchased from Procter and Gamble (Cincinnati, USA), gentamicin sulfate from AppliChem GmbH (Darmstadt, Germany), Pelikan ink 156372 (designated blue dye) with an estimated diffusion coefficient<sup>45</sup> of  $\sim 10^{-10}$  m<sup>2</sup> s<sup>-1</sup> from Pelikan Group GmbH (Falkensee, Germany), and paraffin oil of low viscosity from Carl Roth GmbH + Co. K.G. (Karlsruhe, Germany). All aqueous solutions and media were prepared in deionized water (18.2 M $\Omega$  cm). Phosphate buffered saline

(PBS) was constituted of 137 mM NaCl, 2.7 mM KCl, 1.8 mM KH<sub>2</sub>PO<sub>4</sub>, and 10 mM Na<sub>2</sub>HPO<sub>4</sub>. RPMI 1640 2% G medium (RPMI 1640 medium supplemented with 2%  $D$ -glucose) was composed of 10.4 g L<sup>-1</sup> RPMI 1640, 34.5 g L<sup>-1</sup> MOPS, and 18 g L<sup>-1</sup>  $D$ -glucose. LB agar was made from 25 g L<sup>-1</sup> LB broth and 15 g L<sup>-1</sup> bacto agar. PDA plates and CAMHB medium were prepared according to the manufacturer's instructions. All media and buffer were heat-steam sterilized or sterile-filtered before use. *E. coli* K12 and *Serratia marcescens* (*S. marcescens*) were generously provided by Prof. Sima Yaron (Department of Biotechnology and Food Engineering, Technion – Israel Institute of Technology). *Candida auris* (*C. auris*) DSM 21092 was obtained from the German Collection of Microorganisms and Cell Cultures.

### Preparation of microbial cultures

Microbial cultures were stored as cryo cultures at  $-70$  °C. Prior to AST experiments, the cells were sub-cultured onto LB agar (bacteria) or PDA (yeast) and incubated at 37 °C for 16–24 h. Colonies from these agar plates were directly used to obtain the cell suspensions used in AST experiments.



### 3D printing and post-processing

The computer-aided design (CAD) model was created using SolidWorks 2020 (Dassault Systèmes SolidWorks Corp, Waltham, MA, USA). The model was saved as an .STL file for printing purposes, and as an .SAT file for simulations. All files are provided in the ESI†. Models were printed using a high-resolution 3D printer (ProJet® MJP 2500 Plus, 3D Systems, SC, USA) with a xyz resolution of 32, 28 and 32  $\mu\text{m}$ , respectively. The GG was printed with its inlets facing up, as shown in Fig. S1†. Further information on the accuracy of the printing process is given in Fig. S2 and Table S1†. The printed device was removed from the printing platform after incubation at  $-18\text{ }^{\circ}\text{C}$  for 10 min. Afterward, all pieces were placed in EasyClean units from 3D systems (water vapor bath and hot paraffin oil bath at  $65\text{ }^{\circ}\text{C}$ ) to remove the wax support material. The interior structures were flushed at least three times with hot paraffin oil using a syringe. To remove oil residues, the parts were then submerged in an ultrasonic bath (Elma Elmasonic S30, Elma, Schmidbauer GmbH, Singen, Germany) with water and detergent at  $50\text{ }^{\circ}\text{C}$  for at least three times. Subsequently, the device was cleaned with deionized water and dried at  $70\text{ }^{\circ}\text{C}$  for 1 hour.

### Computational fluid dynamics (CFD) simulations

The functionality of the design was tested *via* running a computational fluid dynamics (CFD) simulation using COMSOL® Multiphysics 5.5 (COMSOL Inc., Stockholm, Sweden). General simulation settings were chosen according to Enders *et al.*<sup>41</sup> As physical properties, a density of  $1\text{ g cm}^{-3}$  and a dynamic viscosity of  $10^{-3}\text{ kg m}^{-1}\text{ s}^{-1}$  were chosen for water. For inlet A, the concentration of a fictive substance with a diffusion constant of  $10^{-9}\text{ m}^2\text{ s}^{-1}$  was set to  $1\text{ mol m}^{-3}$ , while the concentration of inlet B was defined as  $0\text{ mol m}^{-3}$ . To simulate the performance of the designed GG, the inflows at inlet A and inlet B were defined as  $323\text{ }\mu\text{L min}^{-1}$  and  $677.3\text{ }\mu\text{L min}^{-1}$ , respectively.

### Experimental gradient generating accuracy studies

The source fluids – blue dye (ink; 1:30 diluted), glucose ( $6\text{ g L}^{-1}$ ), and ciprofloxacin ( $1\text{ mg L}^{-1}$ ) – were introduced into the device by a syringe pump into inlet A at a flow rate of  $323\text{ }\mu\text{L min}^{-1}$ , while the sink fluid water was introduced by a second syringe pump into inlet B at a flow rate of  $677.3\text{ }\mu\text{L min}^{-1}$ . After 5 min, the first fractions were collected from the six outlets, the pumps were stopped, and the solutions were transferred into a 96 well plate or reaction tubes. Next, the pumps were started again, and after 30 s a second batch was collected. This procedure was repeated again, for the collection of a third batch from every outlet. The dye was quantified at 600 nm (NanoDrop™ 2000 spectrophotometer, Thermo Fisher Scientific GmbH, Dreieich, Germany), the glucose concentration was measured using a Cedex BioAnalyzer (Roche Diagnostics Deutschland GmbH, Mannheim, Germany), and ciprofloxacin was quantified *via* a fluorescence assay ( $\lambda_{\text{ex}}\ 272\text{ nm}$ ,  $\lambda_{\text{em}}\ 421\text{ nm}$ ; Varioskan

Flash, Thermo Scientific, USA). For every source fluid, a different GG device was used. The photograph of the dye-water gradient was obtained using a VHX-6000 digital microscope (Keyence Deutschland GmbH, Neu-Isenburg, Germany).

### Broth microdilution

Gold standard BMD was performed using the protocols that are recommended by EUCAST, namely ISO 20776-1:2020 standard for bacteria<sup>18</sup> and the EUCAST AFST protocol for yeast.<sup>16</sup> Two-fold dilutions of the antimicrobials in growth medium (CAMHB for bacteria and RPMI 2% G medium for yeast) were prepared in 96 well plates and tested against a standardized cell density of  $5 \times 10^5\text{ cells mL}^{-1}$  (bacteria) or  $10^5\text{ cells mL}^{-1}$  (yeast) unless otherwise stated. For bacterial species, the MIC was determined visually after 18 h incubation at  $37\text{ }^{\circ}\text{C}$  supported by absorbance measurements at 600 nm (Varioskan Flash, Thermo Scientific, USA). The MIC of *C. auris* (yeast) was determined by absorbance measurements at 530 nm after incubation for 24 h at  $37\text{ }^{\circ}\text{C}$ . Every gold standard BMD test was repeated at least three times with  $n \geq 3$  for every concentration tested. Before obtaining the antimicrobial dilutions for the GG-based BMD, the GG device was heat-steam sterilized and employed as described in the previous section. Accordingly, the source fluids ciprofloxacin ( $1\text{ mg L}^{-1}$ ), gentamicin ( $1\text{ mg L}^{-1}$ ), and voriconazole ( $0.25\text{ mg L}^{-1}$ ) in growth medium were diluted by the sink fluid (CAMHB or RPMI 2% G medium) to obtain the desired two-fold dilutions.

### Photonic silicon Chip integration

Silicon chips with microwells (width of approx.  $4\text{ }\mu\text{m}$  and depth of approx.  $4\text{ }\mu\text{m}$ ) were fabricated by laser writing and reactive ion etching technologies at the micro- and nano-fabrication and printing unit (Technion – Israel Institute of Technology.<sup>44</sup> A stepwise protocol for the fabrication procedure of the chips is given in the ESI† (section S2). The chips (diced into  $5 \times 5\text{ mm}$ ) were individually placed into the square-shaped cavities ( $5.1 \times 5.1\text{ mm}$ ) of the GG. UV-curable glue (Norland Optical Adhesive 72, Norland Products Inc., NJ, USA) was carefully applied to the chip backside of the photonic silicon sensor and allowed to cure for 30 min under UV-light at  $365\text{ nm}$  with  $1.5\text{ mW cm}^{-2}$  (VL-6.LC UV lamp 365/254 nm 6 W, Vilber Lourmat, Collégien, France) to seal the system leakage-free. To improve the optical properties, UV-curable lacquer (luxaprint® shellac, DETAX GmbH, Ettlingen, Germany) was applied into rectangular depressions on top of the 3D-printed surfaces above the integrated photonic silicon chips and cured for 5 min under UV-light using the same conditions as for the Norland Optical Adhesive.

### Gradient generator-based PRISM assay

The GG device with integrated photonic silicon chips was placed onto a heat-controlled aluminium sub-structure ( $37\text{ }^{\circ}\text{C}$ ) and connected *via* a 3D-printed adapter to a motorized



linear stage (Thorlabs, Inc., USA) for movement control. 70% ethanol was used to disinfect the system before growth medium (CAMHB) was introduced – allowing devices, temperature, and medium to equilibrate. Subsequently, suspensions of *E. coli* (McFarland 0.5) and 1 mg L<sup>-1</sup> ciprofloxacin (source fluid) and *E. coli* (McFarland 0.5) without antibiotic (sink fluid) were introduced for 5 min. The outlets were then closed (using silicone tubing and Luer adapters), and the bacteria were given 10 min to settle within the microstructure before the optical assay (PRISM) was initiated. Data acquisition and analysis were performed according to our previous work:<sup>43,44</sup> a bifurcated fibre optic (Ocean Optics, USA) equipped with a collimating lens was arranged normal to the photonic silicon chips. Through the bifurcated fibre, the chips were illuminated *via* a HL-2000 white light source (Ocean Optics, USA), and the reflected light was transmitted to a USB4000 CCD spectrometer (Ocean Optics, USA). Fast Fourier transform (FFT) frequency analysis

was performed on the acquired spectra in the range of 450–900 nm. In the resulting peak, the peak position corresponds to the  $2nL$ , where  $n$  represents the refractive index of the medium filling the microstructure and  $L$  the height of the microwells. The  $2nL$  values were plotted *versus* time to monitor bacterial growth. The percent changes of  $2nL$  ( $\Delta 2nL$ ) were calculated as follows:

$$\Delta 2nL (\%) = \frac{2nL - 2nL_0}{2nL_0} \times 100\%;$$

where  $2nL$  is the  $2nL$  value at a given time, and  $2nL_0$  corresponds to the  $2nL$  when the PRISM assay was started.

### Photonic silicon chip characterization

The photonic silicon microstructure was studied by high-resolution scanning electron microscopy (HR-SEM) using a

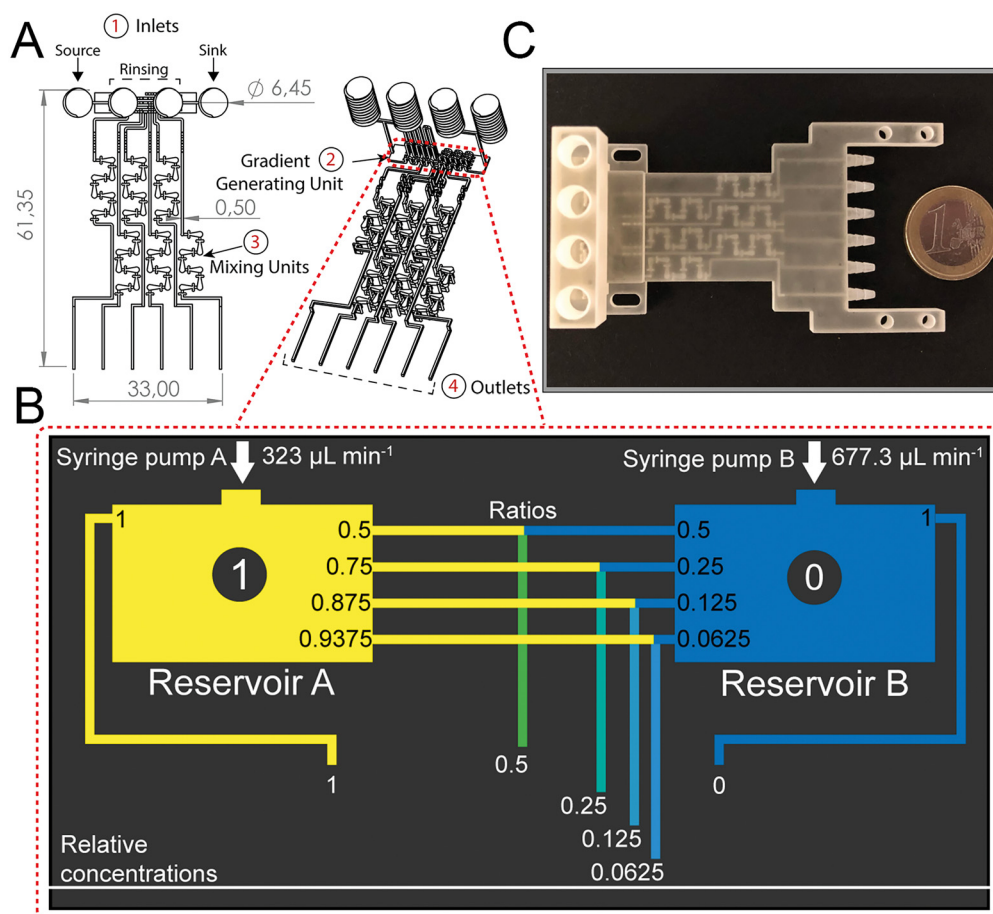


**Fig. 2** Design and principle of the 3D-printed GG for two-fold dilutions dosing. (A) The technical drawing depicts the different modules of the device: (1) inlets to introduce source and sink fluids and rinsing with ethanol, (2) gradient generating unit where the dosing of the required concentrations is achieved, (3) mixing unit with integrated micromixers facilitates homogenous mixing and (4) outlets from where the solutions are collected. Dimensions are shown in millimeters (mm). If not further specified, the microfluidic channels were printed with dimensions of 0.5 mm × 0.5 mm (width × height). The internal volume of the whole device is 455 μL. (B) Schematic presenting the principles of the gradient generating unit. The source fluid is introduced into reservoir A, whereas the sink fluid is pumped into reservoir B. White numbers within the black circle represent the relative concentrations of the source fluid in reservoir A and reservoir B. By adjusting the flow rate ratio according to the channel length ratios (black annotations) of the conjoining horizontal channels, a two-fold dilution series is obtained (white lettering). (C) Photograph of the final 3D-printed GG device after post-processing procedure.



Zeiss Ultra Plus high-resolution scanning microscope (Carl Zeiss, Germany).

## Results and discussion

### Gradient generator principle and design

The design of the 3D-printed GG consists of different functional units (modular design), as illustrated in Fig. 2A. Both source (*e.g.*, antimicrobial solution) and sink (*e.g.*, buffer or medium) fluids are introduced from the outer inlets into the device. The inner inlets serve as a port through which ethanol can be introduced to remove air bubbles and disinfect the device. The gradient generating unit is the core module of the device – this is where the dosing of the required concentrations (*i.e.*, two-fold dilutions) is achieved. In Fig. 2B, the gradient generating principle is schematically illustrated: the source fluid is introduced *via* a syringe pump (at a constant flow rate) into the reservoir A/inlet A, while a second syringe pump likewise introduces the sink fluid into the reservoir B/inlet B. Both these reservoirs are connected by a series of parallel microfluidic channels where the source and sink fluid combine and mix with each other. The concentration dosing is achieved by adjusting the length ratios of these connected channels, based on the simple principle of fluid mechanics, which holds that the longer the channel, the higher the hydrodynamic resistance – resulting in reduced flow rates in comparison to shorter channels.<sup>33,46</sup> For example, when the length of both channels is equivalent (see the first horizontal channel in the center), the sink and source fluids merge at the same flow rate, and dosing of 50% (relative concentration of the source fluid) is achieved. However, when the channel from the sink fluid reservoir is shorter than the channel that transfers the source fluid (see the fourth horizontal channel in the center), the latter is diluted to much lower concentrations (here 6.25%) since it perfuses at a much lower flow rate. Please note that a higher volume of the sink fluid, compared to the source fluid, is required to achieve a two-fold dilution series, and, accordingly, the sink fluid is introduced at a higher flow rate ( $677.3 \mu\text{L min}^{-1}$ ) than the source fluid ( $323 \mu\text{L min}^{-1}$ ). For a detailed step-by-step explanation of the gradient generating principle and how the parallel channel length ratios are adjusted, the reader is referred to the ESI† (see section S3 for equations and description). Also, this section (Fig. S3†) provides additional detailed technical drawings of the GG unit and the micromixers.

From the GG unit, the merged fluids are then transferred to the mixing unit, where the integration of passive HC-micromixers<sup>41</sup> enables homogenous mixing of these solutions emphasized by computational fluid dynamic (CFD) simulations as depicted in Fig. S4.† Homogenous mixing is critical when surface-based sensing elements such as the PRISM silicon chips are integrated into the device for bioanalytical analysis. Our group<sup>47</sup> and others<sup>48,49</sup> have demonstrated that providing uniform analyte concentration to the silicon sensor surface is crucial in minimizing the

analyte depletion and hindered mass transfer. After leaving the mixing unit, the fluids flow towards the outlets, where they are collected for quantification or subsequent AST. According to the GG design, the calculated flow rate at every outlet is  $\sim 166.7 \mu\text{L min}^{-1}$ , and indeed Fig. S5† shows equivalent flow rates at the various outlets with an overall outlet flow rate ( $940 \mu\text{L min}^{-1}$ ) that is consistent with the total inlet flow rate ( $\sim 1000 \mu\text{L min}^{-1}$ ).

### Gradient generator characterization

The dosing accuracy of the GG was studied by conducting CFD simulations and experimental analyses of various model solutions (*i.e.*, dye, glucose, and ciprofloxacin) with distinct properties. For example, dyes are often used to investigate the (mixing) performance in microfluidic systems;<sup>11,31,41</sup> in this work, the dye (blue ink) concentration was quantified by absorbance measurements at 600 nm. Glucose served as a hydrophilic model compound to reflect the behavior of aminoglycoside antibiotics, such as gentamicin, and its concentration was determined using a photometric enzymatic (hexokinase) assay.<sup>50</sup> As a relevant model antibiotic, which is also used in the subsequent AST assays, ciprofloxacin is employed, harnessing its intrinsic fluorescence.<sup>51</sup> Fig. 3A presents a CFD simulation of the device at the designated flow rates and the corresponding photograph of the generated gradient using an aqueous dye solution. Fig. 3B compares the simulated concentration values to those collected experimentally for all three model solutions.

The measured concentrations of the generated solutions depict an accurate two-fold dilution series with high values of the coefficient of determination ( $R^2$  simulation = 0.9995;  $R^2$  dye = 0.9974,  $R^2$  glucose = 0.998, and  $R^2$  ciprofloxacin = 0.9929) which are comparable to accuracies presented in previously published GG systems.<sup>8,12</sup> The results also suggest that possible adsorption effects of the solutions to the 3D-printing material are negligible. The small differences in the determined concentrations for the different source fluids are ascribed to slight deviations in the channel dimensions that may influence the network of finely balanced channel lengths (ratios) and effectively also the concentrations at the outlets. Please refer to Table S1† for further information on the printing accuracy.

### GG-enabled AST

The successful miniaturization, integration, and automation of the various steps required in AST methods (*e.g.*, generation of two-fold antimicrobial dilution series, cell inoculum, sensing, and MIC determination) are considered essential prerequisites for providing rapid and easy-to-use AST assays for point-of-care applications.<sup>14,52</sup> We thus envisioned a microfluidic system that automatically generates the desired antimicrobial concentrations and also integrates the sensing elements for convenient and time-saving real-time optical AST directly within the microfluidic channels of the GG-system. Before integrating photonic silicon chips as sensing



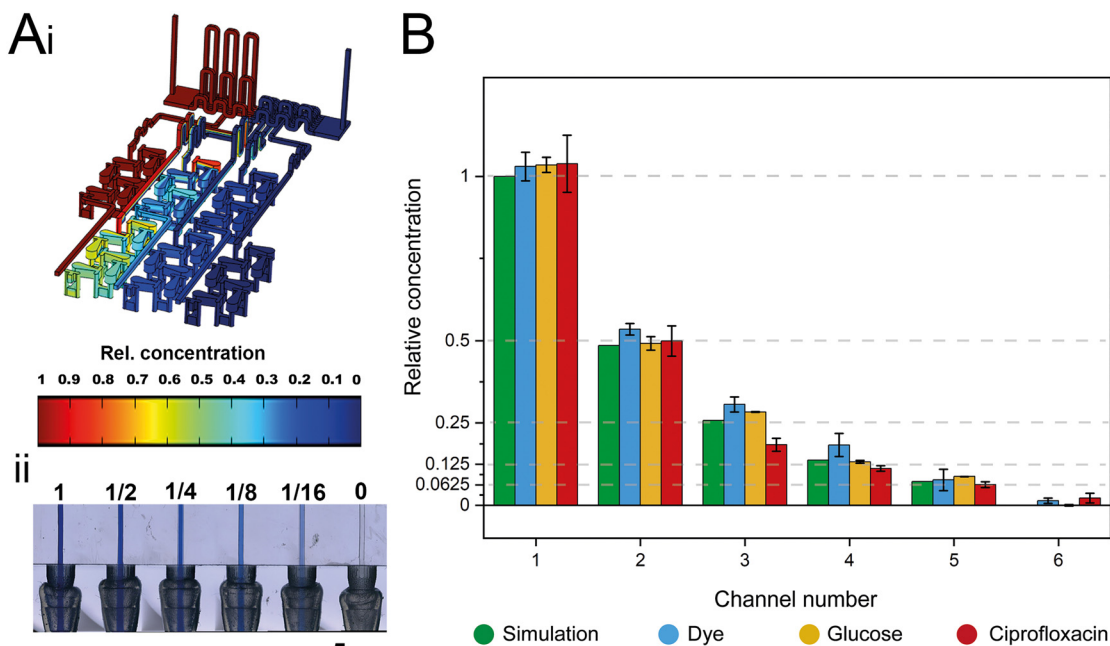


**Fig. 3** Characterization of the gradient generator using simulation and experimental gradient generating accuracy studies. (A-i) CFD simulation using COMSOL Multiphysics® at a total flow rate of  $1000 \mu\text{L min}^{-1}$ . (A-ii) Photograph at the outlets of the 3D-printed gradient generator depicting a two-fold dilution gradient using dye (source) and water (sink). (B) Relative concentrations for the six channels determined by CFD simulation and experimental studies using a dye (blue ink), glucose, and ciprofloxacin as source solutions. Error bars indicate the standard deviation of three consecutive experiments. Dashed lines indicate desired concentrations for each outlet.

elements for on-chip AST into our device, we first test the compatibility of the 3D-printed GG with the gold-standard BMD assay (schematically illustrated in Fig. 1A). We used three clinically-relevant model pathogen-drug combinations – namely, *S. marcescens* vs. ciprofloxacin, *E. coli* vs. gentamicin, and *C. auris* vs. voriconazole. *S. marcescens* and *E. coli* are both Gram-negative bacteria that can cause, among other serious ailments, urinary tract infections (UTIs), diarrheal diseases, pneumonia, and sepsis;<sup>53,54</sup> their susceptibility was tested against antibiotics with different modes of action. While ciprofloxacin (fluoroquinolone) inhibits the gyrase enzyme, which plays an essential role in DNA replication,<sup>55</sup> gentamicin (aminoglycoside) binds to the 30S subunit of the ribosomes and thus inhibits the protein biosynthesis.<sup>56</sup> As a fungal pathogen, *C. auris* (an opportunistic yeast) causes severe invasive infections and shows alarming rates of acquired antifungal resistance;<sup>57,58</sup> it was studied against the antifungal drug voriconazole, which inhibits the ergosterol synthesis (crucial cell wall component) and is applied for invasive candidiasis and aspergillosis treatment.<sup>59</sup> From the gradient generator, five consecutively obtained fractions (F1–F5) were collected for every tested concentration (GG-enabled BMD), and the attained relative growth values for all pathogen-drug combinations are presented in Fig. 4 and compared to reference BMD results (see grey panels). Although at least at subinhibitory antimicrobial concentrations, the growth behaviour can deviate between fractions, the MIC values that were calculated for the GG-

enabled BMD – defined as the lowest drug concentration which completely inhibits the growth (bacteria) or induces 50% growth inhibition (yeast) – were accurately determined. Moreover, they agree with the reference BMD and MIC values published by the European Commission for Antimicrobial Susceptibility Testing (EUCAST); see Table S3† for a detailed summary and comparison. Accordingly, we determined that this GG allows for MIC determination of antimicrobials in a concentration range of  $0.016 \text{ mg L}^{-1}$  to  $0.125 \text{ mg L}^{-1}$ , which is suitable for the vast majority of drug-pathogen combinations according to EUCAST.<sup>60</sup> To allow for a complete on-chip AST, we modified the 3D-printed GG to include “growth chambers”, which house the PRISM photonic silicon chips, as shown in Fig. 5A-i and S6A.† These PRISM chips are diffraction gratings consisting of periodic arrays of square-shaped microwells, with dimensions of  $\sim 4 \times 4 \mu\text{m}$ , as depicted by the scanning electron micrograph in Fig. 5A-ii.

We demonstrate that the integration of these optical sensing elements does not impair the dosing performance of the 3D-printed GG (see Fig. S6B†), where the obtained coefficients of determination ( $R^2$ ) are  $>0.994$ , similar to the results obtained for the GG itself (Fig. 3B). Next, we conducted a proof-of-concept on-chip AST study, where we chose *E. coli* as our model pathogen, in light of the major role it plays in causing UTIs (85–95% of reported cases) and severe sepsis (17% of reported cases)<sup>61</sup> and the emergence of drug-resistant *E. coli* variants.<sup>62,63</sup> The principle of the on-



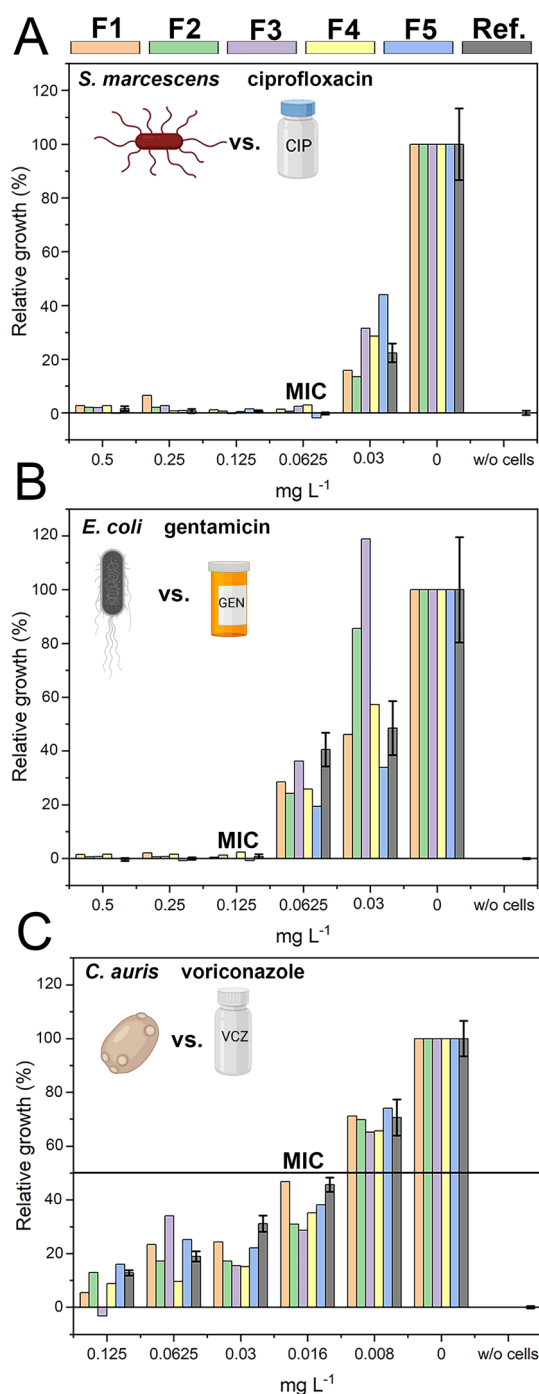


**Fig. 4** Comparison of GG-enabled BMD and manual reference BMD for AST of (A) *S. marcescens* and ciprofloxacin, (B) *E. coli* K12 and gentamicin and (C) *C. auris* and voriconazole. For bacterial species, the MIC is defined as the lowest drug concentration that inhibits bacterial growth determined visually and supported by absorbance measurements at 600 nm. For *C. auris*, the MIC is defined as the lowest drug concentration that induces a 50% growth inhibition obtained from absorbance measurements at 530 nm, as emphasized by the threshold line. For the GG-enabled BMD, five separately and consecutively collected fractions (F1–F5) were tested against the respective pathogens. For all reference BMD tests (ref.), every concentration was tested with  $n \geq 3$ ; error bars depict the standard deviation of these measurements. Growth in the absence of drug was defined as 100% growth.

chip PRISM assay was as follows: In the GG-based PRISM AST, *E. coli* and the highest tested antibiotic concentration (here ciprofloxacin at 1 mg L<sup>-1</sup>) were both introduced into inlet A (Fig. 5A-i), while only *E. coli* was introduced into inlet B. Both suspensions were introduced into the heat-controlled device at the designated flow rates for 5 min; the dosing was achieved in the GG unit, and in the mixing unit, the suspensions were homogeneously mixed before being transferred onto the “growth chambers” that house the photonic silicon chips. Please refer to the ESI† (Fig. S7) demonstrating that such an experimental procedure in which *E. coli* is exposed to the highest tested ciprofloxacin concentration for 5 min before being diluted to the designated antibiotic concentrations does not result in flawed MIC values. The assay was operated at a cell density value of McFarland 0.5 (a turbidity standard corresponding to  $\sim 10^8$  cells mL<sup>-1</sup>), which is of high clinical relevance and used to standardize the cell density in most clinical AST assays<sup>18,64,65</sup> and is either directly used for inoculation (agar-based *E-test*)<sup>65</sup> or further diluted (BMD and state-of-the-art automated Vitek 2),<sup>18,66</sup> as detailed in the ESI† Table S4. By avoiding the additional dilution step and directly using a cell suspension at McFarland 0.5, the assay is simplified and tailored for current clinical procedures and involves minimal handling, which improves reproducibility and allows for high throughput. Also, higher cell densities potentially allow a faster time to growth detection and may better reflect clinically relevant scenarios as microbial infections in the human body are often caused by bacterial biofilms (large number of interacting cells).<sup>67</sup>

The PRISM assay enables real-time monitoring of bacterial growth by analyzing changes in the reflectance spectra of the photonic chip over time.<sup>43,68</sup> Fig. 5A-iii shows a characteristic reflectance spectrum at a single time point, which is analyzed to track bacterial growth by monitoring the  $2nL$  value (where  $n$  is the refractive index of the medium within the periodic microwells, and  $L$  represents the depth of the wells) as detailed in Fig. 1B. The resulting PRISM curves, depicting a continuous change in  $2nL$  vs. time, allow sensitive and quantitative detection of changes in bacterial growth upon exposure to antibiotics (see Fig. 5B-i). The MIC value is defined as the lowest drug concentration at which no increase in the  $2nL$  occurs. Fig. 5B-i displays characteristic PRISM curves of *E. coli* upon exposure to varying ciprofloxacin concentrations generated on-chip (at a range of 0–1 mg L<sup>-1</sup>), where the percent changes in  $2nL$  ( $\Delta 2nL$ ) are plotted over time. For both no and low antibiotic concentrations (0–0.125 mg L<sup>-1</sup>), a continuous increase in  $\Delta 2nL$  is observed (slope:  $\sim 0.05 \Delta 2nL \text{ h}^{-1}$ ), while at elevated drug concentrations (0.25–0.5 mg L<sup>-1</sup>), the slope values decrease ( $\sim 0.03 \Delta 2nL \text{ h}^{-1}$ ), indicative of hindered bacterial growth. At a concentration of 1 mg L<sup>-1</sup> ciprofloxacin, the slope remains largely unchanged, and as such, the PRISM MIC value is determined to be 1 mg L<sup>-1</sup>. Fig. 5B-ii summarizes the attained  $\Delta 2nL$  values after 90 min from three independent PRISM experiments, and statistical analysis



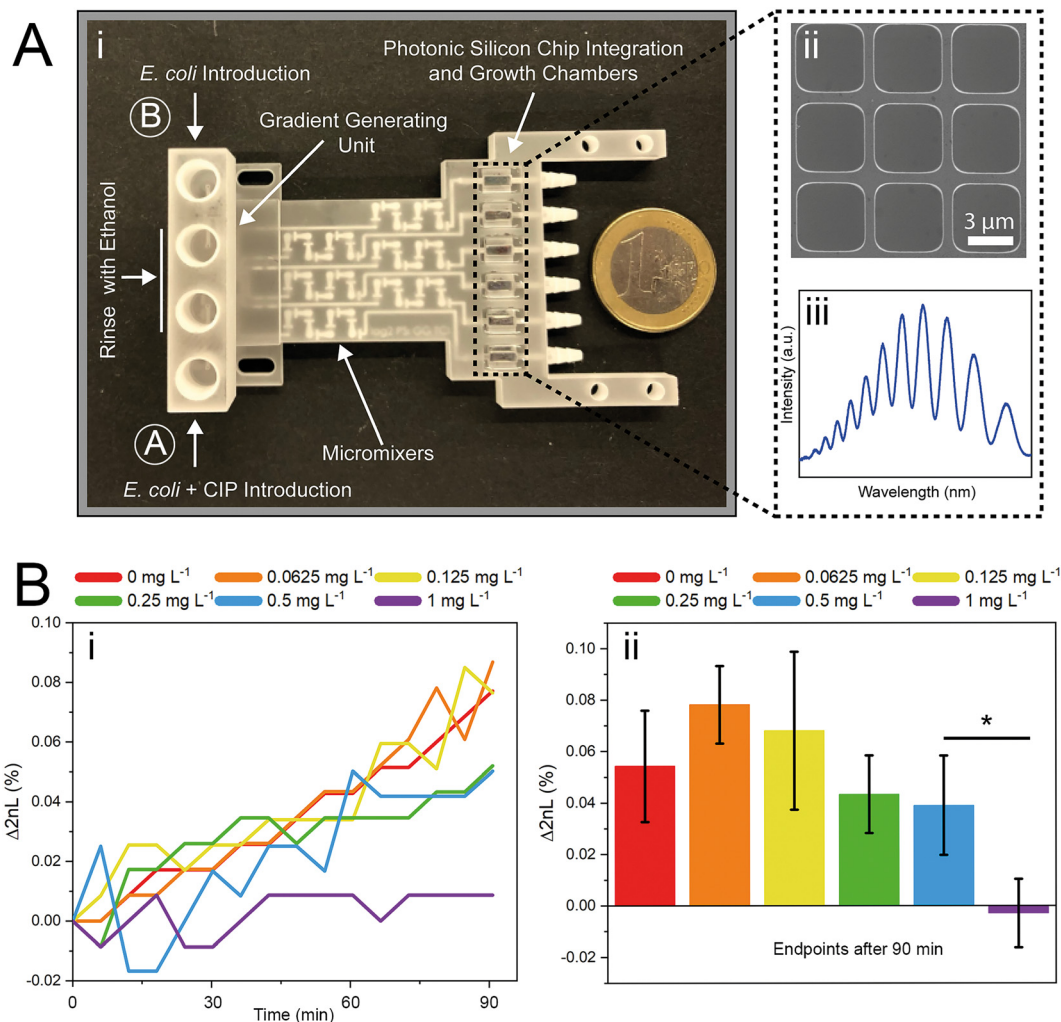


**Fig. 5** 3D-printed gradient generator for PRISM experiments. (A-i) A photograph of the 3D-printed gradient generator device depicts the different modules of the device, including a square-shaped ( $5.01 \times 5.01$  mm) unit for photonic silicon chip integration. The black dashed rectangle emphasizes the integrated photonic silicon chips that (A-ii) feature a silicon diffraction grating of microwells with a width of  $\sim 4$   $\mu\text{m}$  and a depth of  $\sim 4$   $\mu\text{m}$  and (A-iii) allows obtaining reflectivity spectra with characteristic interference fringes. (B-i) Characteristic PRISM growth curves ( $\Delta 2nL$  over time) from the six growth chambers of the gradient generator for a two-fold dilution series ( $0$ – $1$   $\text{mg L}^{-1}$ ) of ciprofloxacin (CIP) against *E. coli*. (B-ii)  $\Delta 2nL$  (%) endpoints from three experiments (error bars = standard deviation) demonstrate that the MIC value can be determined within 90 min.

**Table 2** MIC value for *E. coli* and ciprofloxacin obtained from the GG-based PRISM assay compared to other (reference) AST methods

Method	Inoculum	MIC	Time
PRISM (gradient generator)	McF. $0.5$ ( $\sim 10^8$ cells $\text{mL}^{-1}$ )	$1$ $\text{mg L}^{-1}$	$90$ min <sup>a</sup>
Non-gradient PRISM (aluminum flow cell)	$10^7$ cells $\text{mL}^{-1}$	$0.05$ $\text{mg L}^{-1b}$	$2$ – $3$ h <sup>a,b</sup>
Vitek 2	$\sim 10^7$ cells $\text{mL}^{-1}$	$\leq 0.25$ $\text{mg L}^{-1b}$	$8$ h <sup>b</sup>
BMD	$5 \times 10^5$ cells $\text{mL}^{-1}$ (used in reference BMD)	$0.016$ $\text{mg L}^{-1}$	$18$ h
BMD	McF. $0.5$ ( $\sim 10^8$ cells $\text{mL}^{-1}$ )	$0.25$ – $0.5$ $\text{mg L}^{-1}$	$18$ h

<sup>a</sup> The reduced assay time of 90 min compared to 2–3 h is ascribed to the higher cell concentration (shift from  $10^7$  cells  $\text{mL}^{-1}$  to  $\sim 10^8$  cells  $\text{mL}^{-1}$ ), which facilitates a more rapid signal detection. <sup>b</sup> Value retrieved from our previous work.<sup>43</sup>

(*t*-test) reveals significant differences between the MIC and subinhibitory concentrations within 90 min.

Note also that the MIC determined by this on-chip PRISM assay is higher compared to reference methods (see Table 2), including both BMD and the automated Vitek 2 test. This deviation is mainly attributed to differences in the inoculum

size, where larger initial inoculum is shown to result in higher MIC values for many antibiotics,<sup>69</sup> including ciprofloxacin.<sup>70–72</sup>

For example, Davey and Barza demonstrated that increasing the inoculum from  $10^5$  to  $10^7$  CFU  $\text{mL}^{-1}$  results in a 4 to 32-fold higher MIC value for *E. coli* and ciprofloxacin depending on the tested strain.<sup>71</sup> We demonstrate that this effect is also





apparent for the BMD (Table 2); when changing the cell density from  $5 \times 10^5$  cells mL<sup>-1</sup> to  $\sim 10^8$  (McFarland 0.5), the MIC value increases from 0.016 to 0.25–0.5 mg L<sup>-1</sup>.

Yet, the obtained MIC for the GG-enabled PRISM assay is  $\sim$ two-fold higher (1 mg L<sup>-1</sup>) in comparison to the latter values; this is ascribed to the obvious differences in the growth environment. While the BMD analyzes bacterial growth in a liquid medium, the PRISM assay monitors bacteria behavior on and within the silicon microtopologies – which, in fact, may reflect more clinically-relevant scenarios since an estimated  $\sim$ 80% of chronic and recurrent microbial infections in the human body are due to bacterial biofilms.<sup>67</sup> Thus, the higher MIC values did not impair the functionality of the assay, and we suggest calibrating our system for important pathogen-drug combinations with strains that are known to be susceptible or resistant. Isolates with unknown behavior could be classified in accordance with their MIC into “resistant” and “susceptible” categories while still benefitting from the profoundly accelerated ( $\leq 90$  min) MIC determination at higher cell densities. It should be noted that such calibration is required for all AST methods, including the gold-standard BMD,<sup>73</sup> as well as the automated systems, such as the Vitek 2.<sup>74</sup>

In comparison to other recently developed microfluidic AST systems, which often still require several hours for completion,<sup>9,10,22,24,28</sup> our GG-based PRISM assay enables rapid analysis within 90 min with minimal sample handling. It is equivalent or inferior in terms of assay time to some microfluidic AST methods relying on sophisticated single-cell analyses.<sup>13,75,76</sup> For example, single-cell imaging of bacteria entrapped in microfluidic channels allowed to differentiate between resistant and susceptible isolates by monitoring their growth at breakpoint antibiotic concentrations within only 30 min.<sup>26</sup> Indeed, working at the single cell level allows to detect changes at high resolution (*e.g.*, in the cell morphology) in short timescales, in contrast to phenotypic tests based on detecting bulk bacterial growth. Yet, it is controversial whether the behavior of single immobilized or confined (in a microchannel) cells is representative of a bacterial population,<sup>76</sup> and as such how many cells should be analyzed.<sup>75</sup> In contrast to the latter methods, the PRISM signal represents the averaged behavior of a large population of cells, colonizing on the chip that are free to move, interact and form a community. Moreover, the method is label-free and does not require additional reagents as many microfluidic-assisted phenotypic AST techniques *e.g.*, resazurin for metabolic analysis,<sup>28,75,76</sup> and it employs a simple and portable optical setup, which can be further miniaturized.

Thus, while assay time is a critical parameter for AST, there are many considerations that should be carefully weighed when designing a clinically applicable AST technique for point-of-care settings.

## Conclusions

In this paper, we demonstrate a 3D-printed microfluidic gradient generator that is suitable for rapid and label-free

phenotypic AST using integrated photonic silicon chips. Both the performance and accuracy of this GG device were comprehensively assessed and confirmed using several different model fluids, and GG-enabled BMD testing was conducted using three different pathogen-drug combinations.

For rapid optical AST, the bacteria were colonized on microstructured photonic silicon chips – which, when integrated into the GG-system, also provided the optical transducer elements. Bacterial growth at defined antibiotic concentrations was monitored in real-time by observing changes in the reflectivity spectra collected from the photonic silicon chips. Using the GG-based PRISM assay and *E. coli* and ciprofloxacin as a model pathogen-drug combination, we demonstrated that MIC value determination is feasible within 90 min. Therefore, this assay is significantly faster than the current gold standard BMD and classical agar-based methods ( $\geq 16$  h), and we believe that it paves a clear path toward more convenient and expeditious point-of-care AST procedures.

To the best of our knowledge, this is the first demonstration of a microfluidic GG-device that automatically creates desired and clinically relevant two-fold antimicrobial dilutions integrated with an optical sensing element for label-free phenotypic monitoring of bacterial behavior. While this assay was demonstrated for *E. coli* and ciprofloxacin, we envision that it could potentially be extended to a number of other species and antimicrobials as well – since we have shown that AST of different pathogen-drug combinations on these photonic silicon chips is feasible.<sup>43,44</sup>

We acknowledge that the MIC value obtained from the GG-based PRISM assay is higher than that obtained using reference methods, and also that calibration of our system will be required to guide clinical treatment decisions. Accordingly, future research on calibrating our platform with pathogens of known resistant or susceptible behavior will be required. In the future, however, we envision that GG design will be flexibly adjusted (*i.e.*, *via* rapid prototyping achieved through 3D printing) for other gradients (*e.g.*, linear) as well as through the integration of different sensing elements. This would facilitate rapid characterization of various (bio)sensors – in terms of both binding affinities and performance – under varying conditions, including different buffer compositions and target concentrations.

## Author contributions

C. H. and J.-A. P. contributed equally. Conceptualization: C. H. and J.-A. P.; methodology: C. H., J.-A. P., and M. B.; investigation: C. H., J.-A. P., and M. B.; data curation: C. H.; writing-original draft preparation: J.-A. P. and C. H.; writing-review and editing: C. H., J.-A. P., T. S., E. S., and J. B.; visualization: C. H. and J.-A. P.; supervision: E. S., T. S., and J. B.; project administration: E. S. and J. B.; funding acquisition: J. B., T. S. and E. S.



## Conflicts of interest

There are no conflicts to declare.

## Acknowledgements

This research was funded by the German Research Foundation (DFG) via the Emmy Noether program (project ID 346772917), by the VolkswagenStiftung via the program “Niedersächsisches Vorab: Research Cooperation Lower Saxony—Israel”, and by the DFG via the grant SCHE 279/32-2. We also wish to thank Dima Peselev and Orna Ternyak of the Technion's at the micro- and nano-fabrication and printing unit for the microfabrication of the photonic silicon chips. Part of the cartoons in Fig. 1 and 4 were obtained from <https://BioRender.com> under a publishing license. The open access publication of this article was supported by the DFG sponsored Open Access Fund of the University of Augsburg.

## References

- 1 T. K. Burki, *Lancet Respir. Med.*, 2018, **6**, 668.
- 2 D. A. Gray and M. Wenzel, *ACS Infect. Dis.*, 2020, **6**, 1346–1385.
- 3 Antimicrobial Resistance Collaborators, *Lancet*, 2022, **399**, 629–655.
- 4 Interagency Coordination Group on Antimicrobial Resistance, No time to wait: Securing the future from drug-resistant infections. Report to the secretary-general of the United Nations, [https://www.who.int/docs/default-source/documents/no-time-to-wait-securing-the-future-from-drug-resistant-infections-en.pdf?sfvrsn=5b424d7\\_6](https://www.who.int/docs/default-source/documents/no-time-to-wait-securing-the-future-from-drug-resistant-infections-en.pdf?sfvrsn=5b424d7_6), (accessed 17 June 2022).
- 5 S. Doron and L. E. Davidson, *Mayo Clin. Proc.*, 2011, **86**, 1113–1123.
- 6 J. Carlet, V. Jarlier, S. Harbarth, A. Voss, H. Goossens and D. Pittet, *Antimicrob. Resist. Infect. Control*, 2012, **1**, 1–13.
- 7 M. DiCicco and S. Neethirajan, *BioChip J.*, 2014, **8**, 282–288.
- 8 H. Shi, Z. Hou, Y. Zhao, K. Nie, B. Dong, L. Chao, S. Shang, M. Long and Z. Liu, *Chem. Eng. J.*, 2019, **359**, 1327–1338.
- 9 W. Zeng, P. Chen, S. Li, Q. Sha, P. Li, X. Zeng, X. Feng, W. Du and B.-F. Liu, *Biosens. Bioelectron.*, 2022, **205**, 114100.
- 10 Y. Im, S. Kim, J. Park, H. J. Sung and J. S. Jeon, *Lab Chip*, 2021, **21**, 3449–3457.
- 11 E. Sweet, B. Yang, J. Chen, R. Vickerman, Y. Lin, A. Long, E. Jacobs, T. Wu, C. Mercier, R. Jew, Y. Attal, S. Liu, A. Chang and L. Lin, *Microsyst. Nanoeng.*, 2020, **6**, 92.
- 12 S. C. Kim, S. Cestellos-Blanco, K. Inoue and R. N. Zare, *Antibiotics*, 2015, **4**, 455–466.
- 13 H. Leonard, R. Colodner, S. Halachmi and E. Segal, *ACS Sens.*, 2018, **3**, 2202–2217.
- 14 C. Heuer, J. Bahnemann, T. Scheper and E. Segal, *Small Methods*, 2021, **5**, 2100713.
- 15 A. van Belkum, C. A. D. Burnham, J. W. A. Rossen, F. Mallard, O. Rochas and W. M. Dunne, *Nat. Rev. Microbiol.*, 2020, **18**, 299–311.
- 16 EUCAST, EUCAST definitive document E.DEF 7.3.2 Method for the determination of broth dilution minimum inhibitory concentrations of antifungal agents for yeasts, [https://www.eucast.org/fileadmin/src/media/PDFs/EUCAST\\_files/AFST/Files/EUCAST\\_E\\_Def\\_7.3.2\\_Yeast\\_testing\\_definitive\\_revised\\_2020.pdf](https://www.eucast.org/fileadmin/src/media/PDFs/EUCAST_files/AFST/Files/EUCAST_E_Def_7.3.2_Yeast_testing_definitive_revised_2020.pdf), (accessed 17 June 2022).
- 17 EUCAST, EUCAST disk diffusion method for antimicrobial susceptibility testing, [https://www.eucast.org/fileadmin/src/media/PDFs/EUCAST\\_files/Disk\\_test\\_documents/2022\\_manuals/Manual\\_v\\_10.0\\_EUCAST\\_Disk\\_Test\\_2022.pdf](https://www.eucast.org/fileadmin/src/media/PDFs/EUCAST_files/Disk_test_documents/2022_manuals/Manual_v_10.0_EUCAST_Disk_Test_2022.pdf), (accessed 17 June 2022).
- 18 International Organization for Standardization, ISO 20776-1:2020.
- 19 CLSI, M100Ed32 | Performance Standards for Antimicrobial Susceptibility Testing, 32nd Edition, <https://clsi.org/standards/products/microbiology/documents/m100/>, (accessed 17 June 2022).
- 20 N. Qin, P. Zhao, E. A. Ho, G. M. Xin and C. L. Ren, *ACS Sens.*, 2021, **6**, 3–21.
- 21 Z. A. Khan, M. F. Siddiqui and S. Park, *Biotechnol. Lett.*, 2019, **41**, 221–230.
- 22 L. Y. Ma, M. Petersen and X. N. Lu, *Appl. Environ. Microbiol.*, 2020, **86**, e00096-20.
- 23 Y. Liu, T. Lehnert, T. Mayr and M. A. M. Gijs, *Lab Chip*, 2021, **21**, 3520–3531.
- 24 W. T. Qiu and S. Nagl, *ACS Sens.*, 2021, **6**, 1147–1156.
- 25 D. C. Spencer, T. F. Paton, K. T. Mulrone, T. J. J. Inglis, J. M. Sutton and H. Morgan, *Nat. Commun.*, 2020, **11**, 5328.
- 26 Ö. Baltekin, A. Boucharin, E. Tano, D. I. Andersson and J. Elf, *Proc. Natl. Acad. Sci. U. S. A.*, 2017, **114**, 9170–9175.
- 27 K. W. Chang, H. W. Cheng, J. Shiue, J. K. Wang, Y. L. Wang and N. T. Huang, *Anal. Chem.*, 2019, **91**, 10988–10995.
- 28 J. Avesar, D. Rosenfeld, M. Truman-Rosentsvit, T. Ben-Arye, Y. Geffen, M. Bercovici and S. Levenberg, *Proc. Natl. Acad. Sci. U. S. A.*, 2017, **114**, E5787–E5795.
- 29 K. Churski, T. S. Kaminski, S. Jakiela, W. Kamysz, W. Baranska-Rybak, D. B. Weibel and P. Garstecki, *Lab Chip*, 2012, **12**, 1629–1637.
- 30 M. Azizi, A. V. Nguyen, B. Dogan, S. Zhang, K. W. Simpson and A. Abbaspourrad, *ACS Appl. Mater. Interfaces*, 2021, **13**, 19581–19592.
- 31 M. Azizi, B. Davaji, A. V. Nguyen, S. Zhang, B. Dogan, K. W. Simpson and A. Abbaspourrad, *ACS Sens.*, 2021, **6**, 1560–1571.
- 32 M. H. Tang, X. Y. Huang, Q. Chu, X. H. Ning, Y. Y. Wang, S. K. Kong, X. P. Zhang, G. H. Wang and H. P. Ho, *Lab Chip*, 2018, **18**, 1452–1460.
- 33 J. M. Cabaleiro, *Chem. Eng. J.*, 2020, **382**, 122742.
- 34 3D systems, VisiJet M2S-HT90 (MJP), <https://www.3dsystems.com/materials/visijet-m2s-ht90-mjp>, (accessed 17 June 2022).
- 35 T. Habib, C. Brämer, C. Heuer, J. Ebbecke, S. Beutel and J. Bahnemann, *Lab Chip*, 2022, **22**, 986–993.
- 36 S. Arshavsky-Graham, A. Enders, S. Ackerman, J. Bahnemann and E. Segal, *Microchim. Acta*, 2021, **188**, 1–12.
- 37 A. Enders, J. A. Preuss and J. Bahnemann, *Micromachines*, 2021, **12**, 1060.
- 38 S. R. Bazaz, O. Rouhi, M. A. Raoufi, F. Ejeian, M. Asadnia, D. Y. Jin and M. E. Warkiani, *Sci. Rep.*, 2020, **10**, 5929.



- 39 P. Panjan, V. Virtanen and A. M. Sesay, *Analyst*, 2018, **143**, 3926–3933.
- 40 N. Bhattacharjee, A. Urrios, S. Kanga and A. Folch, *Lab Chip*, 2016, **16**, 1720–1742.
- 41 A. Enders, I. G. Siller, K. Urmann, M. R. Hoffmann and J. Bahnemann, *Small*, 2019, **15**, 1804326.
- 42 N. P. Macdonald, J. M. Cabot, P. Smejkal, R. M. Guijt, B. Paull and M. C. Breadmore, *Anal. Chem.*, 2017, **89**, 3858–3866.
- 43 H. Leonard, S. Halachmi, N. Ben-Dov, O. Nativ and E. Segal, *ACS Nano*, 2017, **11**, 6167–6177.
- 44 C. Heuer, H. Leonard, N. Nitzan, A. Lavy-Alperovitch, N. Massad-Ivanir, T. Scheper and E. Segal, *ACS Infect. Dis.*, 2020, **6**, 2560–2566.
- 45 M. H. V. Werts, V. Raimbault, R. Texier-Picard, R. Poizat, O. Français, L. Griscom and J. R. G. Navarro, *Lab Chip*, 2012, **12**, 808–820.
- 46 K. W. Oh, K. Lee, B. Ahn and E. P. Furlani, *Lab Chip*, 2012, **12**, 515–545.
- 47 S. Arshavsky Graham, E. Boyko, R. Salama and E. Segal, *ACS Sens.*, 2020, **5**, 3058–3069.
- 48 Y. Zhao, G. Gaur, S. T. Retterer, P. E. Laibinis and S. M. Weiss, *Anal. Chem.*, 2016, **88**, 10940–10948.
- 49 T. M. Squires, R. J. Messinger and S. R. Manalis, *Nat. Biotechnol.*, 2008, **26**, 417–426.
- 50 Roche Custom Biotech, Glucose Bio Test kit for the Cedex Bio Analyzer, <https://custombiotech.roche.com/global/en/products/cb/glucose-bio-3810241.html>, (accessed 17 June 2022).
- 51 S. N. Muchohi, N. Thuo, J. Karisa, A. Muturi, G. O. Kokwaro and K. Maitland, *J. Chromatogr., B*, 2011, **879**, 146–152.
- 52 A. Vasala, V. P. Hytonen and O. H. Laitinen, *Front. Cell. Infect. Microbiol.*, 2020, **10**, 308.
- 53 S. D. Mahlen, *Clin. Microbiol. Rev.*, 2011, **24**, 755–791.
- 54 J. B. Kaper, J. P. Nataro and H. L. T. Mobley, *Nat. Rev. Microbiol.*, 2004, **2**, 123–140.
- 55 L. M. Fisher, J. M. Lawrence, I. C. Josty, R. Hopewell, E. E. C. Margerrison and M. E. Cullen, *Am. J. Med.*, 1989, **87**, S2–S8.
- 56 K. M. Krause, A. W. Serio, T. R. Kane and L. E. Connolly, *Cold Spring Harbor Perspect. Med.*, 2016, **6**, a027029.
- 57 A. S. Sultan, T. Villa, D. Montelongo-Jauregui and M. A. Jabra-Rizk, *Clin. Infect. Dis.*, 2021, **72**, 178–179.
- 58 B. L. Wickes, *J. Clin. Microbiol.*, 2020, **58**, e02083-19.
- 59 L. B. Johnson and C. A. Kauffman, *Clin. Infect. Dis.*, 2003, **36**, 630–637.
- 60 EUCAST, EUCAST wild-type distribution, [https://mic.eucast.org/search/?search%5Bmethod%5D=mic&search%5Bantibiotic%5D=-1&search%5Bspecies%5D=261&search%5Bdisk\\_content%5D=-1&search%5Blimit%5D=50](https://mic.eucast.org/search/?search%5Bmethod%5D=mic&search%5Bantibiotic%5D=-1&search%5Bspecies%5D=261&search%5Bdisk_content%5D=-1&search%5Blimit%5D=50), (accessed 17 June 2022).
- 61 T. A. Russo and J. R. Johnson, *Microbes Infect.*, 2003, **5**, 449–456.
- 62 Z. Peng, Z. Hu, Z. Li, X. Zhang, C. Jia, T. Li, M. Dai, C. Tan, Z. Xu, B. Wu, H. Chen and X. Wang, *Nat. Commun.*, 2022, **13**, 1116.
- 63 A. McNally, T. Kallonen, C. Connor, K. Abudahab, D. M. Aanensen, C. Horner, S. J. Peacock, J. Parkhill, N. J. Croucher and J. Corander, *MBio*, 2019, **10**, e00644-19.
- 64 E. A. Idelevich, I. Schüle, B. Grünastel, J. Wüllenweber, G. Peters and K. Becker, *J. Clin. Microbiol.*, 2014, **52**, 4058–4062.
- 65 bioMérieux, Etest Application Guide, [https://www.biomerieux-usa.com/sites/subsidiary\\_us/files/supplementary\\_inserts\\_-\\_b\\_-\\_en\\_-\\_eag\\_-\\_etest\\_application\\_guide-3.pdf](https://www.biomerieux-usa.com/sites/subsidiary_us/files/supplementary_inserts_-_b_-_en_-_eag_-_etest_application_guide-3.pdf), (accessed 17 June 2022).
- 66 M. Ligozzi, C. Bernini, M. G. Bonora, M. de Fatima, J. Zuliani and R. Fontana, *J. Clin. Microbiol.*, 2002, **40**, 1681–1686.
- 67 D. Sharma, L. Misba and A. U. Khan, *Antimicrob. Resist. Infect. Control*, 2019, **8**, 1–10.
- 68 H. Leonard, X. Jiang, S. Arshavsky-Graham, L. Holtzman, Y. Haimov, D. Weizman, S. Halachmi and E. Segal, *Nanoscale Horiz.*, 2022, **7**, 729–742.
- 69 I. Brook, *Rev. Infect. Dis.*, 1989, **11**, 361–368.
- 70 I. Morrissey and J. T. George, *J. Antimicrob. Chemother.*, 1999, **43**, 423–425.
- 71 P. G. Davey and M. Barza, *J. Antimicrob. Chemother.*, 1987, **20**, 639–644.
- 72 R. J. Fass, *Antimicrob. Agents Chemother.*, 1983, **24**, 568–574.
- 73 EUCAST, Clinical breakpoints - breakpoints and guidance, [https://www.eucast.org/clinical\\_breakpoints/](https://www.eucast.org/clinical_breakpoints/), (accessed 17 June 2022).
- 74 bioMérieux, How does VITEK® 2 Generate MIC Values? - BIOMÉRIEUX iNEWS, <https://www.biomerieux-microbio.com/how-does-vitek-2-generate-mic-values/>, (accessed 17 June 2022).
- 75 W. Postek, N. Pacocha and P. Garstecki, *Lab Chip*, 2022, **22**, 3637–3662.
- 76 K. Syal, M. N. Mo, H. Yu, R. Iriya, W. W. Jing, G. Sui, S. P. Wang, T. E. Gryns, S. E. Haydel and N. J. Tao, *Theranostics*, 2017, **7**, 1795–1805.



## Supporting Information

### A 3D-Printed Microfluidic Gradient Generator with Integrated Photonic Silicon Sensors for Rapid Antimicrobial Susceptibility Testing

Christopher Heuer<sup>†,a,c</sup>, John-Alexander Preuss<sup>†,a,b</sup>, Marc Buttkewitz<sup>a</sup>, Thomas Scheper<sup>a</sup>, Ester Segal<sup>c\*</sup> and Janina Bahnemann<sup>a,b\*</sup>

<sup>a</sup> Institute of Technical Chemistry, Leibniz University Hannover, 30167 Hannover, Germany

<sup>b</sup> Institute of Physics, University of Augsburg, 86159 Augsburg, Germany, \*email: janina.bahnemann@uni-a.de

<sup>c</sup> Department of Biotechnology and Food Engineering, Technion – Israel Institute of Technology, 320003 Haifa, Israel, \*email: esegal@technion.ac.il

† Christopher Heuer and John-Alexander Preuss contributed equally to this work

#### S1. 3D Printing: Orientation and Repeatability

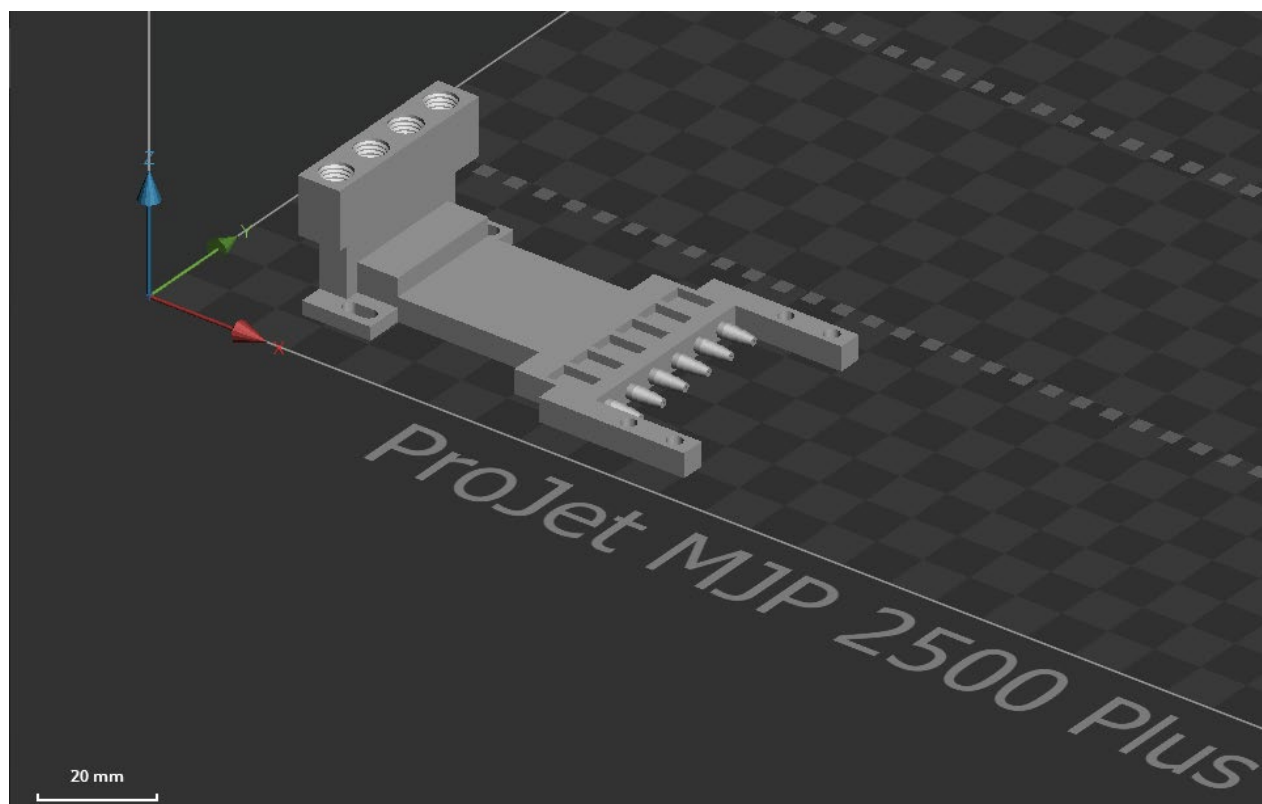


**Figure S1.** Orientation of the 3D model in the printing software “3D sprint”. The large flat bottom surface is oriented towards the printing platform, and the inlets are facing upwards.

## Results

The printing accuracy was determined as follows: 3D models with open channels of different heights (300  $\mu\text{m}$ , 500  $\mu\text{m}$ , and 750  $\mu\text{m}$ ) were designed and 3D-printed in different directions (x, y, z). Using a digital microscope (VHX-6000, Keyence GmbH, Neu-Isenburg, Germany), height profiles were recorded using the options “depth composition” and “profile” (100x magnification). The channel height was determined as the height difference between the top and the bottom of the structure.

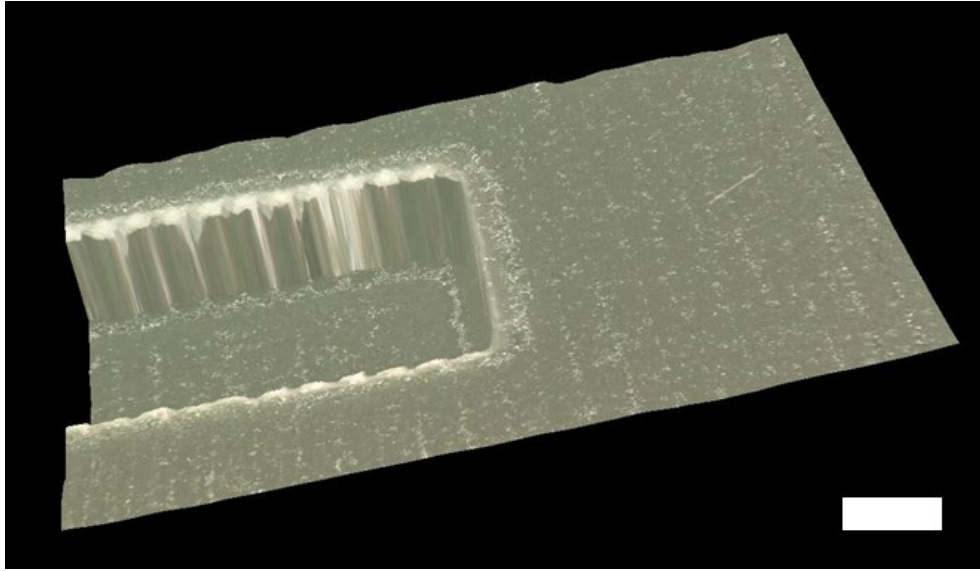


**Figure S2.** 3D visualization of the 3D-printed open channel with a designed height of 500  $\mu\text{m}$  recorded by digital microscopy. The scale bar indicates 500  $\mu\text{m}$ .

**Table S1.** Design vs. measured heights for different printing orientations (standard deviation for n=3).

Design ( $\mu\text{m}$ )	X ( $\mu\text{m}$ )	Y ( $\mu\text{m}$ )	Z ( $\mu\text{m}$ )
300	305 $\pm$ 10	314 $\pm$ 8	282 $\pm$ 1
500	489 $\pm$ 13	499 $\pm$ 9	475 $\pm$ 3
750	729 $\pm$ 11	750 $\pm$ 11	720 $\pm$ 4

## Results

### **S2. Fabrication of Microwell Photonic Silicon Chips**

1. 4-inch silicon wafers (Siltronic, France) with a SiO<sub>2</sub> layer (hard mask) of ~1000 Å thickness were used for the fabrication of the microwell photonic silicon chips.
2. Vaporized hexamethyldisilazane (HMDS) acting as an adhesion promoter was applied to the wafer before a positive photoresist AZ1512 was applied, and the wafer was baked at 110 °C for 90 s. All processes were performed using an automatic coater (Delta 80 Rc, SUSS Microtec, Germany).
3. Laser writing using a laser lithography system (DWL 66+, Heidelberg Instruments, Germany) was used to pattern the desired microstructure for the following etching procedures.
4. Tetramethylammonium hydroxide (TMAH) 10 % as developer reagent was added to the wafer dissolve residual photoresist using an automatic developer (Delta 8+, SUSS Microtec, Germany).
5. Reactive ion etching (Plasma-Therm Etching System 790, Plasma-Therm LLC, USA) was used to open the hard mask (SiO<sub>2</sub>) at the designated positions before deep reactive ion etching (Plasma Etcher Versaline, Plasma-Therm LLC, USA) was applied to etch the microwell structure into the silicon substrate.
6. Residual photoresist and hard mask were removed from the areas that were not exposed to light and etched. For this purpose, the wafer was treated with 1-Methyl-2-pyrrolidone (NMP) for 25 min at 70 °C, MLO 07 for 15 min at 70 °C, piranha solution (H<sub>2</sub>SO<sub>4</sub>:H<sub>2</sub>O<sub>2</sub> = 2:1), and buffer oxide etchant (BOE) for 5 min.
7. RCA cleaning of the wafer was performed. For this purpose, the wafer was treated with piranha solution (H<sub>2</sub>SO<sub>4</sub>:H<sub>2</sub>O<sub>2</sub> = 2:1) for 10 min, diluted HF solution HF(49 %):H<sub>2</sub>O (1:50) for 10 s and NH<sub>4</sub>OH(30 %):H<sub>2</sub>O<sub>2</sub>(30 %):H<sub>2</sub>O (1:1:4) at 75 °C.
8. The resulting wafers were coated again with photoresist to protect their microstructure during the dicing procedure into 5 × 5 mm chips using an automated dicing saw (DAD3350, Disco, Japan).
9. The photonic silicon chips were washed with acetone to remove the photoresist and oxidized for 1 h at 800 °C in a furnace (Lindberg/Blue M 1200 °C Split-Hinge, Thermo Scientific, USA).

## Results

### S3. Gradient Generator Design and Principle

For a gradient generator with  $n$  outlets, each outlet  $Out_i$  is supposed to carry the same volume flow. Thus, for incoming inflows  $Q_A$  and  $Q_B$  with relative concentrations of  $c_A = 1$  and  $c_B = 0$ , respectively, the total flow rate  $C$  is

$$C = Q_A + Q_B \quad (1)$$

Accordingly, the total flow rate of each outlet  $i$  is

$$\frac{1}{n}C = Q_{A_i} + Q_{B_i} \quad (2)$$

With

$$\sum_{i=1}^n Q_{A_i} = Q_A \quad (3)$$

$$\sum_{i=1}^n Q_{B_i} = Q_B \quad (4)$$

Each concentration can be described as a mixing ratio  $a$  to  $b$ . For instance, a concentration of 0.25 requires a mixing ratio  $a = 1$  and  $b = 3$ . Since the mixing ratio of a mixing level  $i$  is

$$\frac{Q_{A_i}}{Q_{B_i}} = \frac{a}{b} \quad (5)$$

Regarding equation (2), the sum of two flow rates needs to result in  $\frac{1}{n}C$ . We define  $P_{i,A}$  as the fraction from A on the mixture at outlet  $i$  and  $P_{i,B}$  vice versa.

$$\frac{P_{i,A}}{n(P_{i,A} + P_{i,B})}C + \frac{P_{i,B}}{n(P_{i,A} + P_{i,B})}C = \frac{1}{n}C \quad (6)$$

The sum of all fractions is calculated as

$$P_A = \sum_{i=1}^n \frac{P_{i,A}}{n(P_{i,A} + P_{i,B})} \quad (7)$$

$$P_B = \sum_{i=1}^n \frac{P_{i,B}}{n(P_{i,A} + P_{i,B})} \quad (8)$$

The second flow rate  $Q_B$  can be calculated for a given flowrate  $Q_A$  as

$$Q_B = \frac{P_B}{P_A} \cdot Q_A \quad (9)$$

The mixing channels of each level  $i$  are parallelized resistances/ lengths. Therefore, the length of each side of a level is inversely proportional to the fraction of each flow rate.

$$L_{i,A} = \frac{1}{\frac{P_{i,A}}{n(P_{i,A} + P_{i,B})}} \quad (10)$$

$$L_{i,B} = \frac{1}{\frac{P_{i,B}}{n(P_{i,A} + P_{i,B})}} \quad (11)$$

## Results

For clarity, the length of each channel can be normalized to the first channel of a side

$$L_{i,A}^{norm} = \frac{L_{1,A}}{L_{i,A}} \quad (12)$$

$$L_{i,B}^{norm} = \frac{L_{1,A}}{L_{i,B}} \quad (13)$$

The resulting parameters for a six-outlet, two-fold dilutions series gradient generator are summarized in Table S1. For a total flow rate of  $1000 \mu\text{L min}^{-1}$   $Q_A$  and  $Q_B$  are 323 and  $677.3 \mu\text{L in}^{-1}$ , respectively, as  $\frac{P_B}{P_A}$  is approximately 2.096.

**Table S2:** Summary of mixing ratio parameters  $a$  and  $b$  as well as resulting relative lengths for an exponential (two-fold dilution series) gradient generator.

Mixing level $i$	Relative concentration	$a$	$b$	$L_{i,A}^{norm}$	$L_{i,B}^{norm}$
1	1	1	/	1	/
2	0.5	1	1	2	2
3	0.25	1	3	4	1.333
4	0.125	1	7	8	1.143
5	0.0625	1	15	16	1.066
6	0	/	1	/	1



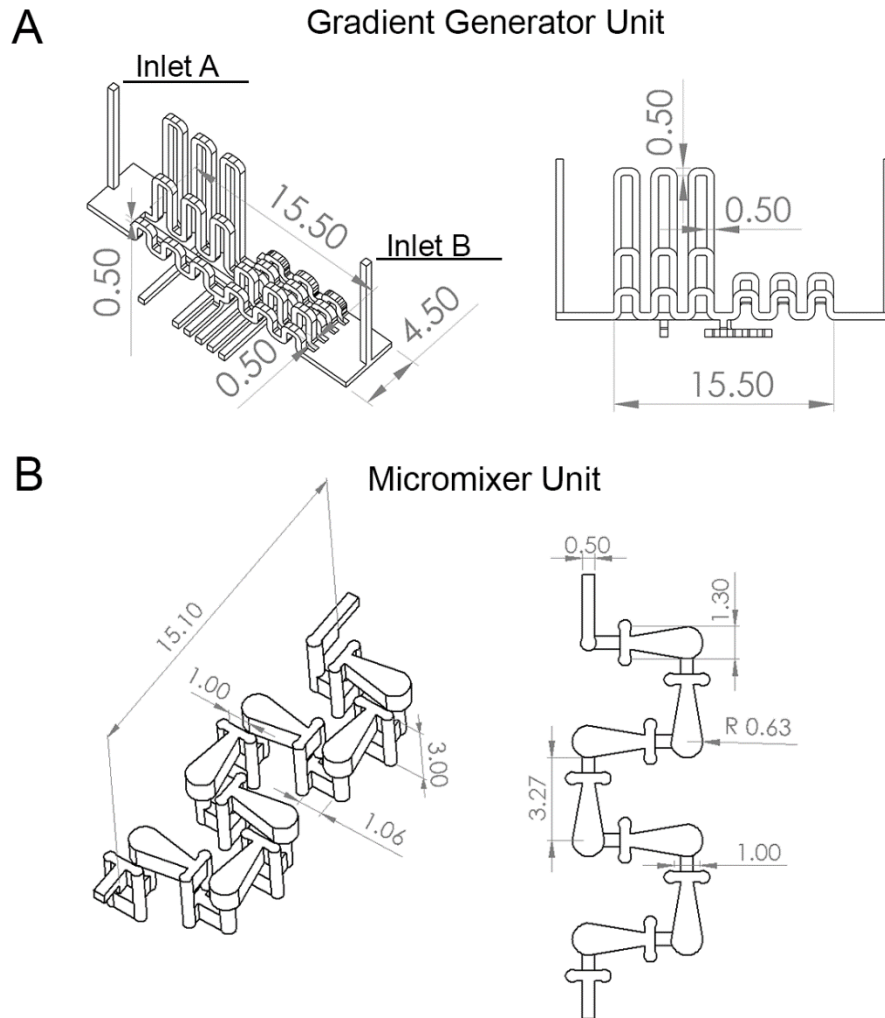


**Figure S3.** Detailed technical drawings of (A) the gradient generator unit and (B) the micromixer unit of the microfluidic gradient generator device. All dimensions (grey) are stated in mm.

#### S4. Gradient Generator Characterization

To study the impact of micromixers on the gradient accuracy and concentration homogeneity at each outlet, we performed CFD simulations with and without integrated HC-micromixers. As depicted in Figure S1, the results indicate that the averaged concentration is the same with and without micromixer integration. However, for on-chip measurements, we recommend micromixer integration since high inhomogeneities appear in outlets numbers 2-5 at the chosen flow rate of  $1000 \mu\text{L min}^{-1}$  when no micromixers are integrated.

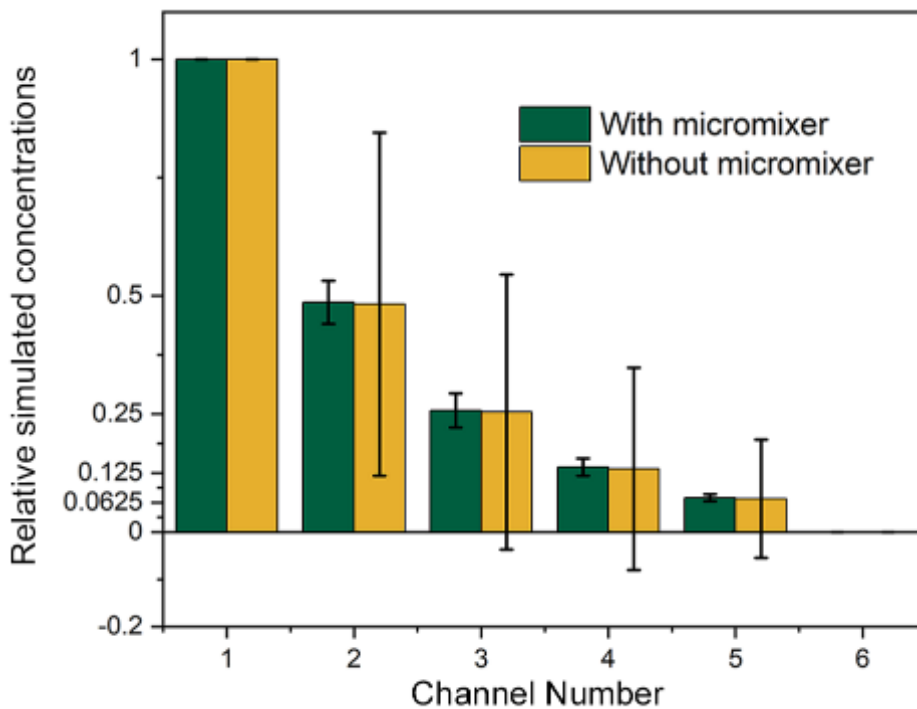


**Figure S4.** Impact of HC-micromixers on gradient accuracy and concentration homogeneity at each outlet. CFD simulations at a total flow rate of  $1000 \mu\text{L min}^{-1}$  were used to determine the concentration at each outlet with and without integrated micromixers. Error bars indicate the standard deviation of the concentration distribution at each outlet. Low standard deviations indicate high homogeneity, while high standard deviations indicate low homogeneity.

## Results

For experimental flow rate determination, deionized water was introduced at a total flow rate of  $\sim 1000 \mu\text{L min}^{-1}$  ( $677.3 \mu\text{L min}^{-1} + 323 \mu\text{L min}^{-1}$ ) and collected from every outlet for 1 min and weighted using an analytical balance (BCE 2241-1S, Sartorius AG, Göttingen, Germany). The flow rate was determined using  $1 \text{ g mL}^{-1}$  as the density of water.

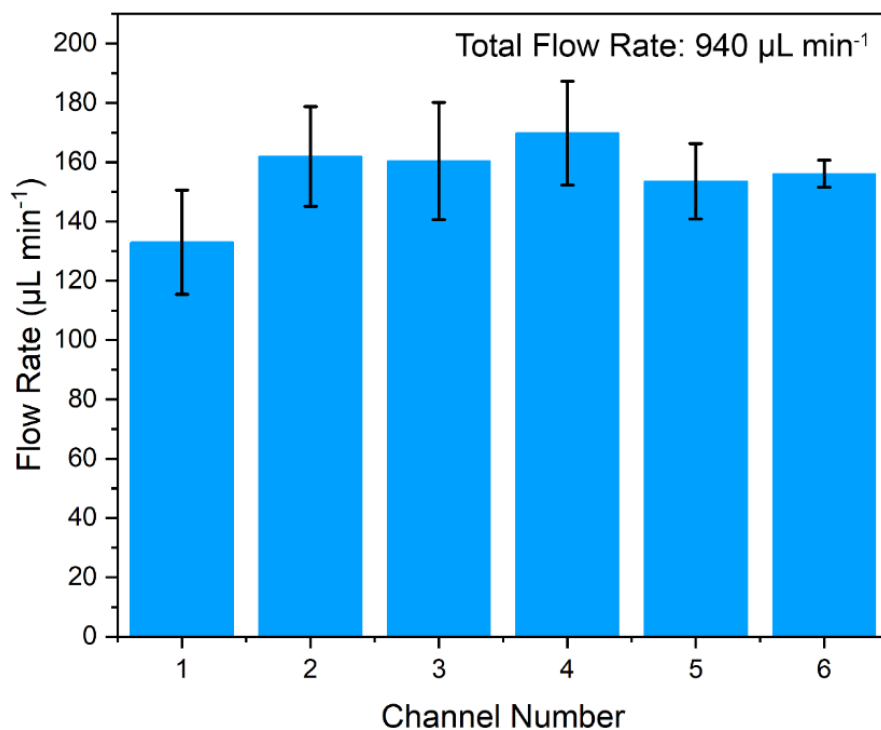


**Figure S5.** Experimental evaluation of flow rates at each outlet. Error bars indicate the standard deviation of three experiments. The total flow rate of  $940 \mu\text{L min}^{-1}$  is consistent with the initial flow rate of  $1000 \mu\text{L min}^{-1}$ . The slight discrepancy may be explained because the fluids cannot be continuously collected from the outlets as they emerge only drop by drop.

## Results

### S5. GG-enabled BMD results

**Table S3** Summary and comparison of MIC values obtained by GG-enabled BMD, manual reference BMD, and MIC values published by EUCAST.

Pathogen - Drug Combination	GG-enabled BMD. (MIC)	Reference BMD (MIC)	EUCAST Data (MIC) <sup>c)</sup>
<i>S. marcescens</i> vs. ciprofloxacin	0.0625 mg L <sup>-1</sup>	0.0625 mg L <sup>-1</sup> <sup>a)</sup>	0.008 – 0.25 mg L <sup>-1</sup> <sup>[1]</sup>
<i>E. coli</i> vs. gentamicin	0.125 mg L <sup>-1</sup>	0.125 mg L <sup>-1</sup> <sup>a)</sup>	0.008 – 2 mg L <sup>-1</sup> <sup>[1]</sup>
<i>C. auris</i> vs voriconazole	0.016 mg L <sup>-1</sup>	0.016 mg L <sup>-1</sup> – 0.03 mg L <sup>-1</sup> <sup>b)</sup>	0.008 – 4 mg L <sup>-1</sup> <sup>[2]</sup>

<sup>a)</sup> Three BMD tests, each with  $n \geq 3$  wells for every concentration tested; <sup>b)</sup> five BMD assays, each with  $n \geq 3$  wells for every concentration tested; <sup>c)</sup> MIC range for susceptible wild-type bacteria and entire range for *C. auris*.

## S6. GG-enabled PRISM assay

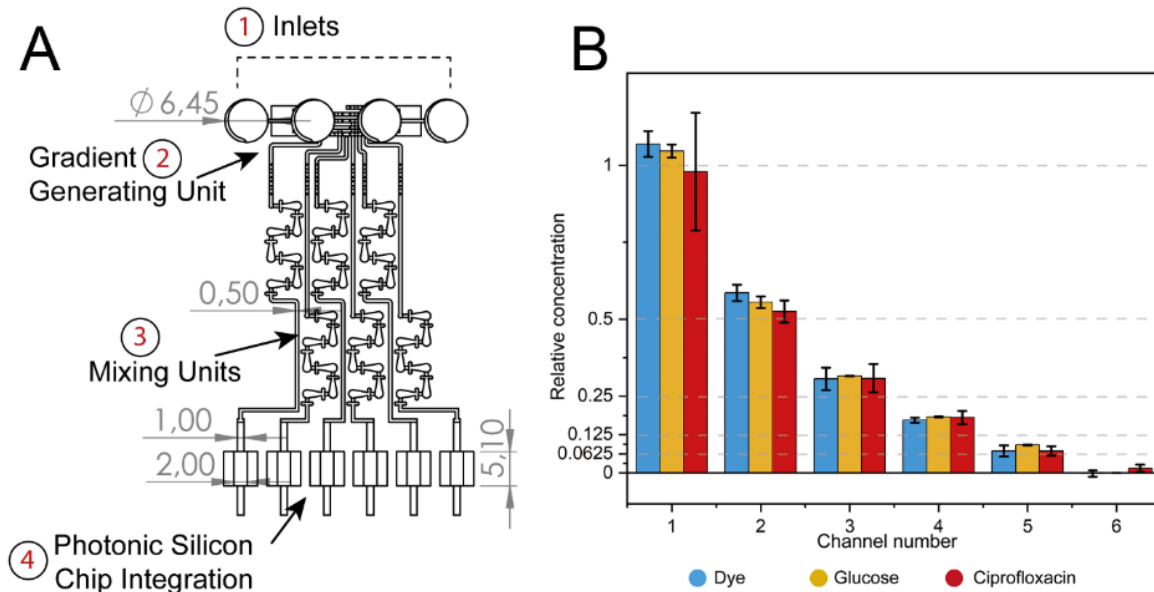


**Figure S6.** Microfluidic GG device for photonic silicon chip integration. (A) Technical drawing of the GG that has been modified for photonic silicon chip integration. The individual integration of the chips (size 5 x 5 mm) is enabled by six square-shaped chambers (size 5.1 x 5.1 mm) that are open to their bottom. (B) Importantly the chip integration does not impair the gradient generating accuracy as accurate gradients with high coefficients of determination ( $R^2$ ) of 0.9966 (dye), 0.9967 (glucose), and 0.9941 (ciprofloxacin) are obtained. All calibration curves were accurate with  $R^2 \geq 0.999$ .

## Results

In the GG-based PRISM assay, suspensions of *E. coli* (McFarland 0.5) and 1 mg L<sup>-1</sup> ciprofloxacin (source fluid) and *E. coli* (McFarland 0.5) without antibiotic (sink fluid) are introduced for 5 min into the GG-device before the bacteria are given 10 minutes to settle within the microstructure, and the optical assay (PRISM) is initiated. To confirm that such an experimental procedure in which the bacteria are exposed to the highest tested ciprofloxacin concentration for 5 minutes before being diluted to the designated antibiotic concentrations does not cause flawed MIC values, a standard BMD with *E. coli* (McFarland 0.5) and ciprofloxacin (Figure S4A) and a modified BMD (Figure S4B) for this pathogen drug combination were performed. In the modified BMD, *E. coli* (McFarland 0.5) is incubated at 1 mg L<sup>-1</sup> ciprofloxacin for 5 minutes before a two-fold dilution series is performed in cell suspensions at the same cell density to reach the designated antibiotic concentrations. As demonstrated in Figure S4, for both procedures, the same MIC value is obtained.

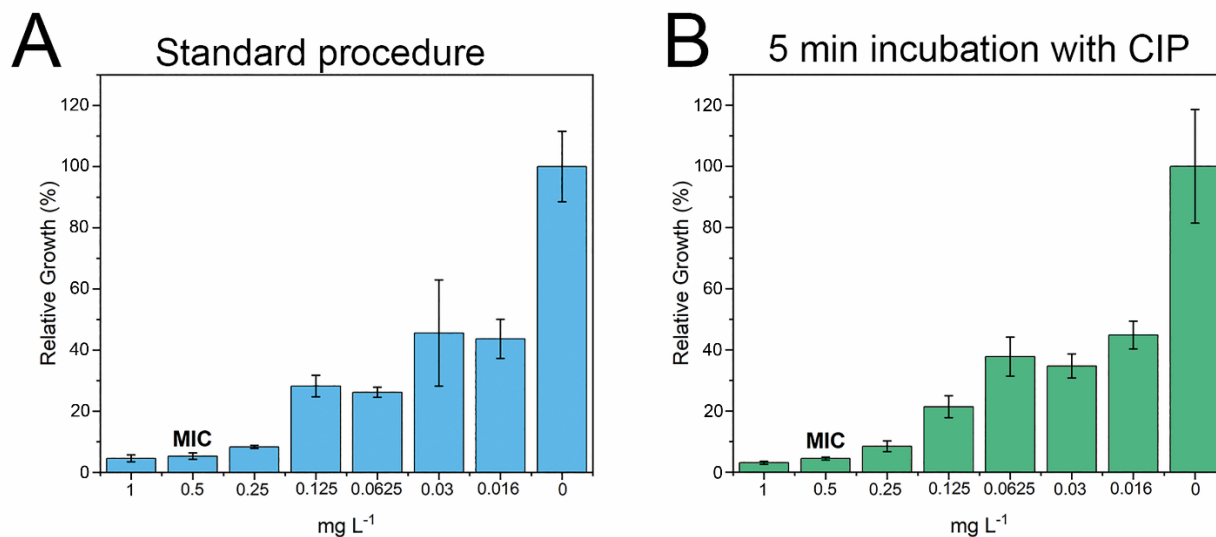


**Figure S7.** Comparison of BMD results for *E. coli* (McFarland 0.5) and ciprofloxacin (CIP) for (A) a standard procedure and (B) a modified BMD in which the bacteria are exposed for 5 minutes to the highest tested antibiotic concentration (CIP: 1 mg L<sup>-1</sup>) before being diluted to the designated antibiotic concentrations. The MIC was defined as the lowest antibiotic concentration at which no growth was visible.

## Results

A typical clinical workflow consists of pathogen isolation from the patient and identification, which precede the AST step.<sup>3,4</sup> Thus, culturing remains a prerequisite for AST, and typically, the inoculum for AST is prepared from microbial cultures grown on agar plates overnight and standardized to a cell density corresponding to the McFarland 0.5 standard, see Table S4. Thus, our assay and the use of McFarland 0.5 is tailored to the clinical workflow and highly suitable for application in clinical settings.

**Table S4.** Comparison of the GG-based PRISM assay to gold standard BMD and commercialized clinically relevant AST methods.

Method	Principle	Sample Matrix	Test Matrix	Cell Density Standardization	Inoculum	Time
GG-based PRISM	Refractive index changes within a silicon diffraction grating	Colonies from fresh agar medium	Microstructured photonic silicon sensors in liquid growth medium	McFarland 0.5 (10 <sup>8</sup> cells mL <sup>-1</sup> )	McFarland 0.5	90 min
Gold Standard BMD <sup>5,6</sup>	Visual or spectrophotometric observation of turbidity	Colonies from fresh agar medium	Liquid growth medium	McFarland 0.5	5 x 10 <sup>5</sup> cells mL <sup>-1</sup>	18 h
State-of-the-Art Vitek 2 <sup>7,8</sup>	Automated turbidity measurements	Colonies from fresh agar medium	Liquid growth medium	McFarland 0.5	~10 <sup>7</sup> cells mL <sup>-1</sup>	8 h
Agar-based Etest <sup>9,10</sup>	Zone of inhibition around a strip with an antifungal gradient	Colonies from fresh agar medium	Agar plate	McFarland 0.5	McFarland 0.5	16 - 20 h

## References

- 1 European Committee on Antimicrobial Susceptibility Testing, EUCAST Antimicrobial wild type distributions of microorganisms, <https://mic.eucast.org/>, (accessed: June 20, 2022).
- 2 M. C. Arendrup, A. Prakash, J. Meletiadis, C. Sharma, A. Chowdhary, *Antimicrob. Agents Chemother.*, 2017, 61, e00485-17.
- 3 C. Heuer, J. Bahnemann, T. Scheper and E. Segal, *Small Methods*, 2021, 5, 2100713
- 4 H. Leonard, R. Colodner, S. Halachmi and E. Segal, *ACS Sens.*, 2018, 3, 2202–2217.
- 5 EUCAST, EUCAST definitive document E.DEF 7.3.2 Method for the determination of broth dilution minimum inhibitory concentrations of antifungal agents for yeasts, [https://www.eucast.org/fileadmin/src/media/PDFs/EUCAST\\_files/AFST/Files/EUCAST\\_E\\_Def\\_7.3.2\\_Yeast\\_testing\\_definitive\\_revised\\_2020.pdf](https://www.eucast.org/fileadmin/src/media/PDFs/EUCAST_files/AFST/Files/EUCAST_E_Def_7.3.2_Yeast_testing_definitive_revised_2020.pdf), (accessed June 17, 2022).
- 6 International Organization for Standardization, ISO 20776 1:2020.
- 7 Ligozzi, C. Bernini, M. G. Bonora, M. de Fatima, J. Zuliani and R. Fontana, *J. Clin. Microbiol.*, 2002, 40, 1681–1686.
- 8 bioMérieux, Vitek2 GN Card Instructions REF21341. Can be downloaded from the bioMérieux Resource Center after registration: <https://resourcecenter.biomerieux.com/search/>
- 9 bioMérieux, Etest Application Guide, [https://www.biomerieux-usa.com/sites/subsidiary\\_us/files/supplementary\\_inserts\\_-\\_16273\\_-\\_b\\_-\\_en\\_-\\_eag\\_-\\_etest\\_application\\_guide-3.pdf](https://www.biomerieux-usa.com/sites/subsidiary_us/files/supplementary_inserts_-_16273_-_b_-_en_-_eag_-_etest_application_guide-3.pdf), (accessed June 17, 2022).
- 10 bioMérieux, Etest Ciprofloxacin Instructions REF412311/423766. Can be downloaded from the bioMérieux Resource Center after registration: <https://resourcecenter.biomerieux.com/search/>

## 6 Discussion

This chapter aims to critically discuss this thesis work and highlight its strengths and remaining scientific and technological gaps.

### Advantages of iPRISM for AFST

The application of photonic silicon chips for rapid AFST of the mould model species *A. niger* and the emerging yeast pathogen *C. auris* by label-free monitoring of intensity changes in the white light reflectance (iPRISM) in real-time was established. Using the iPRISM assay, MIC values for clinically relevant antifungals (voriconazole, amphotericin B, and anidulafungin) were expeditiously determined within 10 – 12 h (*A. niger*) and  $\leq 6$  h (*C. auris*). Therefore, the iPRISM provides a significant time reduction compared to the gold standard BMD (48 h for *A. niger* and 24 h for *C. auris*)<sup>16,19</sup> and the automated state-of-the-art Vitek2 system (typically 12 – 18 h for yeasts).<sup>20,21</sup> In addition, the small size of the photonic silicon chips allows integration into microfluidic systems, and the chip microstructure can be tuned for the size and morphology of different microorganisms.

### Are iPRISM MIC values consistent with the gold standard AFST?

In most cases, the determined MIC values were higher in the iPRISM assay compared to the gold standard BMD but agreed with the expected MIC value range for the respective pathogen-drug combinations. These elevated MIC values are mainly ascribed to the distinct growth environments, where the iPRISM assay provides a microstructured surface with which the fungi may interact while the BMD tests the growth of fungi suspended in a liquid growth medium. Another important aspect concerns the reproducibility of the assay. While the presented iPRISM method is highly reproducible under the tested conditions (same operator, same batch of growth medium and antifungal stock) in terms of MIC determination, the error of this assay under varying conditions (*e.g.*, different setting and operator) will need to be investigated in the future. Such studies appear crucial as even in the gold standard BMD, inter- and intra-laboratory variations are often described.<sup>43,44</sup>

### Importance of chip design for targeting different microorganisms

The design of the silicon microstructure is of great importance as it defines where the various tested microorganisms (*e.g.*, mould, yeast, bacteria) colonize on the photonic silicon chip. In this research, the microstructure was first carefully designed (width:  $\sim 3$   $\mu\text{m}$  depth:  $\sim 4$   $\mu\text{m}$ ) to capture the conidia of *A. niger* within the wells and to allow hyphal growth on top of the microwell structure. Subsequently, the dimensions were enlarged (width:  $\sim 4$   $\mu\text{m}$  and depth:  $\sim 4$   $\mu\text{m}$ ) to confine most of the larger *C. auris* cells within the microstructure. Thus, the assay represents a universal platform that can potentially be extended and adjusted for growth monitoring of other important fungal pathogens, where even larger organisms like *Candida albicans* (length:  $\sim 6$   $\mu\text{m}$  and width:  $\sim 5$   $\mu\text{m}$ <sup>45</sup>) could reside and colonize within the microwells.



## Discussion

However, the silicon microstructures can potentially also be used for size exclusion where only specific microorganisms can grow within the microstructure, while larger species remain on the top of the microstructure with the result that distinct growth profiles (2nL and intensity changes) can be obtained.

### **Can (i)PRISM go beyond susceptibility testing?**

Compared to most standard methods for susceptibility testing, which only monitor growth by one parameter (typically turbidity or visual growth on agar), the presented assay allows the monitoring of two parameters, namely, the intensity of the reflected light (iPRISM) and the 2nL value (PRISM). Thus, the optical platform allows for establishing a “playground for microbes” and can potentially distinguish different types of pathogens by their unique behaviour and signals from the chips. For example, bacterial species such as *E. coli* cause an increase in the 2nL value, while for yeast species such as *C. auris* and *S. cerevisiae*, a 2nL decrease is observed. At this stage, we were not able to pinpoint the underlying mechanism for these observations, and future studies should be directed at unravelling the physical principles behind this phenomenon by carefully correlating the yeast behaviour with the 2nL signal. Nevertheless, considering the work by Leonard *et al.*, who show distinct behaviours and varying intensity and 2nL changes for various microbial species on different functionalized microstructures,<sup>46</sup> the application of (i)PRISM for obtaining species-specific growth profiles and subsequent species differentiation or even identification is envisioned. The combination of species identification and susceptibility testing in one assay on the same chips would represent a breakthrough and disrupt the current clinical workflow consisting of pathogen isolation, identification, and susceptibility testing, and its feasibility will need to be investigated in further studies. In terms of fungal pathogen diagnostics, this optical platform could potentially present a valuable tool for the differentiation of bacterial species and pathogenic yeast, for example, in urinary tract infections in which emerging incidences of fungal infections are observed.<sup>47</sup>

### **Towards point-of-care: 3D-printed microfluidics for integrated and automated AST as a solution?**

The main limitation of the (i)PRISM assay is that, to date, it was only established for susceptibility testing, which is the last step in a lengthy clinical workflow and preceded by pathogen isolation and species identification. Thus, the successful combination of these various steps, including required preparation operations (*e.g.*, concentrating cells, adjusting the inoculum, generation of the antimicrobial dilution series), into a miniaturized holistic and automated device is considered essential to perform AST as a point-of-care diagnostic test.<sup>14,31</sup> Realizing this gap that exists in all current A(F)ST methods, a 3D-printed microfluidic system that automatically generates the desired two-fold dilution series of antimicrobials was designed. Furthermore, this gradient generator was interfaced with the photonic silicon chips and the assay was tailored to current clinical procedures for convenient, phenotypic, on-chip AST. Using the pathogen-drug combination *E. coli* and ciprofloxacin, the MIC was determined within 90 minutes compared to 8 – 24 h in

## Discussion

current clinical procedures.<sup>39</sup> Thus, this gradient generator emphasizes how 3D printing can be used to coalesce different functional units. However, to evolve the presented microfluidic device into a system truly applicable for point-of-care testing, existing gaps need to be closed. For example, the miniaturization of the periphery (*e.g.*, pumps, syringes and tubing) and the integration of additional unit operations (*e.g.*, concentrating cells, adjusting cell density) is required and suggested for future work. In combination with the concept of a “microbial playground” for species identification, such an improved device could represent a powerful tool to replace the lengthy clinical workflow for AST by including all required steps into one holistic, automated microfluidic system.

## 7 Conclusion and Outlook

The main achievements presented in this work are the following:

A rapid AFST for the mould model species *A. niger* is presented. Morphological changes of this fungal species at a liquid-solid interface at varying antifungal concentrations are optically monitored in real time and in a label-free manner by using the iPRISM assay. MIC values are successfully determined for two antifungal agents with different mechanisms of action within 10 h (amphotericin B) and 12 h (voriconazole), respectively. Thus, iPRISM provides a rapid alternative (time reduction >36 h) to the gold standard BMD, which typically takes 48 h.

The optical platform is extended to a morphologically distinct fungal microorganism - the yeast *Candida auris* - a species which is often multi-drug resistant. The microwell dimensions of the microstructure were rationally designed and enlarged to confine most of the yeast cells within the structure. Tracking the fungal growth at varying antifungal concentrations by iPRISM enables AFST and MIC determination within 3.5 h for anidulafungin and 6 h for amphotericin B, a time reduction of > 18 h compared to the BMD that typically requires 24 h for yeast species.

A 3D-printed microfluidic gradient generator made from a biocompatible polyacrylate material for automated dilution of the desired antimicrobial concentrations is presented. The generator is first applied for gold standard BMD testing of different pathogen-drug combinations and then interfaced with the photonic silicon chips to provide an automated, on-chip, and label-free phenotypic assay for rapid AST. Using the bacterial species *E. coli* and the antibiotic ciprofloxacin, the MIC is successfully determined within 90 minutes by PRISM and monitoring 2nL changes. Thus, the gradient generator-enabled PRISM assay provides an expeditious alternative to current clinical practices for bacterial species, which require up to 24 h.

The various pathogens studied in this research show distinct morphological behaviours with different intensity and 2nL signals. These varying signals for *A. niger* (only intensity decrease) *C. auris* (2nL decrease and intensity decrease), and *E. coli* (2nL increase and intensity decrease) emphasize that the photonic silicon chips can potentially be employed as a “microbial playground” for species identification. While future research will need to be directed at developing such an optical assay for species differentiation/identification, this could represent a breakthrough for the clinical A(F)ST procedure, as pathogen identification is a prerequisite for susceptibility testing in current workflows.

Finally, to develop a diagnostic system for convenient point-of-care susceptibility testing that is as easy to use as a COVID-19 rapid antigen test, the different parts presented in this thesis – namely rapid A(F)ST, a “microbial playground” for species identification and different operations provided by 3D-printed microfluidics – will need to come together in a holistic, integrated diagnostic device.

## 8 References

- 1 M. C. Fisher, A. Alastruey-Izquierdo, J. Berman, T. Bicanic, E. M. Bignell, P. Bowyer, M. Bromley, R. Brüggemann, G. Garber, O. A. Cornely, S. J. Gurr, T. S. Harrison, E. Kuijper, J. Rhodes, D. C. Sheppard, A. Warris, P. L. White, J. Xu, B. Zwaan and P. E. Verweij, Tackling the emerging threat of antifungal resistance to human health, *Nature Reviews Microbiology*, 2022, **20**, 557–571.
- 2 A. McDermott, Drug-resistant fungi on the rise, *Proceedings of the National Academy of Sciences*, 2022, **119**, e2217948119.
- 3 K. Benedict, M. Richardson, S. Vallabhaneni, B. R. Jackson and T. Chiller, Emerging issues, challenges, and changing epidemiology of fungal disease outbreaks, *The Lancet Infectious Diseases*, 2017, **17**, e403-e411.
- 4 A. Rokas, Evolution of the human pathogenic lifestyle in fungi, *Nature Microbiology*, 2022, **7**, 607–619.
- 5 N. E. Nnadi and D. A. Carter, Climate change and the emergence of fungal pathogens, *PLoS pathogens*, 2021, **17**, e1009503.
- 6 U. Hofer, *Candida auris*' potential link to climate change, *Nature Reviews Microbiology*, 2019, **17**, 588.
- 7 D. S. Perlin, R. Rautemaa-Richardson and A. Alastruey-Izquierdo, The global problem of antifungal resistance: prevalence, mechanisms, and management, *The Lancet Infectious Diseases*, 2017, **17**, e383-e392.
- 8 N. A. R. Gow, C. Johnson, J. Berman, A. T. Coste, C. A. Cuomo, D. S. Perlin, T. Bicanic, T. S. Harrison, N. Wiederhold, M. Bromley, T. Chiller and K. Edgar, The importance of antimicrobial resistance in medical mycology, *Nature Communications*, 2022, **13**, 5352.
- 9 A. Arastehfar, A. Carvalho, M. H. Nguyen, M. T. Hedayati, M. G. Netea, D. S. Perlin and M. Hoenigl, COVID-19-Associated Candidiasis (CAC): An Underestimated Complication in the Absence of Immunological Predispositions?, *Journal of fungi*, 2020, **6**, 211.
- 10 N. A. F. Janssen, R. Nyga, L. Vanderbeke, C. Jacobs, M. Ergün, J. B. Buil, K. van Dijk, J. Altenburg, C. S. C. Bouman, H. I. van der Spoel, B. J. A. Rijnders, A. Dunbar, J. A. Schouten, K. Lagrou, M. Bourgeois, M. Reynders, N. van Regenmortel, L. Rutsaert, P. Lormans, S. Feys, Y. Debavaye, F. Tamion, D. Costa, J. Maizel, H. Dupont, T. Chouaki, S. Nseir, B. Sendid, R. J. M. Brüggemann, F. L. van de Veerdonk, J. Wauters and P. E. Verweij, Multinational Observational Cohort Study of COVID-19-Associated Pulmonary Aspergillosis, *Emerging Infectious Diseases*, 2021, **27**, 2892–2898.
- 11 A. K. Singh, R. Singh, S. R. Joshi and A. Misra, Mucormycosis in COVID-19: A systematic review of cases reported worldwide and in India, *Diabetes & metabolic syndrome*, 2021, **15**, 102146.
- 12 S. E. Jacobs, J. L. Jacobs, E. K. Dennis, S. Taimur, M. Rana, D. Patel, M. Gitman, G. Patel, S. Schaefer, K. Iyer, J. Moon, V. Adams, P. Lerner, T. J. Walsh, Y. Zhu, M. R. Anower, M. M. Vaidya, S. Chaturvedi

## References

- and V. Chaturvedi, *Candida auris* Pan-Drug-Resistant to Four Classes of Antifungal Agents, *Antimicrobial agents and chemotherapy*, 2022, **66**, e0005322.
- 13 CDC report: antibiotic resistance threats in the United States 2019, <https://www.cdc.gov/drugresistance/pdf/threats-report/2019-ar-threats-report-508.pdf>, (accessed April 2023).
  - 14 C. Heuer, J. Bahnemann, T. Scheper and E. Segal, Paving the Way to Overcome Antifungal Drug Resistance: Current Practices and Novel Developments for Rapid and Reliable Antifungal Susceptibility Testing, *Small methods*, 2021, **5**, e2100713.
  - 15 E. L. Berkow, S. R. Lockhart and L. Ostrosky-Zeichner, Antifungal Susceptibility Testing: Current Approaches, *Clinical Microbiology Reviews*, 2020, **33**, e00069-19.
  - 16 European Committee on Antimicrobial Susceptibility Testing, Definitive Document E. DEF 7.3.2., [https://www.eucast.org/fileadmin/src/media/PDFs/EUCAST\\_files/AFST/Files/EUCAST\\_E\\_Def\\_7.3.2\\_Yeast\\_testing\\_definitive\\_revised\\_2020.pdf](https://www.eucast.org/fileadmin/src/media/PDFs/EUCAST_files/AFST/Files/EUCAST_E_Def_7.3.2_Yeast_testing_definitive_revised_2020.pdf), (accessed April 2023).
  - 17 European Committee on Antimicrobial Susceptibility Testing, Breakpoint tables for interpretation of MICs fo antifungal agents, Version 10.0, [https://www.eucast.org/fileadmin/src/media/PDFs/EUCAST\\_files/AFST/Clinical\\_breakpoints/AFST\\_BP\\_v10.0\\_200204\\_updatd\\_links\\_200924.pdf](https://www.eucast.org/fileadmin/src/media/PDFs/EUCAST_files/AFST/Clinical_breakpoints/AFST_BP_v10.0_200204_updatd_links_200924.pdf), (accessed April 2023).
  - 18 M. Sanguinetti and B. Posteraro, New approaches for antifungal susceptibility testing, *Clinical microbiology and infection: the official publication of the European Society of Clinical Microbiology and Infectious Diseases*, 2017, **23**, 931–934.
  - 19 European Committee on Antimicrobial Susceptibility Testing, EUCAST Definitive Document E. DEF 9.3.1., [https://www.eucast.org/fileadmin/src/media/PDFs/EUCAST\\_files/AFST/Files/EUCAST\\_EDef\\_9.4\\_method\\_for\\_susceptibility\\_testing\\_of\\_moulds.pdf](https://www.eucast.org/fileadmin/src/media/PDFs/EUCAST_files/AFST/Files/EUCAST_EDef_9.4_method_for_susceptibility_testing_of_moulds.pdf)
  - 20 M. Cuenca-Estrella, A. Gomez-Lopez, A. Alastruey-Izquierdo, L. Bernal-Martinez, I. Cuesta, M. J. Buitrago and J. L. Rodriguez-Tudela, Comparison of the Vitek 2 antifungal susceptibility system with the clinical and laboratory standards institute (CLSI) and European Committee on Antimicrobial Susceptibility Testing (EUCAST) Broth Microdilution Reference Methods and with the Sensititre YeastOne and Etest techniques for in vitro detection of antifungal resistance in yeast isolates, *Journal of clinical microbiology*, 2010, **48**, 1782–1786.
  - 21 E. Borghi, R. Iatta, R. Sciota, C. Biassoni, T. Cuna, M. T. Montagna and G. Morace, Comparative evaluation of the Vitek 2 yeast susceptibility test and CLSI broth microdilution reference method for testing antifungal susceptibility of invasive fungal isolates in Italy: the GISIA3 study, *Journal of clinical microbiology*, 2010, **48**, 3153–3157.

## References

- 22 A. Vella, E. de Carolis, L. Vaccaro, P. Posteraro, D. S. Perlin, M. Kostrzewa, B. Posteraro and M. Sanguinetti, Rapid antifungal susceptibility testing by matrix-assisted laser desorption ionization-time of flight mass spectrometry analysis, *Journal of clinical microbiology*, 2013, **51**, 2964–2969.
- 23 L. A. Vale-Silva and V. Buchta, Antifungal susceptibility testing by flow cytometry: is it the future?, *Mycoses*, 2006, **49**, 261–273.
- 24 U. Furustrand Tafin, C. Orasch and A. Trampuz, Activity of antifungal combinations against *Aspergillus* species evaluated by isothermal microcalorimetry, *Diagnostic microbiology and infectious disease*, 2013, **77**, 31–36.
- 25 U. Furustrand Tafin, M. Clauss, P. M. Hauser, J. Bille, J. F. Meis and A. Trampuz, Isothermal microcalorimetry: a novel method for real-time determination of antifungal susceptibility of *Aspergillus* species, *Clinical microbiology and infection: the official publication of the European Society of Clinical Microbiology and Infectious Diseases*, 2012, **18**, E241-5.
- 26 C. J. Ingham, S. Boonstra, S. Levels, M. de Lange, J. F. Meis and P. M. Schneeberger, Rapid susceptibility testing and microcolony analysis of *Candida* spp. cultured and imaged on porous aluminum oxide, *PloS one*, 2012, **7**, e33818.
- 27 B. L. Wickes and N. P. Wiederhold, Molecular diagnostics in medical mycology, *Nature communications*, 2018, **9**, 5135.
- 28 H. Leonard, S. Halachmi, N. Ben-Dov, O. Nativ and E. Segal, Unraveling Antimicrobial Susceptibility of Bacterial Networks on Micropillar Architectures Using Intrinsic Phase-Shift Spectroscopy, *ACS nano*, 2017, **11**, 6167–6177.
- 29 S. Arshavsky-Graham and E. Segal, Lab-on-a-Chip Devices for Point-of-Care Medical Diagnostics, *Advances in biochemical engineering/biotechnology*, 2022, **179**, 247–265.
- 30 S. H. Needs, S. I. Donmez, S. P. Bull, C. McQuaid, H. M. I. Osborn and A. D. Edwards, Challenges in Microfluidic and Point-of-Care Phenotypic Antimicrobial Resistance Tests, *Frontiers in Mechanical Engineering*, 2020, **6**.
- 31 A. Vasala, V. P. Hytönen and O. H. Laitinen, Modern Tools for Rapid Diagnostics of Antimicrobial Resistance, *Frontiers in cellular and infection microbiology*, 2020, **10**, 308.
- 32 N. Massad-Ivanir, Y. Mirsky, A. Nahor, E. Edrei, L. M. Bonanno-Young, N. Ben Dov, A. Sa'ar and E. Segal, Trap and track: designing self-reporting porous Si photonic crystals for rapid bacteria detection, *The Analyst*, 2014, **139**, 3885–3894.
- 33 T. Davidov, N. Granik, S. Zahran, H. Leonard, I. Adir, O. Elul, T. Fried, A. Gil, B. Mayo, S. Ohayon, S. Sarig, N. Shasha, S. Tsedef, S. Weiner, M. Brunwasser-Meirom, A. Ereskovsky, N. Katz, B. Kaufmann, Y. Haimov, E. Segal and R. Amit, Designing Bacterial Chemotactic Receptors Guided by

## References

- Photonic Femtoliter Well Arrays for Quantifiable, Label-Free Measurement of Bacterial Chemotaxis, *ACS Biomaterials Science and Engineering*, 2019, **5**, 603–612.
- 34 H. Leonard, L. Holtzman, Y. Haimov, S. Halachmi, O. Nativ, E. Segal, Y. Kashi and D. Weizman, in *Light-Based Diagnosis and Treatment of Infectious Diseases*, ed. T. Dai, SPIE, Bellingham, Washington, USA, 2018, p. 6.
- 35 Y. Mirsky, A. Nahor, E. Edrei, N. Massad-Ivanir, L. M. Bonanno, E. Segal and A. Sa'ar, Optical biosensing of bacteria and cells using porous silicon based, photonic lamellar gratings, *Applied Physics Letters*, 2013, **103**, 33702.
- 36 A. Enders, I. G. Siller, K. Urmann, M. R. Hoffmann and J. Bahnemann, 3D Printed Microfluidic Mixers-A Comparative Study on Mixing Unit Performances, *Small*, 2019, **15**, e1804326.
- 37 ISO 20776-1:2020, Susceptibility testing of infectious agents and evaluation of performance of antimicrobial susceptibility test devices
- 38 B. O'Brien, J. Liang, S. Chaturvedi, J. L. Jacobs and V. Chaturvedi, Pan-resistant *Candida auris*: New York subcluster susceptible to antifungal combinations, *The Lancet Microbe*, 2020, **1**, e193-e194.
- 39 H. Leonard, R. Colodner, S. Halachmi and E. Segal, Recent Advances in the Race to Design a Rapid Diagnostic Test for Antimicrobial Resistance, *ACS sensors*, 2018, **3**, 2202–2217.
- 40 M. Fiema, A. Wlodarczyk, J. Wojkowska-Mach, J. Garlicki and I. Gregorczyk-Maga, Atypical Presentation of *Aspergillus niger* Infection in the Oral Cavity as a Prediction of Invasive Pulmonary Aspergillosis in a Patient with COVID-19: Case Report and Literature Review, *Microorganisms*, 2022, **10**, 1630.
- 41 R. Kean, J. Brown, D. Gulmez, A. Ware and G. Ramage, *Candida auris*: A Decade of Understanding of an Enigmatic Pathogenic Yeast, *Journal of fungi*, 2020, **6**, 30.
- 42 G. Bravo Ruiz and A. Lorenz, What do we know about the biology of the emerging fungal pathogen of humans *Candida auris*?, *Microbiological Research*, 2021, **242**, 126621.
- 43 A. A. Bhalodi, N. Oppermann, S. A. Campeau and R. M. Humphries, Variability of Beta-Lactam Broth Microdilution for *Pseudomonas aeruginosa*, *Antimicrobial agents and chemotherapy*, 2021, **65**, e0064021.
- 44 A. Espinel-Ingroff, M. C. Arendrup, M. A. Pfaller, L. X. Bonfietti, B. Bustamante, E. Canton, E. Chryssanthou, M. Cuenca-Estrella, E. Dannaoui, A. Fothergill, J. Fuller, P. Gaustad, G. M. Gonzalez, J. Guarro, C. Lass-Flörl, S. R. Lockhart, J. F. Meis, C. B. Moore, L. Ostrosky-Zeichner, T. Pelaez, S. R. B. S. Pukinskas, G. St-Germain, M. W. Szeszs and J. Turnidge, Interlaboratory variability of Caspofungin MICs for *Candida* spp. Using CLSI and EUCAST methods: should the clinical laboratory be testing this agent?, *Antimicrobial agents and chemotherapy*, 2013, **57**, 5836–5842.

## References

- 45 F. M. Klis, C. G. de Koster and S. Brul, Cell wall-related bionumbers and bioestimates of *Saccharomyces cerevisiae* and *Candida albicans*, *Eukaryotic cell*, 2014, **13**, 2–9.
- 46 H. Leonard, X. Jiang, S. Arshavsky-Graham, L. Holtzman, Y. Haimov, D. Weizman, S. Halachmi and E. Segal, Shining light in blind alleys: deciphering bacterial attachment in silicon microstructures, *Nanoscale horizons*, 2022, **7**, 729–742.
- 47 D. Trofa, A. Gácsér and J. D. Nosanchuk, *Candida parapsilosis*, an emerging fungal pathogen, *Clinical Microbiology Reviews*, 2008, **21**, 606–625.



## **Acknowledgements**

First and foremost, I would like to express my gratitude to my advisors, Prof. Thomas Scheper and Prof. Ester Segal, for giving me the opportunity to pursue a dual PhD program at Leibniz University Hannover and the Technion. This experience has allowed me to meet wonderful people, gain invaluable insights, and immerse myself in a different culture. I am deeply grateful for your guidance, mentorship, and support, which have made my research complete and meaningful.

I would also like to extend a special thanks to Prof. Janina Bahnemann, who welcomed me into her research group and gave me the chance to combine my research with the benefits of 3D printing. Thank you for your ongoing support, and I look forward to continuing in Augsburg and working on exciting new research projects together. In addition, I would like to thank PD Dr. Ulrich Krings and Prof. Sascha Beutel for their willingness to serve on my PhD defence committee.

I am grateful for the wonderful working atmosphere at the TCI and would like to express my appreciation to Martina Weiß, Ulla Dreschel, Christiane Hellweg, Martin Pähler, and Frank Stahl, as well as Friedbert Gellermann, Thorsten Stempel, and Thorleif Hentrop from the workshops at TCI. I would also like to thank the PCR core team, Johanna, Alina, John, and Torsten; it was great working with you on this project. A special thank you to Jana for her friendship and for sharing the “TCI career” from the bachelor to the doctoral studies.

I am also thankful to the members of the Bahnemann group, including Carlotta, Katharina, Michi, Xenia, Anton, John, Steffen, Nicolas, Marc, Taieb, and Jonathan, for engaging in valuable scientific discussions and the great time outside of the lab. I would like to thank John, in particular, for his hard work on the gradient generator project.

Of course, I cannot forget to thank the members of my office, including Anton, John, Riekje, Tessa, Laura, Laura, and Nico, for creating a great atmosphere and keeping me fueled with coffee and snacks.

I would like to extend my deepest gratitude to the past and present members of the Segal group, including Naama, Heidi, Sofi, Michal, Andy, Racheli, Nelli, Ofer, Talya, Yuexi, Xin, Lisa, Hanan, and Kayan. Thank you for welcoming me to the Technion and making my stay in Israel both enjoyable and successful. I would like to thank Heidi, in particular, for introducing me to the world of silicon-based sensors, and Xin for complementing my research with her hard work in the lab.

Last but certainly not least, I would like to thank my family for their unconditional support throughout my studies, especially during my time abroad, and for laying the foundation that made this work possible.

## List of Publications and Academic Activities

### List of Publications:

- 1 M. von der Haar, **C. Heuer**, M. Pähler, K. von der Haar, P. Lindner, T. Scheper and F. Stahl, Optimization of Cyanine Dye Stability and Analysis of FRET Interaction on DNA Microarrays, *Biology*, 2016, **5**.
- 2 H. Leonard, **C. Heuer**, D. Weizmann, N. Massad-Ivanir, S. Halachmi, R. Colodner and E. Segal, in *Frontiers in Biological Detection: from Nanosensors to Systems XI*, ed. A. Danielli, B. L. Miller and S. M. Weiss, SPIE, Bellingham, Washington, USA, 2019, p. 3.
- 3 **C. Heuer\***, H. Leonard\*, N. Nitzan, A. Lavy-Alperovitch, N. Massad-Ivanir, T. Scheper and E. Segal, Antifungal Susceptibility Testing of *Aspergillus niger* on Silicon Microwells by Intensity-Based Reflectometric Interference Spectroscopy, *ACS infectious diseases*, 2020, **6**, 2560–2566. (\*equal contribution)
- 4 M. Witt, **C. Heuer**, L. Miethke, J.-A. Preuß, J. S. Rehfeld, T. Schüling, C. Blume, S. Thoms and F. Stahl, Nachweismethoden von SARS-CoV-2, *Chem. Unserer Zeit*, 2020, **54**, 368–376.
- 5 J. Aranda Hernandez, **C. Heuer**, J. Bahnemann and N. Szita, Microfluidic Devices as Process Development Tools for Cellular Therapy Manufacturing, *Advances in biochemical engineering/biotechnology*, 2021, **179**, 101–127.
- 6 **C. Heuer**, J. Bahnemann, T. Scheper and E. Segal, Paving the Way to Overcome Antifungal Drug Resistance: Current Practices and Novel Developments for Rapid and Reliable Antifungal Susceptibility Testing, *Small methods*, 2021, **5**, e2100713.
- 7 **C. Heuer**, J.-A. Preuß, T. Habib, A. Enders and J. Bahnemann, 3D printing in biotechnology-An insight into miniaturized and microfluidic systems for applications from cell culture to bioanalytics, *Engineering in life sciences*, 2022, **22**, 744–759.
- 8 S. Arshavsky-Graham, **C. Heuer**, X. Jiang and E. Segal, Aptasensors versus immunosensors - Which will prevail?, *Engineering in life sciences*, 2022, **22**, 319–333.
- 9 T. Habib, C. Brämer, **C. Heuer**, J. Ebbecke, S. Beutel and J. Bahnemann, 3D-printed microfluidic device for protein purification in batch chromatography, *Lab on a chip*, 2022, **22**, 986–993.
- 10 S. Winkler, K. V. Meyer, **C. Heuer**, C. Kortmann, M. Dehne and J. Bahnemann, In vitro biocompatibility evaluation of a heat-resistant 3D printing material for use in customized cell culture devices, *Engineering in life sciences*, 2022, **22**, 699–708.
- 11 **C. Heuer\***, J.-A. Preuss\*, M. Buttkewitz, T. Scheper, E. Segal and J. Bahnemann, A 3D-printed microfluidic gradient generator with integrated photonic silicon sensors for rapid antimicrobial susceptibility testing, *Lab on a chip*, 2022, **22**, 4950–4961. (\*equal contribution)

## List of Publications and Academic Activities

- 12 M. A. Buttkewitz, **C. Heuer**, and J. Bahnemann, Sensor Integration into Microfluidic Systems: Trends and Challenges, *Current Opinion in Biotechnology*, 2023, **83**, 102978.
- 13 **C. Heuer**, X. Jiang, T. Scheper, J. Bahnemann, and E. Segal, Photonic Si Microwell Architectures for Rapid Antifungal Susceptibility Determination of *Candida auris*, *Chemical Communications*, 2024.

## List of Conferences:

### Oral Presentations:

- 1 X. Jiang\*, **C. Heuer\***, T. Borkum, H. Leonard, N. Massad-Ivanir, R. Colodner, M. Strauss, S. Halachmi, S. Shprits, E. Segal, Diagnostic System for Rapid Antimicrobial Susceptibility Testing, of Clinical Samples, Porous Semiconductors Science and Technology International Conference, Lido di Camaiore, Italy, 2022. (\*shared oral presentation)

### Poster Presentations:

- 1 **C. Heuer**, H. Leonard, N. Nadav, A. Lavy-Alperovitch, N. Massad-Ivanir, J. Bahnemann, T. Scheper, E. Segal, Rapid Antifungal Susceptibility Testing on Silicon Microwells, MicroTAS, online conference, 2020
- 2 J.A. Preuß\*, **C. Heuer\***, M. Buttkewitz, J. Bahnemann, Integration of Photonic Silicon Chips in a 3D-Printed Microfluidic Gradient Generator for Antimicrobial Susceptibility Testing, 13th European Congress of Chemical Engineering & 6th European Congress of Applied Biotechnology (ECCE/ECAB), DECHEMA, online conference, 2021. (\*equal contribution)
- 3 J.A. Preuß\*, **C. Heuer\***, M. Buttkewitz, S. Arshavsky-Graham, E. Segal, J. Bahnemann, A 3D-Printed Microfluidic Gradient Generator for Parallelization of Porous Silicon-Based Sensor Systems, MicroTAS, Palm Springs, USA, 2021. (\*equal contribution)
- 4 **C. Heuer**, H. Leonard, N. Nitzan, A. Lavy-Alperovitch, N. Massad-Ivanir, T. Scheper, E. Segal, Antifungal Susceptibility Testing of *Aspergillus niger* in Silicon Microwells by Intensity-Based Reflectometric Interference Spectroscopy, Porous Semiconductors Science and Technology International Conference, Lido di Camaiore, Italy, 2022.

**Supervised research thesis:**

Marc Alexander Buttkewitz: „Parallelisierung von optischen PSi-Sensoren mittels 3D-gedruckten mikrofluidischen Systemen“, Master Thesis at the Institute for Technical Chemistry, Leibniz University Hannover, 2021.

**Other activities:**

Participation in the Mobile Corona Analytik (MCA) project at the Institute for Technical Chemistry, Leibniz University Hannover (April – November 2020)

## Curriculum Vitae

### Personal Information

Name Christopher Heuer

Date and Place of Birth 18. October 1994, Gehrden

Nationality German

### Education

Since 2019 PhD student at the Institute of Technical Chemistry, Leibniz University Hannover and the Department of Biotechnology and Food Engineering, Technion – Israel Institute of Technology (International PhD program).

2016 – 2018 M. Sc. in Life Science at Leibniz University Hannover

2018 Master thesis project (Mar. – Aug.) in the research group of Prof. Ester Segal at the Technion - Israel Institute of Technology, Haifa, Israel

2017 Research project (Sept. – Dec.) in the research group of Prof. Alexander Frey at Aalto-University, Helsinki, Finland

2013 – 2016 B. Sc. in Life Science at Leibniz University Hannover

2005 – 2013 General qualification for university entrance, Georg Büchner Gymnasium Letter

### Work Experience

Since 2022 Research associate at the Institute of Physics, Augsburg University

2019 – 2022 Doctoral research assistant at the Institute of Technical Chemistry, Leibniz University Hannover

2016 – 2017 Student assistant at the Institute of Technical Chemistry, Leibniz University Hannover